Characterization of transiting exoplanets and their host stars by *K2*

Teo Močnik

Doctor of Philosophy
Keele University
December 2018

Abstract

The WASP project has discovered many transiting gas giant exoplanets. Some of these exoplanet systems have been observed by the *K2* space-based telescope. The much higher photometric precision, shorter cadence and extended continuous follow-up observations provided by the *K2* mission enabled the most detailed photometric characterization yet of the WASP and other planetary systems presented in this thesis, which contributes to our understanding of how planets form and evolve.

I analysed the majority of transiting exoplanet systems observed by the *K2* in the 1-min short-cadence mode within the first 14 regular observing campaigns. I present here the analysis and results for a total of 10 planetary systems observed in the short-cadence mode. I detected starspot occultation events in two aligned and one misaligned planetary system and proved that detecting starspot occultation events is possible in the *K2* data. I also detected optical phase-curve modulations in two systems, rotational modulations in four and γ Doradus pulsations in one planetary system. I refined the system parameters for all short-cadence targets and used non-detections to provide tight upper limits. In addition, I discovered a hot Jupiter using the long-cadence *K2* data and refined the ephemeris with the WASP data of another *K2*-discovered planet.

Acknowledgements

I would like to thank all collaborators for their valuable help and contributions. In particular, I wish to thank my supervisor Prof. Coel Hellier for his brilliant advice, which helped me steer through the PhD.

I gratefully acknowledge the financial support from the Science and Technology Facilities Council and Keele University.

This thesis includes data collected by the *K2* mission. Funding for the *K2* mission is provided by the NASA Science Mission directorate. This research has made use of the NASA Exoplanet Archive, which is operated by the California Institute of Technology, under contract with NASA under the Exoplanet Exploration Program. Some of the data presented in this thesis were obtained from the Mikulski Archive for Space Telescopes (MAST). STScI is operated by the Association of Universities for Research in Astronomy, Inc., under NASA contract NAS5-26555. This work made use of `PyKE` software package for the reduction and analysis of *Kepler* data, which is developed and distributed by the NASA *Kepler* Guest Observer Office. WASP-South is hosted by the South African Astronomical Observatory and WASP-North by the Isaac Newton Group of Telescopes and the Instituto de Astrofísica de Canarias. We are grateful for their ongoing support and assistance. TRAPPIST is funded by the Belgian Fund for Scientific Research (Fond National de la Recherche Scientifique, FNRS) under the grant FRFC 2.5.594.09.F, with the participation of the Swiss National Science Fundation (SNF). The Euler Telescope is operated by the University of Geneva thanks to a grant by the Swiss National Science Foundation.

The Author

The author graduated in physics at the University of Ljubljana in 2012. During his undergraduate studies, he worked as a tutor at the university's Observatory Golovec, and in the final year also as a researcher in laser technology at the Jožef Stefan Institute in Ljubljana.

In 2013, the author obtained a degree of MSc by Research in Astronomy and Astrophysics at The University of Manchester. His research project was based in the field of planetary nebulae, kindly supervised by Dr Myfanwy Lloyd.

The author gained substantial professional observing experience between September 2013 and December 2014 while working as a student support astronomer at the 2.5-m Isaac Newton Telescope. This 15-month-long studentship programme was offered by the Isaac Newton Group of Telescopes, which operates at the Roque de Los Muchachos Observatory on the Canary island of La Palma.

Following the ING Studentship Programme, the author started his PhD course in astrophysics at Keele University in January 2015. This thesis presents the author's research work conducted at Keele University in the field of exoplanets.

Teo Močnik

The author is funded by
the Science and Technology Facilities Council and Keele University.

Contents

Abstract 3

Acknowledgements 4

The Author 5

1 Introduction 14

1.1 Motivation 14
1.2 Definition of an Exoplanet 15
1.3 Formation and Migration Theories 16
1.4 Transiting Planets 18
1.4.1 Transit Observables 21
1.4.2 Transit-timing and Transit-duration Variations 24
1.5 Phase-curve Modulations 28
1.5.1 Tidal Ellipsoidal Distortion 29
1.5.2 Doppler Beaming 30
1.5.3 Reflection and Thermal Emission 32
1.6 Starspots on Exoplanet-host Stars 35
1.6.1 Rotational Modulations 35
1.6.2 Starspot Occultations 38
1.7 WASP Transit Survey 40
1.8 *K2* Mission 43
1.9 Conclusion and Thesis Outline 47

2 *K2* Data Reduction Procedure 49

2.1 Description of *K2* Data 49
2.2 Using Raw *K2* Data as an Early Preview 52
2.3 Default Data Reduction Procedure 54
2.3.1 Defining Extraction Aperture 54
2.3.2 Light Curve Extraction 56
2.3.3 Removal of Low-frequency Modulations 58
2.3.4 Self-flat-fielding Correction 60
2.4 Modified `K2SC` Procedure 67
2.5 Procedures for Correcting *K2* Systematics 70

3 *K2* Observing Campaigns 73

4 WASP-85 76
4.1 Abstract 76
4.2 Introduction 77
4.3 The *K2* Observations 79
4.4 Analysis and Results 82
4.4.1 System Parameters 82
4.4.2 TTV and TDV 87
4.4.3 Starspot Detection 89
4.4.4 Are the Starspots Recurring? 92
4.4.5 Rotational Modulation 93
4.4.6 Phase-curve Variations 94
4.5 Conclusion and Discussion 96

5 WASP-47 98
5.1 Introduction 98
5.2 Detecting Additional Transiting Planets 99

6 WASP-75 and WASP-55 102
6.1 Abstract 102
6.2 Introduction 103
6.3 Data Reduction 104
6.3.1 Data Extraction 104
6.3.2 De-trending 105
6.4 System Parameters 107
6.5 No Transit Duration or Timing Variations 111
6.6 No Starspot Occultations but Stellar Variation in WASP-75 112
6.7 No Phase-curve Variations 114
6.8 No Additional Transiting Planets 115
6.9 Conclusions 116

7 WASP-157 118
7.1 Abstract 118
7.2 Introduction 119
7.3 Observations 120
7.4 Spectral Analysis 123
7.5 Light Curve Modulations 124
7.6 System Parameters 126
7.7 Stellar Age 130
7.8 Conclusions 131

8 Qatar-2 133
8.1 Abstract 133

8.2 Introduction 134
8.3 *K2* Observations 136
8.4 Barycentric-corrected TRES RVs 137
8.5 System Parameters 138
8.6 TTV and TDV 141
8.7 Rotational Modulation 142
8.8 Starspots 143
  8.8.1 Detection 143
  8.8.2 Rotational Period 147
  8.8.3 Obliquity 149
  8.8.4 Starspot Lifetimes 153
8.9 Phase-curve Modulation 154
8.10 No Additional Transiting Planets 156
8.11 Age of the Host Star 156
8.12 Conclusions 157

9 WASP-118 and WASP-107 159
9.1 Abstract 159
9.2 Introduction 160
9.3 The *K2* Observations 162
9.4 System Parameters 166
9.5 No TTV or TDV 169
9.6 Starspots on WASP-107 169
9.7 Rotational Modulation of WASP-107 172
9.8 Stellar Pulsations of WASP-118 173
9.9 No Phase-curve Modulations 176
9.10 No Additional Transiting Planets 177
9.11 Ages of the Host Stars 177
9.12 Conclusions 179

10 WASP-28 and WASP-151 180
10.1 Abstract 180
10.2 Introduction 180
10.3 Targets 182
10.4 *K2* Observations and Data Reduction 182
  10.4.1 Background Brightening Events 185
10.5 System Parameters 189
10.6 No TTV or TDV 192
10.7 No Starspots 195
10.8 No Phase-curve Modulations 196
10.9 No Additional Transiting Planets 197

10.10 Conclusions 197

11 K2-140 199

11.1 Ephemeris Refinement 199

12 WASP-104 202

12.1 Abstract 202

12.2 Introduction 203

12.3 *K2* Observations and Data Reduction 204

12.4 Refinement of System Parameters 207

12.5 No TTV or TDV 210

12.6 Rotational Modulation 211

12.7 No Starspot Occultations 213

12.8 Phase-curve Modulation 215

12.9 No Additional Transiting Planets 218

12.10 Conclusions 219

13 Results Overview 221

14 Discussion 225

14.1 Stellar Activity 225

14.2 Photometric Signatures of Orbital Motion 227

14.3 Planetary Radii Inflation 228

15 Conclusions and Future Work 232

15.1 *K2* and My Research Contribution 232

15.2 *TESS* 234

15.3 Overview of Upcoming Space-based Missions 237

Acronyms 242

Publications 243

Lead-authored 243

Co-authored 244

References 245

List of Figures

1.1: Evolution tracks of a giant planet 18
1.2: Numbers of confirmed exoplanets 19
1.3: Transit light curve observables 21
1.4: TTVs of Kepler-18 26
1.5: TTVs and TDVs of KOI-142b 27
1.6: Phase-curve modulation components 29
1.7: Amplitudes of phase-curve modulation components 34
1.8: Rotational modulation and positions of starspots 36
1.9: Simulated planetary transit of the spotted Sun 39
1.10: WASP-South instrument 41
1.11: Photometric precision of WASP instruments 42
1.12: Celestial distribution of WASP planets 42
1.13: Diagram of the *K2* spacecraft components 44
1.14: Photometric precision of *Kepler* and uncorrected *K2* light curves 45
1.15: *K2* CCD modules 46
1.16: Timeline of the *K2* mission 47
2.1: Full frame *K2* long-cadence image 50
2.2: Photometric extraction aperture 55
2.3: Flattening and normalization procedure 59
2.4: Modified `kepsff` tool 62
2.5: Gaussian convolution 63
2.6: Transit masking 64
2.7: Theoretical *Kepler* photometric precision 65
2.8: Photometric precision as a function of position in the *K2* FOV 66
2.9: Comparison between `kepsff` and `K2SC` 69
2.10: Comparison between `kepsff`, `K2SC` and `EVEREST 2.0` 71
3.1: *K2* FOV for every observing campaign 75
4.1: High resolution image of WASP-85 binary 78
4.2: SFF calibration procedure 81
4.3: Light curve of WASP-85 82

4.4: Best-fit MCMC model for WASP-85Ab 86
4.5: Corner plot of posterior distributions for MCMC model for WASP-85Ab 87
4.6: TTV and TDV for WASP-85Ab 88
4.7: Starspot occultations in the model-subtracted light curve of WASP-85Ab 90
4.8: Autocorrelation function of the WASP-85 light curve of 93
4.9: Phase curve of WASP-85 95
5.1: A section of WASP-47 light curve 99
5.2: BLS periodograms for WASP-47 101
6.1: Asteroid flyby near WASP-75 105
6.2: Asteroid-brightening event in WASP-75b light curve 105
6.3: Performance of systematics removal procedure for WASP-75 106
6.4: Light curves of WASP-55 and WASP-75 107
6.5: Transit model for WASP-55b 110
6.6: Transit model for WASP-75b 111
6.7: Potential rotational modulation of WASP-75 113
6.8: Phase curves of WASP-75 and WASP-55 115
7.1: Light curve of WASP-157 122
7.2: Phase curve of WASP-157 125
7.3: Transit models for WASP-157b 129
7.4: RV model for WASP-157b 130
7.5: Isochrone of WASP-157 131
8.1: Light curve of Qatar-2 137
8.2: Transit model for Qatar-2b 140
8.3: TTV and TDV for Qatar-2b 142
8.4: Lomb–Scargle periodogram for Qatar-2 143
8.5: Starspot occultations for Qatar-2b 145
8.6: Starspot longitudes and phases for Qatar-2 148
8.7: Starspot models for Qatar-2b transits 46–50 152
8.8: Starspots latitudes and longitudes for Qatar-2b transits 46–50 153
8.9: Phase curve of Qatar-2b 155
9.1: Light curve of WASP-107 164
9.2: Light curve of WASP-118 165
9.3: Pulsations of WASP-118 165
9.4: Transit model for WASP-107b. 167
9.5: Transit model for WASP-118b. 168

9.6: Starspot occultations for WASP-107b ... 170
9.7: Lomb–Scargle periodogram of WASP-107 ... 173
9.8: Lomb–Scargle periodogram of WASP-118 ... 174
9.9: Position of WASP-118 in the HR diagram of pulsation types ... 175
10.1: Light curve of WASP-28 ... 184
10.2: Light curve of WASP-151 ... 185
10.3: Brightening events ... 187
10.4: The passage of Mars through the *K2*’s FOV ... 188
10.5: WASP-151 asteroid flyby, causing the brightening event at BJD 2457799. ... 188
10.6: Transit model of WASP-28 ... 190
10.7: Transit model of WASP-151 ... 191
10.8: Long-term transit-timing stability of WASP-28 ... 193
11.1: BLS periodogram of WASP light curve of K2-140 ... 200
12.1: Light curve of WASP-104 ... 206
12.2: Transit model of WASP-104b ... 209
12.3: Rotational modulation of WASP-104 ... 212
12.4: Lomb–Scargle periodogram for WASP-104 ... 212
12.5: Phase curve of WASP-104b ... 216
13.1: Radius versus orbital period distribution of analysed planets ... 224
13.2: Radius versus mass distribution of analysed planets ... 224
14.1: Planet radius inflation versus mass and insulation ... 230
15.1: Photometric precision of *TESS* ... 236
15.2: Durations of current and future exoplanet space-based missions ... 237

List of Tables

2.1: Overview of available procedures for correcting drift artefacts 70
3.1: *K2* observing campaigns 74
4.1: System parameters for WASP-85 85
4.2: Starspot occultation events of WASP-85 91
6.1: System parameters for WASP-55 108
6.2: System parameters for WASP-75 109
7.1: Log of WASP-157 observations 122
7.2: RVs and bisector spans for WASP-157 123
7.3: Spectroscopic parameters for WASP-157 124
7.4: System parameters for WASP-157 128
8.1: TRES barycentric-corrected RVs for Qatar-2 138
8.2: System parameters for Qatar-2 140
8.3: Starspot phases and longitudes for Qatar-2 146
8.4: Stellar rotational period of every starspot for Qatar-2 148
8.5: Starspot positions for Qatar-2b transits 46–50 152
9.1: System parameters for WASP-107 and WASP-118 168
9.2: Starspot phases and longitudes for WASP-107 171
10.1: Light-curve brightening events for WASP-107 and WASP-118 186
10.2: System parameters for WASP-28 191
10.3: System parameters for WASP-151 192
10.4: Transit timings of WASP-28b and WASP-151b 194
12.1: System parameters for WASP-104 209
13.1: Overview of performed analysis and detections 222

1 Introduction

1.1 Motivation

How planets form and migrate is not yet fully understood. One way to study these is through numerical simulations, whose outcomes must match observational data. One of the best readily-accessible observational tracers of planets' formation and migration history are the orbital and physical parameters for a large number of planetary systems and in particular the orientations of orbital planes with respect to the rotations of their host stars.

High-precision photometry and extended continuous observing campaigns of short-cadence space-based observations allow us to characterize transiting planetary systems in great level of detail. Compared to typical ground-based photometric instrumentation, such observations may reveal additional shallower planetary transit signals and more precise measurements of transit-timing variations which provide a more complete view of planetary configurations. Short-cadence and high-precision photometric observations of a large number of transits are also crucial for detecting and tracing starspot occultation events, which may reveal the misalignment angle between stellar rotational and planet's orbital axis.

Besides searching for photometric signatures of any additional planets and attempts to measure obliquities through starspot occultations, obtaining and analysing high-quality light curves of stars hosting known transiting planets is motivated further by the possibility to refine system parameters and to detect any low-amplitude astrophysical signals that are usually elusive to ground-based telescopes. These include measuring stellar rotational periods through the rotational modulations, and searching for phase-curve and any other photometric modulations such as pulsations.

The aim of this thesis is to present a data reduction procedure and results of analysing a significant fraction of transiting exoplanetary systems observed by the *Kepler* telescope during the *K2* mission in the 1-min short-cadence observing mode.

1.2 Definition of an Exoplanet

According to the working definition of an exoplanet, set by the Working Group on Extrasolar Planets (WGESP) of the International Astronomical Union (IAU) (WGESP 2003), an exotrasolar planet is:

- a celestial object that orbits a star other that the Sun or a stellar remnant;
- its mass does not exceed 13 Jupiter masses (M_J). Calculations performed prior to 2003 have shown that for an object with solar metallicity and mass higher than 13 M_J the primordial deuterium in the core would begin to fuse into helium-3 (Burrows et al. 1996);
- the minimum mass of an exoplanet has to satisfy the criteria for a planet in our solar system, set out by Resolution 5A at the 26th General Assembly of the IAU (IAU 2006):
    - its mass has to be sufficient that the object gains a round shape due to its own gravity;
    - sufficient mass and sufficient number of orbits must ensure that its orbit has been cleared of other objects.

The sensitivities of the current observing techniques are often limited to detecting massive planets with short orbital periods. Therefore, the most important term among the definition terms for an exoplanet listed above is the upper mass limit, which distinguishes between exoplanets and brown dwarfs. However, the planetary status of a few least-massive exoplanets, such as PSR B1257+12b with an assumed mass of 0.02 Earth masses (M_{E}) (Konacki & Wolszczan 2003), is uncertain since their low mass might not be sufficient to clear their orbits and thus may have to be classified as dwarf exoplanets.

Most planets analysed and presented in this thesis are close-in massive gas giant planets, classified as hot Jupiters. Although the official definition for hot Jupiters does not yet exist, some authors define them as planets with masses between 0.1 and 13 M_{J} and orbital periods of less than 10 days (e.g. Wright et al. 2012; Wang et al. 2015). According to the classification by the *Kepler* team (Borucki et al. 2011), Jupiter-sized planets have radii between 6 and 15 Earth's radii (R_{E}).

Giant planets with masses below 0.1 M_{J} are termed ice giants, and separated further into super-Neptunes if their radius is 4–6 R_{E} and sub-Neptunes (2–4 R_{E}) (Sheets & Deming 2017). Even smaller planets are defined as super-Earths (1.25–2 R_{E}) and Earths-sized (<1.25 R_{E}) (Borucki et al. 2011).

1.3 Formation and Migration Theories

Terrestrial planets are thought to form via accretion of initially small solid bodies orbiting their host star, known as planetesimals, until the spacing of planetary orbits becomes large enough that the configuration is stable for the age of the system (Seager 2010). The gas giant planets on the other hand are formed in two steps according to most models: first, a solid core with a critical mass $\sim 10\,M_{\mathrm{E}}$ forms in a similar process as terrestrial planets, then the gas from the protoplanetary disc starts to accrete onto a gaseous envelope around a protoplanet which is embedded in the protoplanetary disc (Mordasini et al. 2012).

Although the possibility of planet migration was introduced early by Goldreich & Tremaine (1980) the interest in planet migration studies grew significantly only after the discovery of the first exoplanet orbiting a main-sequence star, 51 Peg (Mayor & Queloz 1995). The planet was found to be too massive ($0.47\,M_J$) to be able to form so close to its host star (0.053 AU). The discovery of 51 Peg b and later other hot Jupiters shaped the current generally accepted theory of planet formation which predicts that the temperature is too high and the protoplanetary disc's material insufficient at such small radii for the hot Jupiters to form in situ. It is currently believed that while the gas from the protoplanetary disc is being accreted on the protoplanets, the gravitational interaction exchanges the angular momentum between the protoplanetary disc and embedded protoplanets. The exchange of angular momentum causes the accreting protoplanet to migrate inwards for typically several million years until the protoplanetary disc dissipates (Mordasini et al. 2012). Fig. 1.1 illustrates the formation and migration of a giant protoplanet.

The above-described disc migration mechanism results in a system in which the orbital axes of the planets are aligned with the rotational axis of the star, i.e. low stellar obliquity, such as in our solar system (Carrington 1863; Stark & Wöhl 1981; Souami & Souchay 2012). However, according to the Transiting Extrasolar Planets Catalogue (TEPCat[1], Southworth 2011) there are currently 61 systems with projected obliquity higher than 10° among 123 systems with measured obliquity. Furthermore, 17 exoplanets have been found to orbit their host star in a retrograde orbit. The observational evidence that many hot Jupiters are found in misaligned orbits cannot be accounted for solely by disc migration mechanism. Instead, it is believed that planet-

---

[1] http://www.astro.keele.ac.uk/jkt/tepcat/tepcat.html

planet scattering, Kozai mechanism and tidal dissipation play an additional role in shaping misaligned orbits of hot Jupiters (e.g. Triaud et al. 2010).

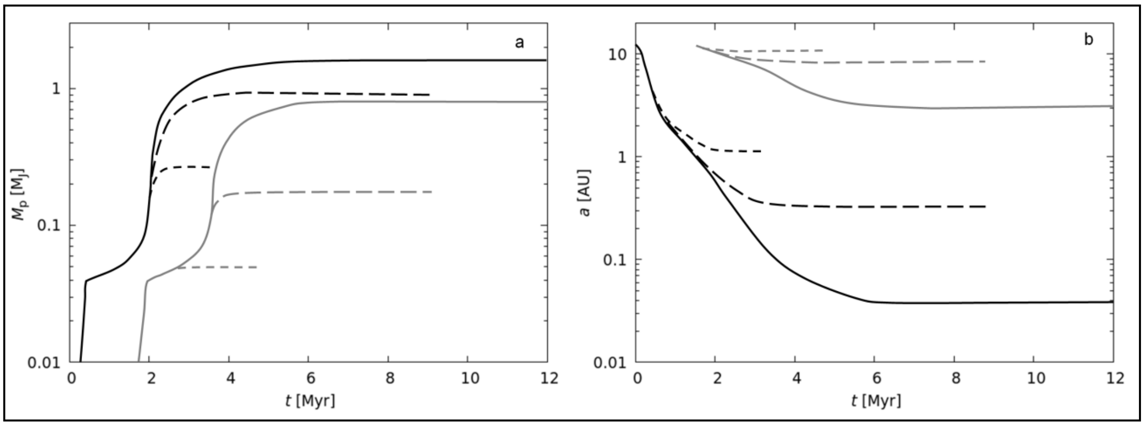

Figure 1.1: Evolution tracks of a giant planet. a: Planet's mass versus time, i.e. planet formation. b: Planet's orbital radius versus time, i.e. planet migration. Two sets of tracks represent cases in which the planet evolution begins at time 0 (black lines) and at 1.5 Myr (grey lines). Within each set of tracks, three different line types represent different values of the rate of ionizing photons emitted by the star (10^{41} s^{-1} solid line, 10^{42} s^{-1} long dashed line, $5 \cdot 10^{42}$ s^{-1} short dashed line). The protoplanetary discs with low photoevaporation and early onset of planet formation lead to substantial migration of giant planets. Adapted from Seager (2010).

1.4 Transiting Planets

So far, seven different detection methods have been used to discover exoplanets. According to the NASA Exoplanet Archive[2] (Akeson et al. 2013) among 3725 confirmed[3] exoplanets to date, 2926 planets have been discovered by detecting planetary transits or transit-timing variations. Fig. 1.2 shows the cumulative number of discovered exoplanets for every discovery method in each calendar year. Each method has its own selection effects in mass, radius, semi-major axis or inclination of the exoplanetary orbit. The rest of this section introduces the transit method in more detail since it is the foundation of my research project.

---

[2] http://exoplanetarchive.ipac.caltech.edu/

[3] Quoted numbers of confirmed planets throughout this thesis include also validated planets.

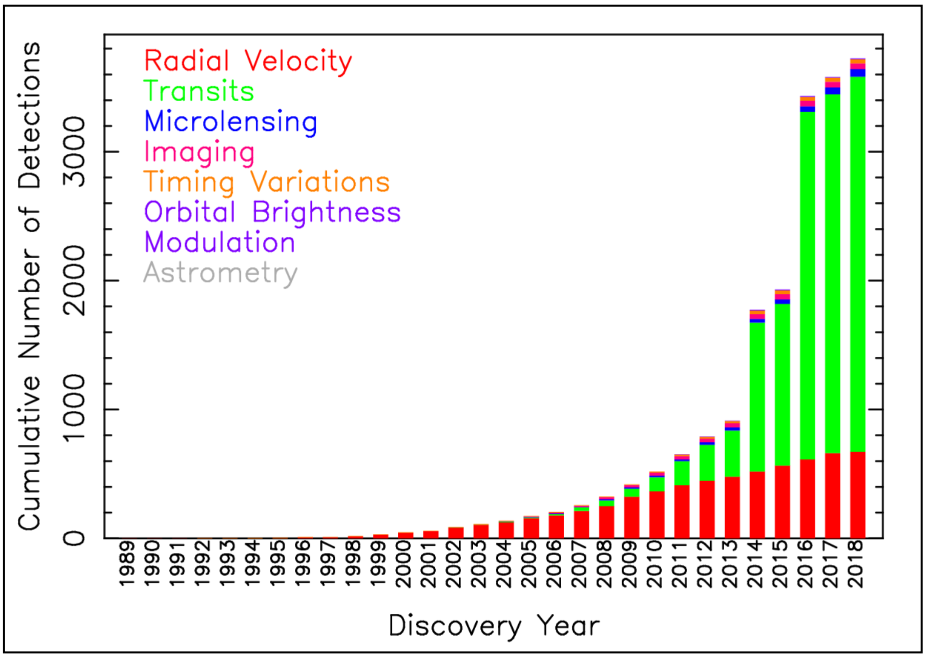

Figure 1.2: The cumulative number of confirmed exoplanets for each of the seven discovery methods. The numbers of discovered exoplanets are accurate as of 2018 May 8. Note the pronounced increase of exoplanets discovered by the transit method in 2014 and 2016, mostly due to the batched *Kepler* planet discoveries announced by Rowe et al. (2014) and Morton et al. (2016), respectively. Plot was retrieved from NASA Exoplanet Archive on 2018 May 8.

An exoplanetary transit occurs when a planet passes in front of a star. Conversely, an exoplanetary occultation (or secondary eclipse) happens when a planet passes behind its host star. Transits and occultations can only be detected in nearly edge-on systems. The probability, $p_{\rm tra}$, to see a transit in a planetary system is (Winn 2010)

$$p_{\rm tra} = \frac{R_* \pm R_{\rm p}}{a} \left(\frac{1 + e \sin \omega}{1 - e^2} \right) , \qquad (1.1)$$

where R_* is the stellar and $R_{\rm p}$ is the planet radius, a is the orbital semi-major axis, e is eccentricity and ω is the argument of periastron. The + sign in equation (1.1) is used to include grazing transits, and – sign applies for only full transits that include the second and third contact points (see Section 1.4.1).

We see from equation (1.1) that the probability of detecting a transiting exoplanet is higher for smaller orbital separations. Due to the limited observing time, it is also more probable to discover exoplanets which transit their host stars more frequently as a result of shorter orbital periods. In addition to close-in orbits, the detections are biased also towards larger planets because they produce deeper transits which are easier to detect.

To illustrate this detection bias, we currently know of 371 planets with periods shorter than 10 days and radius larger than $6\,R_{\mathrm{E}}$, according to NASA Exoplanet Archive. These probable hot Jupiters represent 13% of the 2914 currently confirmed transiting planets with known period and radius. In contrast, hot Jupiters are believed to represent only ∼1% of the entire exoplanet sample according to Doppler surveys (e.g. Wright et al. 2012; Wang et al. 2015), and even less according to the photometric *Kepler* survey, ∼0.4% (Howard et al. 2012; Fressin et al. 2013).

The increased number of discovered transiting exoplanets in recent years is mostly a result of a successful progress of the *Kepler* mission (Borucki et al. 2010) with 2319 confirmed transiting exoplanets and its successor, *K2* (Howell et al. 2014), currently with 292 planets (see Section 1.8). Other notable transit surveys are: Wide Angle Search for Planets (WASP, Pollacco et al. 2006; 123 confirmed transiting planets), *COnvection, ROtation and planetary Transits* (*CoRoT*, Baglin et al. 2006; 29 planets) and the Hungarian-made Automated Telescope (HAT, Bakos et al. 2004; 96 planets). The numbers of confirmed transiting planets are accurate as of 2018 May 8 and were sourced from NASA Exoplanet Archive.

The search for new transiting exoplanets and follow-up observations with the transiting method is scientifically valuable because the analysis of a transit light curve can provide many system parameters (see e.g. Table 4.1), some of which would otherwise not be possible to measure with other methods.

1.4.1 Transit Observables

A light curve of a single transit has four direct observables: transit epoch, transit depth (ΔF), total transit duration between the first and fourth contact points (t_{14}), and transit duration between the second and third contact points (t_{23}). If the light curve contains more than one transit, one can also directly measure the orbital period (P) of the transiting planet. Shown in Fig. 1.3 are two schematic transit light curve scenarios with corresponding contact points.

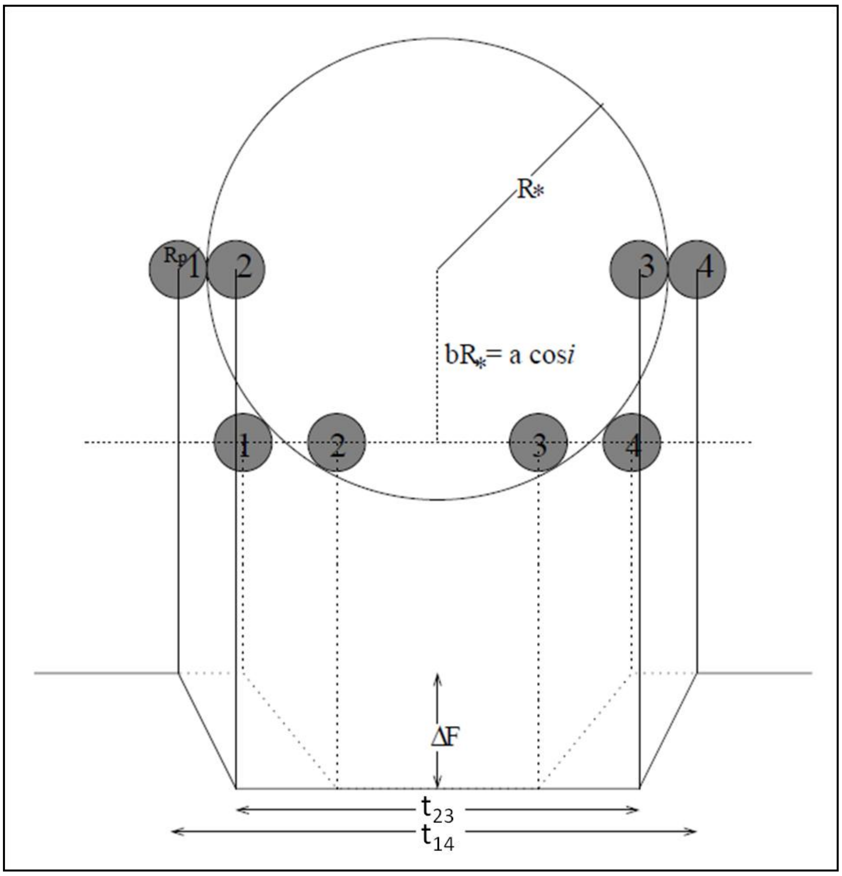

Figure 1.3: Transit light curve observables ΔF, t_{14} and t_{23}. Dark-gray circles represent planet positions at all four contact points during the transit which progresses from left to right. The schematic light curve with a solid line corresponds to the transiting planet that passes the centre of the star, whereas the dotted light curve corresponds to the planet at a higher impact parameter, *b*. Ingress and egress are the dropping and rising components of the light curve, respectively, caused by the planetary motion between contact points from 1 to 2, and from 3 to 4. Credit: Seager & Mallén-Ornelas (2003).

Assuming that a planet is orbiting a much more massive star in a circular orbit and that the star does not exhibit any limb darkening (as in Fig. 1.3), it is possible to derive a set of physical and orbital parameters from the transit light-curve observables alone (Seager & Mallén-Ornelas 2003):

$$\frac{R_\mathrm{p}}{R_*} = \sqrt{\Delta F} \tag{1.2}$$

$$b = \frac{a}{R_*}\cos i = \sqrt{\frac{(1-\Delta F)^2 - (t_{23}/t_{14})^2(1-\Delta F)^2}{1-(t_{23}/t_{14})^2}} \tag{1.3}$$

$$\frac{a}{R_*} = \frac{2P}{\pi}\frac{\Delta F^{1/4}}{(t_{14}^2 - t_{23}^2)^{1/2}} \tag{1.4}$$

$$\rho_* = \frac{32}{G\pi}P\frac{\Delta F^{3/4}}{(t_{14}^2 - t_{23}^2)^{3/2}}\ , \tag{1.5}$$

where ρ_* is the stellar density, *G* is the gravitational constant and *i* the inclination of the planet's orbit. Knowing also the stellar mass-radius relation:

$$R_* = k\, M_*^x\ , \tag{1.6}$$

where *k* and *x* are coefficients specific to certain stellar types (e.g. *k* = 1 for main-sequence stars and *x* = 0.8 for F–K main sequence stars) (Cox 2000), it is possible to derive several physical parameters:

$$\frac{M_*}{M_\odot} = \left(k^3\frac{\rho_*}{\rho_\odot}\right)^{x/(1-3x)} \tag{1.7}$$

$$\frac{R_*}{R_\odot} = k\left(\frac{M_*}{M_\odot}\right)^x = \left(k^{1/x}\frac{\rho_*}{\rho_\odot}\right)^{x/(1-3x)} \tag{1.8}$$

$$\frac{R_p}{R_\odot} = \frac{R_*}{R_\odot}\sqrt{\Delta F} = \left(k^{1/x}\frac{\rho_*}{\rho_\odot}\right)^{x/(1-3x)}\sqrt{\Delta F} \tag{1.9}$$

$$a = \left(\frac{P^2 G M_*}{4\pi^2}\right)^{1/3} , \tag{1.10}$$

where $R_\odot$, $M_\odot$ and $\rho_\odot$ are solar radius, mass and density, respectively.

This simplified set of equations is shown here as a quick reference and to demonstrate how system parameters can be extracted from transit light curve observables. The actual transit light curve analysis and derivation of system parameters performed throughout this thesis follows the procedure presented in Collier Cameron et al. (2007) and is further described in Pollacco et al. (2008). The brief descriptions of the applied procedures are given in sections presenting the system parameter analysis of each analysed planet, and a somewhat more detailed explanation is given for the first analysed planet in Section 4.4.1.

In reality, stellar photospheres do exhibit limb darkening effects, which needs to be taken into account when obtaining transit observables. Equation (1.11) shows the four-parameter limb-darkening law, which was also applied in the analysis of all planetary systems presented in this thesis (Claret 2000):

$$\frac{I(\mu)}{I(1)} = 1 - \sum_{k=1}^{4} a_k\left(1 - \mu^{\frac{k}{2}}\right) , \tag{1.11}$$

where I is the intensity of the stellar photosphere, $\mu = \cos\gamma$ with γ being the angle between the line of sight and the emergent intensity, and a_k are the four limb-darkening coefficients.

The transit photometry itself does not reveal the mass of the planet (see equations 1.2–1.10). However, if the transit photometry is supported by the spectroscopic radial velocity (RV) measurements of the host star, one can obtain the mass ratio between the host star and the planet (see equation 1.12; Cumming, Marcy & Butler 1999), and then by using the stellar mass estimate from equation (1.7) it is possible to derive the mass of the planet.

$$K_1 = \left(\frac{2\pi G}{P \left(M_* + M_\mathrm{p} \right)^2} \right)^{1/3} \frac{M_\mathrm{p} \sin i}{\sqrt{1 - e^2}} \,, \tag{1.12}$$

where K_1 is the RV semi-amplitude of the host star, and e is eccentricity of planetary orbit which can be derived from the amplitude and shape of the RV curve (e.g. Shen & Turner 2008).

1.4.2 Transit-timing and Transit-duration Variations

Close-in planets undergo tidal interactions with their host stars. This leads to orbital decay, circularisation and spin-orbit synchronisation (e.g. Rodríguez et al. 2011 and citations therein). The orbital decay causes the gradual shortening of the orbital period, which can be measured through the transit-timing variations (TTVs) as the long-term monotonic deviations from the constant orbital period.

On the other hand, the short-term and periodic TTVs can be produced by the gravitational interactions between a transiting planet and a third object. Therefore, the periodic TTVs may reveal the presence of any non-transiting perturbing planets in the system (Holman & Murray 2005).

The amplitude and period of TTVs depend on the masses, periods and eccentricities of the perturbed and perturbing planets, and how close the two planets are to a resonant orbit (Δ) (Lithwich, Xie & Wu 2012)

$$\Delta = \frac{P_{\mathrm{out}}}{P_{\mathrm{in}}}\frac{j-1}{j} - 1 \ , \tag{1.13}$$

where P_{out} and P_{in} are the orbital periods of the outer and inner planet, respectively, with a ratio of $P_{\mathrm{out}} : P_{\mathrm{in}} \approx j : j{-}1$, with j being a small integer. The TTV period is then

$$P_{\mathrm{TTV}} = \frac{P_{\mathrm{out}}}{j|\Delta|} \ . \tag{1.14}$$

The semi-amplitudes of the sinusoidal TTVs of the inner and outer planets in circular orbits are

$$TTV_{\mathrm{in}} = P_{\mathrm{in}} \frac{M_{\mathrm{out}}/M_{*}}{\pi j^{2/3}(j-1)^{2/3}\Delta}(-f) \tag{1.15}$$

$$TTV_{\mathrm{out}} = P_{\mathrm{out}} \frac{M_{\mathrm{in}}/M_{*}}{\pi j \Delta}(-g) \ , \tag{1.16}$$

where f and g are the coefficients listed in Table 3 of Lithwich, Xie & Wu (2012). An assumption of circular orbits is typically applicable for close-in planets as they are expected to circularise in short time-scales (Dobbs-Dixon, Lin & Mardling 2004). Eccentric planets, however, produce a higher-amplitude and non-sinusoidal TTVs. A complete set of equations describing TTVs of eccentric planets is given in Lithwich, Xie & Wu (2012).

Shown in Fig. 1.4 is an example of a planetary system Kepler-18 in which the gravitational interactions between an inner planet c and outer planet d near a 2:1 resonance produce easily measurable TTVs. The amplitudes and the period of TTVs of the two transiting Neptune-mass planets can be reproduced with a set of equations (1.13)–(1.16) (shown with a red curve in Fig 1.4).

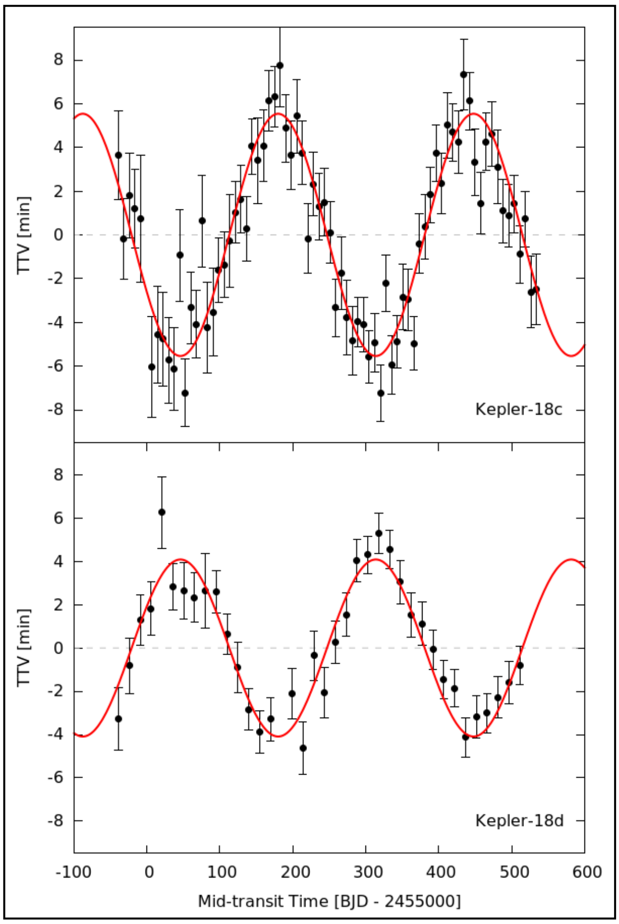

Figure 1.4: TTVs of Kepler-18c (top panel) and Kepler-18d (lower panel). The red curve marks the calculated TTVs using equations (1.13)–(1.16). The measurements to produce this plot were taken from Cochran et al. (2011).

Searching for TTVs is important as it can reveal additional objects in the system and provide an independent mass estimate of interacting objects. Moreover, not accounting for the variable transit timings in systems with non-negligible TTVs may result in erroneous system parameter analysis.

Similarly, the gravitational interactions between a transiting planet and a perturbing object may also cause measurable transit-duration variations (TDVs). TDVs are expected to occur at smaller amplitudes and in phase with TTVs if both variations are caused by the same perturber (Nesvorný et al. 2013). Fig. 1.5 shows an example of TTVs and TDVs of a transiting sub-Neptune perturbed by a non-transiting warm Jupiter near a 2:1 resonance.

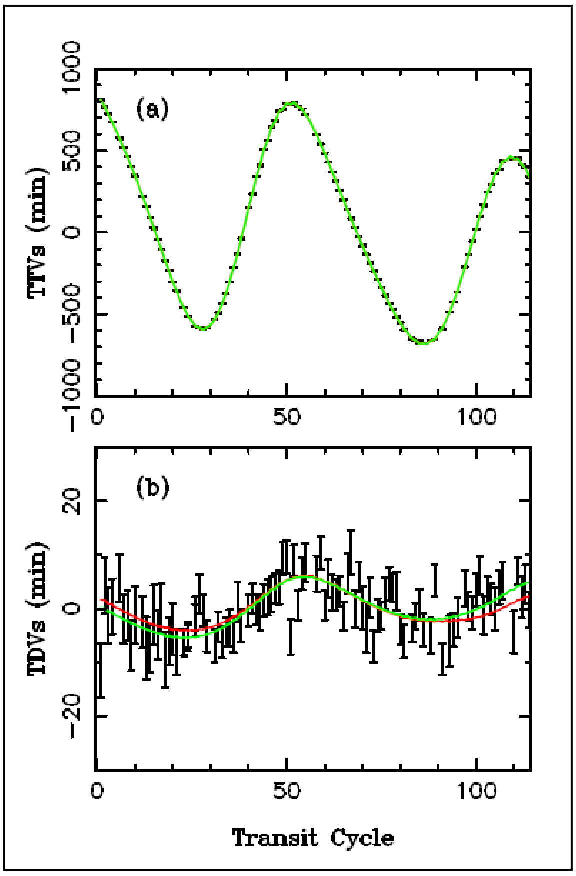

Figure 1.5: TTVs (upper panel) and TDVs (lower panel) of KOI-142b. Credit: Nesvorný et al. (2013).

TTVs and TDVs may also be caused by the perturbing objects that orbit the transiting planet itself. Kipping (2009) suggested that the ratio of TDV to TTV amplitudes could reveal the mass of an exomoon. However, other than one detection of a Neptune-sized exomoon candidate (Teachey, Kipping & Schmitt 2018), there are no reliable detections of exomoons reported so far.

1.5 Phase-curve Modulations

A phase-curve modulation is a photometric modulation caused by an orbital motion in a two-body system. It is a superposition of four components:

- rotation of the ellipsoidally-shaped host star due to the gravitational interaction with the planet (Pfahl, Arras & Paxton 2008);
- Doppler beaming of starlight due to the orbital motion of the star (Loeb & Gaudi 2003);
- reflection of starlight from the surface of the orbiting planet (Jenkins & Doyle 2003);
- thermal emission of the planet (Charboneau et al. 2005).

All four modulation components are in the first order approximation sinusoidal. Because the reflection and thermal emission components have the same period and are also in phase, they are often indistinguishable. Therefore, the reflection and emission components are sometimes jointly referred to as the atmospheric phase-curve modulation. Schematic phase-curve components are shown in Fig. 1.6 and can be expressed with (Mazeh & Faigler 2010)

$$F_{\mathrm{ell}} = -A_{\mathrm{ell}} \cos\left(\frac{2\pi}{P/2} t\right) \tag{1.17}$$

$$F_{\mathrm{Dop}} = A_{\mathrm{Dop}} \sin\left(\frac{2\pi}{P} t\right) \tag{1.18}$$

$$F_{\mathrm{atm}} = -A_{\mathrm{atm}} \cos\left(\frac{2\pi}{P} t\right) \ , \tag{1.19}$$

where F_{ell}, F_{Dop} and F_{atm} are ellipsoidal, Doppler and atmospheric components in a normalized phase curve and A_{ell}, A_{Dop} and A_{atm} are the corresponding semi-amplitudes.

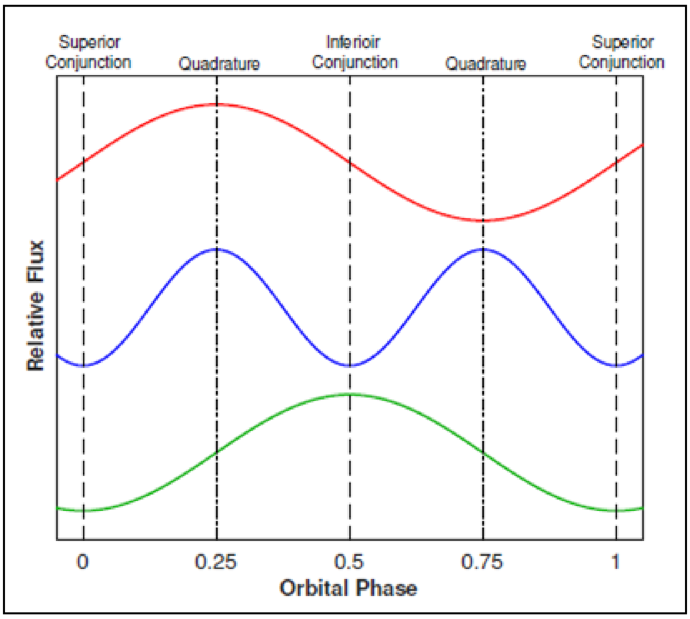

Figure 1.6: Schematic phase-curve modulation components: Doppler (top), ellipsoidal (middle) and atmospheric (bottom). Credit: Shporer (2017).

The following three subsections describe the individual phase-curve components in more detail and provide equations for estimating their amplitudes.

1.5.1 Tidal Ellipsoidal Distortion

The presence of a close-in companion object exerts a gravitational pull, which distorts the primary into a tri-axial ellipsoid. The areas in the stellar photosphere are stretching further away from the centre of the star in a pair of tidal bulges on either side of the star, where the stellar surface gravity is weakest. Due to the gravitational darkening effect, the stellar surface regions with weaker surface gravities exhibit lower effective temperatures and are thus darker than other areas in stellar photosphere (e.g. Espinosa Lara & Rieutord 2011). As a consequence, a star appears darker whenever a gravitationally-darkened tidal bulge is pointing towards an observer. Because there are two tidal bulges on the opposite sides of the star and because their orientation is tracking the orbital motion of the companion, the ellipsoidal modulations exhibit two minima within one orbital period, at superior and inferior conjunctions (see blue curve in Fig. 1.6). The semi-amplitude of the ellipsoidal modulation component can be estimated with (Shporer 2017)

$$A_{\mathrm{ell}} = 13\alpha_{\mathrm{ell}} \sin i \left(\frac{R_*}{R_\odot}\right)^3 \left(\frac{M_*}{M_\odot}\right)^{-2} \left(\frac{P}{\mathrm{day}}\right)^{-2} \left(\frac{M_{\mathrm{p}} \sin i}{M_{\mathrm{J}}}\right) \mathrm{ppm} \ , \tag{1.20}$$

where α_{ell} is of the order of unity and depends on stellar linear limb- (u) and gravity-darkening (g) coefficients:

$$\alpha_{\mathrm{ell}} = 0.15 \frac{(15+u)(1+g)}{3-u} \ . \tag{1.21}$$

Equation 1.20 is the first-order approximation, ignoring the higher order effects, such as the phase lag between a tidal bulge and a planet, or a fast and possibly misaligned stellar rotation. The equation is applicable to main-sequence stars with low-mass companions and is correct within 1% of the more elaborate equations available in e.g. Morris (1985) or Pfahl, Arras & Paxton (2008). As we can see from equation (1.20), the ellipsoidal modulation is most pronounced for a large, low mass star, hosting a massive planet in a close-in edge-on orbit.

The first detection of ellipsoidal modulation induced by an exoplanet was announced by Welsh et al. (2010) in planetary system HAT-P-7.

1.5.2 Doppler Beaming

Doppler beaming (also termed Doppler boosting) is a photometric modulation caused by the stellar motion along the line of sight as the star orbits a common centre of mass with its companion. The resulting periodically-changing RV of the host star affects the perceived stellar flux through the Doppler shift, time dilation and light aberration (Prša et al. 2016). While the time dilation and light aberration make the star appear brighter when the star is moving towards the observer and dimmer when the star is receding, the net effect of the Doppler shift depends on the stellar spectrum and bandpass of the optical system. Since Doppler beaming is directly related to RV of the host star, it has the same period as the planetary orbit and is zero at superior and inferior conjunctions (red curve in Fig. 1.6). For $\mathrm{RV} \ll c$ and $M_\mathrm{p} \ll M_*$ the extent of the effect can be estimated with (Shporer 2017)

$$A_\mathrm{Dop} = 2.7\alpha_\mathrm{Dop} \sin i \left(\frac{P}{\mathrm{day}}\right)^{-1/3} \left(\frac{M_*}{M_\odot}\right)^{-2/3} \left(\frac{M_\mathrm{p} \sin i}{M_\mathrm{J}}\right) \mathrm{ppm} \ , \qquad (1.22)$$

where α_Dop depends on the contribution of Doppler shift to the overall Doppler beaming. The value of α_Dop can be calculated by integrating equation (5) from Shporer (2017) across the stellar spectrum weighted by the transmission curve, or read out from their plot of calculated values in Fig. 2. α_Dop is close to unity for Sun-like stars in the optical wavelengths, higher for cooler stars observed with shorter-wavelength bandpasses, and smaller for hotter stars at longer wavelengths. Similarly as for the ellipsoidal modulations, the Doppler beaming is strongest for low-mass stars, orbited by massive, close-in planets with large inclinations.

Doppler beaming was first theorised by Rybicki & Lightman (1979) and was detected only once before the era of high-precision space-based photometry, in an eclipsing binary system KPD 1930+2752 with a very short orbital period of less than 2.5 hours (Maxted, Marsh & North 2000). Loeb & Gaudi (2003) predicted that Doppler beaming should be detectable also for planetary systems with space-based telescopes, and seven years later, Mazeh & Faigler (2010) announced the first such detection for a sub-stellar object CoRoT-3b.

1.5.3 Reflection and Thermal Emission

Reflectional phase-curve modulation is a result of a variable amount of light reflected towards the observer from a surface of an unresolved companion while it is orbiting a primary. If the companion is in a circular orbit and its dayside hemisphere reflects the incoming stellar flux isotropically, the reflectional modulation is sinusoidal (see equation (1.19)), with maxima at inferior conjunctions (see green curve in Fig. 1.6) when the companion's surface is maximally illuminated as seen by the observer. The amount of atmospheric reflection in a normalized phase curve is (Shporer 2017)

$$A_{\mathrm{atm}} = 570 A_{\mathrm{g}} \sin i \left(\frac{M_*}{M_\odot}\right)^{-2/3} \left(\frac{P}{\mathrm{day}}\right)^{-4/3} \left(\frac{R_{\mathrm{p}}}{R_{\mathrm{J}}}\right)^{2} \mathrm{ppm}\ , \tag{1.23}$$

which depends on the companion's geometric albedo, A_{g}.

However, because close-in companions are hot and expected to be tidally-locked (Mazeh 2008), the thermal emission from their dayside hemispheres also produces a modulation that is in the first order approximation sinusoidal and in phase with reflection. Therefore, the observable amplitude of the atmospheric phase-curve modulation is a superposition of the two underlying processes, reflection and emission, and A_{g} in equation (1.23) should be treated as an *observed* geometric albedo, $A_{\mathrm{g,obs}}$. The *true* geometric albedo, $A_{\mathrm{g,true}}$, can be calculated from $A_{\mathrm{g,obs}}$ by subtracting the contribution of the thermal emission (Cowan, Agol & Charbonneau 2007; Heng & Demory 2013)

$$
\begin{aligned}
A_{\mathrm{g,true}} &= A_{\mathrm{g,obs}} - \frac{F_{\mathrm{day}} - F_{\mathrm{night}}}{F_*}\left(\frac{a}{R_{\mathrm{p}}}\right)^2 = \\
&= A_{\mathrm{g,obs}} - \frac{\pi \int_{\lambda_1}^{\lambda_2} B_\lambda(T_{\mathrm{day}})\mathrm{d}\lambda - \pi \int_{\lambda_1}^{\lambda_2} B_\lambda(T_{\mathrm{night}})\mathrm{d}\lambda}{\pi \int_{\lambda_1}^{\lambda_2} B_\lambda(T_*)\mathrm{d}\lambda}\left(\frac{a}{R_*}\right)^2 \ ,
\end{aligned}
\tag{1.24}
$$

where $(F_{\mathrm{day}} - F_{\mathrm{night}})/F_*$ is a fractional thermal emission modulation. The thermal emission signal can be calculated by integrating the Planck functions B_λ over the photometer's wavelength range λ_1–λ_2 at desired temperatures. T_* is the stellar effective temperature, and T_{day} and T_{night} are the companion's dayside and nightside atmospheric temperatures, respectively (Cowan, Agol & Charbonneau 2007):

$$
T_{\mathrm{day}} = T_* \left(\frac{{R_*}^2}{2a^2}\right)^{1/4} (1 - A_{\mathrm{B}})^{1/4}(1 - f_{\mathrm{dist}})^{1/4} \tag{1.25}
$$

$$
T_{\mathrm{night}} = T_* \left(\frac{{R_*}^2}{2a^2}\right)^{1/4} (1 - A_{\mathrm{B}})^{1/4} f_{\mathrm{dist}}^{1/4} \ , \tag{1.26}
$$

where A_{B} is Bond albedo of the companion and f_{dist} is the heat redistribution parameter. f_{dist} equals 0 if there is no heat redistribution between day- and nightside of the companion, and 0.5 in case of complete heat redistribution. Larger contrasts between day and nightside temperatures produce thermal phase-curve modulations with higher amplitudes.

Thermal phase-curve modulations are routinely searched in the infrared, such as with the *Spitzer* space telescope (e.g. Wong et al. 2016), where the thermal emission of close-in gas giant planets is strongest, at 1–2 μm (Heng & Demory 2013). However, in the optical wavelengths the extent of thermal emission is 1–2 orders of magnitude lower (Shporer 2017).

If a companion object is in an edge-on orbit and passes behind the primary during an inferior conjunction, the reflected and thermally emitted light gets blocked by the occulting star, producing a secondary eclipse. The drop in brightness during this occultation event equals the combined light of reflection and emission, and it lasts as long as transits if the orbit is circular (e.g. Angerhausen, DeLarme & Morse 2015).

Unlike the ellipsoidal and Doppler beaming effects, which are gravitational processes, the atmospheric phase-curve modulation is not a function of the companion’s mass but instead the function of its radius. The amplitude of atmospheric phase-curve modulation is smaller at longer orbital periods, dropping quicker than Doppler beaming and slower than ellipsoidal modulations. Fig. 1.7 visualizes the theoretically expected fractional semi-amplitudes, according to equations (1.20), (1.22) and (1.23) for a hypothetical 10 M_J Jupiter-sized companion orbiting a Sun-like star. The underlying assumption in all three equations is that the companion object is of low-enough mass that any emission emerging from the fusion on the companion is negligible.

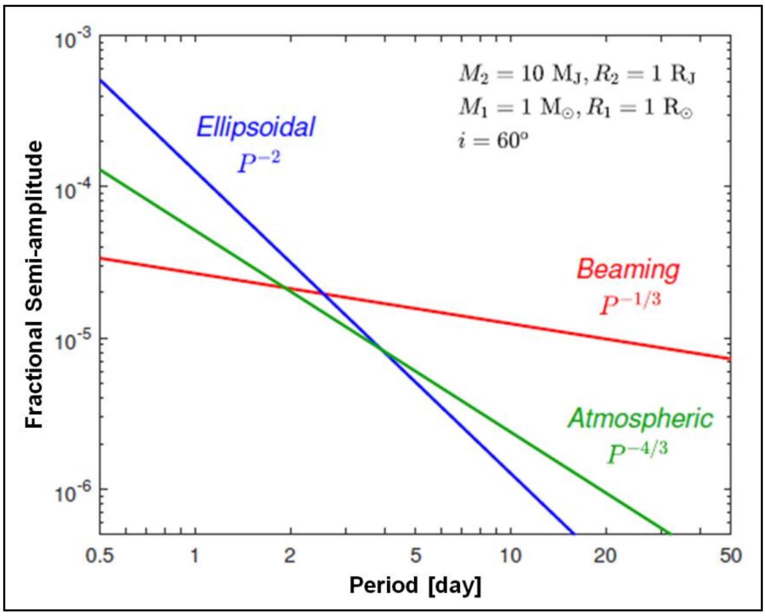

Figure 1.7: Fractional semi-amplitudes of ellipsoidal (blue line), Doppler beaming (red) and atmospheric (green) modulation components. The lines have been calculated using equations (1.20, 1.22 and 1.24) for a 10 M_J, 1 R_J object with $A_{g,obs} = 0.1$ orbiting a Sun-like star with an orbital inclination of 60°. Credit: Shporer (2017).

Detecting ellipsoidal and Doppler beaming modulations can provide an independent estimate of the companion-to-star mass ratio, whereas the atmospheric modulations may reveal basic atmospheric characteristics such as the geometric albedo and companion’s heat distribution (e.g. Esteves, De Mooij & Jayawardhana 2013). Phase-curve modulations may also reveal any non-transiting companions which would otherwise remain unseen in the absence of RV measurements (e.g. Silvotti et al. 2014).

1.6 Starspots on Exoplanet-host Stars

Centuries of direct starspot observations have led to the determination of the solar differential rotation rates (Solanki 2003) and the 7° misalignment angle between solar rotation and ecliptic plane (Carrington 1863). A variety of stars with external convective envelopes have been observed to exhibit magnetic activity similar to that of the Sun (e.g. Kron 1947; Vogt 1975; Kipping 2012). Although starspots are not spatially resolved with the currently available instruments, the rotational periods and obliquities of spotted stars can instead be measured photometrically through the rotational modulations and starspot occultation events.

1.6.1 Rotational Modulations

Stellar rotational periods are measured mainly by two methods: rotational broadening of spectral lines and photometric modulations caused by the rotation of spotted stars. The first advantage of the latter method is that the rotational modulation period is independent of the stellar rotational inclination angle, whereas the line broadening method involves the $\sin i$ uncertainty. And secondly, the rotational modulation method can be applied also to slow rotators which do not exhibit detectable rotational broadenings of spectral lines (Silva-Valio 2008).

Rotational modulations are caused by the presence of dark and bright features on a stellar surface (Kron 1947), namely starspots and plages, respectively. These photospheric features are coming and going from view as the star rotates, resulting in a periodic photometric modulation with minima generally occurring during the highest starspot coverage on the visible surface of the star and maxima at the lowest (see Fig. 1.8).

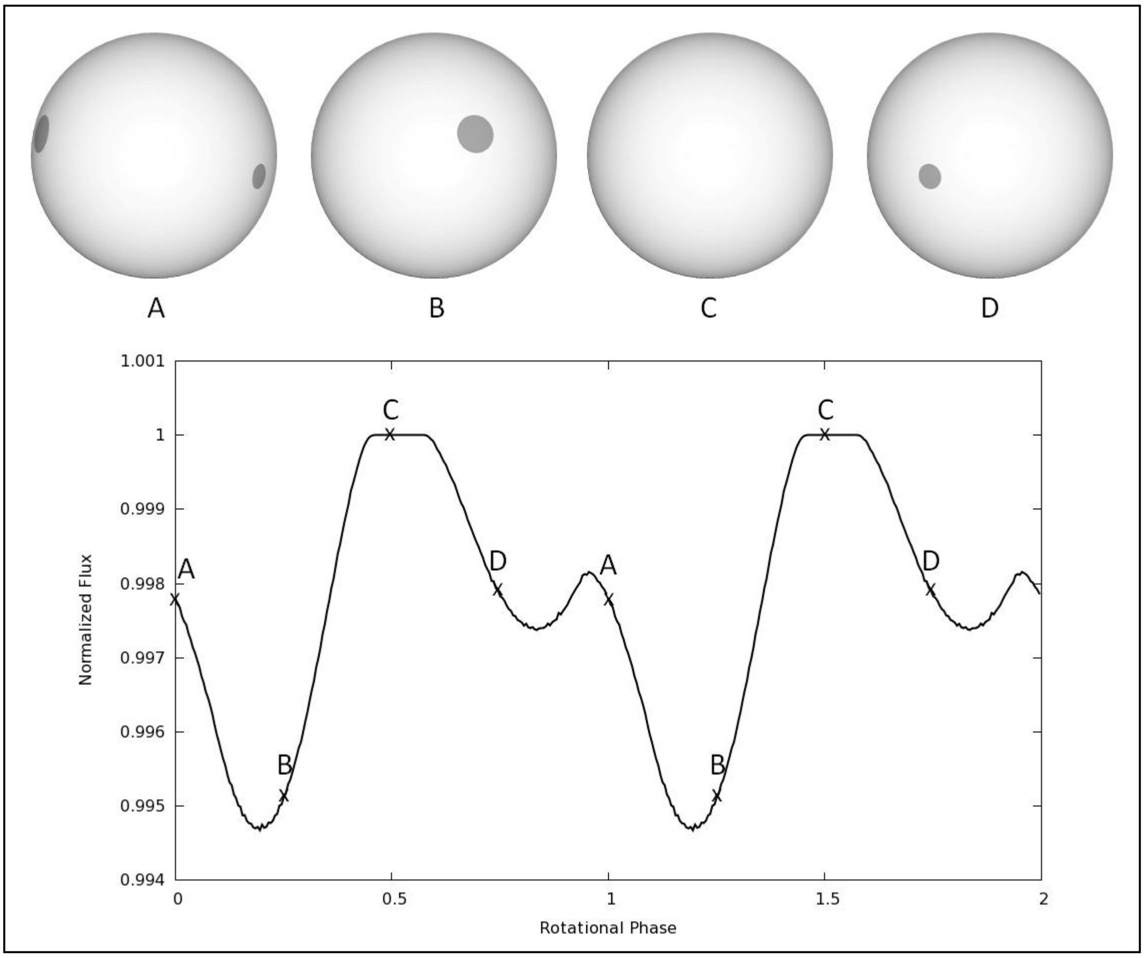

Figure 1.8: Positions of starspots (upper panels) and the corresponding rotational modulation (lower panel). I generated the rotational modulation curve with Spot Oscillation And Planet 2.0 (SOAP 2.0; Dumusque, Boisse & Santos 2014), based on the input parameters of two starspots on a Sun-like star. These are visualised in the upper panels, produced with Planetary Retrospective Integrated Starspot Model (PRISM; Tregloan-Reed, Southworth & Tappert 2013; Tregloan-Reed et al. 2015).

Stellar rotational periods can be measured from rotational modulations with a Lomb–Scargle periodogram (e.g. Nielsen et al. 2013) or autocorrelation analysis (e.g. McQuillan, Aigrain & Mazeh 2013). Stellar rotational periods have several astrophysical uses (Kipping 2012). It is possible to infer the stellar rotational inclination angle by coupling the rotational period, projected rotational velocity and stellar radius (Hirano et al. 2012). Rotational periods may also be used in gyrochronology to estimate the ages of stars (Barnes 2007). However, the gyrochronologically-determined ages of stars hosting planets have often been found to be discrepant with age estimates of other methods, indicative of tidal interactions and a consequent spin-up of the host stars by their planets (Maxted, Serenelli & Southworth 2015b).

Detecting rotational modulations requires extensive observing campaigns that cover several rotational periods and have sufficient photometric precision for a given rotational modulation amplitude. Continuous high-precision photometric monitoring of many stars at once with space-based telescopes, such as *Kepler* (see Section 1.8), are ideally suited for detecting rotational modulations.

McQuillan, Mazeh & Aigrain (2014) published the largest sample of stellar rotational periods to date based on observing quarters Q3–Q14 of the *Kepler* mission. From the $\sim$196,000 stars observed and downlinked by the *Kepler* mission, they chose to analyse 133,030 stars, after excluding giants, eclipsing binaries, stars with transits, stars without convective envelopes at $T_{\text{eff}} > 6500$ K and stars without known T_{eff} or $\log g$. Among 133,030 analysed stars, they detected rotational modulations in light curves of 34,030 (26%) stars. The rotational modulation periods were spanning between 0.2 and 70 days, with typical amplitudes between 950 (5th percentile) and 22,700 ppm (95th percentile) and a median of 5600 ppm (McQuillan, Mazeh & Aigrain 2014). They also found that rotational modulation amplitudes are generally larger for faster-rotating and cooler stars, confirming the previous studies which were based on much smaller stellar samples (e.g. Pizzolato et al. 2003; Basri et al. 2010; Hartman et al. 2011; McQuillan, Aigrain & Roberts 2012).

1.6.2 Starspot Occultations

Direct observations of starspots is not yet feasible and would require further instrumental development to be able to resolve such sub-miliarcsec features even for the closest main-sequence stars. Silva (2003) proposed that transiting planets could be used to probe stellar photospheric features such as starspots. When a transiting planet passes over a dark starspot along its transit chord, it blocks less light compared to an unspotted photosphere. As a result, an occultation of a starspot by a transiting planet will produce a temporary brightening event within a transit light curve. If, on the other hand, a planet occults a bright plage, it temporarily blocks more starlight than before or after the occultation, which produces a dimming in the transit light curve. Shown in Fig. 1.9 are examples of sunspot occultations, generated by using real solar images and a simulated transiting planet.

As shown in example in Fig 1.9, the same sunspot is occulted twice in two consecutive transits, separated by an orbital period of 3 days. During that time, the sunspot has moved to a larger solar topocentric longitude due to the rotation of the Sun, whereas its topocentric latitude has not changed much because the shown planetary system is nearly fully aligned. As a result, the sunspot still lay inside the transit chord 3 days later, producing the second starspot occultation event, but at a larger orbital phase. This orbital phase difference between the recurring occultations can then be used to calculate the rotational period of the host star (Silva-Valio 2008), given that the physical migration of sunspots is several orders of magnitude slower than solar rotation (Gyenge, Baranyi & Ludmány 2014). Stellar rotational periods determined through starspot occultations are typically more precise and accurate than periods measured via the rotational modulation method, which is probing all visible starspots at once and is thus more prone to unstable presence and evolution of starspots.

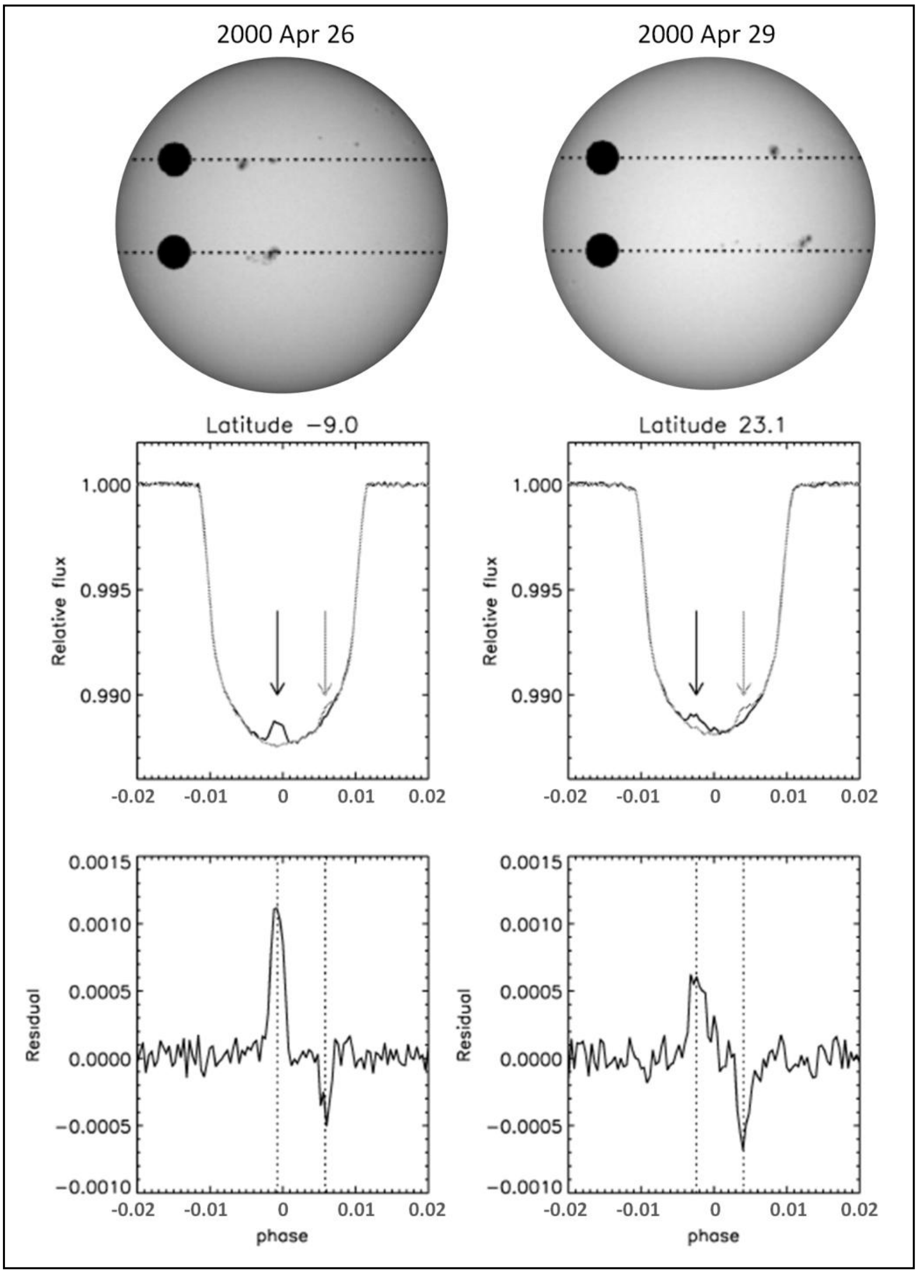

Figure 1.9: Simulated planetary transit of the spotted Sun. Upper panels: Real solar images from 2000 Apr 26 (left panel) and Apr 29 (right). The black circles represent a simulated Jupiter-sized planet in a 3-day orbit transiting from left to right along the dotted line at solar latitudes of -9° and 23°. Middle panels: Transit light curves for the latitude of -9° (left) and 23° (right). Black lines are the transit light curves of the transit occurring on Apr 26 and grey lines of the transit on Apr 29. Starspot occultation events are marked with arrows. Lower panels: Subtraction of the two light curves for the transiting planet at latitudes -9° (left) and 23° (right). Adopted from Silva-Valio (2008).

By modelling the widths, amplitudes and phase-positions of starspot occultation events it is possible to determine physical properties of individual spots, such as their size, contrast and location on the stellar surface (e.g. Tregloan-Reed, Southworth & Tappert 2013). This enables us to track the evolution of starspots (Silva 2003) and to determine the spin-orbit misalignment angle (Désert et al. 2011; Sanchis-Ojeda et al. 2011). The change in the best-modelled topocentric longitudes and latitudes of recurring starspots can be used to calculate the obliquity, whereas the non-recurrences may in some cases reveal a lower limit. If the misalignment angle of the planetary system shown in Fig. 1.9 was larger, the sunspot could not be fully or possibly even partially occulted in consecutive transits.

The distribution of stellar obliquities and its dependence on stellar and planetary parameters provide clues about the formation, migration and tidal evolution of close-in planets (e.g. Winn et al. 2005; Winn & Fabrycky 2015). The Rossiter–McLaughlin (RM) effect (Queloz et al. 2000b) is another efficient method for measuring stellar obliquities. Unlike the spectroscopic RM method, the photometric starspot tracking does not require high-resolution spectroscopy and can be applied to fainter stars. However, the starspot method does require substantial photometric datasets covering several consecutive transits at sufficiently high photometric precision. As a result, this method has been successfully applied for only about a dozen planetary systems to date, mostly by using the *CoRoT* and *Kepler* observations (Dai et al. 2018).

1.7 WASP Transit Survey

Most planets presented in this thesis, 10 out of 12, were discovered by the Wide Angle Search for Planets (WASP; Pollacco et al. 2006). The WASP exoplanet transit survey consists of two observing stations, at the Observatorio del Roque de los Muchachos on the Canary island of La Palma (WASP-North), and at the South African Astronomical Observatory in the Sutherland (WASP-South). WASP-North and WASP-South are operated remotely by Warwick and Keele University, respectively. Together with St Andrews University, who provided the data reduction and analysis pipelines, the three British universities represent the core of the WASP consortium.

Each observing station is equipped with eight Canon 200 mm f/1.8 lenses with Andor 2048×2048 e2v CCD cameras, on a single robotic mount (see Fig. 1.10). This provides a field of view (FOV) of 482 deg^2 with an angular scale of 13.7 arcsec pix^{-1}. Broadband-filtered WASP cameras are sensitive at 400–700 nm and are capable of delivering a photometric precision better than 1% for stars between $V = 7$ and 11.5 (Pollacco et al. 2006, also see Fig. 1.11).

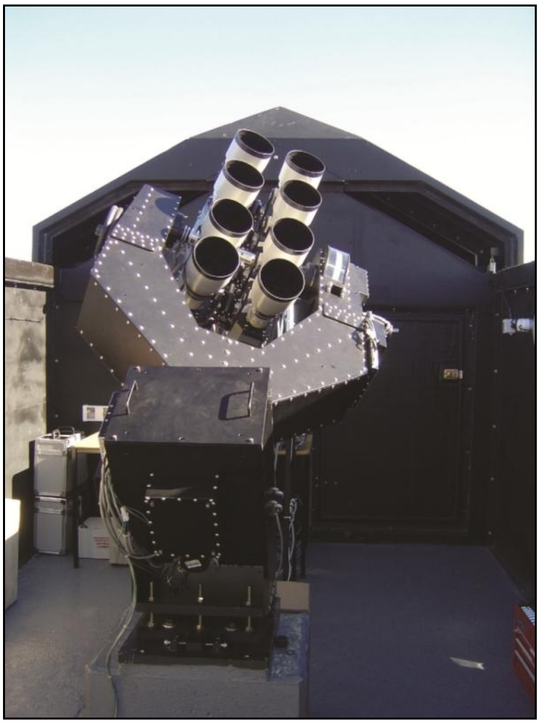

Figure 1.10: WASP-South instrument, consisting of eight telephoto lenses on the robotic mount inside the roll-off enclosure. Credit: Pollacco et al. (2006).

The main goal of the consortium is to search for gas giant planets transiting bright stars (Pollacco et al. 2006). Depending on the shape, depth and noise of the transit signal, generated using the data from several observing seasons, the observed target may get selected for photometric and spectroscopic follow-up observations. Details of the

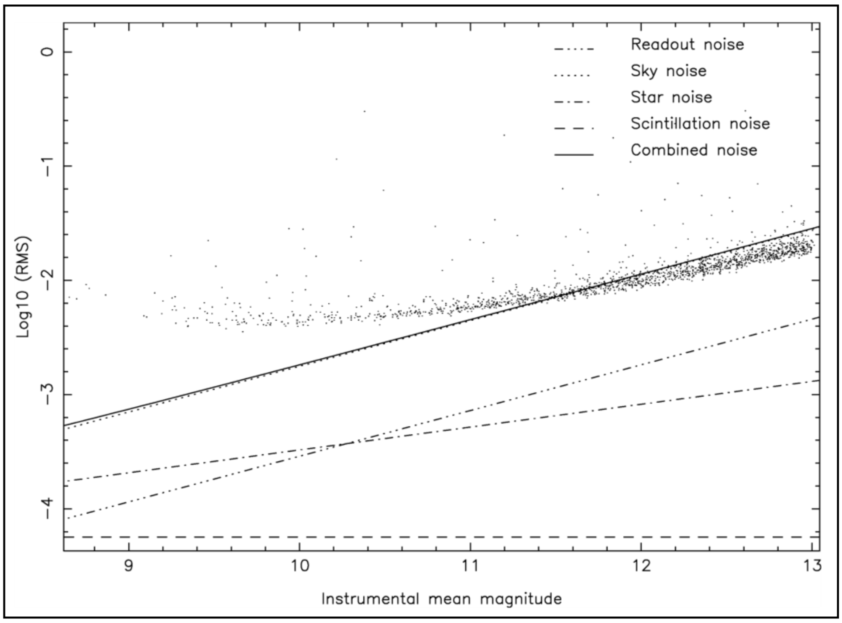

Figure 1.11: Photometric precision of WASP instruments. Also shown are the individual noise contributions and the approximated combined noise model. Credit: Pollacco et al. (2006).

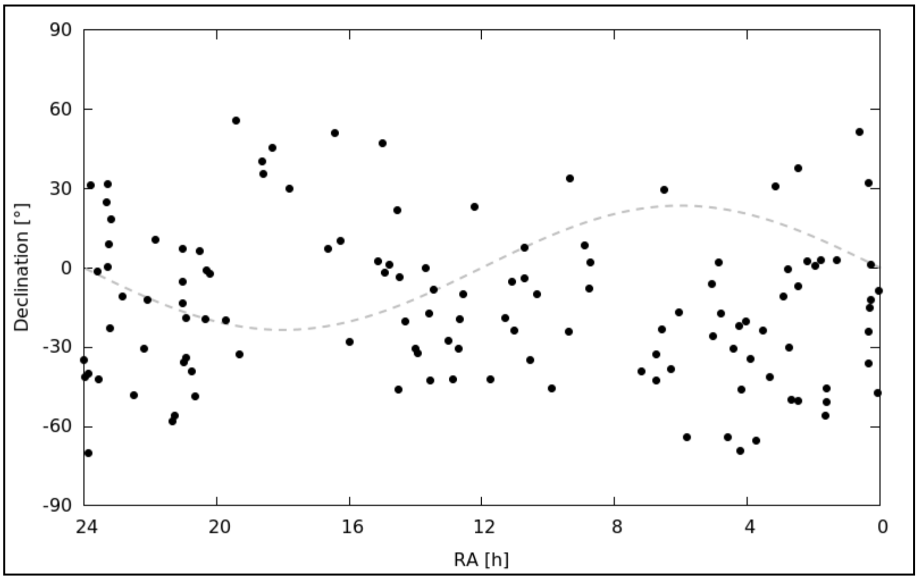

Figure 1.12: Celestial distribution of all 123 transiting planets discovered by the WASP consortium. Note that several WASP planets are located close to the ecliptic (dashed line), which is targeted by the *K2* mission (see Sections 1.8 and 3). The data to produce this plot were sourced from NASA Exoplanet Archive.

exoplanet candidate selection procedure can be found in Collier Cameron et al. (2007). As of the time of writing, the WASP consortium discovered 123 confirmed transiting planets in 120 planetary systems (NASA Exoplanet Archive). This represents nearly a half of all 280 transiting planets discovered with ground-based instruments. Fig. 1.12 shows the sky distribution of WASP-discovered planets. Due to the observing constraints, limited photometric precision and lower transiting likelihood at longer orbital periods (see equation 1.1), all but three planets discovered by the WASP consortium have orbital periods less than 10 days and radii larger than 6 R_E, and may thus be considered as hot Jupiters.

1.8 *K2* Mission

Kepler space telescope was launched in 2009 and was designed to provide high-precision photometry in the optical wavelengths (half-maximum bandpass 435–845 nm, >1% relative spectral response 420–905 nm; Thompson et al. (2017)), capable of detecting an Earth-sized planet at 4σ in a single 6.5-hour transit of a 12th magnitude Sun-like star (Borucki et al. 2010). With nearly-continuous wide-field observations of ~200,000 stars between 2009 and 2013 in a single pointing towards the field in-between the constellations of Cygnus and Lyra, the *Kepler* mission yielded 2327 confirmed exoplanets and a further 2244 exoplanet candidates to date (NASA Exoplanet Archive, 2018 May 15). Among the confirmed *Kepler* exoplanets, 78 planets have been found in habitable zones (where the planet's equilibrium temperature ranges between 180 and 310 K, NASA Exoplanet Archive), with 6 of them being Earth-like planets (planet's radius between 0.8 and 1.25 R_E; Fressin et al. 2013).

The high photometric precision of the *Kepler* mission was made possible owing to the stable pointing of the spacecraft, which was ensured by the four on-board reaction wheels (see Fig. 1.13). The main purpose of the reaction wheels is to prevent the solar radiation pressure from tilting the spacecraft. Instead, the exerted angular momentum is consumed by the rotation of the reaction wheels. In May 2013, however, the second out of four reaction wheels broke down and stable pointing in the direction of Cygnus and Lyra was no longer possible, which marked the end of the *Kepler* mission.

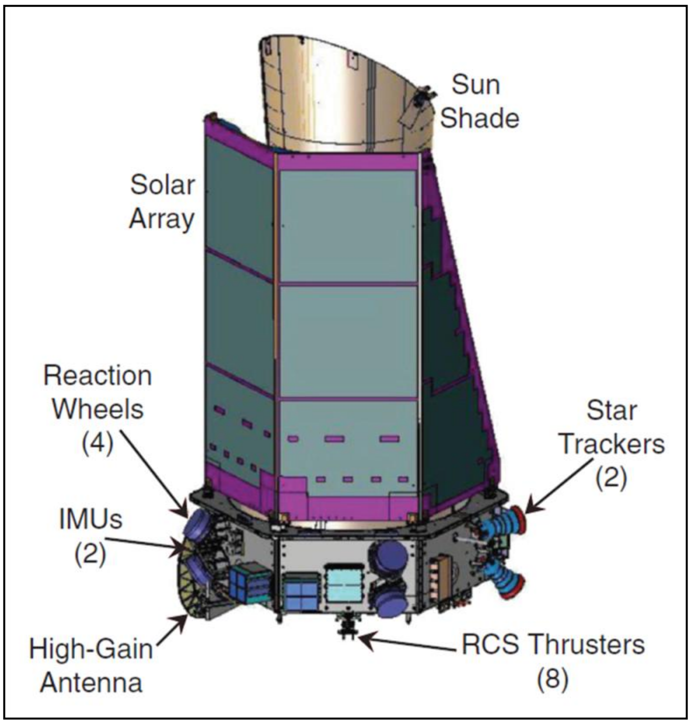

Figure 1.13: Diagram of the *K2* spacecraft components. Reaction wheels' rotation prevents the solar radiation pressure from tilting the spacecraft. Hydrazine thrusters provide pointing corrections, movements and enable stable desaturations of the reaction wheels. The numbers in brackets indicate how many components of each type are installed. Credit: Howell et al. (2014).

Months of development following the failure of the second reaction wheel resulted in a new observing strategy, according to which the *Kepler* telescope is balanced against the solar radiation pressure by pointing towards the fields along the plane of its orbit, the ecliptic (Howell et al. 2014). Following the Two-wheel Concept Engineering Test, which took place between 2014 February 4 and 13, the new mission concept was approved by NASA on 2014 May 16 (Sobeck & Johnson 2014) and named *K2* (hereafter *K2* mission, *K2* spacecraft, *K2* telescope).

Despite the new observing strategy to balance the solar radiation pressure, the telescope exhibits an increased pointing jitter of a few arcsec. The reduced pointing precision introduces drift artefacts in the obtained light curves, leading to a factor of 3 to 4 lower photometric precision than the original *Kepler* mission (Howell et al. 2014; see Fig. 1.14). However, because the drift artefacts are correlated with the spacecraft's pointing, it is possible to correct the degraded photometric precision (see Chapter 2), similarly as done in some other space-based missions with unstable pointing such as *Spitzer* (e.g. Ballard et al. 2010).

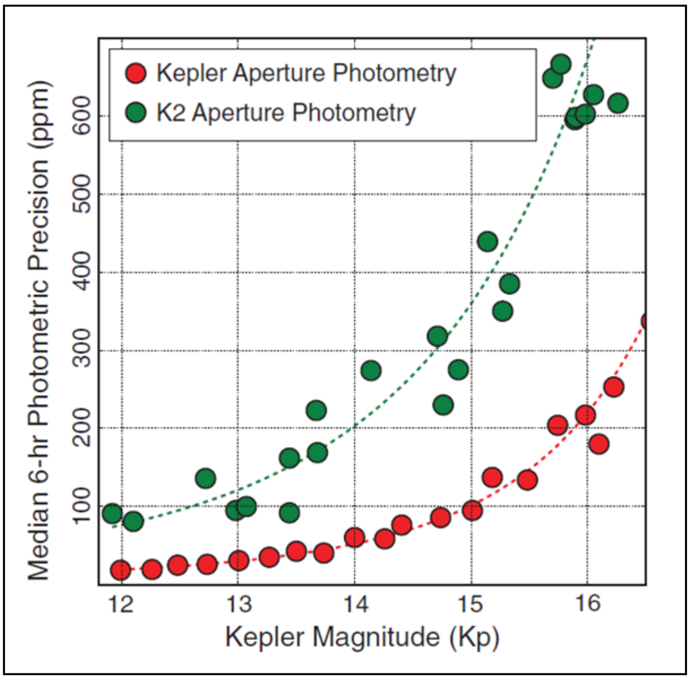

Figure 1.14: Median photometric precision of the *Kepler* (red data points) and the uncorrected *K2* light curves (green). Credit: Howell et al. (2014).

In the *K2* mission, the telescope is able to point at a single FOV for ~83 days, of which ~75 days are dedicated to science observations, before moving to the next field (Howell et al. 2014). *K2* began scientific observations with the test observing Campaign 0 (between 2014 March 8 and May 27). Since then, the *K2* completed the observations of 17 observing campaigns, denoted C1–C17 (see Table 3.1).

On average, *K2* observes and downlinks the data for ∼30,000 targets in each observing campaign in the 30-min long-cadence observing mode, and ∼100 targets in the 1-min short-cadence mode (see Section 2.1 for details about observing modes and data description). Which targets get selected for observations and in which of the two observing modes is based on the observing proposals submitted by members of the astronomical research community. However, once the data are downlinked following each observing campaign, they are made available publically.

The *K2* detector consists of 21 CCD modules (see Fig. 1.15), together covering a FOV of 116 deg^2 at a pixel scale of 4 arcsec pix^{-1}. Currently, only 18 CCD modules remain operational. Modules 3 and 7 failed before the beginning of the *K2* mission, in January 2010 and 2013, respectively (Howell et al. 2014). The third module, number 4, failed in August 2016 during the observing Campaign 10. All three failed CCD modules are marked in red in Fig. 1.15.

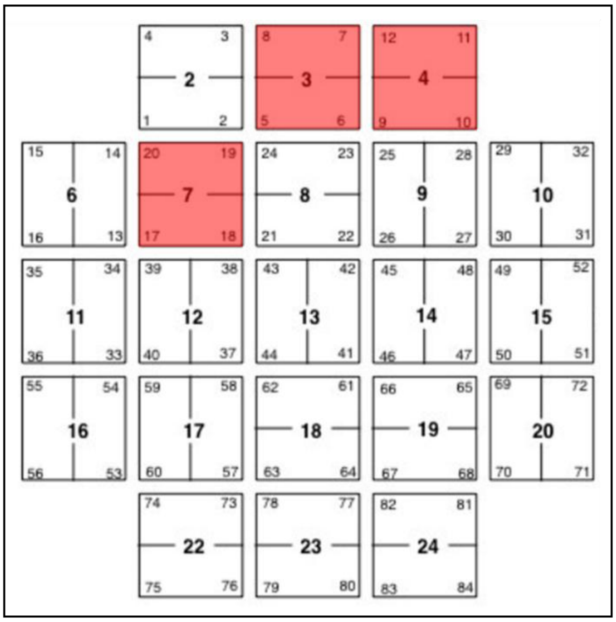

Figure 1.15: *K2* CCD modules. Failed modules 3, 4 and 7 are marked in red. Each CCD module consists of two 2200×1024 CCD detectors, which are further divided into two output channels each (marked with numbers in small font). Adapted from Thompson et al. (2017).

The timeline of the *K2* mission is shown in Fig. 1.16.

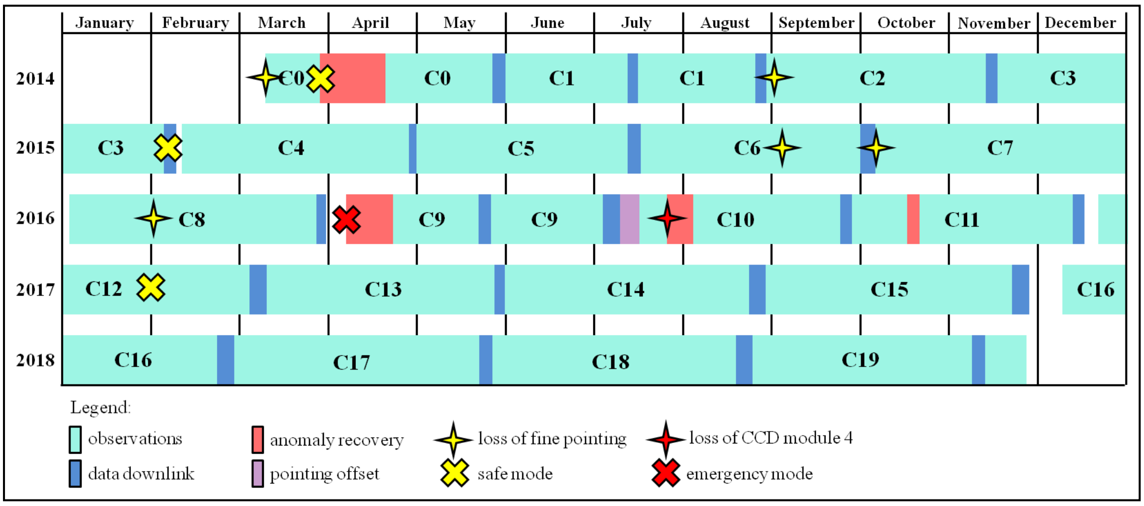

Figure 1.16: Timeline of the *K2* mission. Adapted from Van Cleve & Bryson (2017).

1.9 Conclusion and Thesis Outline

Exoplanet science advanced significantly since the turn of the century. We now know of well over 3500 confirmed planets, owing to many instruments and missions that became available to the community and were designed specifically to search and characterize exoplanets. The *Kepler* space telescope alone has led to the discovery of most currently-known exoplanets. Large samples of planets enabled us to study their occurrence rates and revealed an unexpected diversity of planetary systems. However, for only a small subsample of planets we were able to detect weak, yet, informative photometric signatures that require high precision and short cadence (e.g. TTVs, starspot occultations) or extended observing campaigns (e.g. phase-curve modulations). These elusive astrophysical signals may reveal additional planets, starspot activity, planetary albedos and many other characteristics of planetary systems that are typically undetectable with ground-based photometers.

Despite only two remaining reaction wheels in the *K2* mission, the *Kepler* telescope continues to provide the community with nearly-continuous high-quality light curves. With observing campaigns along the ecliptic and each lasting for about 80 days, the *K2* observes several previously-discovered planets with highest precision yet. Most of these planets were discovered by the WASP consortium.

In this research project I devise a data reduction procedure to extract short-cadence *K2* light curves and improve their photometric precision for several transiting planetary systems discovered with ground-based telescopes. Besides refining the system parameters, I search for TTVs, rotational and phase-curve modulations, starspot occultations, additional transiting planets and other astrophysical signals. This work presents the results of analysing the majority of the transiting planetary systems observed by the *K2* in the short-cadence mode. Beside several actual detections of high scientific value, this work serves as a demonstration of the *K2* detection capabilities.

The thesis proceeds as follows: In Chapter 2 I present the *K2* data reduction procedure and different methods to correct the photometric precision due to the unstable spacecraft pointing. Chapter 3 provides an overview of the *K2* observing campaigns along with the list of targets analysed in this project. In Chapters 4–12 I present the analysis and results of individual planetary systems. Most of these chapters are based on published, submitted or accepted lead-authored journal papers, and are presented in this thesis in a similar form as the corresponding papers. I explain in the preamble of each of these chapters the status of the paper, contributions from the co-authors involved, and any additions or changes applied for this thesis. Chapter 6 is based on a co-authored paper, and Chapter 5 presents the work done before the announcement of the publication by another team and it serves as a demonstration of the technique used to search for additional transiting planets. An overview of the results for all planets is given in Chapter 13. Chapter 14 discusses the detected astrophysical signals and their significance. Chapter 15 summarises the thesis and presents the near-future prospects with space-based observations of transiting planets.

2 *K2* Data Reduction Procedure

2.1 Description of *K2* Data

The *K2* spacecraft is in a heliocentric Earth-trailing orbit with an orbital period of 372.5 days (Haas et al. 2010). Consequently, the spacecraft is receding from Earth with the current distance being 1.02 AU (2018 May 16; JPL HORIZONS service[4]). This large and ever-increasing distance affects communication capabilities with the spacecraft (Bryson et al. 2010a). *K2* downlinks the collected data typically at the end of each observing campaign with its Ka-band high-gain antenna (HGA, see Fig. 1.13), which has a nominal downlink bandwidth of 4.3 Mbps (JPL HORIZONS). The downlink bandwidth constraints and the inability to collect science observations while the HGA is pointing towards Earth, make it impossible to downlink all the data collected with the 96 Mpixels onboard *K2* (Bryson et al. 2010a). Instead, (1) the recorded intensities of only selected pixels get downlinked for approved targets; and (2) individual short-exposure images are mean-combined to reduce the number of downlinked pixel-intensity strings for each target.

All *K2* science images are obtained with an exposure time of 6.02 s, followed by a 0.52 s readout (Van Cleve et al. 2016a). To reduce the downlink time, the sets of 9 and 270 images are combined on-board using the arithmetic mean for short- and long-cadence observing modes, respectively. This results in one short-cadence data point every $9 \times (6.02\ \mathrm{s} + 0.52\ \mathrm{s}) = 58.85\ \mathrm{s}$, with an effective exposure time of 54.18 s. In the long-cadence mode, each data point represents $270 \times (6.02\ \mathrm{s} + 0.52\ \mathrm{s}) = 1765\ \mathrm{s}$ (29.42 min), with an effective exposure time of 1625 s (27.08 min).

---

[4] https://ssd.jpl.nasa.gov/?horizons

K2 downlinks on average ~1% of all pixels in the long-cadence mode and ~0.01% of all pixels in the short-cadence mode. These are selected based on submitted observing proposals from the community. Shown in Fig. 2.1 is an example of a full frame long-cadence image from an output channel containing WASP-107 (see Chapter 9), which illustrates the limitations of the downlink capabilities.

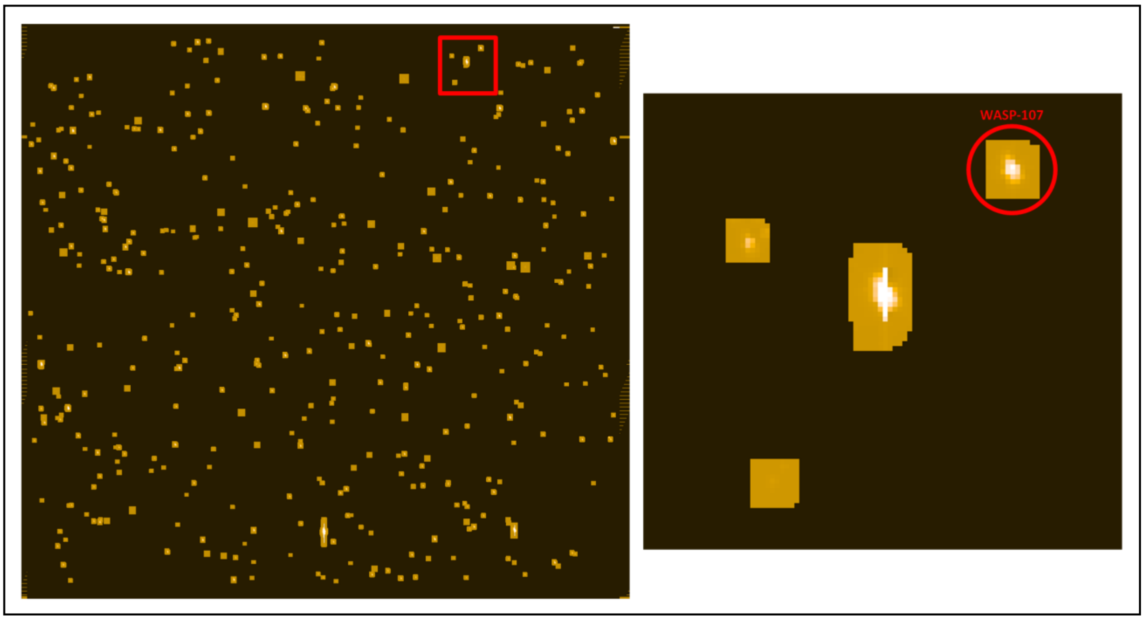

Figure 2.1: Full frame long-cadence image obtained with the output channel 16 during observing Campaign 10 (left panel), and a zoomed region containing WASP-107 (right). Only about 1% of all pixels get selected for downlink in the long-cadence mode and 0.01% in the short-cadence mode.

To further minimize the downlink time, *K2* does not downlink the actual images, but only strings of pixel intensities, along with time and telemetry data (Thompson et al. 2017). Once these data are received at Space Telescope Science Institute, they are sorted by cadence (long or short) and type (science, background, collateral), and converted into FITS files. At this point the data are referred to as “raw”, which become publically available almost immediately after the downlink. These data may serve as an early preview until the consequent processing outlined below is complete and the data officially released (see Section 2.2 for the necessary steps when using raw *K2* data).

The raw data are then sent to the Science Operations Center (SOC) at NASA Ames. Long and short-cadence data both undergo the calibration module of the SOC's *Kepler* Science Pipeline (Quintana et al. 2010). This calibration module converts the downlinked strings of raw data counts and pre-defined pixel locations into target pixel files (TPF), sometimes also referred to as time-series of pixel or postage stamps. The SOC's pipeline corrects the data within TPFs in many ways: it subtracts bias and dark current, applies flat-field and readout smear correction, converts raw counts into $e^- s^{-1}$, applies barycentric time correction, and assigns a range of quality flags to the images affected by any anomalies. The latter may either be identified by the pipeline directly from the downlinked telemetry file, such as reaction wheel desaturation events, or from the data itself, such as cosmic rays. From Campaign 3 onwards the SOC's pipeline also subtracts the background signal for both observing modes and assigns quality flags to the data taken during the thrusters firing events, which simplifies the procedure for correcting drift artefacts (see Section 2.3.4). A single TPF contains calibrated data of a particular object for all exposures obtained during an entire observing campaign. An example of a single image within TPF is shown in Fig. 2.2.

Long-cadence data are processed further with additional functionality of the SOC's photometric analysis module. The module calculates the flux-weighted centroid positions of all targets in all cadences and extracts the target's flux by summing the pixels within the automatically-determined optimal photometric apertures. This is termed simple aperture photometry (SAP). In the final step, the long-cadence data also undergo the pre-search data conditioning (PDC) module, which compares the SAP light curves with ancillary engineering data and centroid positions to identify and remove correlated systematics. PDC was originally designed for *Kepler* observations to decorrelate small flux modulations caused by the differential velocity aberration, residual spacecraft fine pointing errors, mechanical vibrations, electrical interferences between on-board devices, and the changes in the telescope focus caused by thermal variations and consequent flexure of the optics (Stumpe et al. 2012). All these systematic errors are orders of magnitude smaller than drift artefacts present in the *K2* light curves. However, since drift artefacts are also correlated noise, the PDC module does partially correct it but with very limited success. The unsatisfactory removal of drift artefacts by the SOC pipeline's PDC module triggered the development of specialized pipelines to address the drift artefacts (see Section 2.5). As of Campaign 15, the short-cadence data also undergo the above-mentioned additional processing steps by the SOC's photometric analysis and PDC modules.

Once the processing with the SOC pipeline is complete, the data are uploaded to the Mikulski Archive for Space Telescopes (MAST[5]) where they are officially released and made publically available. Specifically, this includes the TPFs for short- and long-cadence targets, light-curve files of long-cadence targets, and light-curve files of short-cadence targets as of Campaign 15. The SOC-processed data are uploaded to MAST for each observing campaign typically a few months after downlink (see Table 3.1).

2.2 Using Raw *K2* Data as an Early Preview

The raw *K2* data for recent observing campaigns become publically available through MAST only within a few days after downlink, much earlier than the official data release. For earlier campaigns, the raw data initially became available only for selected campaigns following the request from the community to enable rapid time-critical ground-based follow up observations. However, because the raw data are not processed with the SOC pipeline (see Section 2.1), the use of such data requires a few additional processing steps described below.

---

[5] https://archive.stsci.edu/

The first step is to construct a TPF for the desired target. Raw data are archived on MAST as one FITS file for each exposure for all targets combined. After downloading the FITS files for all exposures, I extracted the data into a TPF for a particular target with the `kadenza` pipeline (Barentsen 2016, 2017), which uses a pixel mapping reference file to identify the pixels corresponding to the target.

The time stamps within TPFs produced with `kadenza` were in the spacecraft-specific time. I applied the barycentric time correction with an IDL code `UTC2BJD` (Eastman, Siverd & Gaudi 2010) and *Kepler*'s orbital parameters from JPL HORIZONS to convert the on-board time into barycentric Julian date (BJD).

The rest of the data reduction is similar as presented in Sections 2.3. However, because the raw data are neither calibrated nor quality-flagged, I additionally subtracted the background signal during the photometric extraction and manually identified and flagged any data anomalies (see Section 2.3).

Because of the lower quality of the raw data compared to the official data release, the *K2* team discourages its use for publications except if time-critical. Throughout this research project and wherever possible I used raw *K2* data to inspect the light curves and to prepare the data reduction and analysis procedures for when the official data were released.

Objects observed during the Engineering Campaign were also not processed with the SOC pipeline and require a similar treatment as raw data (e.g. WASP-28 in Chapter 10). Additionally, understanding the properties and limitations of raw *K2* data also provides an important insight when comparing the results with other publications which used raw data, such as Demangeon et al. (2018) in the case of WASP-151 (see Chapter 10).

2.3 Default Data Reduction Procedure

In this section, I present the *K2* short-cadence data reduction procedure applied to most targets analysed in this research project (the exact procedures and types of data used for each target are specified in Chapters 4–12). The prodedure is based on `PyRAF` tools for *Kepler* version 2.6.2 (`PyKE`; Still & Barclay 2012), which I modified to improve its performance for short-cadence data. The initial version of this procedure was ready in March 2015, followed by several improvements described in this section. The procedure is presented step-by-step using the example data of the most recently-reduced planetary system WASP-104 from the observing Campaign 14. Any deviations from this procedure are specified in Chapters 4–12 of individual targets.

2.3.1 Defining Extraction Aperture

The short-cadence data provided by the official data release (see Section 2.1) or compiled using the raw data (see Section 2.2), are in the form of a TPF. A TPF is a set of as many pixel stamps containing a target as there are downlinked mean-combined exposures in an observing campaign, along with ancillary data stored in the image header. A short-cadence TPF typically contains 10^5 pixel stamps per observing campaign, while a long-cadence TPF contains about 4000.

The first step is to define a photometric extraction aperture. The size and the location of the aperture depend on several factors. First, optimal apertures for brighter stars are generally larger because the background noise is small compared to the stellar signal to larger distances from the target centre (Vanderburg & Johnson 2014). Second, single stars are not necessarily circular in appearance. Instead, their signal is distributed according to a specific pixel response function (PRF), which is a composite of the *K2*'s optical point spread function (PSF), integrated spacecraft pointing jitter during each effective exposure and other systematics (Bryson et al 2010b). Depending on the position of the star on the detector, the diameter of 95% encircled energy ranges between 3.1 and 7.5 pixels (Rebull et al. 2016), larger towards the edges of the FOV. Third, the optimal aperture position and size are also affected by any nearby stars and other light sources. In case a nearby star is resolved, it may be possible to avoid or at least minimize the contamination by shifting the position or modifying the shape of the extraction aperture. With 4"×4" pixels and a large PSF FWHM, *K2* is sometimes unable to fully resolve stars within a few arcsec from the target. In this case, the extraction aperture should be made large enough to reliably encompass the light of all sources throughout the observing campaign in order to prevent any significant partial signal-leaking during the spacecraft drifts. Once the light curve is extracted, it can then be corrected for dilution (e.g. Daemgen et al. 2009). One such example was WASP-85

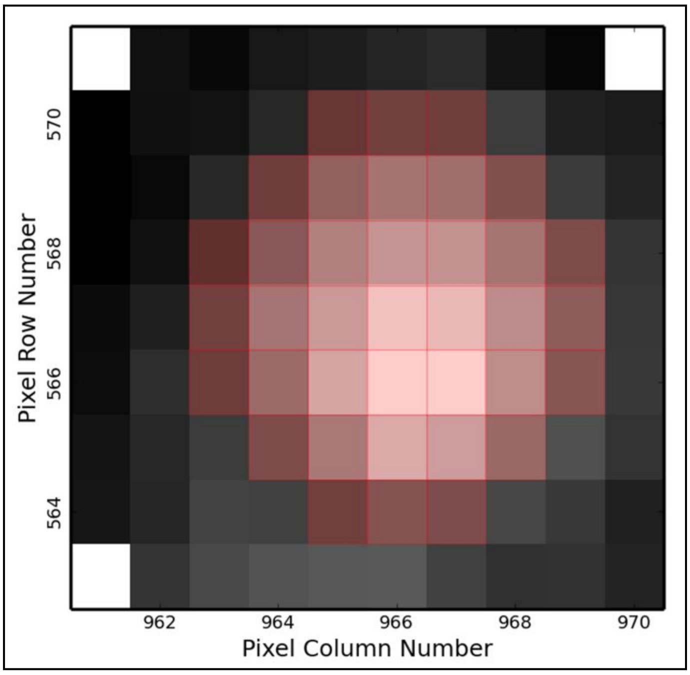

Figure 2.2: Photometric extraction aperture for WASP-104. The additional flux visible at the bottom of the pixel stamp originates from an approximately equally bright star located 30 arcsec below the target outside the pixel stamp. The drift direction was predominantly horizontal (see Fig. 2.4a), which prevented any non-negligible signal leakage into the fixed aperture from this potential contaminant. Note that the intensity scaling is logarithmic. The three white pixels in the corners of the pixel stamp were not downlinked.

with a contaminant only 1.5 arcsec away from the planet host (see Chapter 4). Lastly, due to the occasional spacecraft attitude tweaks, such as during Campaign 10, it is sometimes necessary to re-define an aperture to accommodate a new target position.

I determined the exact size and position of fixed extraction aperture for each target on case-to-case bases by taking into account the above-mentioned considerations and by trial and error to achieve the best final photometric precision. In general, selecting the aperture too large results in higher background noise and selecting the aperture too small results in the loss of stellar signal and more pronounced drift artefacts. I defined photometric extraction apertures with `PyKE` tool `kepmask`, which allows an interactive selection of extraction pixels. Shown in Fig. 2.2 is an example aperture for WASP-104.

2.3.2 Light Curve Extraction

Once the extraction aperture was defined, I extracted the light curve from the TPF by summing the data values of all pixels inside the aperture. Simultaneously, I calculated the 1st moment of target's light distribution to determine the exact position of the target within each pixel stamp. The target positions are needed in later steps to correct the position-correlated drift artefacts (see Section 2.3.4). The photometric extraction and position calculation was done with the `kepextract` tool. This tool also calculates the PSF centroid positions. However, using the PSF-positions for the correction of drift artefacts in the short-cadence data consistently produced worse results than when using the moment positions. In addition, because the PSF calculations were much slower than moments (5 hours on a typical desktop computer for $\sim 10^5$ short-cadence pixel stamps, compared to 8 min for moments), I disabled the PSF fitting in `kepextract` for most extractions to speed up the process. Two possible contributing factors to poorer performance of the PSF positions are that (1) pixel response functions of analysed targets were not Gaussian as assumed by `kepextract` tool, and (2) each short-cadence pixel stamp has a factor of 30 shorter effective exposure time and accordingly lower signal-to-noise ratio compared to a long-cadence pixel stamp, for which most of the publically available data reduction tools were designed for, including `kepextract`.

Starting in Campaign 3, all officially released TPFs already have background signal subtracted. However, I had to manually subtract the background signal for WASP-85 from Campaign 1, WASP-28 from the Engineering Campaign and any targets analysed from the raw data. For these targets, I calculated the median intensity of pixels within each pixel stamp outside the extraction aperture, and subtracted it from the aperture pixel sum of the target given by `kepextract`. The procedure of sky subtraction requires a sufficient number of pixels that are unaffected by any objects. This condition is met for WASP-85 in Campaign 1 and WASP-28 in Engineering Campaign because of their large pixel stamps, namely 18×18 and 50×50 pixels, respectively. However, pixel stamps are typically smaller than this (see Fig. 2.2) and thus require more careful selection of pixels to estimate the background signal. Fewer number of pixels from which the sky signal is calculated increases the uncertainty of the derived value and thus higher white noise in the final light curve. Therefore, unless the pixel stamps are large enough and clear of other objects, determining local sky signal from the pixels within pixel stamps should be used with caution and serve only as an approximation. The background signal subtracted by the SOC's calibration pipeline is derived from the background model, which is calculated from several dedicated pixel regions distributed across the FOV. This means that background subtraction provided by the SOC pipeline is more accurate, has smaller noise and is therefore superior to the quick background estimation outlined above. However, because the SOC's background model is built from the long-cadence data and then interpolated to correct also the short-cadence data, it may not subtract sky correctly if the background brightness changes significantly within 30 min (such as in Campaign 12 due to the reflections of Mars as it was passing the FOV, see Chapter 10).

2.3.3 Removal of Low-frequency Modulations

In the next step, I temporarily removed from the extracted and background-subtracted light curves any low-frequency photometric variabilities, such as rotational modulations or gradual astrophysical and instrumental brightness changes. Low frequency variability had to be removed to isolate drift artefacts for the decorrelation data reduction step described in the following subsection. A failure to do so could greatly increase the noise in determining the decorrelation function and lead to significant drift artefact residuals in the final processed light curve.

I removed low-frequency modulations with `kepflatten`. This tool fits a set of partially-overlapping polynomials of a specified order to a light curve in a way that each polynomial is fitted to only a small part of the light curve specified by the window size, and the next polynomial is then fitted to the next window which is shifted in time by a specified step size. After all polynomials are calculated, the overlapping sections are merged into a single function with a median.

Significant outliers from this median function correspond to data points obtained either during high-frequency astrophysical or instrumental events, such as planetary transits or drift artefacts. I temporarily removed the high-frequency variability and other outliers by excluding the data points which deviate from the median fit by more than a specified number of standard deviations and then re-calculated a new set of polynomials. This procedure is then repeated a specified number of times. After the final iteration, `kepflatten` flattens and normalizes the original input light curve, inclusive of temporarily excluded data points, by dividing it with the final median polynomial.

The original version of `kepflatten` is designed to initially use all data points, and then identify outliers from the polynomial fit itself. However, the data points obtained during occasional anomalies, such as coarse pointing, may elude the exclusion and could thus affect the shape of the median polynomial close to the affected region. This could then produce flattening artefacts of good data points close to the data anomaly. I addressed this issue by modifying the `kepflatten` procedure to exclude any quality-flagged data points from constructing a median polynomial.

The flattening parameters were chosen on case-to-case basis. In general, the flattening was made more aggressive if the light curve exhibited more pronounced low-frequency modulations and weaker drift artefacts, and the opposite for quiet stars with pronounced drift artefacts to avoid overfitting and flattening the drift artefacts prior to the decorrelation procedure. In case of WASP-104, I used the polynomial order 2,

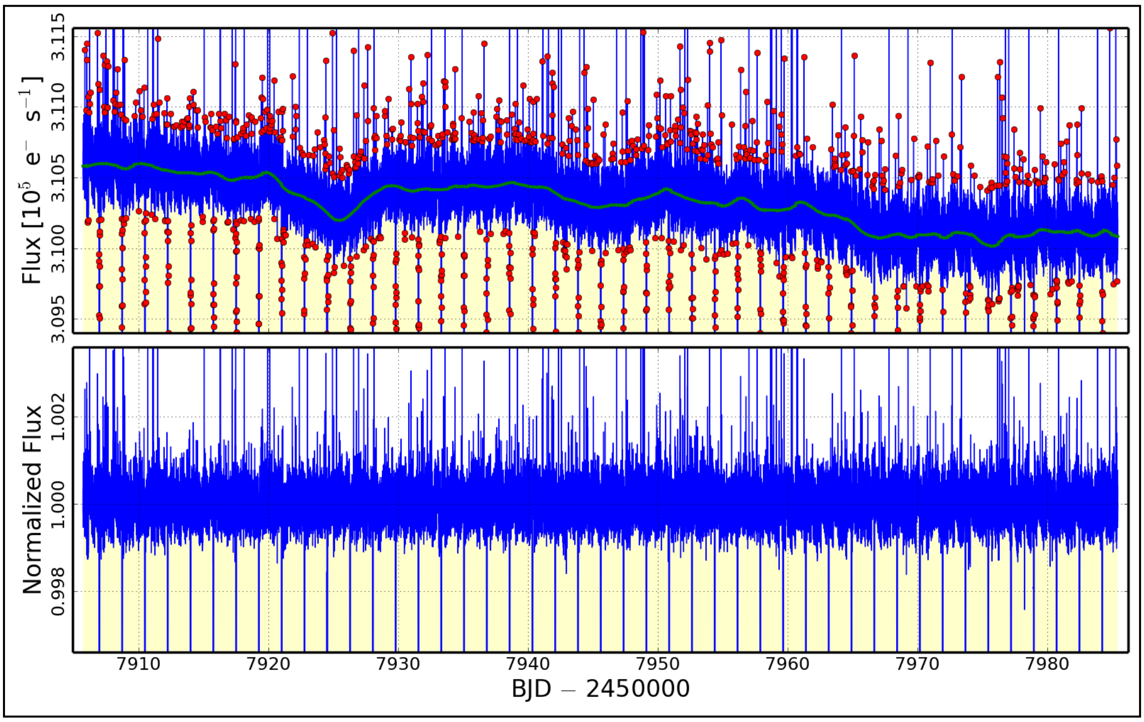

Figure 2.3: Zoomed short-cadence light curve of WASP-104 before (upper panel) and after the flattening and normalization (lower panel). Data points marked with red symbols are >3σ outliers, which were excluded from constructing a flattening polynomial (marked with a green curve in the upper panel). Transits of WASP-104b are partially visible in this figure as periodic vertical lines.

window size of 3 days, step size 0.3 days, 3-σ clipping and 5 iterations. Shown in Fig. 2.3 is the light curve of WASP-104 before and after the removal of low-frequency modulations.

2.3.4 Self-flat-fielding Correction

Because *K2* has only two functioning reaction wheels left (see Section 1.8), its pointing is unstable within a few arcsec, depending on the observing campaign and the position of the target within the FOV. The on-board *K2* star-tracking mechanism monitors positions of stars and roughly every six hours triggers thrusters to correct the pointing back to nominal. As a result, a target slowly drifts within its pixel stamps until a thruster firing brings it back to its initial position. The combination of pointing drifts and thruster firings produces quasi-periodic sawtooth-like photometric drift artefacts firstly because various fractions of the target's flux may fall outside the extraction aperture and secondly because of the non-uniform pixel response function of the detector.

Vanderburg & Johnson (2014) designed a procedure to correct these artefacts by correlating the measured flux and arclength of the drift. They termed this decorrelation procedure self-flat-fielding (SFF) since the target's own flux acts as a flat field calibration. `PyKE` tool `kepsff` is based closely on the SFF procedure introduced by Vanderburg & Johnson (2014).

In this research project I corrected drift artefacts with `kepsff`, which has been significantly modified for this research project to improve its performance for short-cadence data.

Drift trajectory is unlikely to remain stable throughout the observing campaign. It is therefore better to split the light curve into smaller chunks prior to performing the SFF. The selection of the best window size for the SFF correction is based on trial and error as the best compromise between higher drift consistency and a larger number of drifts. The smaller the data window, the less likely it is that the sampled drifts would exhibit different behaviour, however, there will also be fewer number of drifts from which the decorrelation function will be determined from. A typical window size was between 4 and 6 days. By introducing occasional manual break points at sudden changes in drift trajectories, I prevented that the same SFF processing step would cover distinctly different drifts. I also used different window sizes in different parts of the light curve whenever needed to further improve the performance of the SFF.

Once the light curve is split according to the selection of the window size, `kepsff` first determines the direction of drifts within each window. This is done by fitting a polynomial with a specified order (typically linear) to the target's x and y position measurements on each pixel stamp. Shown in Fig. 2.4a is a linear fit to the 1st moment position measurements of WASP-104 in a 5-day SFF window, which were measured in Section 2.3.2 as part of the photometric extraction. In case of WASP-104, the target is drifting in mostly horizontal direction for about 0.2 pixels (0.8 arcsec).

Unlike the long-cadence data, for which `kepsff` was designed for, the short-cadence data typically exhibit positional outliers whenever a thruster is fired. Following a modification of the `kepsff` tool, I identified and flagged all positional outliers as thruster firing events (marked red in Fig. 2.4a) and removed them from the remaining of the data reduction. Thruster flagging was an important data reduction step prior to the observing Campaign 3, which did not have thrusters quality-flagged as part of the official data release, and for the raw *K2* data, which are not quality flagged at all.

Fig. 2.4b shows the deviation from the linear drift behaviour, which serves as a second-order correction in determining drift arclengths. Fig. 2.4c is showing positional time derivatives. Because the position of the target changes most rapidly during thruster firing events, I flagged speed outliers in Fig. 2.4c as any remaining potential thruster firing events which were not flagged earlier as positional outliers.

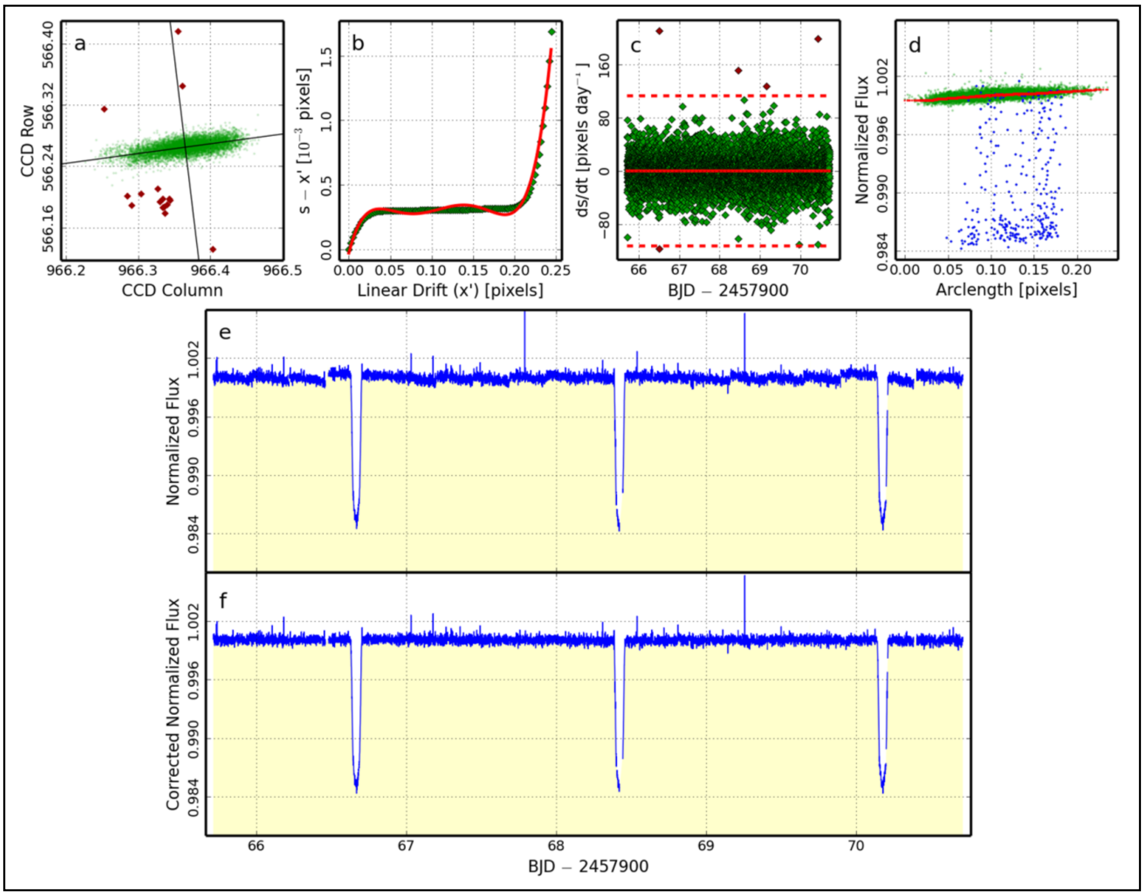

Figure 2.4: Modified `kepsff` tool. All panels show the SFF calibration procedure for WASP-104 for a selected 5-day calibration window. a: Position of the centre of the object given as CCD Row against CCD Column. Spatial outliers are marked with red and flagged as thruster firing events. b: Deviation from the linear drift. c: Drift speed versus time. Speed outliers are marked with red and flagged as thruster firing events. d: Flattened and normalized flux versus drift arclength. The correlation is fitted with a Gaussian convolution (red curve). e: Flattened and normalized light curve before the SFF correction. f: Light curve after the SFF correction.

Shown in Fig. 2.4d are the normalized and flattened flux values of all data points within the 5-day window that are not quality flagged and they are plotted against the length of the spacecraft drift, which is calculated from the linear relation from Fig. 2.4a and the second order correction from Fig. 2.4b. The original version of `kepsff` was designed for the long-cadence data and it used a polynomial to fit the correlation between the flux and drift arclength. However, since there are 30 times as many data points in the short-cadence data it was possible to significantly improve the determination of the correlation with a Gaussian convolution (see Fig. 2.5). The

Gaussian convolution fits a Gaussian function to flux distribution of data points within a specified small range in arclengths and determines the flux-position of the peak while masking any outliers above user-specified number of standard deviations. Then the arclength range is shifted by one data point and the procedure is repeated for all remaining unflagged data points. A track of the Gaussian convolution is shown with a red curve in Fig. 2.4d, which was in this case computed using a convolution width of 50 data points and 4-σ clipping. The Gaussian convolution technique was developed in collaboration with Ben Clark who built the convolution procedure and I integrated it into the `kepsff` tool. Using a Gaussian convolution instead of the polynomial fit nearly doubled the efficiency of correcting drift artefacts for short-cadence datasets.

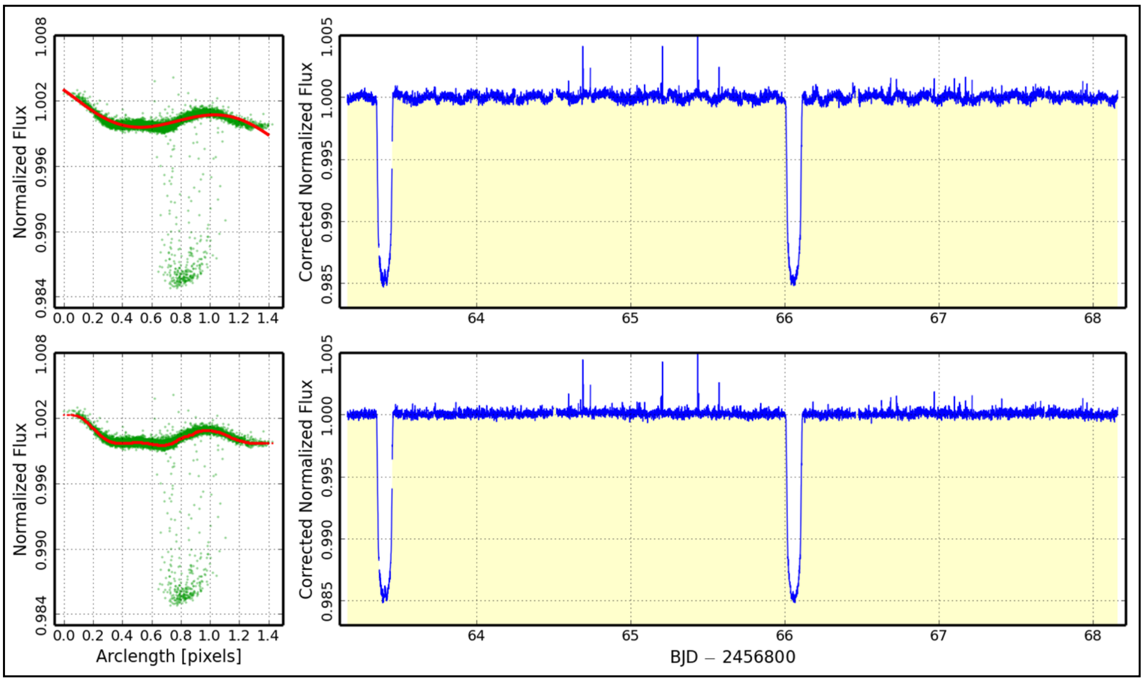

Figure 2.5: Improvement of using a Gaussian convolution (lower panels) compared to a polynomial (upper panels) to fit the correlation between flux and drift arclength. Shown is an example of WASP-85. The polynomial used to produce the correlation fit in the upper left panel is of 5th order. Using a smaller or larger polynomial order produced worse results. Note that the spacecraft drifts are much longer (1.4 pixels) compared to WASP-104 (0.2 pixels).

The original version of `kepsff` was designed to exclude any astrophysical or systematic outliers in the flux-arclength correlation with sigma clipping. For most targets, the sigma clipping successfully excluded planetary transits when determining the correlation function. However, the correlation was occasionally poorly sampled with out-of transit data points at arclengths with transits (see an example for WASP-28 in Fig. 2.6). This was more likely to happen near the edges of the drifts (as in the shown example), near the data gaps or whenever several transits occurred at similar arclengths. I resolved this issue by masking all data points within a specified transit width at specified transit ephemeris (marked with blue data points in Fig. 2.4d and in the lower panel of Fig. 2.6).

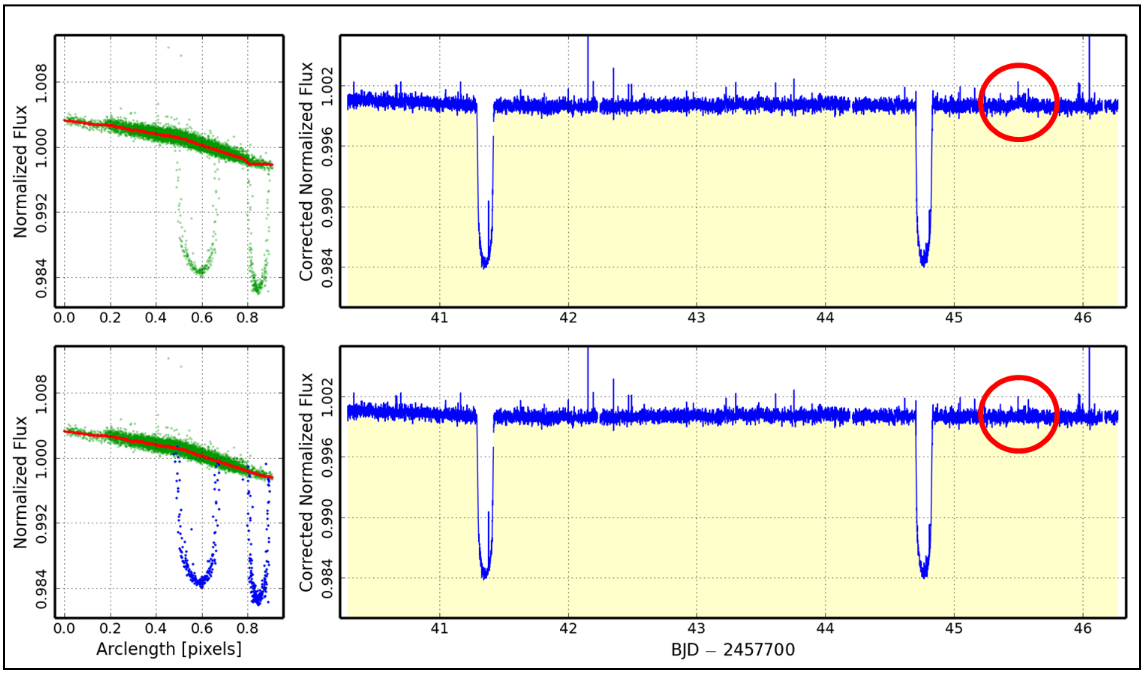

Figure 2.6: Flux-arclength correlation without (upper panel) and with transit signals masked (lower panel). Shown is an example of WASP-28, with a transit occurring at the end of the spacecraft drift (at arclengths 0.8–0.9 pixels), which is poorly sampled by the out-of-transit data points. Masking the transit improves the correlation and eliminates the drift artefact residuals that are present in the light curve corrected without transit masking (marked with red ellipses).

Once the flux-arclength correlation was determined, I divided the flattened and normalized flux (Fig. 2.4e) with the correlation function to produce a light curve with drift artefacts removed (Fig. 2.4f). I also produced drift-corrected fluxed version of the light curve for each target, by multiplying the corrected normalized and flattened light curve with the same function as used in Section 2.3.3 to flatten the light curve.

I evaluated the efficiency of the applied drift correction with a median of out-of-transit standard deviations in a moving window of a given duration. I calculated the precision for all targets with a 6-hour window and under an assumption of white noise I scaled it to the 1-min precision by multiplying it with $\sqrt{360}$. The same procedure was used by other authors, e.g. Vanderburg & Johnson (2014) and Aigrain et al. (2015), who use it instead of and as an approximation of the Combined Differential Photometric Precision (CDPP; Christiansen et al. 2012). For WASP-104 (*Kepler* magnitude (K_p) = 11.6), the SFF procedure improved the 1-min median photometric precision from 362 parts per million (ppm) before the drift correction to 326 ppm after the correction. For comparison, the photometric precision for WASP-85 (K_p = 10.6) was improved from 778 to 260 ppm. The final photometric precision is in both cases comparable to that of the original *Kepler* mission for similarly bright stars (see Fig. 2.7).

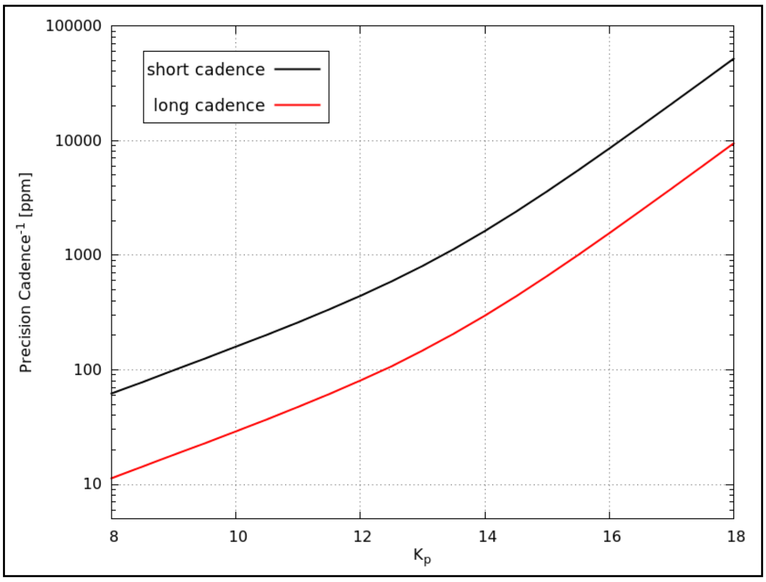

Figure 2.7: Theoretical *Kepler* photometric precision per short- (black curve) and long-cadence data point (red curve) versus *Kepler* magnitude, K_p. The data to generate this plot were sourced from Still (2013).

The main reason why the photometric precision of WASP-85 was much smaller before the SFF correction compared to WASP-104 is that the drifts were longer, which resulted in more pronounced photometric artefacts. The amount of pointing jitter is different for every observing campaign and depends on a number of factors, and it also depends on the position of the target on the detector. The rotation of the spacecraft around the line of sight, also termed roll motion, has larger effect on targets nearer the edges of the FOV (Van Cleve et al. 2016b; see Fig. 2.8). Unlike WASP-85, WASP-104 was located close to the centre of FOV (CCD module 13, output channel 41; see Fig. 1.15 or 2.8) and therefore exhibited shorter drifts and less pronounced drift artefacts.

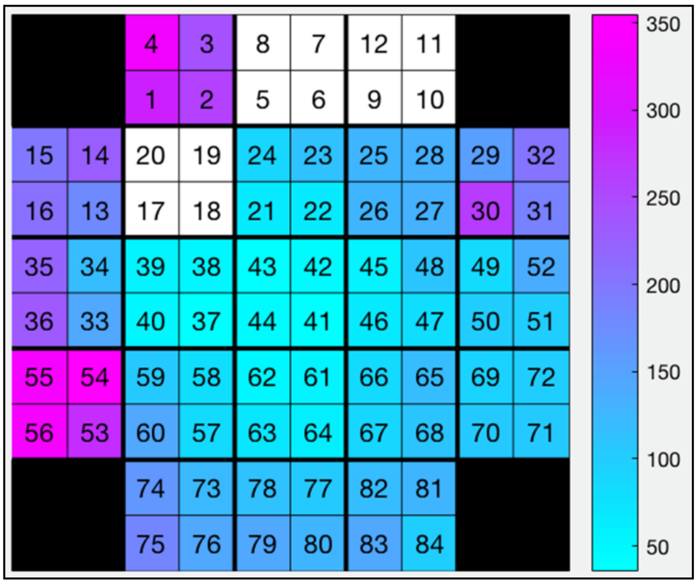

Figure 2.8: Median 6.5-hour photometric precision before the drift artefact correction for 12th magnitude dwarf stars as a function of position in the FOV during the observing Campaign 14. Note that the uncorrected photometric precision of targets near the edges of the detector can be several times lower than near the centre. This is because of the roll motion of the spacecraft which gives rise to longer drifts for targets further away from the centre. Numbers denote output channels. The three CCD modules marked in white are no longer operational. Credit: Data release notes for C14[6].

The procedure described in this section is highly customizable and designed to be fine-tuned for each target individually to achieve the best possible photometric

---

[6] https://keplerscience.arc.nasa.gov/k2-fields.html

performance. I used it at least as an initial data reduction for all targets presented in this thesis, except WASP-157 and K2-140 which were observed in the long-cadence observing mode. The total computer processing time to perform all steps described in Section 2.3 for one short-cadence TPF is less than 15 min, of which 3–4 min are needed for the SFF procedure. The initial version of modified `kepsff` was ready in March 2015, followed by several small improvements throughout this research project.

2.4 Modified `K2SC` Procedure

The direction in which the *K2* spacecraft drifts depends on the net torque induced by the solar radiation pressure. As the spacecraft orbits the Sun during an observing campaign, the angle between the Sun and the spacecraft's pointing varies. This gives rise to changes in drifts' behaviour and even reversals of drift direction if the radiation pressure starts pushing the spacecraft the opposite direction around the rolling axis. The latter is seen once or twice in each observing campaign, which can be addressed by implementing manual break points in drift artefact removal procedures, as also done when using the modified `kepsff` procedure presented in Section 2.3.4. However, certain observing campaigns exhibited larger-than usual drift inconsistencies on shorter timescales, which could not be addressed efficiently with `kepsff`. The procedure failed to provide a satisfactory flux-arclength correlation whenever there were differently-behaving drifts within the same data reduction time window (see middle panel in Fig. 2.9). This established the need for an alternative procedure to be able to correct for inconsistent drifts.

Aigrain, Parviainen & Pope (2016) presented the *K2* Systematic Correction (`K2SC`) procedure to correct drift artefacts using the Gaussian process regression. `K2SC` models the position-dependent systematic and time-dependent variability simultaneously. Its main advantage is that it is capable of correcting differently-behaving drifts robustly. A brief comparison to other available pipelines for correction drift artefacts is given in Section 2.5. Detailed description of the mechanics and performance of `K2SC` can be found in Aigrain, Parviainen & Pope (2016).

The publically available version of `K2SC` is designed for processing long-cadence *K2* data. To be able to use `K2SC` for short-cadence data, I implemented two main modifications, following the discussions and help from Prof. Suzanne Aigrain.

First, the `K2SC`'s total processing time scales steeper than cubic and memory consumption scales quadratically with the number of data points for larger data sets. Processing time for a typical long-cadence data set of 3800 data points is of the order of one minute, depending on selected processing parameters and computer performance, and uses about 0.5 GB of memory. A short-cadence data set with ∼115,000 data points would require several tens of hours to process and several hundreds of GB of memory, unavailable in typical personal computers. A computer with 8 GB of memory is unable to process data sets larger than 15,000 data points. To circumvent the memory issue and to reduce the processing time, I split each short-cadence light curve into a specified number of partly-overlapping sections and applied the `K2SC` artefact removal procedure on each section individually. I then used the overlapping regions to minimize any offsets when merging the light-curve sections back together. I normally used 11 sections, with 10% overlap regions. With this approach, I was able to process the short-cadence data without running out of memory and reduced the total `K2SC` processing time to ∼50 min.

Second, `K2SC` uses the target's position calculated from the spacecraft motion polynomials as the position input. These positions are calculated by the SOC's PDC module and are provided with the official data release but only for the long-cadence data. To instead use the 1st moments target positions, measured with `kepextract` (see Section 2.3.2), I simply changed the names of the header keywords for target positions.

Compared to the modified `kepsff` procedure, `K2SC` performs better in correcting short-cadence light curves whenever the spacecraft drifts are inconsistent (see Fig. 2.9). For observing campaigns with consistent drifts, I generally obtained marginally better results with `kepsff`. `K2SC` occasionally failed to model large low-frequency photometric modulations properly and produced additional artefacts in small parts of light curves. Such light-curve regions had to be reprocessed using a different set of parameters or a different procedure (see e.g. Section 9.3).

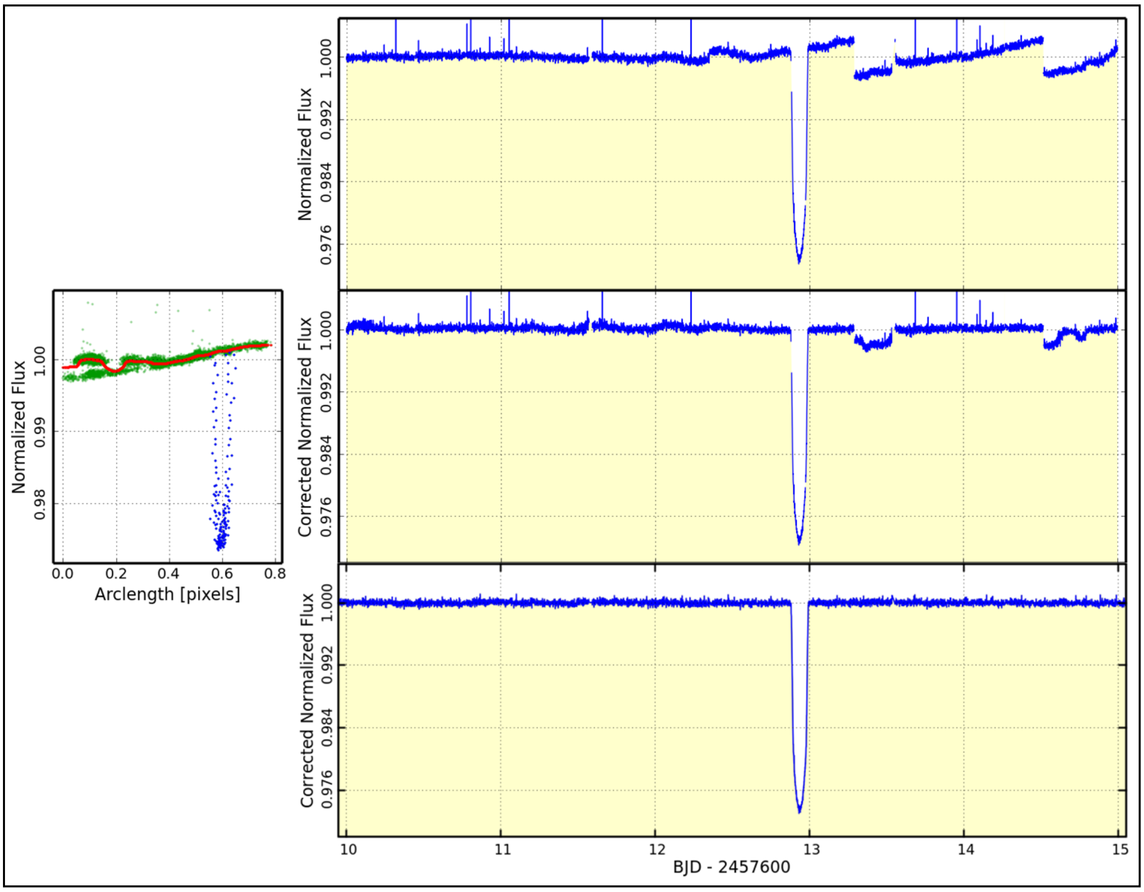

Figure 2.9: Comparison between modified `kepsff` (middle panel) and `K2SC` (bottom panel) procedures at correcting inconsistent drifts in a 5-day section of WASP-107 light curve (top panel). Middle left panel: Flux-arclength correlation, fitted with a Gaussian convolution with modified `kepsff` procedure. Note that different drift trajectories cannot be fitted well with a single function.

Shown in Fig. 2.9 is a comparison between `kepsff` and `K2SC` performance for a section of WASP-107 light curve which was affected by inconsistent spacecraft drifts. I was using the modified `K2SC` procedure from July 2016 onwards and it was used as the final drift-correction procedure for WASP-107, -28 and -151.

2.5 Procedures for Correcting *K2* Systematics

The degraded pointing precision of the *K2* spacecraft triggered the creation of several data reduction pipelines, either specialized for a specific task or an improvement of previously-available pipelines. Table 2.1 lists in chronological order all *K2* data reduction procedures that are capable of correcting pointing drift artefacts, and their products are publically available through MAST as *K2* High Level Science Products. Listed in Table 2.1 are also the two procedures used in this research project, modified `kepsff` and `K2SC`.

Table 2.1: Overview of available procedures for correcting drift artefacts. Initial release dates are approximate. Reduced data availability lists the observing campaigns for which the reduced data are currently available. Cadence type specifies whether the procedure was designed for long-cadence (LC) or short-cadence (SC) *K2* data.

Procedure	Initial release date	Reduced data availability	Cadence type	Reference
`K2SFF`	Aug 2014	CEng, C0-C15	LC	Vanderburg & Johnson (2014)
`K2VARCAT`	Nov 2014	C0-C4	LC	Armstrong et al. (2016)
modified `kepsff`	Mar 2015	any	SC	Močnik et al. (2016a)
`KEGS`	Jul 2015	extragalactic targets: C3-C6, C10	LC	Shaya et al. (2015)
`K2SC`	Mar 2016	C3-C8, C10	LC	Aigrain et al. (2016)
modified `K2SC`	Jul 2016	any	SC	Močnik et al. (2017)
`EVEREST`	Jul 2016	C0-C8	LC	Luger et al. (2016)
`POLAR`	Jul 2016	C1-C6	LC	Barros et al. (2016)
`EVEREST 2.0`	Feb 2017	C0-C8, C10-C13	LC, SC	Luger et al. (2017)

As can be seen from Table 2.1, there were no short-cadence data products or publically available procedures suitable for reducing short-cadence data until 2017. This prompted the construction of the modified `kepsff` procedure (Section 2.3.4), with the initial version ready for use in March 2015. Although the decorrelation method used in the modified `kepsff` tool is capable of recovering *Kepler*-like photometric precision, it fails to correct inconsistent drift artifacts properly. The solution was offered in March 2016 by the `K2SC` procedure (Aigrain, Parviainen & Pope 2016), which corrects inconsistent drifts reliably with the use of Gaussian process regression. However, `K2SC` was designed for long-cadence data and I had to make modifications to be able to use it

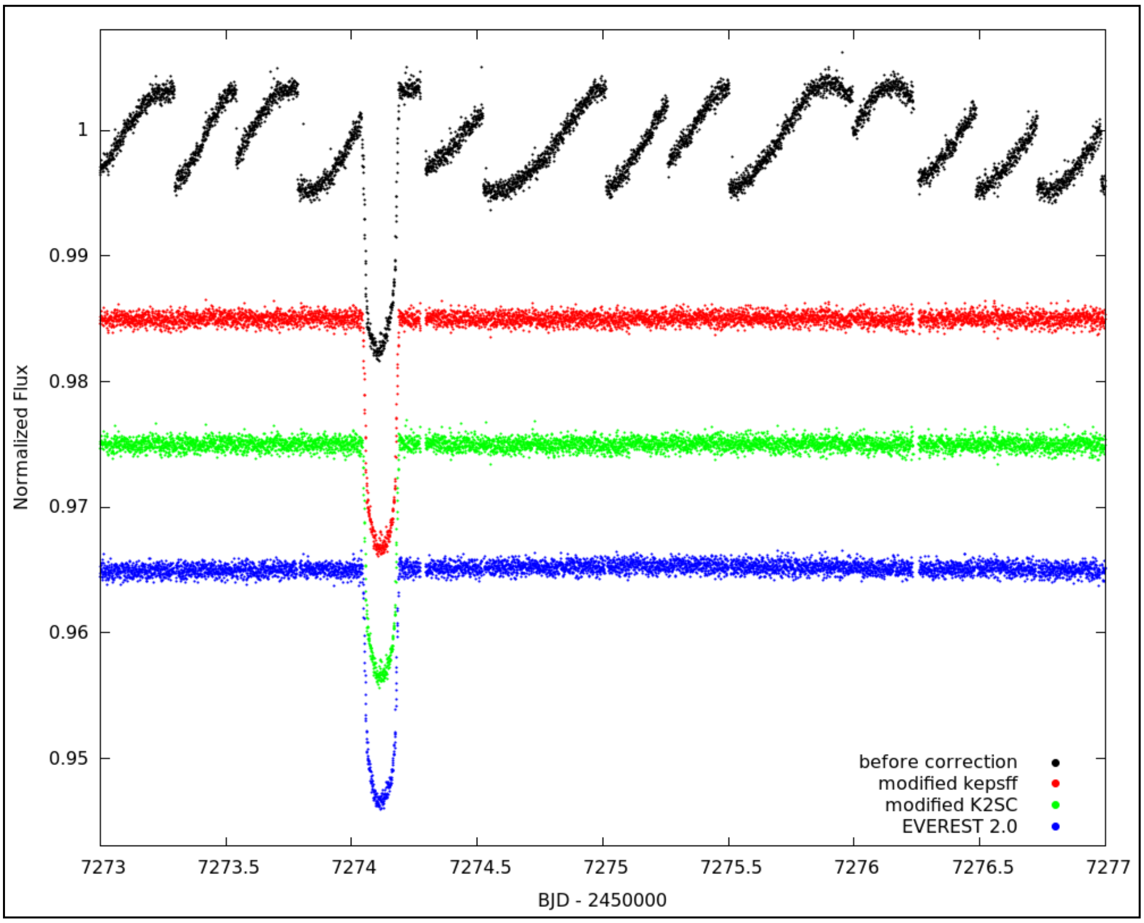

Figure 2.10: Comparison between modified `kepsff` (red data points), modified `K2SC` (green) and `EVEREST 2.0` (blue). Their performance in removing consistent drift artefacts (black) is practically undistinguishable. Shown is an example light-curve section of WASP-55.

with the short-cadence data (see Section 2.4). Modified `K2SC` was ready to use from July 2016.

Modified `kepsff`, modified `K2SC` and `EVEREST 2.0` (Luger et al. 2017) all produce very similar results whenever the spacecraft drifts are consistent (see Fig. 2.10). The pixel-level decorrelation method used by `EVEREST 2.0` also performs similarly in decorrecting inconsistent drifts as the Gaussian processes method used by `K2SC`. The late release of `EVEREST 2.0`, similar performance in removing drift artefacts and better established routines for the earlier procedures were the main reasons to use the modified `kepsff` and modified `K2SC` for the remainder of this research project.

3 *K2* Observing Campaigns

A total of 19 campaigns have been successfully observed in the *K2* mission as of the time of writing (June 2018): The Two-wheel Concept Engineering Test or, shorter, the Engineering Campaign (CEng), the first full-length science observing campaign to prove the viability of the *K2* mission (C0), and 17 regular and consecutively-executed observing campaigns (C1-C17). All the already-observed and downlinked observing campaigns are listed in Table 3.1, along with Campaign 18 which is currently being executed and Campaigns 19 and 20 that are expected to execute provided that the spacecraft does not run out of fuel before the downlink.

Also listed in Table 3.1 in the right-most column are all the targets that are part of this research project and presented in this thesis. The listed targets were selected for observations by the *K2* mission based on the downlink proposals prepared either by the author (C14-19), colleagues (Prof. Coel Hellier (C1, C3), Dr John Southworth (C6), Dr David R. Anderson (C8, C10, C12)), or other investigators (WASP-157 in C6, K2-140 in C10).

All targets presented in this thesis have been observed in the 1-min short-cadence observing mode, except WASP-157 and K2-140 which were observed in the 30-min long-cadence.

The sky-positions of analysed targets and the *K2* FOVs of all observing campaigns are shown in Fig. 3.1.

In the following chapters I present the analysis and results of individual planetary systems listed in Table 3.1, in order of observations. Chapters 4 and 7–12 are based on a lead-authored published, submitted or accepted journal papers. Chapter 6 is based on a co-authored published paper and Chapter 5 serves as demonstration of the procedure to search for additional transiting planets. Chapters 4 and 6–12 were kept mostly unchanged and with the information correct as of the time of writing the corresponding journal papers. Any additions or changes are specified in the preamble of each these chapters, along with the description of contributions from other authors.

Table 3.1: *K2* observing campaigns. Dates of the pending official data releases are approximate. The names of targets presented in this thesis are in the roman font and targets pending analysis or observations are in italic font. Targets for C19 and C20 have not been confirmed yet. WASP targets are abbreviated as W and Qatar-2 is abbreviated as Q2. I sourced the data for this table from *K2* Campaign Fields[7] (last access 2018 June 04).

Campaign	Start	Stop	Data release	Targets
Eng	2014 Feb 04	2014 Feb 13	2014 Mar 25	W28
0	2014 Mar 08	2014 May 27	2014 Sep 08	
1	2014 May 30	2014 Aug 21	2014 Dec 23	W85
2	2014 Aug 23	2014 Nov 13	2015 Mar 16	
3	2014 Nov 14	2015 Feb 03	2015 Jul 17	W47, W75
4	2015 Feb 07	2015 Apr 23	2015 Sep 04	
5	2015 Apr 27	2015 Jul 10	2015 Oct 31	
6	2015 Jul 14	2015 Sep 30	2016 Feb 12	W55, W157, Q2
7	2015 Oct 04	2015 Dec 26	2016 Apr 20	
8	2016 Jan 03	2016 Mar 23	2016 Jul 04	W118
9	2016 Apr 21	2016 Jul 01	2016 Sep 30	
10	2016 Jul 06	2016 Sep 20	2016 Dec 20	W107, K2-140
11	2016 Sep 24	2016 Dec 08	2017 Jun 30	
12	2016 Dec 15	2017 Mar 04	2017 Jul 31	W28, W151
13	2017 Mar 08	2017 May 27	2017 Aug 28	
14	2017 May 31	2017 Aug 19	2017 Nov 20	W104
15	2017 Aug 23	2017 Nov 20	2018 Mar 14	*K2-38*
16	2017 Dec 07	2018 Feb 25	2018 May 30	*K2-34*
17	2018 Mar 01	2018 May 08	2018 Aug-Nov	*W157, K2-99, K2-110*
18	2018 May 12	2018 Aug 02	2018 Nov-Mar	*many*
19	2018 Aug 06	2018 Oct 10	2019 Feb-May	
20	2018 Oct 15	2019 Jan 05	2019 May-Aug	

---

[7] https://keplerscience.arc.nasa.gov/k2-fields.html

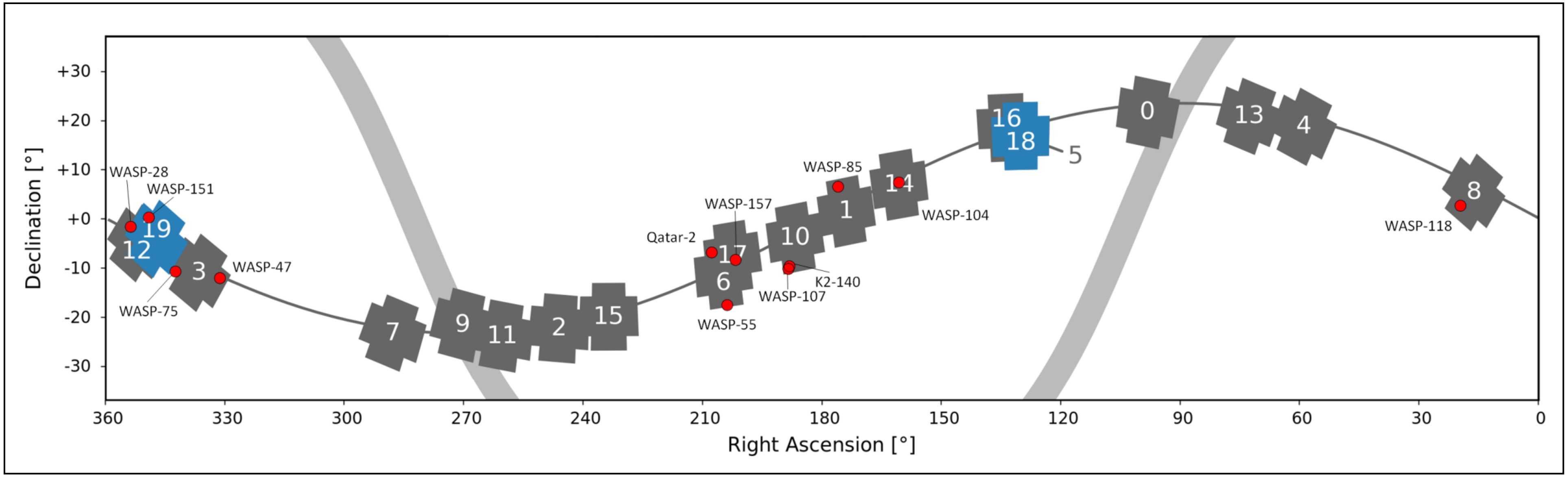

Figure 3.1: Position and orientation of *K2* FOV for every observing campaign. Marked with red circles are the actual locations of all targets presented in this thesis. Dark grey line is the ecliptic and light grey band is the galactic plane. Campaigns marked with blue colour have not been executed yet. Adapted from Barentsen (2018).

4 WASP-85

This chapter is based on Močnik et al. (2016a), AJ, 151, 150. The contributions from the co-authors were as follows: BJMC designed the Gaussian convolution procedure, which I integrated into the modified `kepsff` to correct the drift artefacts; DRA provided advice on the use of the MCMC analysis of system parameters; CH submitted the *K2* downlink proposal, supervised the research and provided general advice; DJAB, who is a lead author of the WASP-85Ab discovery paper, cross-checked our results with the discovery data. All co-authors also helped in identifying starspot occultation events and commented the paper draft before submission. Compared to the published version of the paper, I added in this chapter the WHT high resolution image of the WASP-85 binary, expanded the description of our MCMC procedure for fitting system parameters, added the MCMC corner plot, and provided a brief context for the newly-determined upper limit of WASP-85b's albedo.

4.1 Abstract

By analysing *K2* short-cadence observations we detect starspots on WASP-85A, the host star of the hot Jupiter WASP-85Ab. The detection of recurring starspot occultation events indicates that the planet's orbit is aligned with the star's rotational axis ($\lambda < 14°$) and suggests a stellar rotational period of 15.1 ± 0.6 days. The *K2* light curve reveals a rotational modulation with a period of 13.6 ± 1.6 days, consistent with the period determined from starspots. There are no significant transit-timing variations and thus no evidence of any additional planet in the system. Given the pronounced rotational

modulation we are only able to place an upper limit of 100 parts per million for any phase-curve modulations and the secondary eclipse.

4.2 Introduction

Since the failure of a second reaction wheel, the *Kepler* telescope provides the community with *K2* observations of fields along the ecliptic plane (Howell et al. 2014), and is therefore observing some previously known WASP exoplanets. One result has been the discovery of two additional transiting planets in the WASP-47 system (Becker et al. 2015).

The transiting hot Jupiter WASP-85Ab was discovered by Brown et al. (2014) and was observed by *K2* in Campaign 1. It has a 2.66-day orbit around its G5, $V = 11.2$ host star. WASP-85A forms a close visual binary, with an angular separation of 1.5 arcsec, with a cooler and dimmer K0, $V = 11.9$ WASP-85B (see Fig. 4.1). The WASP photometry showed that one of the two binary components exhibits a 14.6 ± 1.5 days rotational modulation, which indicates stellar activity (Brown et al. 2014).

When a starspot is occulted by a transiting planet the light curve exhibits a “bump” of temporary brightening (Silva 2003). The detection of starspots can provide a measurement or a constraint on the stellar obliquity, i.e. the angle between the stellar rotation and the planet’s orbital axis. For example, the recurrence of the same starspot in consecutive transits has revealed that Kepler-17 has a low obliquity (Désert et al. 2011). The ability to detect the recurring starspot occultation in a particular system depends on the ratio between the stellar rotational and planet orbital periods, and the lifetime of starspots. Alternatively, if starspots are occulted at certain preferential phases of the transit, this may constrain the obliquity if the transit chord crosses the active stellar

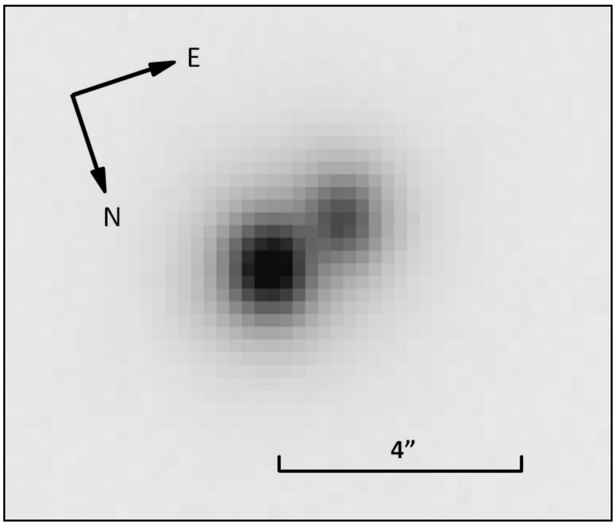

Figure 4.1: High resolution image of WASP-85 binary. WASP-85A (*V* = 11.2) hosts a transiting planet. Fainter WASP-85B (*V* = 11.9) is 1.5 arcsec to the East. In the lower-right is the 4-arcsec *K2* pixel scale for comparison. The image was obtained with the Intermediate dispersion Spectrograph and Imaging System (ISIS) mounted at the William Hershel Telescope (WHT) on 2009 May 28 (PI Prof. Don Pollacco).

latitudes at the observed active phases, as in the case of HAT-P-11 (Sanchis-Ojeda & Winn 2011).

The majority of hot Jupiters around stars cooler than around 6250 K are found in aligned orbits, suggestive of a disc migration mechanism. Hotter stars, on the other hand, host hot Jupiters that are in many cases found in misaligned orbits (Albrecht et al. 2012), which cannot be accounted for solely by planet disc migration mechanism. Instead, it is believed that planet–planet scattering, Kozai mechanism and tidal dissipation play an additional role in shaping misaligned orbits of hot Jupiters (e.g. Triaud et al. 2010).

In this paper, we present a detection of starspots in the *K2* light curve of WASP-85, which we use to constrain the stellar obliquity. We also refine the system parameters and the stellar rotational period, and search for transit-timing variations, as could be caused by an additional body in the system.

4.3 The *K2* Observations

The *K2* Campaign 1 observations cover an 82-day time-span between 2014 May 30 and 2014 August 20 and provide a total of 120,660 short-cadence images. We retrieved the 1-min short-cadence target pixel file for WASP-85 via the Mikulski Archive for Space Telescopes (MAST).

Given the degraded pointing accuracy of *K2*, the photometric precision is reduced because the position of an observed object drifts within the photometric aperture, and because of the non-uniform pixel sensitivity of the on-board detectors. Vanderburg & Johnson (2014) developed a self-flat-fielding (SFF) procedure with which they correct the long-cadence photometry to within a factor of two of the original *Kepler* precision by correlating the measured flux and arclength of the drift. Our *K2* data-reduction procedure for short-cadence observations is similar to the procedure presented by Vanderburg & Johnson (2014).

We first applied a standard data reduction procedure using `PyRAF` tools for *Kepler* (`PyKE`) version 2.6.2 (Still & Barclay 2012). Besides removing all the frames that were originally quality-flagged by *K2*, we manually adjusted quality flags and removed an additional 100 frames between 2014 June 1 18:04 UT and 19:41 UT, since they were obtained while the spacecraft was still in coarse pointing after the attitude tweak. Next, we used a large 100-pixels aperture mask to accommodate the diluted photometric signal from both binary components, WASP-85A and WASP-85B, and to reduce the photometric losses due to the relative drift between the object and the extraction aperture. Photometry of the individual binary components could not be performed because the angular separation (1.5 arcsec) is smaller than the *Kepler* point spread function (full width half maximum of 6 arcsec) – see Fig. 4.1.

After the data extraction and removal of low-frequency modulations, we performed our SFF procedure. The procedure is based on the `PyKE` tool `kepsff` with two main modifications to adjust and improve the efficiency for the short-cadence data. First, the 1-min short-cadence frames obtained during the thruster firing events are seen to have object positions that are outliers from the mean position drift on the detector. Data points with positional deviations of more than 6σ were flagged as thruster firing events and deleted (see Fig. 4.2a). This level was established by trial and error, as rejecting the thruster firing events while removing a minimal number of good data points. A total of 490 data points were quality-flagged as thruster firing events, which represents 0.4 per cent of the entire light curve.

Second, instead of using the polynomial to fit the flux versus arclength of the positional drift of the spacecraft, we used convolution with a Gaussian kernel, which provided an improved fit of the correlation compared to the polynomial. For each data point the Gaussian convolution calculates the peak of the Gaussian flux distribution of a specified number of data points nearest in arclength to a particular data point. At this stage the deviating data points are typically of astrophysical origin and should be rejected to avoid any bias in the SFF calibration. Trial and error indicated that the flux-versus-drift arclength correlation was best fitted when using a Gaussian kernel with a width of 50 data points and a rejection threshold of 4σ (see Fig. 4.2b). After the Gaussian peaks have been calculated for all the data points the flux of every data point was replaced with a corresponding Gaussian peak. Figs. 4.2c and 4.2d show an example light curve of a 5-day calibration time interval, before and after SFF, respectively. The time interval of 5 days was chosen as the best compromise between including a larger statistical sample of spacecraft drifts and a long-term variable drift behaviour.

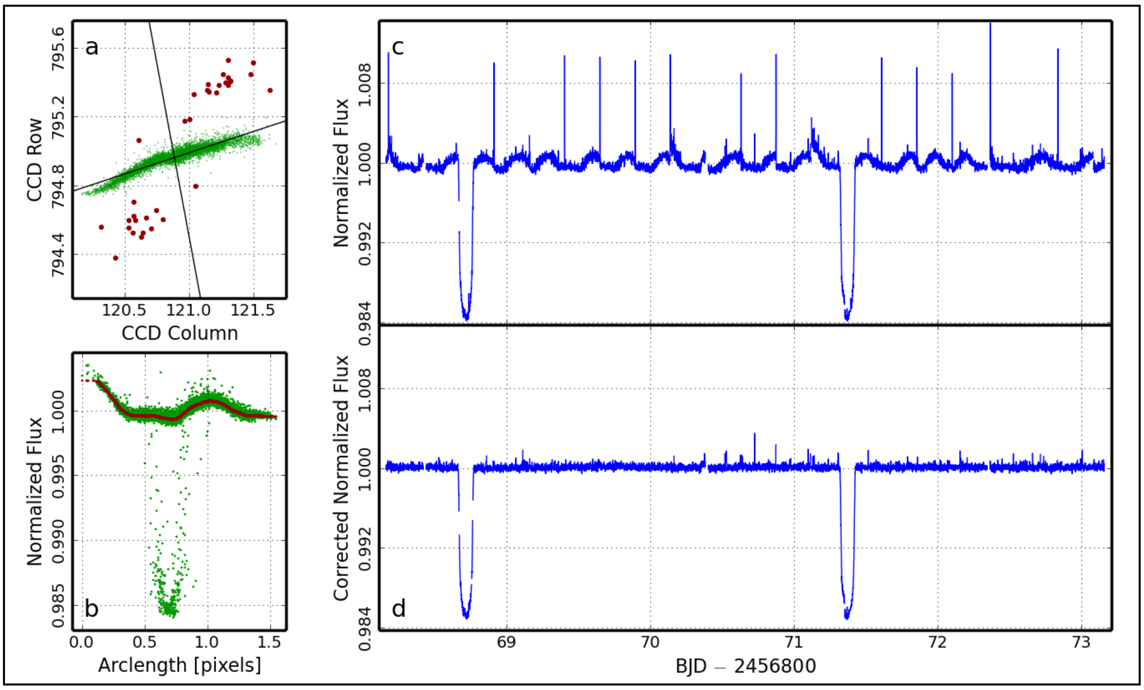

Figure 4.2: SFF calibration procedure. All the panels correspond to a time interval of 5 days. a: Position of the centre of the object given as CCD row vs. CCD column. Spatial outliers are marked with red and flagged as thruster events. b: Measured normalized flux vs. arclength of the spacecraft drift. The correlation is fitted with a Gaussian convolution (marked with red). c: Light curve before the SFF correction with the quality-flagged data points removed. d: Light curve after the SFF correction with the quality-flagged data points removed, including the thruster events which were identified during the SFF procedure. The positive flux excursions in the corrected light curve are the remaining cosmic rays that have avoided being identified and quality-flagged as cosmic rays in the downloaded *K2* target pixel file.

With these two modifications we achieved nearly twice the precision improvement compared to the original `kepsff` `PyKE` tool for the short-cadence dataset of WASP-85. The median 1-min photometric precision for WASP-85 ($K_p = 10.6$) was 778 parts per million (ppm) before SFF and 260 ppm after SFF, an improvement by a factor 3. For a comparison, the 1-min photometric precision of the original *Kepler* mission for a $K_p = 10.5$ star was 202 ppm (Still 2013).

After removal of all the quality-flagged data points, i.e. images affected by the cosmic rays, coarse pointing, spacecraft attitude tweak, thruster firing and reaction wheel de-saturation events, and a downlink data gap near the middle of Campaign 1, the total number of useful data points was reduced from 120,660 to 108,872. Fig. 4.3 shows the entire short-cadence light curve of WASP-85 before and after applying the SFF correction. A total of 30 transits are visible. Also visible is the rotational modulation caused by the presence of starspots.

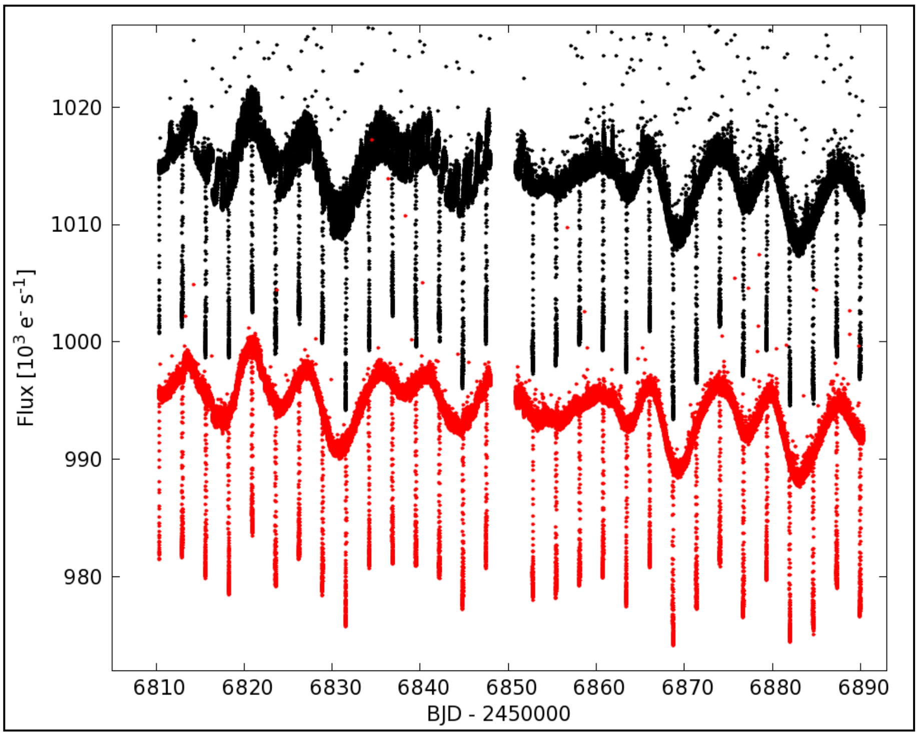

Figure 4.3: *K2* Campaign 1 short-cadence light curve of WASP-85 before (shown in black) and after the SFF correction (red). Note the presence of transits and starspot rotational modulation. The corrected light curve is shown with an offset of -20,000 e$^-$ s^{-1} for clarity.

4.4 Analysis and Results

4.4.1 System Parameters

We obtained the planetary system parameters using the Markov Chain Monte Carlo (MCMC) code presented in Collier Cameron et al. (2007) and further described in Pollacco et al. (2008) and Anderson et al. (2015). Our MCMC code simultaneously models the transit photometry with the transit model of Mandel & Agol (2002) and the radial velocity measurements with the Keplerian orbit. We calculated the transit model using the small planet approximation, where the stellar surface covered by the transiting planet is assumed to be of uniform brightness. This approximation simplifies the calculation of the transit model and is considered to reproduce reliable light curve models for planets smaller than 0.1 R_* (Mandel & Agol 2002). The use of this approximation for larger planets may introduce errors in transit light curve models, which leads to inaccurate determination of limb-darkening parameters and small systematic errors in determining planet-to-star radii from high-precision light curves. However, Neilson et al. (2018) have shown that the differences between the actual and parameterized stellar limb-darkening profiles largely cancel out with the errors introduced by the small planet approximation, and other photometric follow-up studies have also used the small planet approximation to model transits of planets larger than 0.1 R_* (e.g. Wang et al. 2014).

The proposal parameters used in the MCMC are: the epoch of mid-transit time (t_0), orbital period (P), total transit duration (t_{14}), transit flux deficit in the absence of limb darkening (ΔF), impact parameter (b), stellar effective temperature based on the limb-darkening fitting (T_{LD}), systemic radial velocity (γ) and stellar reflex velocity semi-amplitude (K_1). When fitting for orbital eccentricity (e) the MCMC code also uses $\sqrt{e}\cos\omega$ and $\sqrt{e}\sin\omega$ as proposal parameters, where ω is the argument of periastron. The physical properties are derived from the light curve parameters, spectroscopic characteristics of the host star and constraints from theoretical stellar models (e.g. Southworth 2011).

We accounted for stellar limb darkening using a four-parameter law, with coefficients calculated for *Kepler* bandpass and tabulated in Sing (2010). We interpolated the limb-darkening coefficients initially using the [Fe/H] and log(g) from Brown et al. (2014), and interpolated them at each MCMC step with the latest T_{LD}. T_{LD}

was used as a free fitting parameter but constrained with the Gaussian prior set at spectroscopic T_{eff} from the discovery paper.

In addition to the high-quality *K2* photometry presented herein we used the HARPS radial-velocity measurements of WASP-85A from Brown et al. (2014). These measurements are not thought to have been significantly contaminated by WASP-85B. We corrected the *K2* light curve for dilution by WASP-85B using a flux ratio F_B/F_A of 0.50 (Brown et al. 2014). Oshagh et al. (2013) showed that starspot anomalies can lead to an estimate of a planet radius that is up to 4% smaller than the real value and the transit duration may be over- or underestimated by about 4%. To avoid the inaccurate determination of system parameters due to the presence of starspot occultation events, we removed them from the measured light curve prior to the MCMC analysis. However, the unocculted photospheric features such as starspots and plages may reduce or increase the overall brightness of the host star, respectively, which affects the planetary transit depth while preserving the transit duration (Morris et al. 2018). The net effect of stellar activity on the determination of planetary radius depends on the properties and distribution of the photospheric features, which are often unknown. Since our system parameter analysis does not take into account the unocculted features, the derived planetary radius may be overestimated by a small systematic error, assuming that unocculted starspots have a larger effect on stellar brightness in the *Kepler* bandpass than plages (Shapiro et al. 2016). Based on the 1% amplitude of the diluted rotational modulation, the radius of WASP-85Ab should not be overestimated by more than 0.3σ.

We considered the system parameters of the MCMC chain had converged once the χ^2 of the transit and RV models exceeded the median of all previous χ^2 values, with a minimum of 500 iterations. The convergence was then manually examined by plotting the individual system parameters versus iteration number and checked that the values towards the end of the burn-in process remained constant within white noise. We excluded the burn-in iterations from the final MCMC analysis, which was based on a much larger number, 10^5, of post-burn-in iterations.

To refine the ephemeris (but not the other parameters), we produced a separate MCMC analysis that also included the ground-based photometry presented in Brown et al. (2014), with four-parameter limb-darkening coefficients from Claret (2000, 2004), as appropriate for different bandpasses. This extended the photometric baseline from 80 days to 6.5 years and reduced the uncertainty on the period by a factor of 4.

We present the system parameters in Table 4.1 and superimpose the corresponding transit model on the *K2* light curve in Fig. 4.4. The MCMC jump parameter posterior distributions are shown in Fig. 4.5.

Table 4.1: System parameters from MCMC for WASP-85Ab and its host star.

Parameter	Symbol	Value	Unit
Transit epoch[a]	t_0	2456847.472856 ± 0.000014	BJD
Orbital period[a]	P	2.65567770 ± 0.00000044	days
Area ratio	$(R_p/R_*)^2$	0.01870 ± 0.00002	...
Transit width	t_{14}	$0.10816^{+0.00006}_{-0.00002}$	days
Ingress and egress duration	t_{12}, t_{34}	$0.0130377^{+0.000008}_{-0.000016}$	days
Impact parameter	b	$0.028^{+0.027}_{-0.018}$	...
Orbital inclination	i	$89.82^{+0.12}_{-0.17}$	°
Orbital eccentricity	e	0 (adopted)	...
Orbital separation	a	0.039 ± 0.001	au
Stellar temperature[b]	T_{LD}	6112 ± 27	K
Stellar mass	M_*	1.09 ± 0.08	$M_\odot$
Stellar radius	R_*	0.935 ± 0.023	$R_\odot$
Stellar density	ρ_*	1.330 ± 0.007	$\rho_\odot$
Planet equilibrium temperature	T_p	1452 ± 6	K
Planet mass	M_p	1.265 ± 0.065	M_J
Planet radius	R_p	1.24 ± 0.03	R_J
Planet density	ρ_p	0.66 ± 0.02	ρ_J

Notes: [a] Epoch and period derived by fitting the photometric datasets from the *K2* and all the available ground-based observations.
[b] Stellar effective temperature, obtained from a fit to the transit light curve, is discrepant with the spectroscopic value ($T_{eff} = 5685 \pm 65\,K$).

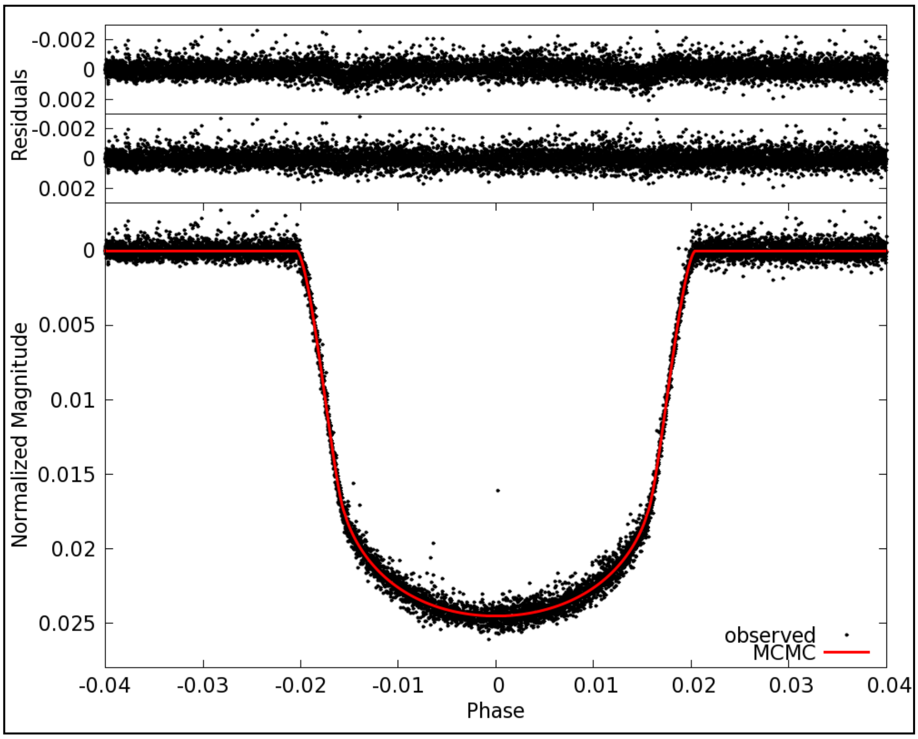

Figure 4.4: Best-fit MCMC model and its residuals from the phase-folded *K2* light curve near the transit. The light curve has been corrected for dilution by WASP-85B, using a flux ratio of 0.50. The lower residual panel corresponds to the photometric temperature of 6112 K as fitted by our MCMC analysis. The upper residual panel serves as a comparison and corresponds to the spectroscopic effective temperature of 5685 K which results in large residuals near ingress and egress.

There is a discrepancy between the stellar effective temperature derived from the HARPS spectra ($T_{\rm eff}$ = 5685 ± 65 K; Brown et al. 2014) and the value obtained from fitting the transits in our MCMC analysis ($T_{\rm LD}$ = 6112 ± 27 K). The same discrepancy, albeit smaller, is present in the discovery paper, which used only the ground-based transits ($T_{\rm LD}$ = 5910 ± 54 K from MCMC; Brown et al. 2014). When fitting the photometry (either ground-based or *K2*) with a transit model generated using the spectroscopic $T_{\rm eff}$, large systematics are evident during ingress and egress (see upper residual panel in Fig. 4.4), suggestive of a poor modelling of the limb darkening. The temperature discrepancy could be explained in part if light from WASP-85B had contaminated the spectra of WASP-85A, leading to a lower apparent $T_{\rm eff}$ for the primary, though any contamination is expected to be at a low level.

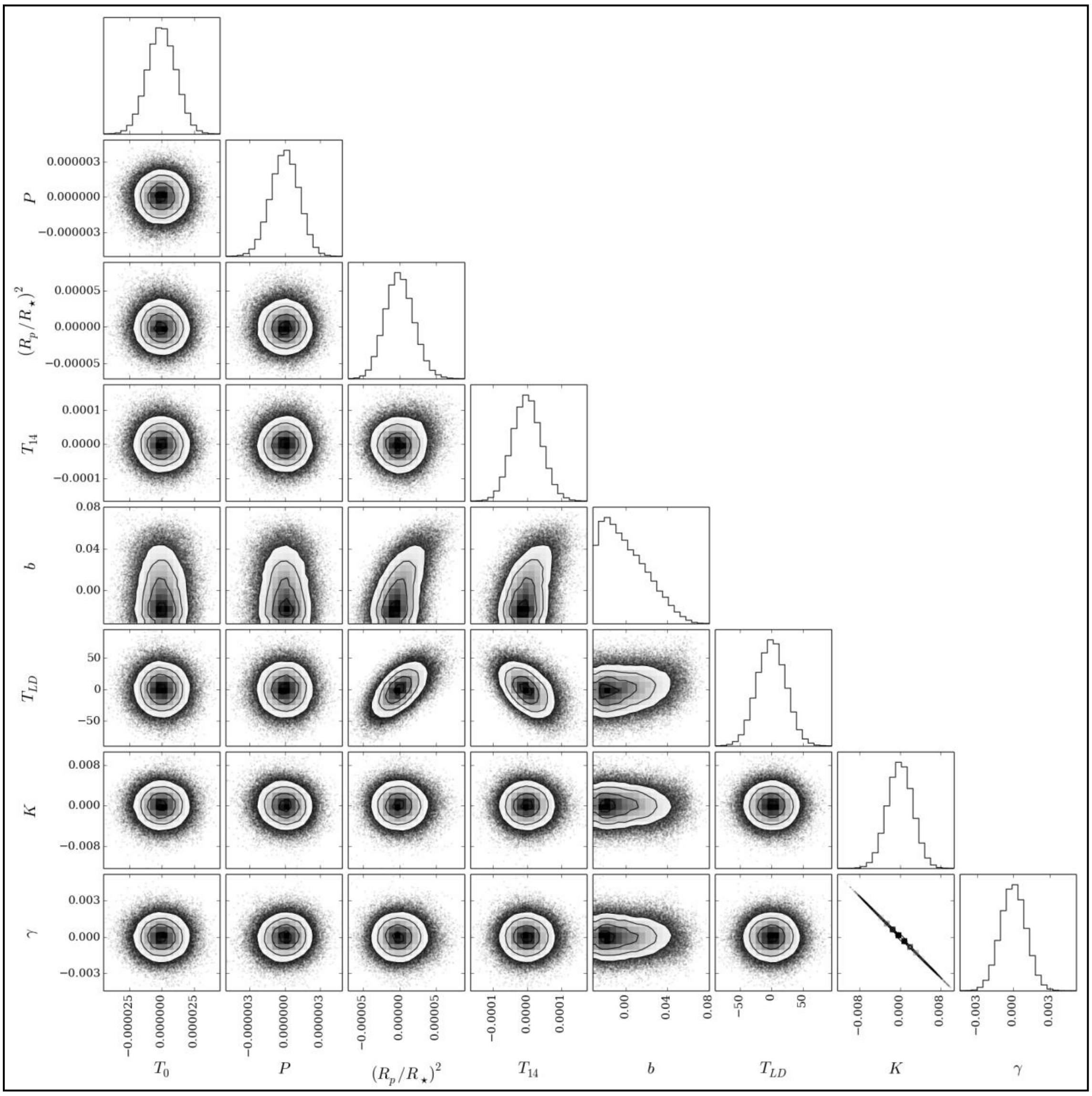

Figure 4.5: Corner plot of posterior distributions for MCMC jump parameters. The values are given as deviations from the best-fit values. The plot was created with corner.py version 2.0.2 (Foreman-Mackey 2016).

4.4.2 TTV and TDV

Transit-timing variations (TTVs) and transit-duration variations (TDVs) can arise from dynamical interactions with additional planets in the system (e.g. Becker et al. (2015) and citations therein). Typical reported TTV amplitudes for perturbed transiting exoplanets are of the order of a few tens of minutes with periods of a few hundred days (Mazeh et al. 2013). TDVs on the other hand are expected to be observed with smaller amplitudes and in phase with TTV. The first unequivocal exoplanet TDV detection was measured for system Kepler-88 and indicated a TDV amplitude of 5 min and a period of 630 days (Nesvorný et al. 2013).

We measured the transit-timings and transit-durations for WASP-85Ab for each of the transits using the MCMC analysis similarly as described in Section 4.4.1, and show the deviations in Fig. 4.6. The detected starpot occultations have again been removed from the light curve prior to the analysis as in Section 4.4.1. The error bars in Fig. 4.6 do not include any contribution due to the remaining unremoved stellar activity features, which will be contributing to the observed scatter of the TTV and TDV data points. One data point has been excluded from TTV and TDV analysis due to the thruster firing event residual that took place at the beginning of ingress of the fifth transit near BJD 2456821.

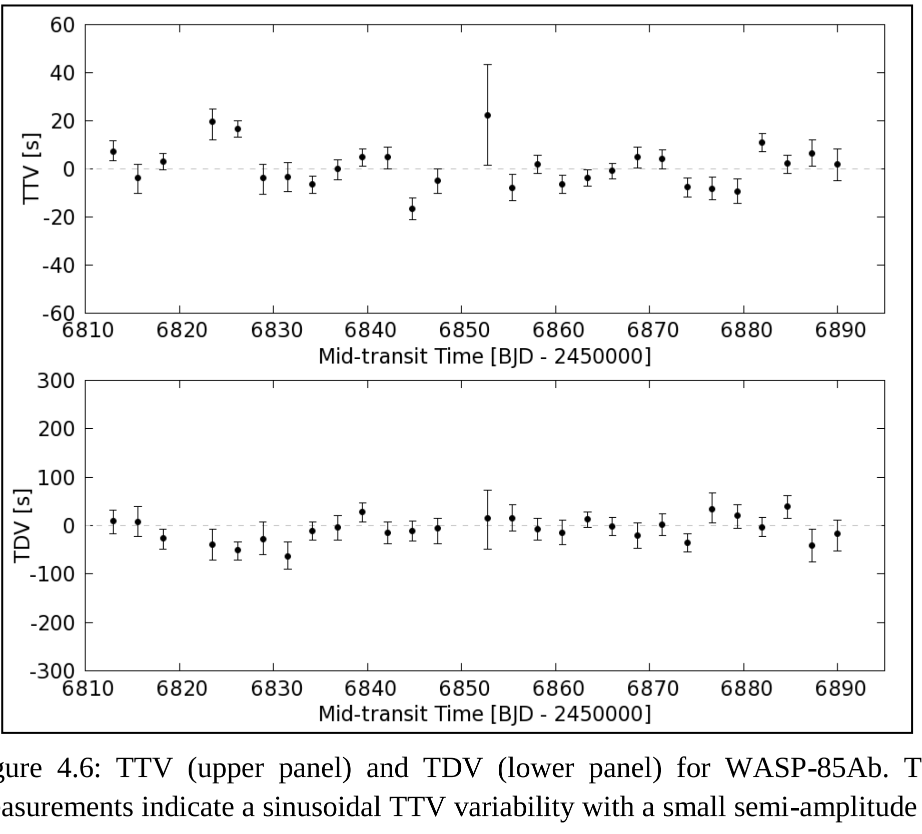

Figure 4.6: TTV (upper panel) and TDV (lower panel) for WASP-85Ab. The measurements indicate a sinusoidal TTV variability with a small semi-amplitude of 7.8 s and a period 14.7 days, likely a signature of stellar activity rather than actual TTVs. The TDV measurements are consistent with the assumption of constant transit-duration. Note that the data point with the largest error bars corresponds to the transit during which a reaction wheel de-saturation took place near the ingress (see transit 17 in Figure 4.7).

The hypothesis of the TDV values being zero gives a χ^2 of 31.8 for 28 degrees of freedom, which means we cannot reject it. The χ^2 for TTV is 90.6 for 28 degrees of freedom which rejects the white noise distribution hypothesis and suggests a sinusoidal TTV signal with a semi-amplitude of 7.8 s and a period of 14.7 days. This TTV signal, if real, would to the best of our knowledge have the smallest detected TTV amplitude to date. On the other hand, it is known that stellar activity can induce TTV signals with semi-amplitudes of up to 200 s (Oshagh et al. 2013) and that the imperfect removal of some of the starspot occultation events, and the effect of the stellar rotational modulation, could have resulted in the TTV variability. The TTV period of 14.7 days is also compatible with the measured rotational period of 15.1 ± 0.6 days (see Section 4.4.4) and it is therefore more likely that the small measured TTV signal results from stellar activity.

The very small TTV amplitude and the absence of statistically significant TDV indicates that a second, non-transiting, massive planet is unlikely, unless at a much longer period.

4.4.3 Starspot Detection

The short 1-min cadence of the *K2* observations and the restored photometric precision using the SFF enabled us to detect individual starspot occultations. We show in Fig. 4.7 the transit light curves after subtracting the transit model, thus showing only the residuals. We first looked for starspots by calculating the χ^2 value compared to a straight line. This was done by setting a box width equal to a phase width of 0.009, and sliding that box in time. The box width was determined by examining a few well defined starspot occultation events in the system. To estimate the threshold of significance we used the same box on out-of-transit data. Using this approach we were able to detect the

12 most prominent starspot occultation events above a χ^2_{red} threshold of 4 (marked with asterisks in Fig. 4.7). Below this threshold the residual light curve proved to be too unstable for this occultation detection technique.

To identify additional occultation events we asked four colleagues to mark definite and possible occultation events in the residual light curves near transits. The order of light curves was shuffled to avoid any bias towards spots that repeat in consecutive transits. All the events which were identified by at least two people as a possible starspot occultation event are listed in Table 4.2 and marked with red ellipses in Fig. 4.7. We identified a total of 23 starspot occultations. The measured χ^2_{red} of the individual occultation events are given in Table 4.2 and starspots are marked with

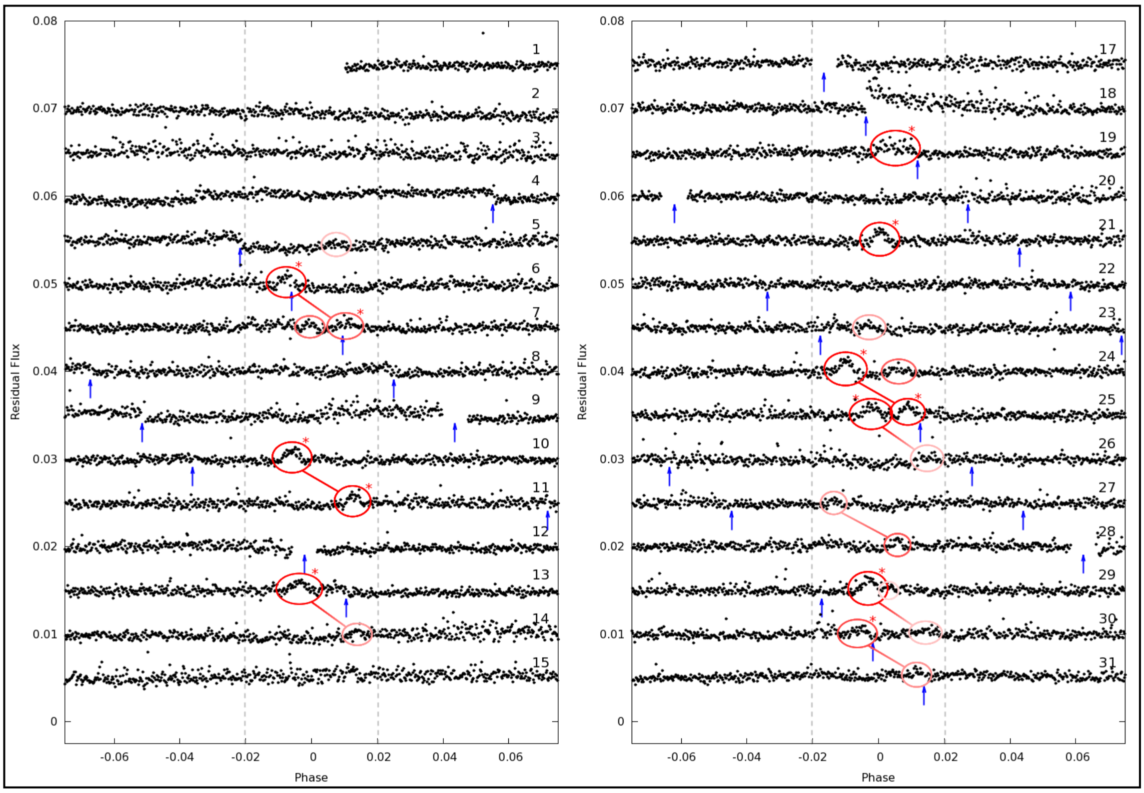

Figure 4.7: Starspot occultations in the model-subtracted light curve of WASP-85Ab. Vertical dashed lines specify the extent of the transit. Red ellipses mark the 23 identified starspot occultation events. The colour intensity denotes the detectability of events and asterisks correspond to events detected by our χ^2 occultation detection technique. Potential starspot occultation pairs are marked with red lines. Blue arrows mark the positions of thruster firing events. Note that transit number 16 lies in the *K2* data gap.

different color intensities in Fig. 4.7 as a rough indicator of their detectability.

Blue arrows are added in Fig. 4.7 to mark the positions of thruster firing events which occasionally introduce artefacts in the light curve. Thruster firing artefacts are especially present in the first quarter of the observing campaign due to the somewhat inconsistent spacecraft drifts which might lead to a confusion with occultation events. Nevertheless, a typical potential thruster firing artefact only causes a small step-like deviation in the light curve and in the out-of-transit WASP-85 light curve never resembles a starspot-like bump. Therefore, it seems unlikely that any of the in-transit starspot-like event would be a thruster firing artefact, despite occasional overlaps.

Table 4.2: Starspot occultation events.

Transit number	χ^2_{red}	Phase	Stellar longitude[a] [°]	Pair	Differential longitude [°]
5	1.57	0.0075	24.9	...	...
6	7.26	-0.0077	-25.6	6 + 7	60.7 ± 3.4
7	2.46	-0.0005	-1.7	...	...
7	4.91	0.0103	35.1	...	...
10	6.65	-0.0059	-19.4	10 + 11	63.7 ± 4.0
11	8.73	0.0125	44.3	...	...
13	5.25	-0.0037	-11.9	13 + 14	62.8 ± 4.2
14	1.65	0.0139	50.9	...	...
19	5.79	0.0051	16.7	...	...
21	6.21	0.0004	1.2	...	...
23	3.16	-0.0028	-9.0	...	...
24	8.13	-0.0100	-33.9	24 + 25	63.8 ± 3.8
24	3.06	0.0062	20.3	...	...
25	5.86	-0.0023	-7.5	25 + 26	63.3 ± 4.5
25	4.21	0.0089	29.9	...	...
26	1.82	0.0148	55.8	...	...
27	2.9	-0.0136	-49.4	27 + 28	68.2 ± 4.2
28	3.1	0.0058	18.8	...	...
29	5.63	-0.0028	-9.0	29 + 30	62.1 ± 4.3
29	2.31	0.0031	10.0	...	...
30	4.95	-0.0064	-20.9	30 + 31	61.3 ± 3.8
30	2.29	0.0143	53.1	...	...
31	1.81	0.0116	40.4	...	...

Note: [a] Stellar longitude of zero corresponds to the meridian that runs through the centre of the stellar disc.

4.4.4 Are the Starspots Recurring?

The presence of 23 starspots occultation events among 30 transits indicates that WASP-85A is magnetically active, that starspots occur uniformly along the transit chord, and that some starspot occultations are potentially occurring in pairs.

If the stellar rotational period is large compared to the orbital period of the planet and if the rotational and orbital axes are aligned, it is possible to see an occultation of the same starspot in consecutive transits. Fig. 4.7 reveals eight such potential starspot occultation pairs at consistent phase shifts. For example, an occultation event at phase 0.013 during transit 11 was likely caused by the same starspot that was responsible for the occultation event at phase -0.006 in transit 10. All eight potential occultation pairs are marked with red lines in Fig. 4.7 and their phase shifts and differential stellar longitudes are given in Table 4.2.

A detection of eight potential occultation pairs (16 spots) among a total of 23 starspot occultation events coupled with the small scatter among measured differential stellar longitudes indicates that occultation pairs were probably caused by occultations of the recurring starspots. It is therefore reasonable to suggest that planet's orbital and stellar rotational axis are aligned. Using the system parameter values from Section 4.4.1 we estimate that the projected obliquity angle has to be <14°. From the mean differential stellar longitude of the starspot pairs of 63.2 ± 2.3° (see Table 4.2) and known orbital period we derive a stellar rotational period of 15.1 ± 0.6 days. This is in agreement with the rotational modulation period (see Section 4.4.5) and with the spectroscopically determined rotational period of 14 ± 4 days for WASP-85A (Brown et al. 2014).

4.4.5 Rotational Modulation

The *K2* light curve shows a clear rotational modulation (see Fig. 4.3). To estimate the period we used an autocorrelation function (ACF). For this task, we first removed the transits from the light curve and then applied 10σ clipping. The rotational period is manifested as the highest ACF peak near 13.6 days and its multiples (see Fig. 4.8). Peaks corresponding to half of this period are caused by starspot regions on opposite sides of the star. The 80-day time-span of the *K2* observations covers five cycles of the 13.6-day periodicity. Following the procedure demonstrated by McQuillan, Aigrain & Mazeh (2013) we determined the rotational period as a median of the intervals Δτ between the ACF peaks associated with the rotational period. We conservatively estimated the error as the FWHM of the highest ACF peak.

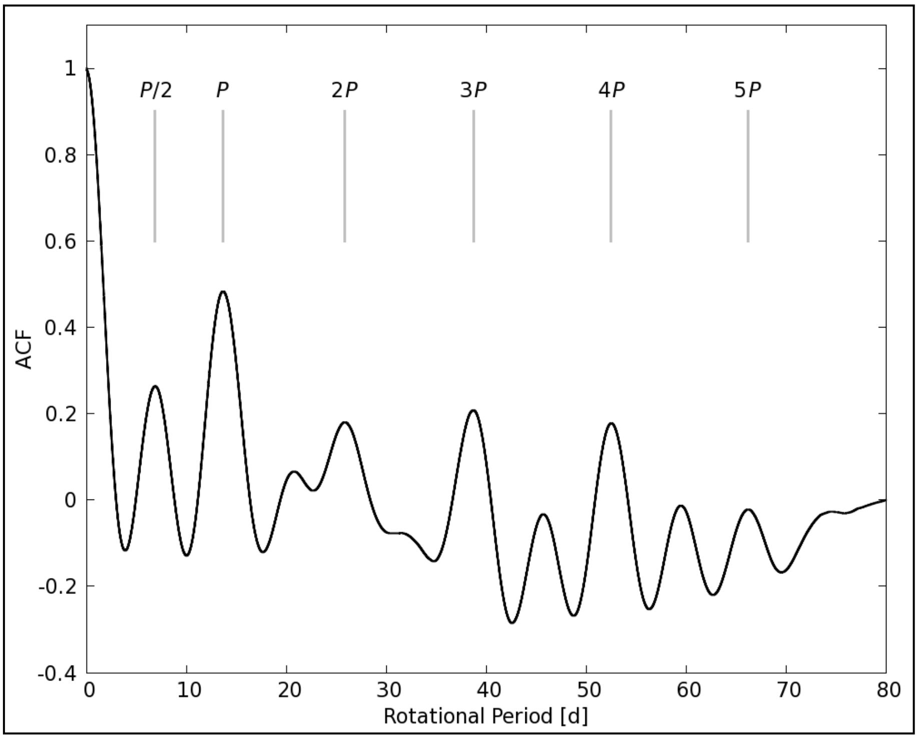

Figure 4.8: Autocorrelation function of the *K2* Campaign 1 short-cadence light curve of WASP-85. Marked with *P* is the first and highest peak corresponding to 13.6-day rotational period. Additional four peaks are visible at multiples of this period. Peaks corresponding to half period are likely caused by another starspot region on the opposite side of the star.

The resulting rotational period of 13.6 ± 1.6 days is in agreement with the spectroscopically determined rotational period for WASP-85A, 14 ± 4 days, if the star's rotational axis is orthogonal to the line of sight. But, the value is also in agreement with the estimated rotational period for WASP-85B, 12 ± 4 days (Brown et al. 2014). Therefore, it is uncertain which of the two binary components is causing the observed rotational modulation. However, because WASP-85A is active (see Fig. 4.7), it is reasonable to assume that the rotational modulation is caused by the rotation of the spotted surface of WASP-85A. Because rotational modulations depend strongly on starspots coming and going, which causes the phase shifts, the period derived from it is therefore less accurate and less reliable than the period determined via starspot occultations (see Section 4.4.4).

We used Spot Oscillation And Planet 2.0 (SOAP 2.0; Dumusque, Boisse & Santos 2014) to fit the starspot rotational modulation of WASP-85 and found that the three characteristic "M"-shaped modulation features can be well fitted with two main starspot regions on the opposite sides of the rotating stellar surface. However, the change in the light curve over time shows that the starspot regions are changing over the *K2* observations.

4.4.6 Phase-curve Variations

We folded the *K2* light curve on the orbital period of the planet. In order to do this we first removed the rotational modulation using our two-region model of the starspots. However, since this model is only an approximation, the folded light curve is still dominated by the residuals of the starspot modulation, which do not average out owing to the limited length of the *K2* observations (Fig. 4.9).

We did not detect the secondary eclipse nor any other phase-curve variations caused by the orbiting exoplanet. Using the system parameters from Table 4.1 the expected semi-amplitudes of ellipsoidal, Doppler, and reflection variations are 3.7, 2.1, and (for an albedo of 0.1) 15.4 ppm, respectively (Pfahl, Arras & Paxton 2008). We conservatively estimate an upper limit of 50 ppm for the semi-amplitude of variations over the planet's phase curve. Fig. 4.9 shows a comparison between the measured phase curve of WASP-85 and the simulated reflection modulation with a semi-amplitude of 50 ppm. The inability to detect the reflection modulation and the secondary eclipse in the measured *K2* phase curve of WASP-85 indicates that the planet's visual geometric albedo is lower than ~0.3 in the *Kepler* bandpass. For comparison, the geometric albedo of Jupiter is 0.50 in a bandpass similar to *Kepler*'s (Mallama, Krobusek & Pavlov 2017), whereas the albedos of hot Jupiters tend to be significantly lower (~0.1; Schwartz & Cowan 2015) due to presence of alkali metals as well as TiO and VO in their atmospheres which become highly optically absorbent at higher temperatures (Demory et al. 2011).

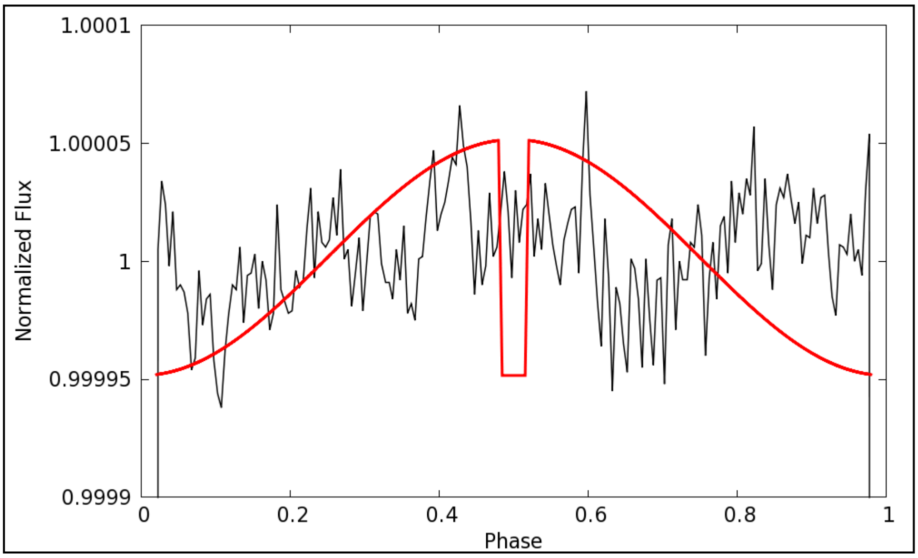

Figure 4.9: Measured phase curve of WASP-85, binned to 200 bins, (shown in black) and a simulated reflection phase-curve modulation with a semi-amplitude of 50 ppm (red). The inability to see the reflection modulation and secondary eclipse in the measured phase curve of similar amplitude as shown in the simulated phase-curve suggests that the actual reflection semi-amplitude is lower than 50 ppm.

4.5 Conclusion and Discussion

We have modified the `PyKE` self-flat-fielding method to nearly double its performance in restoring the degraded short-cadence photometric precision due to the pointing drift of the *K2* spacecraft. We refine the system parameters, measure a rotational modulation period of 13.6 days, and reconstruct the “M”-shaped photometric modulations with two dynamic starspot regions on either side of a magnetically active star. The presence of starspot occultations indicates that the host star WASP-85A is magnetically active and suggests that the stellar rotation and the planet’s orbital axis are aligned. The phase shifts of potential occultation pairs correspond to a stellar rotational period of 15.1 ± 0.6 days. The agreement between the stellar rotation and transit-timing variation period suggests that its small semi-amplitude of 8 s is a consequence of stellar activity rather than an inter-planet gravitational interaction. Measured transit-duration variability is consistent with white noise distribution around zero. We do not detect any phase-curve modulations nor the secondary eclipse of the planet.

Starspots provide one method of constraining the sky-projected obliquity of the host star, while the Rossiter–McLaughlin (RM) effect provides an independent estimate.

For example, in WASP-4 the RM effect implies a projected alignment angle of $\lambda = -4°^{+43}_{-34}$ (Triaud et al. 2010), while Sanchis-Ojeda et al. (2011) report that on two occasions the same starspot was occulted, from which they constrain the alignment to $\lambda = -1°^{+14}_{-12}$. Similarly in WASP-6 the RM angle is $\lambda = 11°^{+14}_{-18}$ (Gillon et al. 2009), and Tregloan-Reed et al. (2015) suggest that the same starspot was occulted in two transits and report $\lambda = 7.2 \pm 3.7°$. In WASP-19 the RM angle is $\lambda = 4.6 \pm 5.2°$ (Hellier et al. 2011), while Tregloan-Reed, Southworth & Tappert (2013) saw the same starspot occulted on consecutive nights and report $\lambda = 1.0 \pm 1.2°$.

HAT-P-11 is misaligned, with an RM angle of $\lambda = 103°^{+26}_{-10}$ (Winn et al. 2010b). The misalignment is confirmed by the analysis of starspots by Sanchis-Ojeda & Winn (2011). Similarly, for Kepler-63 Sanchis-Ojeda et al. (2013) report $\lambda = -110°^{+22}_{-14}$ from analysing both starspots and the RM effect.

There is currently no measurement of the RM effect in our system, WASP-85A, but we predict that it would confirm that the system is aligned. Qatar-2 is a similar case, where starspots indicate alignment (Mancini et al. 2014) though this is not yet confirmed by an RM measurement.

There are no reported cases where the RM angle conflicts with the analysis of starspots, and thus the starspots are a reliable way of measuring alignment in systems too faint for RM measurements. Examples are Kepler-30 (V = 15.6) where occultations of starspots by both Kepler-30c and Kepler-30d indicate alignment (Sanchis-Ojeda et al. 2012), and Kepler-17 (V = 14.3) where starspots also indicate alignment (Désert et al. 2011).

The benefit of ongoing *K2* observations of known WASP planets is that the systems are generally bright enough to enable good measurements of the alignment angle, λ, the stellar rotational period, the stellar radius, and the star's projected rotational broadening, $v \sin i$. Given all of these we obtain, not only the projected alignment λ, but the actual alignment angle ψ (see, e.g., Winn et al. 2005).

Adopting the rotational period of 15.1 ± 0.6 days, and combining with a stellar radius of 0.94 $R_\odot$ (Table 4.1) and a $v \sin i$ of 3.41 ± 0.89 km s^{-1} (Brown et al. 2014) we find that the star's rotational axis must be at >50° to the line of sight. This leads to the constraint that $\psi < 41°$.

The measured effective temperature and spin-orbit alignment of WASP-85 system are consistent with the current sample of predominantly aligned systems with stars below the characteristic effective temperature of 6250 K.

5 WASP-47

This chapter demonstrates the viability of the procedure to search for additional transiting planets, which I used also for other planetary systems presented in this thesis.

5.1 Introduction

WASP-47b was discovered by Hellier et al. (2012) around a $V = 11.9$ host star and was identified as a hot Jupiter with an orbital period 4.16 days and a mass of 1.14 M_J.

WASP-47 was observed by *K2* in Campaign 3 between 2014 November 14 and 2015 February 03 and the data were made publically available on 2015 July 17.

Becker et al. (2015) announced the detection of two additional transiting planets on 2015 August 10, a Neptune-sized planet WASP-47d with an orbital period of 9.0 days and a super-Earth WASP-47e with an orbital period of 0.79 days. In addition, they found significant TTV and TDV variations, as would be expected for close-in companion planets.

WASP-47b is the first hot Jupiter that has been found to have close-in companion planets. This finding suggests that all the WASP-47 planets migrated in a protoplanetary disc or that the tidal dissipation has happened near the end of migration to bring them in the current coplanar and compact configuration (Becker et al. 2015).

5.2 Detecting Additional Transiting Planets

Using the data reduction procedure presented in Section 2.3 I reduced the short-cadence light curve of WASP-47 within two weeks after the data became publically available.

With the help from my colleagues, Dr David R. Anderson and Ben Clark, we found the two additional transiting planets in the light curve of WASP-47, first the hot Neptune and later also the super-Earth. However, almost immediately after our discovery, Becker et al. (2015) announced these additional transiting planets in their paper. Fig. 5.1 shows a section of the reduced WASP-47 light curve, with labels b, d and e corresponding to individual planets.

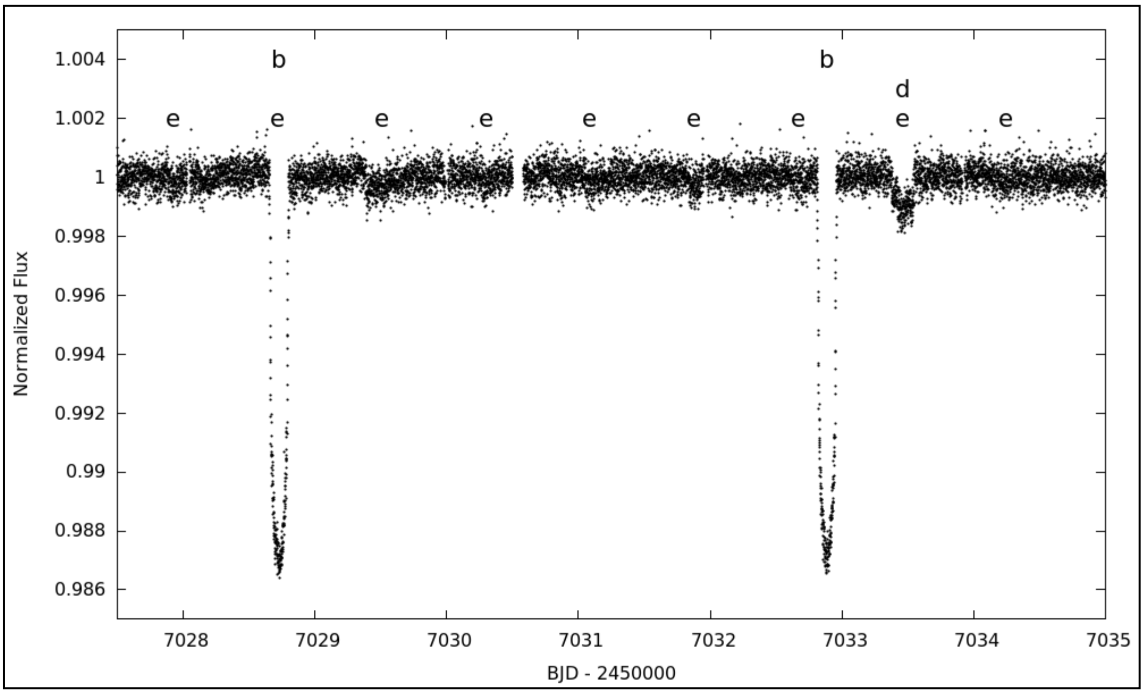

Figure 5.1: A section of WASP-47 light curve. WASP-47b: previously known hot Jupiter (with an orbital period of 4.16 days). WASP-47d: newly discovered hot Neptune (9.0 days). WASP-47e: newly discovered super-Earth (0.79 days).

Kovács, Zucker & Mazeh (2002) presented a box-least-square (BLS) procedure to detect additional transiting planets. BLS fits an actual light curve with a set of box-shaped periodic transits with a range of epochs, periods, depths and widths. At each period, BLS reports the largest signal residual (SR) from the best-fit epoch, relative transit width and depth (δ),

$$SR = \delta\sqrt{r(1-r)}\ , \tag{5.1}$$

where r is the relative time spent in transit within the data set. For continuous observations and short-period planets, r can be approximated as relative transit width, i.e. transit width in units of orbital phase.

An ensemble of *SR*s for a range of periods represents a BLS periodogram. I calculated BLS periodograms throughout this research project either with the `PyKE` tool `kepbls` (Still & Barclay 2012) or with the NASA Exoplanet Archive periodogram service[8]. Shown in Fig. 5.2 are the BLS periodiograms for WASP-47.

The maximum *SR*s of transiting planets b, d and e were $1.9 \cdot 10^{-3}$, $1.0 \cdot 10^{-4}$ and $5.9 \cdot 10^{-5}$, respectively (see Fig. 5.2). This in turn with their best-fit transit widths, r, and equation (5.1) corresponds to transit depths of $1.1 \cdot 10^{-2}$, $7.5 \cdot 10^{-4}$ and $2.0 \cdot 10^{-4}$, respectively, which is within 10% of their transit depths determined from the best-fit transit models (Becker et al. 2015). This demonstrates that the BLS method as applied in this research project is a robust method for detecting additional smaller transiting planets and that the *SR*s closely reflect actual transit depths.

The maximum *SR* in the bottom panel of Fig. 5.2 at 17.3-day period is only 1.5σ above the noise level and phase folding the light curve at this period does not reveal a real transit. Since this peak also corresponds to the largest residual transit depth among all investigated periods, I consider its depth of 130 ppm as an upper limit of any potential remaining transiting planets in the orbital period range of 0.5–30 days.

---

[8] https://exoplanetarchive.ipac.caltech.edu/cgi-bin/Pgram/nph-pgram

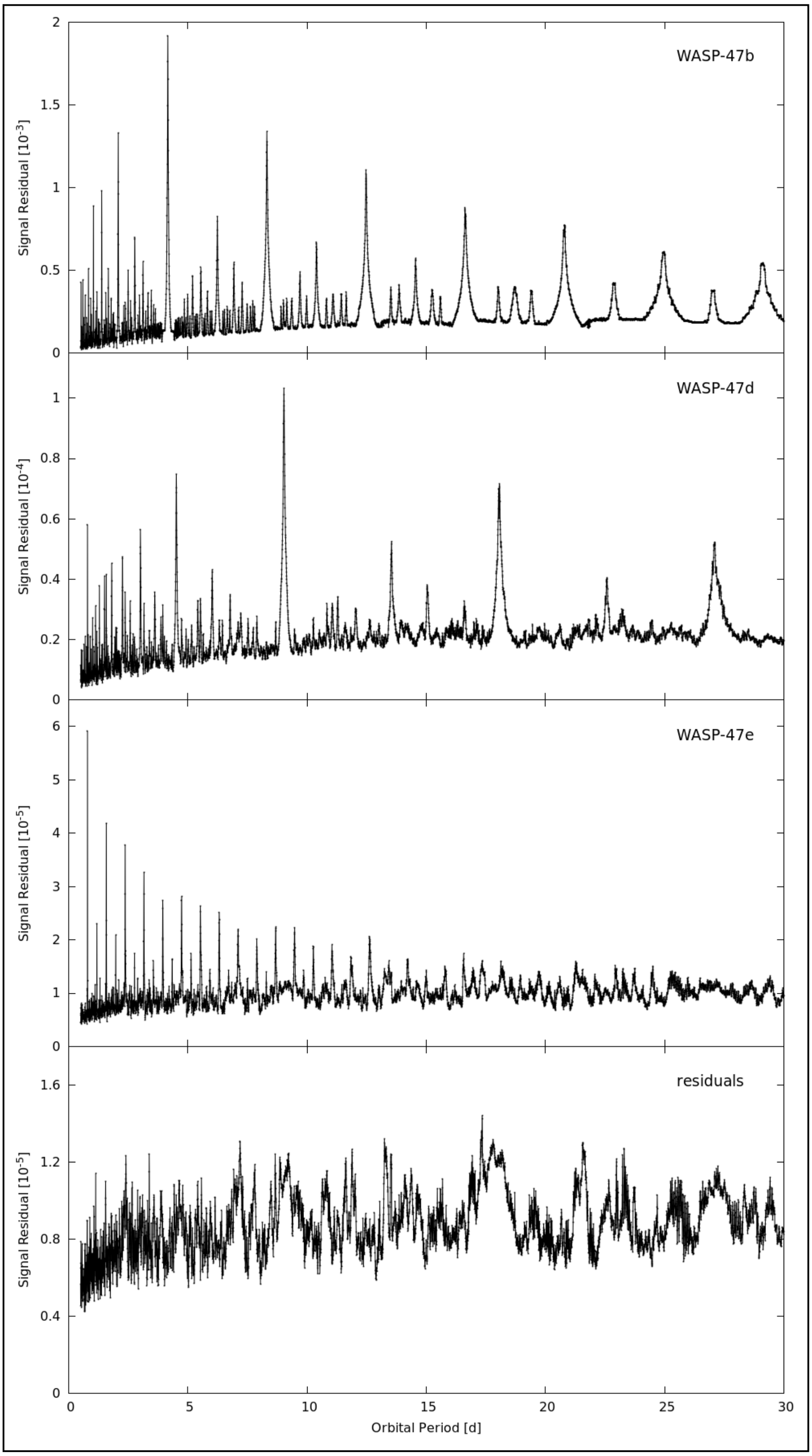

Figure 5.2: BLS periodograms for WASP-47 planets. Each panel has transit signals of planets identified in the panels above it, removed. The highest periodogram peaks in the top three panels correspond to the transiting planets b, d and e, respectively. The highest peak in the bottom panel is used as an upper limit of any remaining transiting planets in the system. Shown periodograms were calculated with NASA Exoplanet Archive BLS tool.

6 WASP-75 and WASP-55

This chapter is based on a co-authored paper Clark et al. (2018), PASP, 130, 034401. My contribution to the research presented in this paper was to perform an initial data reduction with the method from Section 2.3, check for the presence of any astrophysical signals of interest, provide advice about data reduction, and to comment on the paper draft before submission. I added in this section the discussion and Figs. 6.1 and 6.2 about the asteroid flyby near WASP-75.

6.1 Abstract

We present our analysis of the *K2* short-cadence data of two previously known hot Jupiter exoplanets: WASP-55b and WASP-75b. The high precision of the *K2* light curves enabled us to search for transit timing and duration variations, rotational modulation, starspots, phase-curve variations and additional transiting planets. We identified stellar variability in the WASP-75 light curve which may be an indication of rotational modulation, with an estimated period of 11.2 ± 1.5 days. We combined this with the spectroscopically measured $v \sin i_*$ to calculate a possible line of sight projected inclination angle of $i_* = 1 \pm 16°$. We also perform a global analysis of *K2* and previously published data to refine the system parameters.

6.2 Introduction

The *K2* mission has been in operation since May 2014 following the failure of two reaction wheels in the original *Kepler* mission (Howell et al. 2014), monitoring fields along the ecliptic plane. The spacecraft experiences a roll which introduces systematic errors in the photometric light curves on a timescale of approximately 6 hr when it is corrected by a thruster event. As a result the quality of the photometry can be degraded by up to a factor of 4 (Howell et al. 2014). Despite this, methods such as self flat-fielding (SFF) (Vanderburg & Johnson 2014), `K2SC` (Aigrain, Parviainen & Pope 2016) and routines that we have built (Močnik et al. 2016a) can reduce this effect to the extent that the quality of the produced data is near that of the original mission.

Following the initial discovery of an exoplanet, subsequent observations are common if a planet possesses unique characteristics (e.g. WASP-18b – Hellier et al. 2009). They are also frequent if the system is readily observable from Earth; for example, those with a bright host star such as WASP-33b (Christian et al. 2006) or planets with a large transit depth such as WASP-43b (Hellier et al. 2011). For other planets however, follow-up observations can range from infrequent to absent, meaning we can miss crucial discoveries about these systems. An example of this are the recent *K2* observations of the WASP-47 system that revealed two additional companions (Becker et al. 2015). WASP-55b and particularly WASP-75b are examples of two planets that have had little follow-up since their initial discoveries.

WASP-55b was found to be a moderately inflated hot Jupiter with a mass of $0.57 \pm 0.04\, M_{\mathrm{Jup}}$ and a radius of $1.30 \pm 0.05\ R_{\mathrm{Jup}}$ orbiting a G1 star discovered in 2011 (Hellier et al. 2012). WASP-75b was discovered by Gómez Maqueo Chew et al. (2013) as a hot Jupiter with a mass of $1.07 \pm 0.05\, M_{\mathrm{Jup}}$ and a radius of $1.27 \pm 0.05\, R_{\mathrm{Jup}}$. It orbits WASP-75, a F9 star with an orbital period of 2.484 days. In this paper we present a refined set of system parameters for WASP-55b and WASP-75b. We also search the *K2* light curves for transit timing and duration variations, stellar rotational modulation, starspot occultations, phase-curve variations and search the residual light curves for additional transiting companions.

6.3 Data Reduction

6.3.1 Data Extraction

WASP-55b (EPIC 212300977) was observed during Campaign 6 of the *K2* mission, which ran from 2015 July 14 until 2015 September 30. It produced a total of 112,672 short-cadence images. WASP-75b (EPIC 206154641) was observed during Campaign 3, it produced 101,370 short-cadence images between 2014 November 14 and 2015 February 3. We retrieved the target pixel files for each system using the Barbara A. Mikulski Archive for Space Telescopes (MAST[9]).

The large motion of the point spread function (PSF) on the detector in Campaign 3 was cause for concern when reducing the raw images. A traditional fixed-mask method used by a majority of the *K2* data reduction to date (e.g. Močnik et al. 2016a) appeared to degrade the precision of the output light curves. To resolve this issue, we used an aperture photometry routine written using `PyRAF`, with aperture sizes ranging from 0.5 to 8.5 pixels in steps of 0.25 pixels that used a flux-weighted centroid method to re-position the aperture based upon the PSF position in each frame. For the WASP-75b dataset an aperture size of 6.5 pixels led to a reduction in the RMS from 368 PPM to 325 PPM and for WASP-55b, a 5.5 pixel aperture reduced the scatter from 568 PPM to 530 PPM.

---

[9] https://archive.stsci.edu/k2/

Using a smaller extraction aperture for WASP-75 also avoided the light curve contamination by an asteroid, whose trajectory passed the target with a minimum separation of 20 arcsec (see Fig. 6.1). Because WASP-75b was in transit at the closest approach at BJD 2457029.83, the additional signal collected by a larger aperture would produce a temporary brightening event resembling a starspot occultation event (see Fig. 6.2).

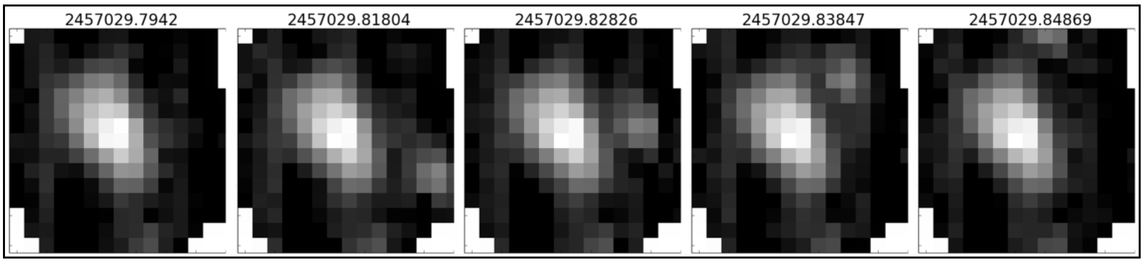

Figure 6.1: Asteroid flyby near WASP-75. BJDs are given in labels above each image.

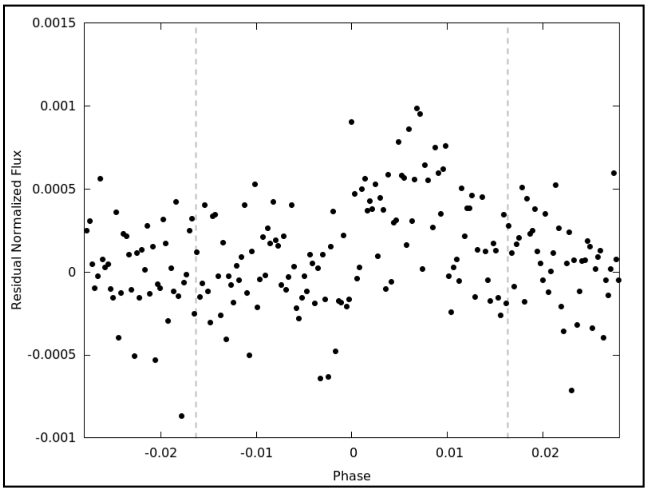

Figure 6.2: Model-subtracted transit of WASP-75b at BJD 2457030, extracted with a larger aperture from the initial data reduction. The brightening event resembling a starspot occultation event is caused by an asteroid flyby. The smaller aperture used in the final data reduction avoided the contamination from the asteroid.

6.3.2 De-trending

As noted in Section 6.2, *K2* light curves contain systematic errors that correlate with position of stellar flux on the detector. This is visible as a sawtooth-like pattern in the light curve, which can be observed in Fig. 6.3. We were able to correct for a majority of these systematic errors using the methods of Močnik et al. (2016a). However, for WASP-75b there were areas of strong systematic errors caused by a high spacecraft jitter, that were not corrected well by this method. The systematic errors correlated heavily with the X and Y position of the PSF on the detector, with large jumps in position and flux at every thruster event. We used a moving gradient to detect the areas with jumps and used these dates as boundaries between windows over which to correct the systematic errors rather than a fixed window size. With this method, a third order polynomial fit to the flux vs. arclength trend was enough to successfully remove the visible trends (Fig. 6.3).

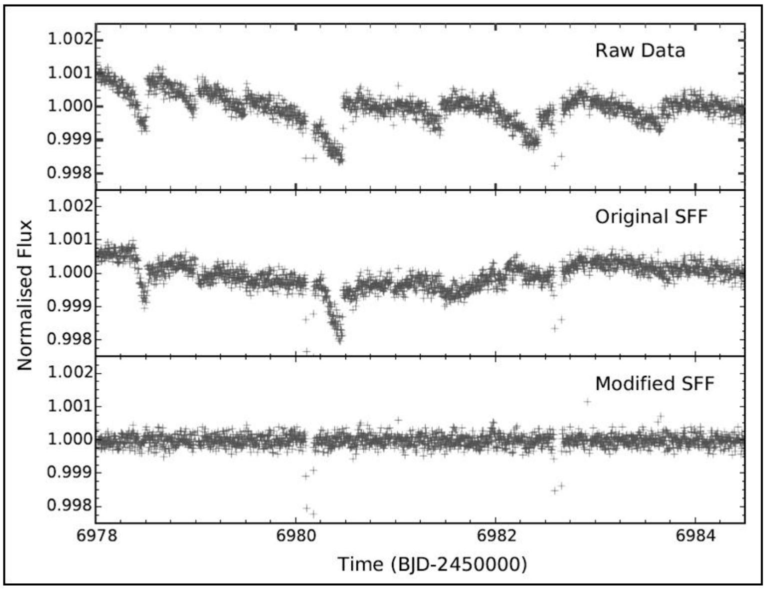

Figure 6.3: The top panel shows a section of the raw WASP-75b light curve that contains strong systematics that correlate with PSF position, binned to 5 minute intervals. The middle panel shows the same section of the de-trended light curve produced by the original self-flat fielding method and the bottom panel shows the de-trended light curve produced by the modified method used in this thesis.

To model the low-frequency variability from the light curve of WASP-75b we used a Gaussian convolution method, similar to that of Močnik et al. (2016a) but with a kernel size larger than the timescales of systematic noise and transit events. This was then removed from the light curve before further analysis. We also performed a running median filter, with a kernel size of 21 points, to clip all data that were greater than 8-σ from the median-filtered residuals. In total, we clipped 2409 and 4905 points from the WASP-55b and WASP-75b light curves respectively. The de-trended light curves are shown in Fig. 6.4.

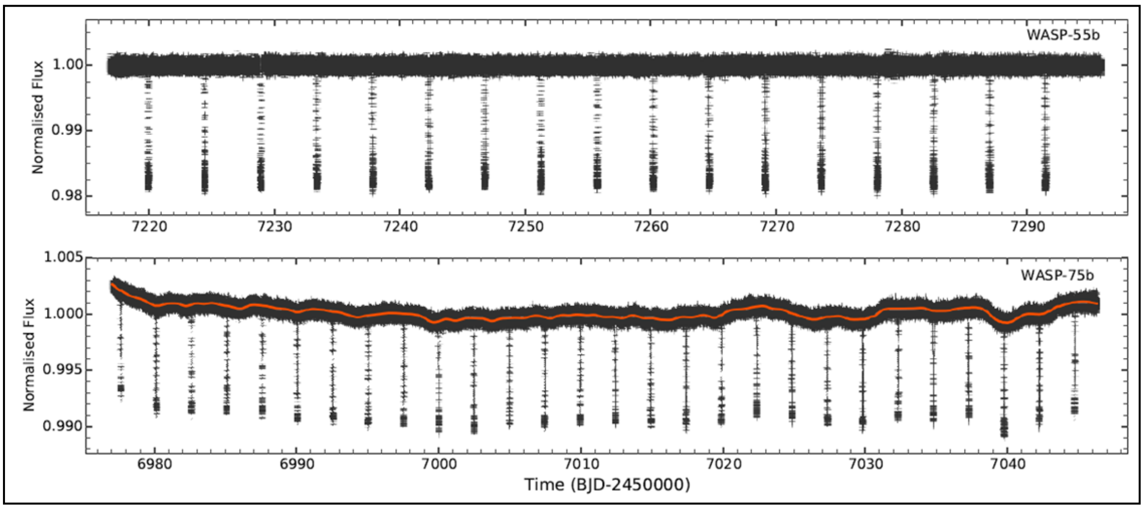

Figure 6.4: The top plot shows the final light curve of WASP-55b obtained by de-trending and clipping the raw light curve as described in Section 6.3.2. The bottom plot shows the SFF de-trended and clipped light curve for WASP-75b. The orange line represents the detected low-frequency stellar variation that is removed before performing the global Markov chain Monte Carlo (MCMC) analysis in Section 6.4.

6.4 System Parameters

To determine the parameters of the system, we used an adaptive Markov chain Monte Carlo (MCMC) routine (Collier Cameron et al. 2007; Pollacco et al. 2008; Anderson et al. 2015) to simultaneously analyse the *K2* light curves with their respective, previously published radial velocity (RV) data.

For WASP-55b and WASP-75b, we used the normalised *K2* light curves with the CORALIE RVs from Hellier et al. (2012) and Gómez Maqueo Chew et al. (2013), respectively. We assumed that the orbit was circular for the main MCMC runs, but set eccentricity as a free parameter on subsequent runs to place a constraint on its upper limit for both systems. We performed an additional run using the ground-based transit light curves from Hellier et al. (2012) for WASP-55b and Gómez Maqueo Chew et al. (2013) for WASP-75b to refine the ephemeris of both planets by extending the baseline. We present the updated system parameters in Tables 6.1 and 6.2 and the phase-folded light curves and models in Figs. 6.5 and 6.6.

Table 6.1: Orbital, stellar and planetary parameters from the MCMC analysis of WASP-55b (EPIC 212300977). We list each of the proposal parameters, derived parameters, and parameters controlled by priors separately. We tabulate our results and those provided by the literature.

Symbol (unit)[a]	This Work	Hellier et al. (2012)	Southworth et al. (2016)
MCMC proposal parameters			
P (days)	4.465630 ± 0.000001	4.465633 ± 0.000004	4.4656291 ± 0.0000011
t_0 (BJD)	2457256.25436 ± 0.00003	2455737.9396 ± 0.0003	2456416.71565 ± 0.00013
t_{14} (days)	0.1459 ± 0.0002	0.147 ± 0.001	0.147 ± 0.003[b]
R_p^2/R_*^2	0.01551 ± 0.00005	0.0158 ± 0.0003	0.0155 ± 0.0002
b	0.18 ± 0.03	0.15 ± 0.12	0.03 ± 0.23[b]
K_1 (m s^{-1})	69 ± 4	70 ± 4	70 ± 4
γ (m s^{-1})	-4324 ± 3	-4324.4 ± 0.9	...
MCMC proposal parameters constrained by priors			
M_* ($M_\odot$)	1.16 ± 0.03	1.01 ± 0.04	$1.162^{+0.029}_{-0.033}$
T_eff (K)	6070^{+51}_{-46}	5960 ± 100	6070 ± 53
[Fe/H]	0.09 ± 0.05	-0.20 ± 0.08	0.09 ± 0.05
MCMC derived parameters			
i (°)	89.0 ± 0.2	89.2 ± 0.6	$89.83^{+0.57}_{-1.20}$
e	0 (fixed) (<0.22 at 3σ)	0 (fixed) (<0.20 at 3σ)	...
a (au)	0.0558 ± 0.0006	0.0533 ± 0.0007	0.0558 ± 0.0005
R_* ($R_\odot$)	1.11 ± 0.01	$1.06^{+0.03}_{-0.02}$	$1.02^{+0.020}_{-0.015}$
$\log g_*$ (cgs)	4.413 ± 0.006	$4.39^{+0.01}_{-0.02}$	$4.419^{+0.009}_{-0.015}$
ρ_* ($\rho_\odot$)	0.85 ± 0.01	$0.85^{+0.03}_{-0.07}$	$0.869^{+0.026}_{-0.041}$
M_p (M_Jup)	0.62 ± 0.04	0.57 ± 0.04	$0.627^{+0.037}_{-0.038}$
R_p (R_Jup)	1.34 ± 0.01	$1.30^{+0.05}_{-0.03}$	$1.335^{+0.031}_{-0.020}$
$\log g_\mathrm{p}$ (cgs)	2.9 ± 0.03	2.89 ± 0.04	2.94 ± 0.03
ρ_p (ρ_Jup)	0.26 ± 0.02	$0.26^{+0.02}_{-0.03}$	$0.247^{+0.017}_{-0.021}$
T_p (K)[c]	1305 ± 12	1290 ± 25	1300^{+15}_{-13}

Notes: [a] Meanings of system parameter symbols are given in Table 6.2.

[b] Calculated using the parameters from Southworth et al. (2016) using the equations of Seager & Mallén-Ornelas (2003).

[c] Assuming a zero bond albedo and efficient day–night redistribution of heat.

Table 6.2: In the same way as Table 6.1 we show the orbital, stellar and planetary parameters from the MCMC analysis of WASP-75b (EPIC 206154641), listing each of the proposal, derived and parameters controlled by priors, separately. We again tabulate our results and those provided by the literature.

Parameter	Symbol (unit)	This Work	Gómez Maqueo Chew et al. (2013)
MCMC proposal parameters			
Orbital period	P (days)	2.4842014 ± 0.0000004	2.484193 ± 0.000003
Transit epoch	t_0 (BJD)	2457009.94594 ± 0.00002	2456016.2669 ± 0.0003
Transit width	t_{14} (days)	0.08097 ± 0.00008	0.0822 ± 0.0011
Area ratio	R_{p}^2/R_*^2	0.01133 ± 0.00005	0.0107 ± 0.0003
Impact parameter	b	0.8926 ± 0.0007	$0.882^{+0.006}_{-0.008}$
RV semi-amplitude	K_1 (m s^{-1})	145 ± 4	146 ± 4
System RV	γ (m s^{-1})	2264 ± 3	2264.29 ± 0.06
MCMC proposal parameters constrained by priors			
Stellar mass	M_* ($M_\odot$)	1.16 ± 0.03	1.14 ± 0.07
Stellar effective temperature	T_{eff} (K)	6035^{+88}_{-93}	6100 ± 100
Stellar metallicity	[Fe/H]	0.07 ± 0.09	0.07 ± 0.09
MCMC derived parameters			
Orbital inclination	i (°)	81.96 ± 0.02	$82.0^{+0.3}_{-0.2}$
Orbital eccentricity	e	0 (fixed) (<0.10 at 3σ)	0 (fixed)
Orbital separation	a (au)	0.0377 ± 0.0006	$0.0375^{+0.007}_{-0.008}$
Stellar radius	R_* ($R_\odot$)	1.27 ± 0.02	1.26 ± 0.04
Stellar surface gravitaty	$\log g_*$ (cgs)	4.294 ± 0.008	4.29 ± 0.02
Stellar density	ρ_* ($\rho_\odot$)	0.566 ± 0.003	0.56 ± 0.04
Planet mass	M_{p} (M_{Jup})	1.08 ± 0.05	1.07 ± 0.05
Planet radius	R_{p} (R_{Jup})	1.31 ± 0.02	1.270 ± 0.048
Planet surface gravity	$\log g_{\mathrm{p}}$ (cgs)	3.16 ± 0.01	$3.179^{+0.033}_{-0.028}$
Planet density	ρ_{p} (ρ_{Jup})	0.48 ± 0.02	$0.52^{+0.06}_{-0.05}$
Planet equilibrium temperature[a]	T_{p} (K)	1688^{+25}_{-26}	1710 ± 20

Note: [a] Assuming a zero bond albedo and efficient day–night redistribution of heat.

We used a four-parameter law to determine the limb darkening coefficients with values interpolated from those of Sing (2010) and based upon stellar temperature. We found that, for both systems, the stellar effective temperatures produced limb darkening coefficients that were in good agreement with the shape of the light curve. There were no visible anomalies in the residuals (see the middle panel in Figs. 6.5 and 6.6) as has been the case for some planets that we have studied (e.g. Močnik et al. 2017).

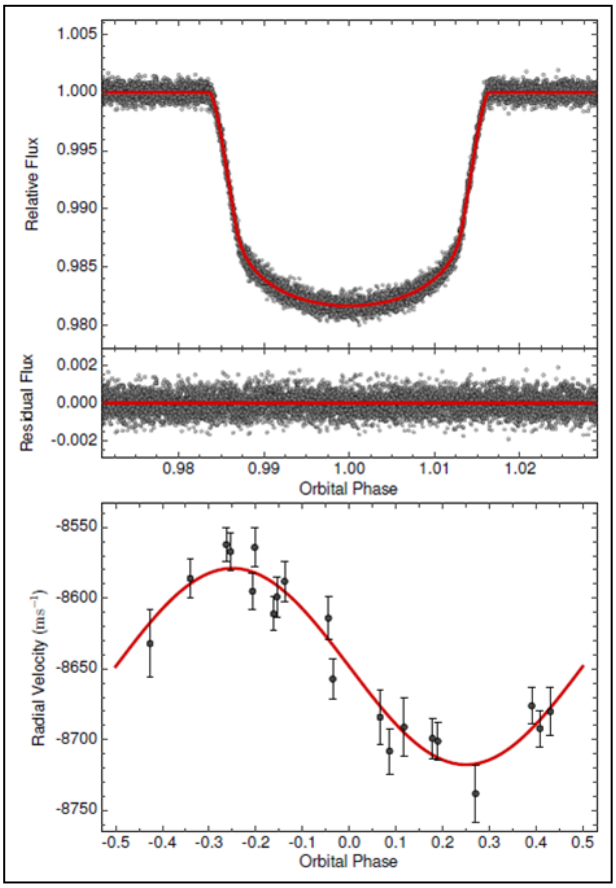

Figure 6.5: The top plot shows the fully de-trended, phase-folded *K2* light curve for WASP-55b. The model produced by the global MCMC run is shown by the red line. The middle panel shows the residuals of the fit and the bottom panel shows the radial velocity measurements with the best-fitting orbital model in red.

We obtained our values of the stellar mass from a comparison with stellar models by using the `BAGEMASS` code of Maxted, Serenelli & Southworth (2015a). This took as inputs, the spectroscopic values of stellar effective temperature and metallicity $\left(\left[\frac{\mathrm{Fe}}{\mathrm{H}}\right]\right)$ as well as stellar density from initial MCMC runs. We used the calculated values as a prior constraint in our global MCMC.

Evans et al. (2016) discovered a faint, nearby companion to WASP-55b. They determined that it had a magnitude difference of 5.210 ± 0.018 using the red camera of the Two Colour Instrument at the Danish 1.54-m Telescope, and that the stars were separated by 4.345 ± 0.010 arcsec, placing it within our aperture. We used equation (3) of Daemgen et al. (2009) to correct our light curve for the additional flux measured from the companion star. The result was a minor difference in the calculated eclipse depth, we find a new value of 0.01551 ± 0.00005 compared to 0.01550 ± 0.00004 before the correction.

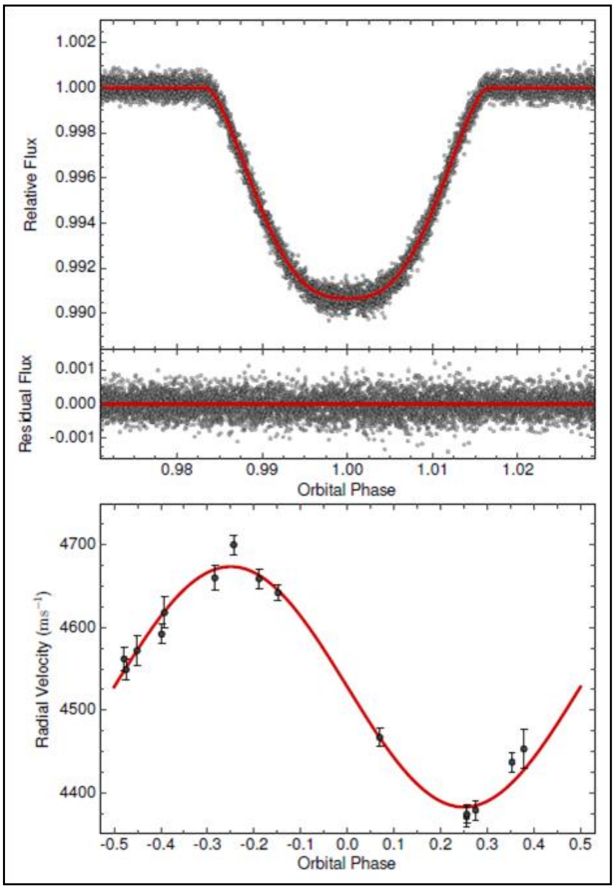

Figure 6.6: The same as Fig. 6.5 except we plot WASP-75b. The top panel shows the fully de-trended, phase-folded *K2* light curve and model in red. The middle panel shows the residuals of the fit and the bottom panel shows the radial velocity measurements with the best-fitting model in red.

6.5 No Transit Duration or Timing Variations

Additional planetary companions can cause variations in the timing of transit events due to the gravitational perturbations that they cause (Agol et al. 2005; Holman & Murray 2005). We searched for transit timing variations (TTVs) and transit duration variations (TDVs) in the WASP-55b and WASP-75b datasets by splitting the light curves at midpoints between each transit. We then performed a single MCMC run for each transit, with no other input data. We used the parameters from the global MCMC run as prior constraints, with transit epoch and duration set as free parameters.

Against the null hypothesis of equally spaced and equal duration transit events, for WASP-55b we found a χ^2 of 28.7 and 6.3 for the TTVs and TDVs, respectively, with 17 degrees of freedom. We place upper limits on the TTVs of 25 s and 100 s for the TDVs. For WASP-75b, the measured TTVs and TDVs had a χ^2 of 24.8 and 36.3, with 28 degrees of freedom. The upper limits for the TTVs and TDVs were 35 s and 120 s respectively. Given the lack of significant TTVs and TDVs, we can rule out the existence of large, close-in companion planets for both systems.

6.6 No Starspot Occultations but Stellar Variation in WASP-75

We performed a thorough visual inspection for starspots in both the de-trended light curves and model-subtracted residuals but we found no evidence of starspot occultations in either the WASP-55b or WASP-75b data.

We find no variations in the WASP-55b light curve but do detect low-frequency variations in the WASP-75b light curve. To investigate these, we used `K2SC` (Aigrain, Parviainen & Pope 2016) to obtain a systematic-corrected light curve from the long-cadence pre-search conditioned *K2* data, which included low-frequency variations but excluded transit events (Fig. 6.7). We used this method as our low-frequency variation light curve included a long-term trend that was removed well by the pre-search data conditioning module. We used the autocorrelation function (ACF) of McQuillan, Aigrain & Mazeh (2013) and a Lomb–Scargle (LS) periodogram to search the light curve for rotational modulation. From the ACF, we found a period of 11.7 ± 0.5 days determined from the first three peaks, that is possibly indicative of rotational modulation. This is in agreement with the value of 11.2 ± 1.5 produced by the LS-periodogram.

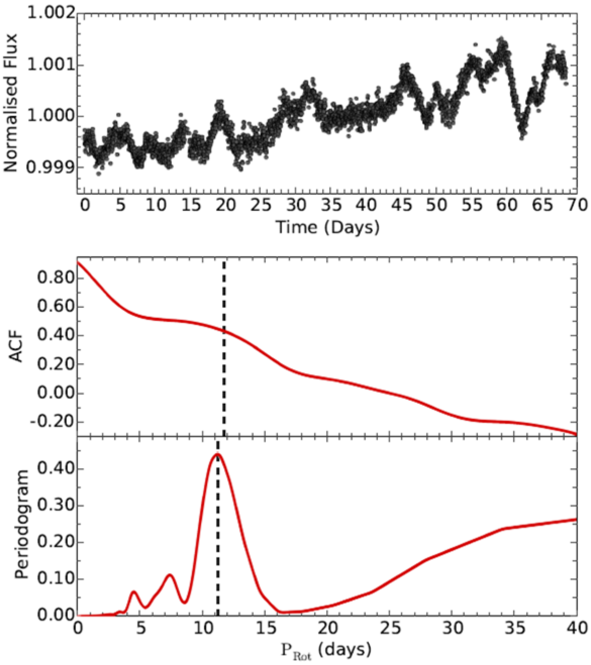

Figure 6.7: The top plot shows the transit-subtracted, SFF de-trended, sigma-clipped WASP-75b light curve, binned to 10 minute intervals. The middle plot shows the ACF profile in red, with the centre of the detected peak represented by a black dashed line. The bottom plot displays the LS periodogram of the system, again with the strongest peak shown by the black vertical line.

For WASP-75b, we calculated an updated value for macroturbulence ($v_{\rm mac}$) of $4.05 \pm 0.41\,{\rm km\,s^{-1}}$ using the calibrations of Doyle et al. (2014) and produced a new value of $v \sin i_* = 3.8 \pm 1.0\,{\rm km\,s^{-1}}$. Assuming spin-orbit alignment, this implies a stellar rotation period of 16.9 ± 4.5 days. The marginal agreement between the predicted and measured values of stellar rotation could hint at the possibility of a non-aligned stellar inclination angle. We used the new $v \sin i_*$ with the more conservative LS-periodogram measurement of the rotation period of the star to determine that WASP-75b has a possible rotation speed of $v = 5.7 \pm 0.8\,{\rm km\,s^{-1}}$ and stellar line-of-sight inclination angle of i_* = 41 ± 16°. If we assumed sun-like starspot latitudes and differential rotation, the stellar line-of-sight inclination angle would be i_* = 39 ± 14°.

It is possible to use the value of i_* with the obliquity angle, that can be measured using the Rossiter–McLaughlin (RM) effect (Rossiter 1924; McLaughlin 1924; Triaud 2017), to calculate the true angle (ψ) between the stellar rotation and orbital axes. ψ is important in theories of the formation and evolution of planetary systems (Campante et al. 2016). A RM measurement of WASP-75b would therefore be beneficial in this case. We estimated the amplitude of the RM effect to be $13 \pm 3\,\mathrm{m\,s^{-1}}$ for WASP-75b. This effect should be measurable with high-resolution spectrographs and we predict a typical RV precision of $\sim 4\,\mathrm{m\,s^{-1}}$ from a 900 s HARPS spectrum of WASP-75.

6.7 No Phase-curve Variations

At optical wavelengths, phase-curve variations are expected to comprise of four main constituents: ellipsoidal variations (Welsh et al. 2010; Jackson et al. 2012), Doppler beaming (Groot 2012), a component of reflected light from the star (Madhusudhan & Burrows 2012) and a secondary eclipse (Esteves, De Mooij & Jayawardhana 2013). Using equations from Mazeh & Faigler (2010) and the system parameters in Tables 6.1 and 6.2 we calculated the predicted amplitudes of these effects and created a phase curve for each of the two systems. We calculated predicted values of the ellipsoidal variations, Doppler beaming, reflection and secondary eclipse depth as 0.4, 0.9 and 13 ppm for WASP-55b and 3.4, 1.9 and 26 ppm for WASP-75b.

We used a Levenberg–Marquardt algorithm to attempt to fit the above model to the phase-folded residual light curve of each system. However, in both cases, we found a negligible amplitude provided the best fit, which was also confirmed visually. We therefore did not detect any phase variations in either system. The predicted values are lower than the precision of the light curves; even if variation of this magnitude were to exist, we would not be able to detect them with the current data. It is possible that the de-trending methods used could have removed phase variations from the original data, but signal injection tests performed by Močnik et al. (2017) have shown that the SFF method should preserve periodic variations. We therefore placed conservative estimates on the upper limits of the phase-curve variations and secondary eclipse depths of 100 ppm for WASP-55b and 60 ppm for WASP-75b. As a result, we have placed upper limits on the geometric albedos of 0.8 and 0.2 for WASP-55b and WASP-75b, respectively. We plot the phase-folded, binned residual light curves in Fig. 6.8 along with the predicted and lower-limit phase-curve models.

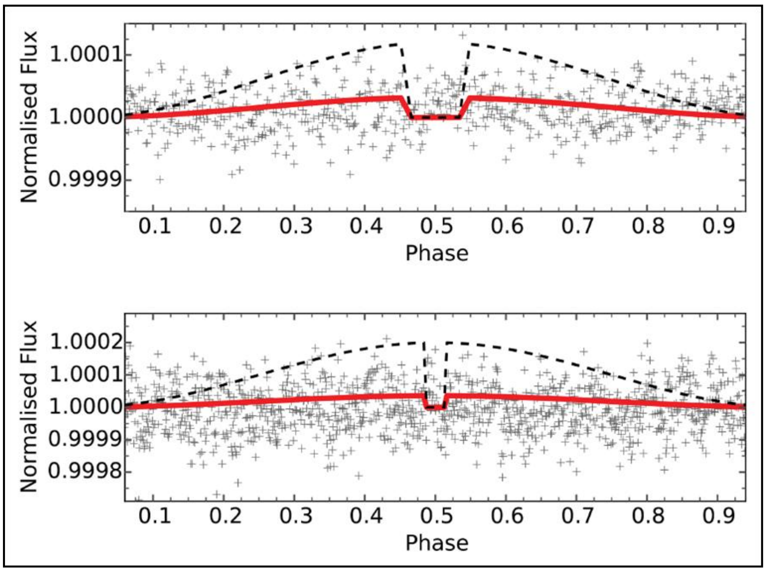

Figure 6.8: The phase-folded residuals for the WASP-75b (top) and WASP-55b (bottom) light curves, binned to 5 minute intervals. The red lines show the models for the predicted phase variations described in Section 6.7 and the predicted secondary eclipses at an orbital phase of 0.5. The black dashed lines show the model for an estimated upper limit for phase variations in each system.

6.8 No Additional Transiting Planets

To search for signals of additional transiting planets we used the box-least-squares method of Collier Cameron et al. (2006) on the model-subtracted residuals for each planet. We found no significant signals in the residuals of WASP-55b dataset but did find significant peaks in the periodogram of WASP-75. However, further inspection revealed that this was due to the presence of residual correlated noise. We therefore found no signals from additional transiting planets with periods between 0.5 and 35 days in either the WASP-55b or WASP-75b data and we placed upper limits on the eclipse depths of additional planets to 280 and 190 ppm at a period of 0.5 days.

6.9 Conclusions

In this paper we have used *K2* data, taken during Campaigns 3 and 6, to produce and analyse light curves for the WASP-75b and WASP-55b systems respectively. We have refined the orbital parameters of both systems, as the high quality light curves allowed us to model the transit with a much greater precision than is possible from ground-based observations.

Generally, the refined parameters agreed well with the previously published results and we found no major discrepancies between the different sets of data for each planet. For WASP-55b the parameters produced by this work, shown in Table 6.1, agreed very well with those of Southworth et al. (2016). We found minor differences between our results and those of Hellier et al. (2012) which have arisen as we used the stellar metallicity from Mortier et al. (2013) rather than CORALIE spectra and we used a different method to estimate the stellar mass.

For the WASP-75b dataset there were minor differences between the values of orbital period, transit depth, transit duration and the impact parameter that we derived and those of Gómez Maqueo Chew et al. (2013) that occur as we are able to better constrain the shape of the transit with higher quality data.

We found no evidence of transit timing or duration variations in both systems, and placed upper limits of 25 s and 35 s for TTVs and 100 s and 120 s for TDVs for WASP-55b and WASP-75b respectively. There was no evidence of starspot occultations in either system, but we did find low-frequency variation in WASP-75b. From this we have tentatively estimated its rotation period as 11.24 ± 1.54 days and calculated an estimate of the stellar line-of-sight inclination angle of i_* = 41 ± 16°. We also found no evidence of phase-curve variations or additional transiting planets in either system.

7 WASP-157

This chapter is based on the lead-authored planet discovery paper Močnik et al. (2016b), PASP, 128, 124403. Contributions from co-authors in alphabetical order: DRA reduced the WASP-South data; DJAB reduced the WASP-North data; LD provided TRAPPIST light curves; CH coordinated WASP-South observations, supervised the research and provided general advice; PFLM provided advice in using `BAGEMASS` and searched for photometric low-frequency modulations in the WASP data; BS performed the spectroscopic analysis; JS provided advice in using `JKTEBOP`; AHMJT provided RV measurements. Other co-authors (ACC, MG, EJ, ML, MNV-M, FP, DP, DQ, DS, SU, RGW) are included in WASP discovery papers due to their overall contribution to the WASP project, such as providing the data reduction and analysis tools, being a member of the observing teams, or maintaining the WASP data archive.

7.1 Abstract

We announce the discovery of the transiting hot Jupiter WASP-157b in a 3.95-d orbit around a $V = 12.9$ G2 main-sequence star. This moderately inflated planet has a Saturn-like density with a mass of 0.57 ± 0.10 M_{Jup} and a radius of 1.06 ± 0.05 R_{Jup}. We do not detect any rotational or phase-curve modulations, nor the secondary eclipse, with conservative semi-amplitude upper limits of 250 and 20 ppm, respectively.

7.2 Introduction

The *K2* mission (Howell et al. 2014) observes fields along the ecliptic. Some of those fields contain planets discovered by the WASP transit search (Pollacco et al. 2006) and so *K2* is also observing some of the current WASP candidates. *K2*'s high-precision photometry has allowed the detection of two additional close-in transiting exoplanets in the WASP-47 system (Becker et al. 2015) and the detection of starspot occultations in WASP-85 (Močnik et al. 2016a), with several more WASP planets either recently observed or scheduled for future *K2* campaigns.

The current planet formation and migration theories predict that hot Jupiters could not have formed in situ and instead must have formed at larger distances from their host stars and migrated inwards after they were formed (Lin, Bodenheimer & Richardson 1996). One of the tracers of hot Jupiters' migration processes is an obliquity, i.e. a misalignment angle between stellar rotation and planet's orbital axis. The aligned systems could result from a disk migration mechanism, whereas planet-planet scattering, Kozai mechanism and tidal dissipation are believed to play an additional role in shaping misaligned orbits of hot Jupiters (e.g. Triaud et al. 2010). Obliquity can be measured in two ways: (1) spectroscopically by measuring the Rossiter–McLaughlin effect if the host star is bright enough (Gaudi & Winn 2007), and (2) photometrically by tracing the recurring starspot occultation events if the host star is photometrically active (Sanchis-Ojeda & Winn 2011).

As of time of writing, the Transiting Extrasolar Planets Catalogue (TEPCat[10]) (Southworth 2011) lists 95 planetary systems with known obliquities. A large portion of these, 75, are transiting hot Jupiters (defined here as planets with orbital periods less than 10 days and masses between 0.3 and 13 M_{Jup}) orbiting stars brighter than $V = 13$. To try to fully understand how planets migrate it is crucial to expand the currently

---

[10] http://www.astro.keele.ac.uk/jkt/tepcat/tepcat.html

modest sample of planets with known obliquities by discovering and characterising additional nearby transiting hot Jupiters.

Many hot Jupiters exhibit radii well in excess of the predictions of the standard model of planets' cooling and contraction. This radius anomaly has been found to be negatively correlated with the planets' age (Leconte et al. 2009). Several mechanisms have been proposed to account for the inflated radii, and are grouped into incident flux-driven mechanisms, tidal mechanisms and delayed contraction (Weiss et al. 2013). However, none of the mechanisms has yet received a consensus. The radius anomaly currently remains unexplained and would benefit from extending a sample of known hot Jupiters.

Here we present the discovery of an inflated transiting hot Jupiter WASP-157b orbiting a fairly bright and photometrically inactive host star. In Section 7.3 we introduce the photometric and spectroscopic datasets. Basic properties of the host star are listed in Section 7.4, in Section 7.5 we discuss light curve modulations. Description of the spectrophotometric analysis and a list of system parameters are shown in Section 7.6, and a stellar age estimate is provided in Section 7.7.

7.3 Observations

WASP-157b was identified as an exoplanet candidate from observations with both WASP-South and SuperWASP-North over 2008–2010 (see Table 7.1). For a detailed description of the WASP telescopes, observing strategy, data reduction, and candidate identification and selection procedures, see Pollacco et al. (2006, 2008) and Collier Cameron et al. (2007). A transit was then observed with the TRAPPIST photometer (Jehin et al. 2011; Gillon et al. 2011) on 2016 February 05.

WASP-157 (EPIC 212697709) was also observed with *K2* in the long-cadence observing mode during Campaign 6 (from 2015 July 13 to 2015 September 30). Since the failure of the second out of four of *Kepler*'s reaction wheels the spacecraft is no longer able to point as stably and the extracted photometry exhibits drift artefacts. Vanderburg et al. (2014) presented a self-flat-fielding (SFF) correction procedure which corrects the drift artefacts by correlating the measured flux with the arclength of the spacecraft's drift. We retrieved the publicly available extracted and SFF-corrected light-curve file provided by the *K2* High Level Science Product `K2SFF`, accessible through Mikulski Archive for Space Telescopes (MAST). The applied SFF correction improved the median 6-hour photometric precision from 450 parts per million (ppm) to 26 ppm, which is comparable to original *Kepler* precision for a similarly bright star. We normalized the downloaded `K2SFF` light curve using a `kepflatten` command which is part of the `PyRAF` tools for *Kepler* (`PyKE`) version 2.6.2 (Still & Barclay 2012). We used a low-order polynomial fit with a window and step size of 3 and 0.3 days, respectively. The reduced and normalized *K2* light curve is shown in Fig. 7.1.

Spectroscopic radial velocity (RV) follow-up was performed using the fibre-fed CORALIE spectrograph at the 1.2-m Swiss Euler Telescope at La Silla (Queloz et al. 2000a). One spectrum was obtained in 2015 June and a further seven in 2016 February and March. We also obtained spectra on four consecutive nights in 2016 March with the HARPS spectrograph mounted at ESO 3.6-m telescope (Mayor et al. 2003), also at La Silla observatory (see Table 7.1). The spectroscopic data have been reduced with the standard HARPS and CORALIE reduction pipelines. The RVs were extracted with the weighted cross-correlation of each spectrum with a G2 mask and the simultaneous Th-Ar wavelength calibration reference (see Pepe et al. (2002) for details). The resulting RVs and bisector spans (BS) are given in Table 7.2.

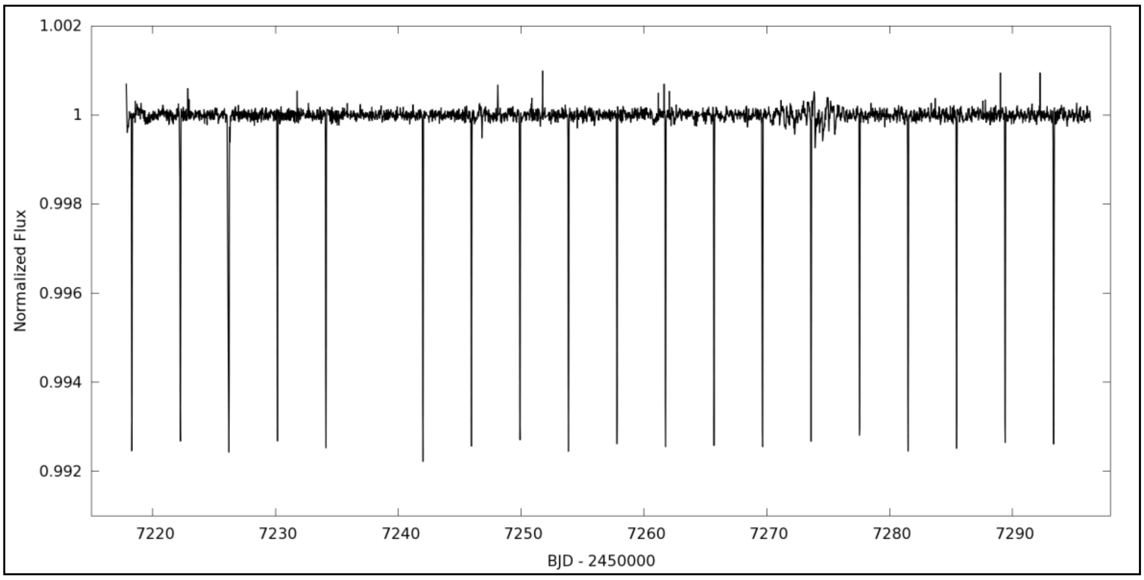

Figure 7.1: Normalized *K2* light curve of WASP-157. The observing Campaign 6 covers a total of 20 transits of WASP-157b. Note, however, that only 19 transits are visible because the data points obtained during the sixth transit were quality-flagged by the *K2* pre-processing pipeline as a detector anomaly and were thus removed from the final light curve. The flux excursions in the final light curve are of instrumental origin, such as cosmic rays that have not been properly flagged by the pre-processing pipeline.

Table 7.1: Log of observations (t_{exp} is the effective exposure time, N_{data} the number of non-quality-flagged data points).

Instrument	Dates	Filter or Wavelength	t_{exp} [s]	N_{data}
WASP	2008 May 04– 2010 Jul 12	R_c	30	42528
K2	2015 Jul 13– 2015 Sep 30	*Kepler*	1625[a]	3381
TRAPPIST	2016 Feb 05	$I + z$’	15	529
CORALIE	2015 Jun 18– 2016 Mar 14	390–680 nm	1800	8
HARPS	2016 Mar 01– 2016 Mar 04	383–693 nm	1000	4

Note: [a] Long-cadence *K2* images are downlinked as a mean of 270 frames of 6.02 s exposure and 0.52 s readout each, resulting in a final effective exposure time of 27.1 min obtained with a cadence of 29.4 min.

Table 7.2: CORALIE and HARPS radial velocities and bisector spans.

BJD – 2450000	RV [km s^{-1}]	BS [km s^{-1}]
CORALIE		
7191.64114	-22.041 ± 0.040	-0.073 ± 0.079
7430.78206	-21.905 ± 0.024	-0.033 ± 0.048
7431.74596	-21.968 ± 0.019	-0.060 ± 0.038
7432.85793	-21.991 ± 0.017	-0.048 ± 0.034
HARPS		
7448.73724	-21.9940 ± 0.0063	-0.019 ± 0.012
7449.89571	-21.8974 ± 0.0052	-0.030 ± 0.010
7450.70282	-21.8708 ± 0.0127	-0.002 ± 0.025
7451.78908	-21.9657 ± 0.0037	-0.018 ± 0.007

7.4 Spectral Analysis

We analysed the spectroscopic properties of the host star from a co-added HARPS spectrum with a final signal-to-noise ratio of 38. The analysis methods are described in Gillon et al. (2009) and Doyle et al. (2013). We used the Hα line to estimate the effective temperature (T_{eff}), and the Na I D and Mg I b lines as diagnostics of the surface gravity ($\log g$). The projected rotational velocity ($v \sin i_*$) was determined by fitting the profiles of the Fe I lines after convolving with the HARPS instrumental resolution (R = 120,000) and a macroturbulent velocity adopted from the calibration of Doyle et al. (2014). The iron abundances were determined from equivalent width measurements of several clean and unblended Fe I lines and are given relative to the solar value presented in Asplund et al. (2009). The [Fe/H] abundance error includes that given by the uncertainties in T_{eff} and $\log g$, as well as the scatter due to measurement and atomic data uncertainties. We calculated the chromospheric activity index $\log R'_{\mathrm{HK}}$ using the emission in the cores of the Ca II H and K lines following Noyes et al. (1984). The resulting parameters are listed in Table 7.3. Only an upper limit is given for Li abundance since we do not detect the Li line at 6707.79 Å, with an upper limit of 2 mÅ.

Table 7.3: Host star parameters derived from our spectroscopic analysis.

Parameter	Value
Identifiers	WASP-157 1SWASP J132637.24–081903.2 2MASS J13263727–0819033 EPIC 212697709 TYC 5544-596-1
Spectral type	G2V
V	12.91
T_{eff}	5840 ± 140 K
$\log g$	4.5 ± 0.2 [cgs]
$v \sin i_*$	1.0 ± 0.9 km s^{-1}
v_{mac}	3.4 ± 0.7 km s^{-1}
[Fe/H]	+0.34 ± 0.09
$\log R'_{\text{HK}}$	-4.8 ± 0.2
log A(Li)	<0.9

Note: The J2000 coordinates can be found in the 1SWASP identifier. *V*-magnitude is taken from Høg et al. (2000).

7.5 Light Curve Modulations

We searched for any rotational modulation of WASP-157 using 2.2 yr of WASP light curves, following the procedure of Maxted et al. (2011). We found no modulations with semi-amplitudes above 2 mmag, which suggests that the host star is inactive. We also exclude any coherent rotational modulations above 250 ppm in the 79-d *K2* fluxed light curve.

We also searched the phase-folded and binned *K2* light curve for any phase-curve modulations including a secondary eclipse. For this task, we normalized the *K2* light curve using larger values for the `kepflatten` window and step size of 5 and 1 day, respectively. These settings were the best compromise between minimizing the removal of the phase-curve modulations while still effectively removing the low-frequency incoherent light curve modulations. To check what portion of a potential phase-curve modulation gets removed using this normalization procedure, we injected various phase-curve modulation signals in the pre-normalized light curve, performed the normalization with the above mentioned settings, and found that we could recover injected signals from the normalized light curve at 75% of their initial amplitudes. Based on χ^2 statistics we could exclude phase-curve modulations with semi-amplitudes above 6 ppm at 95% confidence level, after taking into account the 75% throughput of the normalization procedure. However, the χ^2-based upper limit does not account for the red noise, which is expected to be present in the binned phase curve. Therefore, we provide a more conservative estimate of the phase-curve semi-amplitude upper limit of 20 ppm. Fig. 7.2 shows the *K2* light curve folded on the orbital period along with a reflection modulation model.

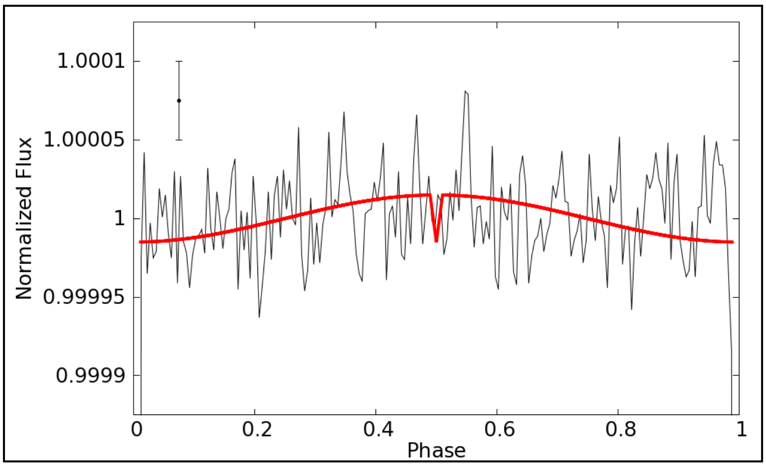

Figure 7.2: Measured phase curve of WASP-157, binned to 200 bins, (shown in black) and a simulated reflection phase-curve modulation with a semi-amplitude of 15 ppm (red). One representative error bar is shown on the left. The absence of any visible reflection modulation or secondary eclipse in the measured phase curve of similar amplitude as shown in the simulated phase curve suggests that the actual reflection semi-amplitude is lower than 20 ppm after taking into account the potential 25% amplitude reduction due to the normalization procedure.

To look for any additional transiting planets we examined the periodogram obtained with `PyKE` tool `kepbls` which searches for periodic transits by utilizing the box least square fitting algorithm by Kovács, Zucker & Mazeh (2002). After removing WASP-157b's transits from the *K2* light curve by replacing the measured normalized flux values around transits with unity, we do not find any significant residual peaks in the period region between 0.5 and 30 d. The upper limit for additional transits is 250 ppm.

Transit-timing variations (TTVs) and transit-duration variations (TDVs) can also reveal additional planets in the system (e.g. Mazeh et al. (2013) and references therein). However, due to the *K2* long-cadence observing mode, TTV and TDV sinusoidal semi-amplitude upper limits are only weakly constrained to 1 and 5 minutes for periods up to 80 days, respectively.

7.6 System Parameters

To obtain stellar and planetary parameters we carried out a simultaneous analysis of the photometric and spectroscopic datasets. For analysing the transit shape we used primarily the *K2* data, which have the best photometric precision, although with a 30-min cadence.

Since the effective exposure time of *K2* long-cadence observations is significant compared to the time-scale at which the transit features occur, we performed the analysis where the transit model was computed with a sampling of 3 min, and integrated to the 30-min *K2* sampling, to avoid any systematic errors on the transit parameters due to the “smearing” effect. The system parameters were fitted using Levenberg-Marquardt minimisation procedure and error bars computed with the Monte Carlo technique around the best-fit parameters. The analysis was performed with publicly available software `JKTEBOP`[11] (Southworth et al. 2004). `JKTEBOP` is based on the earlier `EBOP` code by Popper & Etzel (1981), and has been modified, among many improvements and enhancements, to allow for a simultaneous fit of photometric data and RV measurements (Southworth 2013). The smearing correction can be seen by comparing

---

[11] http://www.astro.keele.ac.uk/jkt/codes/jktebop.html

the numerically integrated `JKTEBOP` fit (blue line) with the unintegrated fit (red line) in Fig. 7.3. Quadratic limb-darkening was used in the `JKTEBOP` analysis.

Since `JKTEBOP` does not provide all the relevant system parameters, such as stellar and planetary mass, we produced a separate Markov chain Monte Carlo (MCMC) analysis using the code presented in Collier Cameron et al. (2007) and further described in Pollacco et al. (2008) and Anderson et al. (2015). We accounted for limb-darkening by interpolating within tables of four-parameter limb-darkening coefficients from Claret (2000, 2004) and Sing (2010), as appropriate for different filters used among the three photometric datasets (see Table 7.1). To avoid any bias because of the *K2* smearing effect, we only included WASP and TRAPPIST photometry along with both spectroscopic datasets to obtain the remaining system parameters. We checked the compatibility between the `JKTEBOP` analysis using the *K2* data, and the MCMC analysis of the ground-based observations alone, and found that the resulting parameters are fully consistent. For determining the epoch and period with the smallest uncertainty possible we ran another MCMC analysis using all the available datasets, which extended the photometric baseline from 79 d for *K2* photometry to 7.8 yr and reduced the uncertainty on the period by a factor of 3.

For all the system parameters analysis we imposed a circular orbit since hot Jupiters are expected to circularise on a time-scale less than their age, and so adopting a circular orbit gives the most likely parameters (e.g. Anderson et al. 2012). To estimate the upper limit on eccentricity, we ran a separate MCMC analysis with eccentricity being fitted as a free parameter and checked the eccentricity distribution in the resulting MCMC chain.

We present the system parameters in Table 7.4 and superimpose the corresponding transit model on the measured light curves and RVs in Fig. 7.3 and Fig. 7.4, respectively.

The bottom panel of Fig. 7.4 shows the measured bisector span (BS) for each spectrum, which characterises the asymmetry in the stellar line profiles (Queloz et al. 2001). A significant correlation between BS and RV may indicate a transit mimic, such as a blended eclipsing binary (Queloz et al. 2001). We, however, do not measure any statistically significant correlation between RVs and BSs.

Table 7.4: System parameters for WASP-157b and its host star.

Parameter	Symbol	Value	Unit
Transit epoch[a]	t_0	2457257.803194 ± 0.000088	BJD
Orbital period[a]	P	3.9516205 ± 0.0000040	d
Area ratio	$(R_\mathrm{p}/R_*)^2$	0.00891 ± 0.00035	...
Transit width	t_{14}	0.0811 ± 0.0043	d
Impact parameter	b	$0.887^{+0.015}_{-0.044}$	...
Orbital inclination	i	$84.93^{+0.45}_{-0.21}$	°
Orbital eccentricity	e	0 (adopted; <0.11 at 2σ)	...
Orbital separation	a	0.0529 ± 0.0017	AU
Stellar effective temperature	T_eff	5838 ± 140	K
Stellar mass	M_*	1.26 ± 0.12	$M_\odot$
Stellar radius	R_*	1.134 ± 0.051	$R_\odot$
Stellar density	ρ_*	0.86 ± 0.14	$\rho_\odot$
Planet equilibrium temperature[b]	T_p	1339 ± 93	K
Planet mass	M_p	0.574 ± 0.093	M_Jup
Planet radius	R_p	1.065 ± 0.047	R_Jup
Planet density	ρ_p	0.48 ± 0.10	ρ_Jup
System RV	γ	–21.9522 ± 0.0026	km s^{-1}
RV semi-amplitude	K_1	0.0616 ± 0.0038	km s^{-1}
RV datasets offset	$\gamma_\mathrm{HAR} - \gamma_\mathrm{COR}$	0.0177 ± 0.0015	km s^{-1}

Notes: [a] Epoch and period derived by fitting the photometric datasets from the *K2* and all the available ground-based observations.

[b] Planet equilibrium temperature is based on assumptions of zero Bond albedo and complete redistribution.

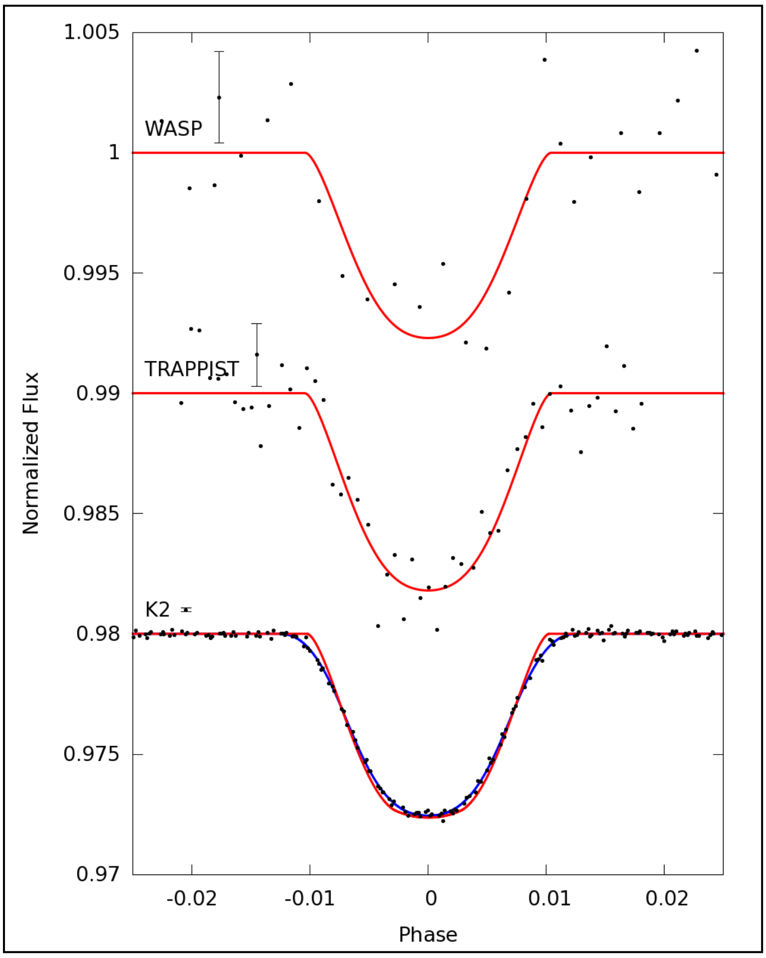

Figure 7.3: Phase-folded light curves near the transit with best-fit transit models superimposed. The phase-folded WASP light curve and the TRAPPIST transit light curve have been binned by factors of 100 and 10, respectively. The *K2* light curve was fitted using `JKTEBOP` with numerical integration (blue line) to correct for the smearing effect caused by the long effective exposure time. The corresponding `JKTEBOP` model without numerical integration is shown in red.

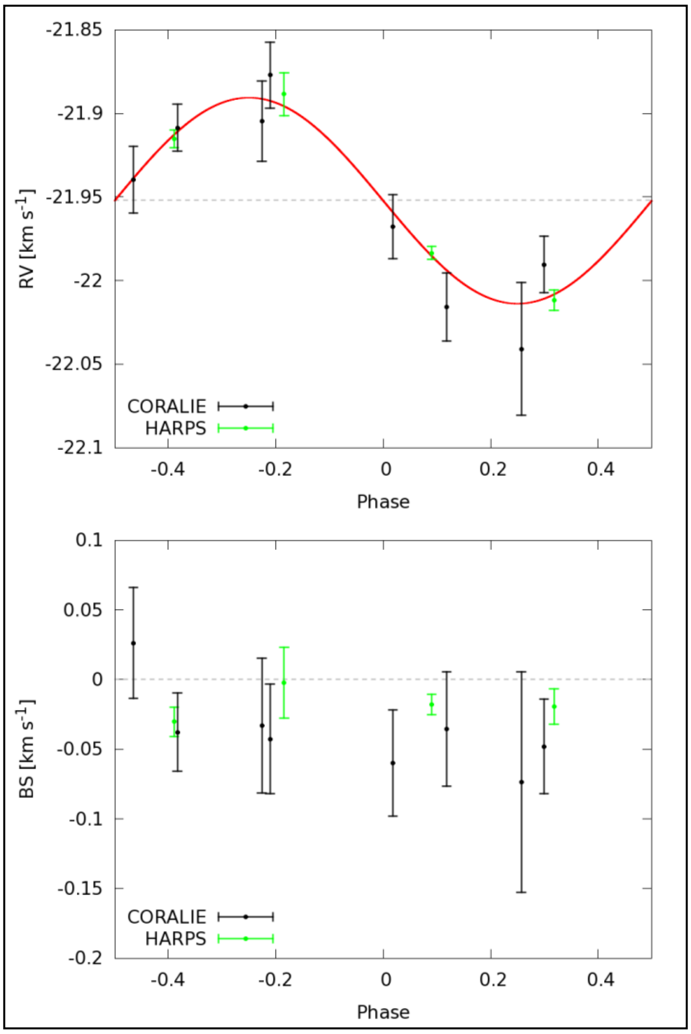

Figure 7.4: Upper panel: Best-fit model of the CORALIE (black) and HARPS (green) RVs. Note that HARPS RVs have been offset by –0.0177 km s^{-1} (see Table 7.4). Bottom panel: CORALIE (black) and HARPS (green) bisector spans.

7.7 Stellar Age

An age constraint can be evaluated through a comparison to theoretical stellar models. As in Maxted et al. (2016) we compare ρ_* and $T_{\rm eff}$ to isochrones and evaluate the age of the star using the Bayesian mass and age estimator `BAGEMASS` by Maxted, Serenelli & Southworth (2015a). The stellar evolution models used in `BAGEMASS` were calculated using the `GARSTEC` code (Weiss & Schlattl 2008). The best-fit stellar evolution track is shown in Fig. 7.5 and provides an age estimate of $1.6^{+2.5}_{-0.8}$ Gyr.

Another age estimator is the chromospheric activity index $\log R'_{\mathrm{HK}}$. Using the measured value from Table 7.3 and the relation between stellar age and activity for solar type stars from Mamajek & Hillenbrand (2008), we derive an age estimate of $3.2^{+3.4}_{-2.1}$ Gyr.

The measured Li abundance upper limit of $\log \mathrm{A(Li)} < 0.9$ (see Table 7.3) constrains the age of this Li-poor star only very weakly as being several Gyr old (Sestito & Randich 2005; Baumann et al. 2010).

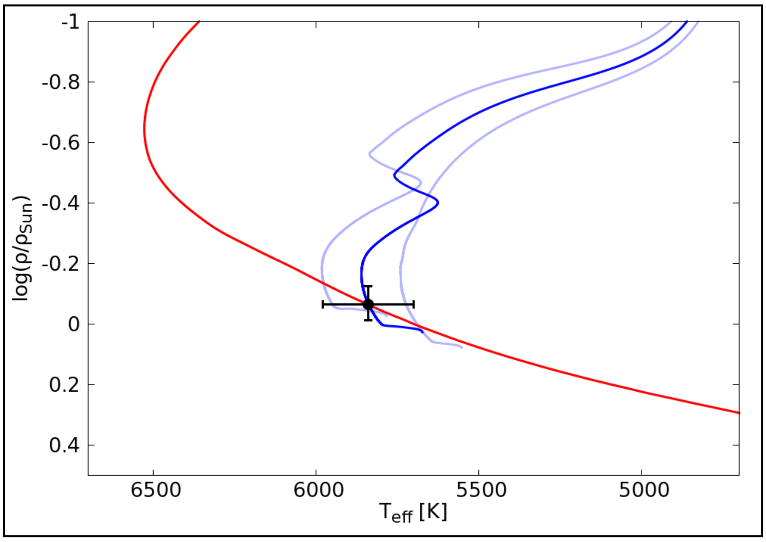

Figure 7.5: WASP-157 host star in the ρ_* versus T_{eff} plane compared to the best-fit evolution track (dark blue line) and isochrone of 1.6 Gyr (red line). Two light blue lines correspond to stellar models at 5% higher and lower mass for comparison.

7.8 Conclusions

WASP-157b is very much a typical hot Jupiter. The orbital period of 3.95 d is typical, while the moderately inflated size (1.1 R_{Jup} for 0.57 M_{Jup}) is also characteristic of hot Jupiters. The impact parameter is higher than average, leading to a shorter, v-shaped transit. WASP-157 is notable for now being one of fewer than 20 hot-Jupiter hosts with $V < 13$ to have a *Kepler*-quality light curve.

Our measured and derived stellar parameters from Tables 7.3 and 7.4 agree within about 1σ with the values provided by the *K2* Ecliptic Planet Input Catalogue (EPIC; Huber et al. 2016). The only discrepant parameter is metallicity, which has only been estimated statistically by the EPIC because no spectroscopic input was provided for this star.

8 Qatar-2

This chapter is based on the lead authored paper Močnik, Southworth & Hellier (2017), MNRAS, 471, 394. Contributions from co-authors: JS submitted the *K2* downlink proposal and advised on how to use `PRISM` to fit starspot occultation events; CH supervised the research and provided general advice. Compared to the published version of the paper, I added the discussion about starspot lifetimes in Section 8.8.4 and I moved the barycentric-corrected TRES RVs from Appendix to Section 8.4.

8.1 Abstract

We announce the detection of recurring sets of recurring starspot occultation events in the short-cadence *K2* light curve of Qatar-2, a K dwarf star transited every 1.34 d by a hot Jupiter. In total we detect 34 individual starspot occultation events, caused by five different starspots, occulted in up to five consecutive transits or after a full stellar rotation. The longest recurring set of recurring starspot occultations spans over three stellar rotations, setting a lower limit for the longest starspot lifetime of 58 d. Starspot analysis provided a robust stellar rotational period measurement of 18.0 ± 0.2 d and indicates that the system is aligned, having a sky-projected obliquity of 0 ± 8°. A pronounced rotational modulation in the light curve has a period of 18.2 ± 1.6 d, in agreement with the rotational period derived from the starspot occultations. We detect a probable ellipsoidal modulation in the phase curve, with a semi-amplitude of 18 ppm, but cannot exclude the possibility that this is the result of red noise or imperfect removal of the rotational modulation. We detect no transit-timing and transit-duration variations

with upper limits of 15 s and 1 min, respectively. We also reject any additional transiting planets with transit depths above 280 ppm in the orbital period region 0.5–30 d.

8.2 Introduction

An obliquity is a misalignment angle between the stellar rotational and planet’s orbital axis and is a key tracer of planet migration. Sky-projected obliquity can be measured spectroscopically by the Rossiter–McLaughlin effect (Gaudi & Winn 2007), and by Doppler tomography (Collier Cameron et al. 2010a) if a system is bright enough, or photometrically by tracing starspot occultation events (Sanchis-Ojeda & Winn 2011). According to the Transiting Extrasolar Planets Catalogue (TEPCat)[12] (Southworth 2011), sky-projected obliquity has been measured for a total of 100 systems, of which 85 host a transiting hot Jupiter (defined here as planets with orbital periods shorter than 10 d and masses between 0.3 and 13 M_{Jup}). The discovery of the first hot Jupiter in 1995 triggered suggestions that such planets cannot form so close to their host stars but have instead formed beyond the ice line and migrated inwards to their current orbits (Mayor & Queloz 1995). The planet formation and migration theories are far from well understood and expanding the sample of systems with known obliquities is of particular interest.

When a transiting planet occults a starspot it produces a bump of temporary brightening in the light curve (Silva 2003). The ability to detect starspot occultations is dependent on sufficient photometric precision and cadence of the observations, and on whether starspots are underneath a transit chord. Depending on the obliquity of the system the same starspot may be occulted in several consecutive transits or even after several stellar rotations.

---

[12] http://www.astro.keele.ac.uk/jkt/tepcat/tepcat.html

Starspot occultations also provide a measurement of the stellar rotational period and add to our knowledge of starspots' lifetimes on stars other than Sun. Starspots' lifetimes are believed to be correlated with spot sizes and anticorrelated with supergranulae sizes (Bradshaw & Hartigan 2014). In the case of the Sun the sunspots' lifetimes range from hours to several months, with a median lifetime of less than a day (Solanki 2003), and a longest recorded lifetime of an individual sunspot of 137 d (McIntosh 1981). On other stars the longest reported starspot lifetime using the occultation technique is 100 d for the active main-sequence star Kepler-17 (Désert et al. 2011), based on nearly continuous 17 months of *Kepler* observations (Borucki et al. 2010).

Since the failure of *Kepler*'s second reaction wheel, its successor, *K2*, suffers a reduced photometric precision due to the degraded pointing accuracy (Howell et al. 2014). Despite the shortcomings, *K2* continues to be able to detect starspots, as demonstrated by the detection of recurring starspot occultation events in the WASP-85 system (Močnik et al. 2016a).

Qatar-2 (2MASS J13503740-0648145, EPIC 212756297) is a moderately bright $V = 13.3$ K dwarf, hosting a hot Jupiter in a 1.34-d orbit which was discovered by Bryan et al. (2012). Multicolour photometry of five transits by Mancini et al. (2014) revealed starspot occultations in all light curves with one potential occultation recurrence. The recurring occultation pair indicated a sky-projected obliquity of 4.3 ± 4.5°. The rotational period was reported as 11.4 ± 0.5 d, which has since been corrected to 14.8 ± 0.3 d due to a calculation error (Mancini et al. 2016). However, the analysis presented in this paper proves that the two starspot occultations analysed by Mancini et al. (2014, 2016) were in fact caused by two different starspots and that even their corrected rotational period is incorrect.

In this paper we use the *K2* short-cadence observations of Qatar-2, which reveals recurring sets of recurring spot crossings. Starspot analysis provided a robust determination of the stellar rotational period and a measurement of the sky-projected obliquity. We also measured the period of the pronounced rotational modulation, refined the system parameters, searched for transit-timing (TTVs) and transit-duration variations (TDVs), additional transiting planets and phase-curve variations. Lastly, we discuss the discrepancy between gyrochronological and isochronal age estimates.

After we submitted and announced this paper, Dai et al. (2017) announced a similar paper analysing the same *K2* data set. Their conclusions are largely in agreement with ours.

8.3 *K2* Observations

Qatar-2 was observed during *K2*'s Campaign 6 between 2015 July 14 and 2015 September 30 in the 1-min short-cadence observing mode. A continuous 79-d monitoring provided a total of 115,890 images. We retrieved the target pixel file via the Minkulski Archive for Space Telescopes (MAST). The photometric extraction and spacecraft-drift artefact removal was carried out as done in Močnik et al. (2016a). In short, we used a 36-pixel fixed photometric aperture mask, temporarily removed the low-frequency stellar variability by normalizing the light curve with a low-order polynomial, and applied a self-flat-fielding (SFF) procedure using the Gaussian convolution of the measured normalized flux versus drift arclength. We then reintroduced low-frequency stellar variability by multiplying the corrected light curve with the same normalization polynomial as used earlier. The applied SFF procedure improved the median 1-min photometric precision from 1271 parts per million (ppm) to 854 ppm, which is within 10 per cent of the original *Kepler* precision for a similarly bright star. After removal of all the quality-flagged data points, such as thruster firing events and cosmic rays, we retained 111,807 data points. The light curve before and after the SFF procedure is shown in Fig. 8.1.

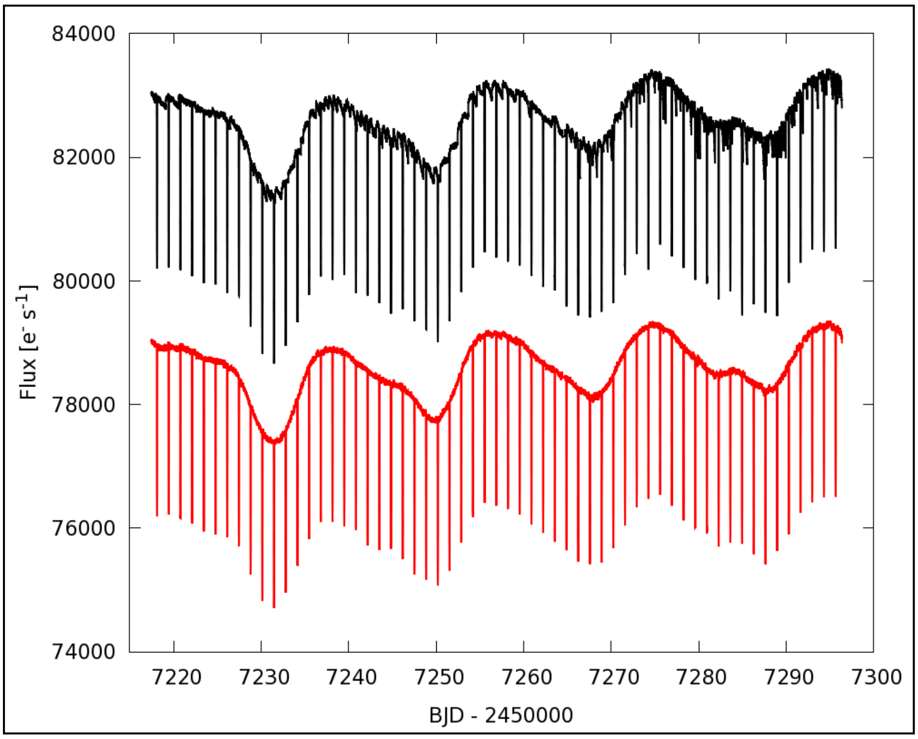

Figure 8.1: Binned short-cadence light curve of Qatar-2 before (shown in black) and after the SFF correction (red). A 10-min binning was used for this plot to reduce the white noise and to display the drift artefacts more clearly. The light curve exhibits a total of 59 transits and a pronounced starspot rotational modulation. The corrected light curve is shown with an offset of -4000 e$^-$ s^{-1} for clarity.

8.4 Barycentric-corrected TRES RVs

Bryan et al. (2012) published 44 Qatar-2 radial velocity (RV) measurements which they obtained with the Tillinghast Reflector Echelle Spectrograph (TRES) between 2011 January 18 to 2011 June 21. As pointed out in their erratum (Bryan et al. 2014) the data reduction pipeline that they used to calculate the RVs had a bug, which parsed Qatar-2's negative declination with positive arcminutes and arcseconds for the barycentric correction. However, they did not provide the corrected RVs in their erratum. Table 8.1 lists TRES RVs of Qatar-2 with correct barycentric correction.

Table 8.1: TRES barycentric-corrected RVs for Qatar-2. The RVs are given relative to the RV measured on BJD 2455646.85.

BJD – 2450000	RV (km s^{-1})	ΔRV (km s^{-1})
5580.011622	0.001	0.034
5581.027117	0.158	0.038
5583.034587	-0.796	0.027
5583.961503	0.066	0.033
5585.003598	0.123	0.027
5587.983438	0.082	0.027
5602.958910	-0.516	0.033
5604.034894	0.097	0.030
5604.966229	-0.051	0.029
5605.966418	-0.844	0.024
5607.001348	-0.638	0.033
5607.987854	0.249	0.036
5608.955271	-0.188	0.028
5610.996605	-0.533	0.037
5615.938163	0.217	0.024
5616.973605	-0.136	0.029
5617.978176	-0.860	0.021
5643.881697	0.211	0.029
5644.849974	-0.641	0.026
5645.901592	-0.803	0.021
5646.846694	0.000	0.017
5647.890953	0.162	0.035
5650.857343	0.060	0.027
5652.895515	-0.599	0.033
5656.870962	-0.706	0.022
5659.877783	0.124	0.025
5662.839965	0.174	0.029
5663.812865	-0.081	0.021
5664.867650	-0.763	0.030
5665.796571	-0.549	0.021
5668.845188	-0.838	0.030
5671.762510	-0.218	0.022
5672.733966	-0.858	0.029
5673.784772	-0.480	0.019
5691.770974	-0.340	0.032
5702.699240	0.146	0.024
5703.727260	-0.559	0.032
5704.730193	-0.816	0.020
5705.694921	0.054	0.042
5706.738098	0.160	0.028
5722.744329	0.168	0.034
5726.718494	0.085	0.030
5728.755461	-0.695	0.032
5733.706680	0.189	0.028

8.5 System Parameters

To determine the system parameters we performed a simultaneous Markov Chain Monte Carlo (MCMC) analysis of the *K2* photometry coupled with the TRES radial-velocity measurements of Qatar-2 listed in Section 8.4. The MCMC code is presented in Collier Cameron et al. (2007) and further described in Pollacco et al. (2008) and Anderson et al. (2015). Prior to the MCMC analysis we removed the starspot occultation events from the *K2* light curve to prevent the potentially inaccurate parameter determination as discussed in Oshagh et al. (2013). We accounted for limb darkening by interpolating through tables of four-parameter limb-darkening coefficients, calculated for the *Kepler* bandpass by Sing (2010).

Because hot Jupiters are expected to circularise on a time-scale less than their age, we imposed a circular orbit to obtain the most likely parameters (e.g. Anderson et al. 2012). To estimate the upper limit on eccentricity, we ran a separate MCMC analysis with eccentricity being fitted as a free parameter and checked the eccentricity distribution in the resulting MCMC chain.

To improve the precision of the orbital period, we produced a separate MCMC analysis that also included the ground-based photometry presented in Bryan et al. (2012), with limb-darkening coefficients from Claret (2000, 2004), as appropriate for different bandpasses. This extended the photometric baseline from 79 d to 5.5 yr and reduced the uncertainty to one fifth of its former value.

Table 8.2 lists the obtained system parameters and Fig. 8.2 shows the corresponding transit model.

We find a very good agreement with the system parameter values reported by Bryan et al. (2012) with a significantly improved precision. Mancini et al. (2014) reported stellar ($1.591 \pm 0.016\ \rho_{\odot}$) and planetary densities ($1.183 \pm 0.026\ \rho_{\mathrm{Jup}}$) significantly lower than Bryan et al. (2012). We find no evidence for the lower densities, as our values agree with those reported by Bryan et al. (2012).

Table 8.2: MCMC system parameters for Qatar-2 and Qatar-2b.

Parameter	Symbol	Value	Unit
Transit epoch	t_0	2457250.2008155 ± 0.0000084	BJD
Orbital period	P	1.33711677 ± 0.00000010	d
Area ratio	$(R_p/R_*)^2$	0.026587 ± 0.000062	...
Transit width	t_{14}	0.075409 ± 0.000046	d
Ingress and egress duration	t_{12}, t_{34}	0.010696 ± 0.000064	d
Impact parameter	b	0.115 ± 0.023	...
Orbital inclination	i	88.99 ± 0.20	°
Orbital eccentricity	e	0 (adopted; <0.05 at 2σ)	...
Orbital separation	a	0.02136 ± 0.00024	au
Stellar mass	M_*	0.727 ± 0.024	$M_\odot$
Stellar radius	R_*	0.7033 ± 0.0080	$R_\odot$
Stellar density	ρ_*	2.090 ± 0.015	$\rho_\odot$
Planet mass	M_p	2.466 ± 0.062	M_J
Planet radius	R_p	1.115 ± 0.013	R_J
Planet density	ρ_p	1.776 ± 0.034	ρ_J
Planet equilibrium temperature[a]	T_p	1285 ± 16	K
RV semi-amplitude	K_1	0.5609 ± 0.0063	km s^{-1}
Limb-darkening coefficients	a_1, a_2, a_3, a_4	0.703, -0.737, 1.486, -0.642	...

Note: [a] Planet equilibrium temperature is based on assumptions of zero Bond albedo and complete day-to-night heat redistribution.

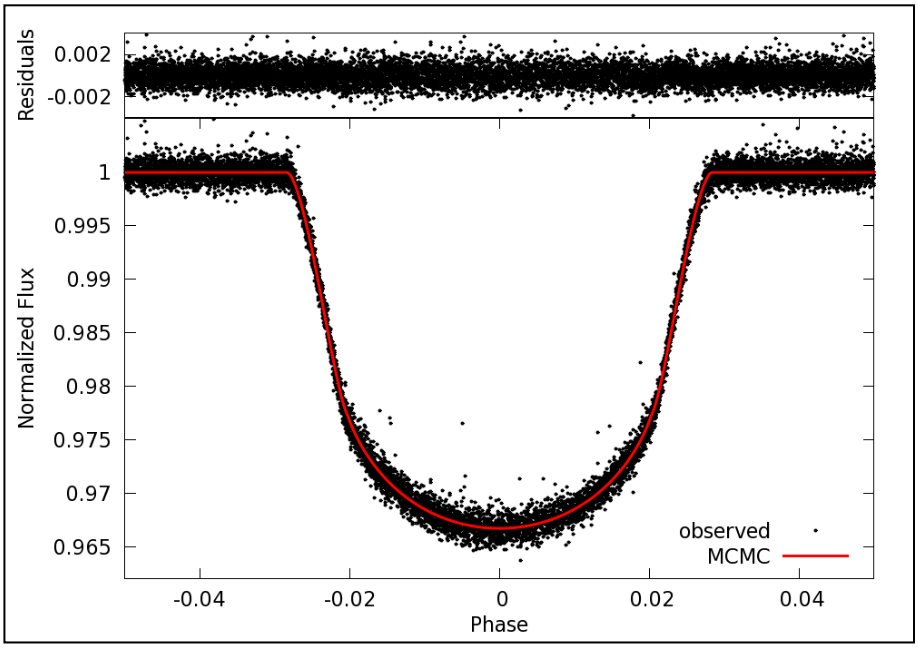

Figure 8.2: Best-fitting MCMC transit model and its residuals from the phase-folded *K2* light curve.

8.6 TTV and TDV

Measurements of mid-transit times and their deviations from a linear period ephemeris (transit-timing variations, or TTVs) can reveal additional and otherwise unobservable planets in planetary systems due to the inter-planet gravitational interactions (Algol et al. 2005). Reported TTV amplitudes for perturbed transiting exoplanets are between a few tens of seconds and several hours, with typical periods of the order of a few hundred days (Mazeh et al. 2013). Similarly, any additional perturbing planet would also cause transit-duration variations (TDVs) of the perturbed transiting planet, in phase with TTVs but with a significantly smaller amplitude (Nesvorný et al. 2013).

We measured the transit-timings and transit-durations for Qatar-2b for each of the transits using the MCMC analysis as described in Section 8.5. Because the stellar activity can lead to inaccurate measurements of timings and durations (Oshagh et al. 2013), we, as in Section 8.5, removed the detected starspot occultations from the light curve prior to the MCMC analysis. The resulting TTV and TDV measurements are shown in Fig. 8.3. The data point near BJD 2457269 has been excluded from the analysis due to the quality-flagged data gap (see transit number 39 in Fig. 8.5).

The TTV and TDV measurements yield χ^2 values of 63.0 and 55.5, respectively, for 58 degrees of freedom, which means that they are statistically consistent with the assumption of white noise distributed around zero. We estimate the semi-amplitude upper limit to be 15 s for TTVs and 1 min for TDVs. The absence of TTVs and TDVs indicates that a second, non-transiting, massive planet is unlikely, unless at a much longer period.

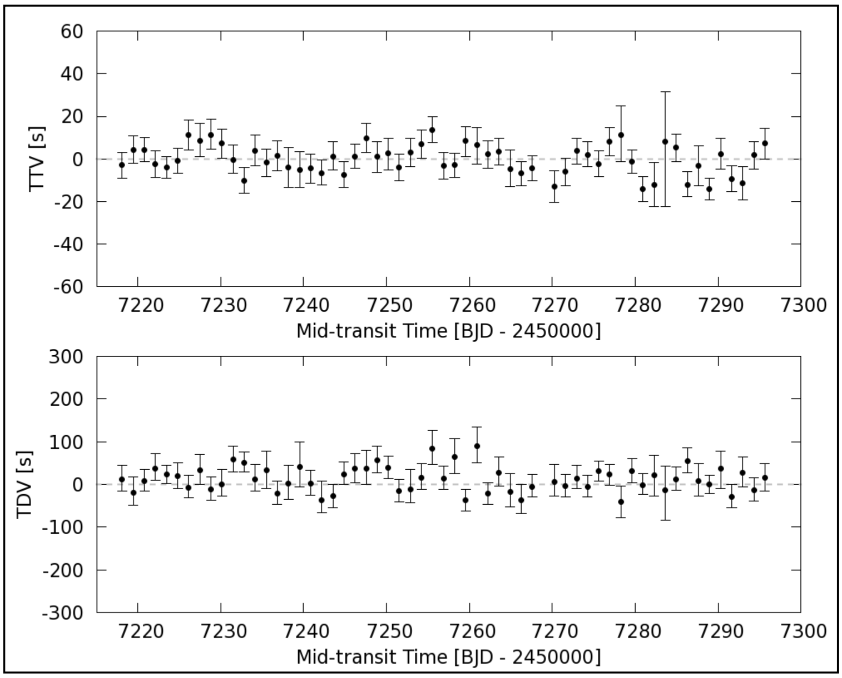

Figure 8.3: The TTV (upper panel) and TDV (lower panel) measurements are statistically consistent with the assumption of strictly periodic transits and constant transit duration.

8.7 Rotational Modulation

The *K2* light curve of Qatar-2 exhibits a pronounced rotational modulation with an amplitude of about 2 per cent (see Fig. 8.1). The modulation is caused by the presence of starspots on the surface of the rotating host star. To measure the period we first removed the transits from the light curve, applied 10σ clipping and then calculated a Lomb–Scargle periodogram. The rotational modulation period is manifested as the highest peak near 18.2 d with a Gaussian standard deviation of 1.6 d (see Fig. 8.4).

The resulting rotational modulation period of 18.2 ± 1.6 d is a direct measure of the rotational period. We measure a similar rotational period well within the uncertainty also when using three publicly available drift-corrected long-cadence light curves (`K2SFF` Vanderburg & Johnson 2014, `K2SC` Aigrain, Parviainen & Pope 2016 and `EVEREST` Luger et al. 2016), which dismisses any doubts of whether our custom artefact removal technique might contaminate the rotational modulation.

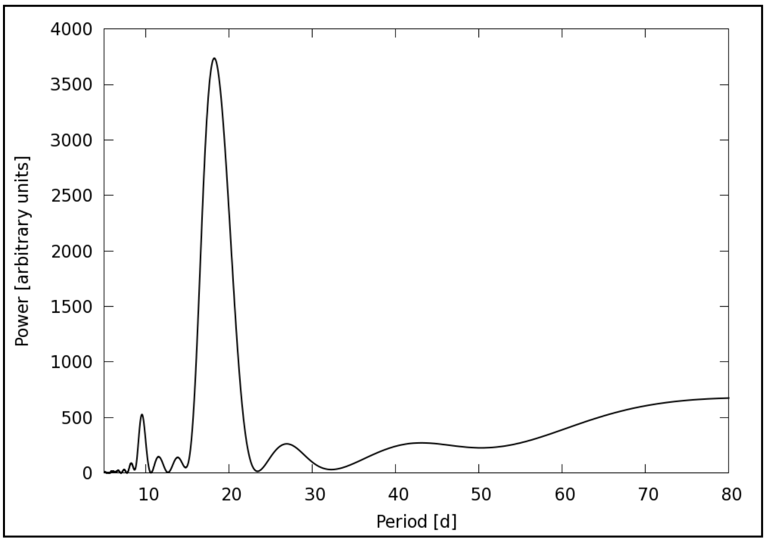

Figure 8.4: Lomb–Scargle periodogram of the rotational modulation. The highest peak suggests the rotational period of 18.2 ± 1.6 d.

The stellar rotational period given above and stellar radius given in Table 8.2 correspond to a stellar equatorial rotational velocity of 2.0 ± 0.2 km s^{-1}, whereas the spectroscopically measured stellar projected rotational velocity is 2.0 ± 1.0 km s^{-1} (Esposito et al. 2017). Although the calculated rotational velocity and the measured projected rotational velocity match, suggesting an edge-on stellar rotation, we can constrain the inclination only very weakly as being larger than 30° owing to a large relative error bar for the projected rotational velocity. A stronger indication for a near-edge-on stellar rotation is revealed by the starspot position measurements in Section 8.5.

8.8 Starspots

8.8.1 Detection

Fig. 8.5 shows the transit light curves after subtracting the best-fitting transit model from Section 8.5. The transits show many temporary brightenings that appear to be starspot occultation events.

We should first consider whether these could be residual artefacts from the *K2* thruster firings. However, this is highly unlikely since: (1) we know the times of thruster firings, and these do not coincide with the starspot features; (2) the starspots recur in relation to the planetary orbital and stellar rotation cycles, which the spacecraft firings do not; (3) the drift artefacts have a step-like appearance, which the starspot features do not; and (4) spacecraft drifts were particularly consistent during the observing Campaign 6, which resulted in only minimal residual drift artefacts. Thus we can conclude that the features are indeed occultations of starspots.

In order to identify starspot occultation events in an unbiased way we shuffled the order of the transits in the residual light curve and then four of our colleagues examined them by eye and searched for any occultation-like features. Firstly, we considered light curve features as starspot occultation candidates only if they were marked as a possible occultation event by at least two colleagues. We then fitted each occultation candidate with a Gaussian function to determine the orbital phase at which it occurs, and its amplitude and width, and calculated the corresponding change in the Bayesian information criterion (BIC). Finally, we report here only those occultation candidates whose BIC change was greater than 6. These are marked with ellipses in Fig. 8.5 and listed in Table 8.3 along with stellar topocentric longitudes, which we calculated using the system parameters from Table 8.2 and the best-fitted occultation phases. Phase uncertainties in Table 8.3 are as quoted by the `SciPy` (Jones, Oliphant & Peterson 2001) Gaussian fits, and stellar longitude uncertainties were calculated from the phase and system parameters uncertainties.

In total we report the detection of 34 starspot occultation events, most of which appear at consistent phase shifts in up to five consecutive transits (transits 46–50). Furthermore, we found that sets of recurring occultations also appear at consistent phase shifts, in full agreement with the rotational modulation period (see Section 8.7) and the assumption that all recurring sets were produced by the same starspots. The occultation recurrence pattern and a very good fit to a single stellar rotational period (see Section 8.8.2) suggests that all the 34 individual starspot occultation events were caused by only five different starspots (each starspot is marked with a different colour in Fig. 8.5).

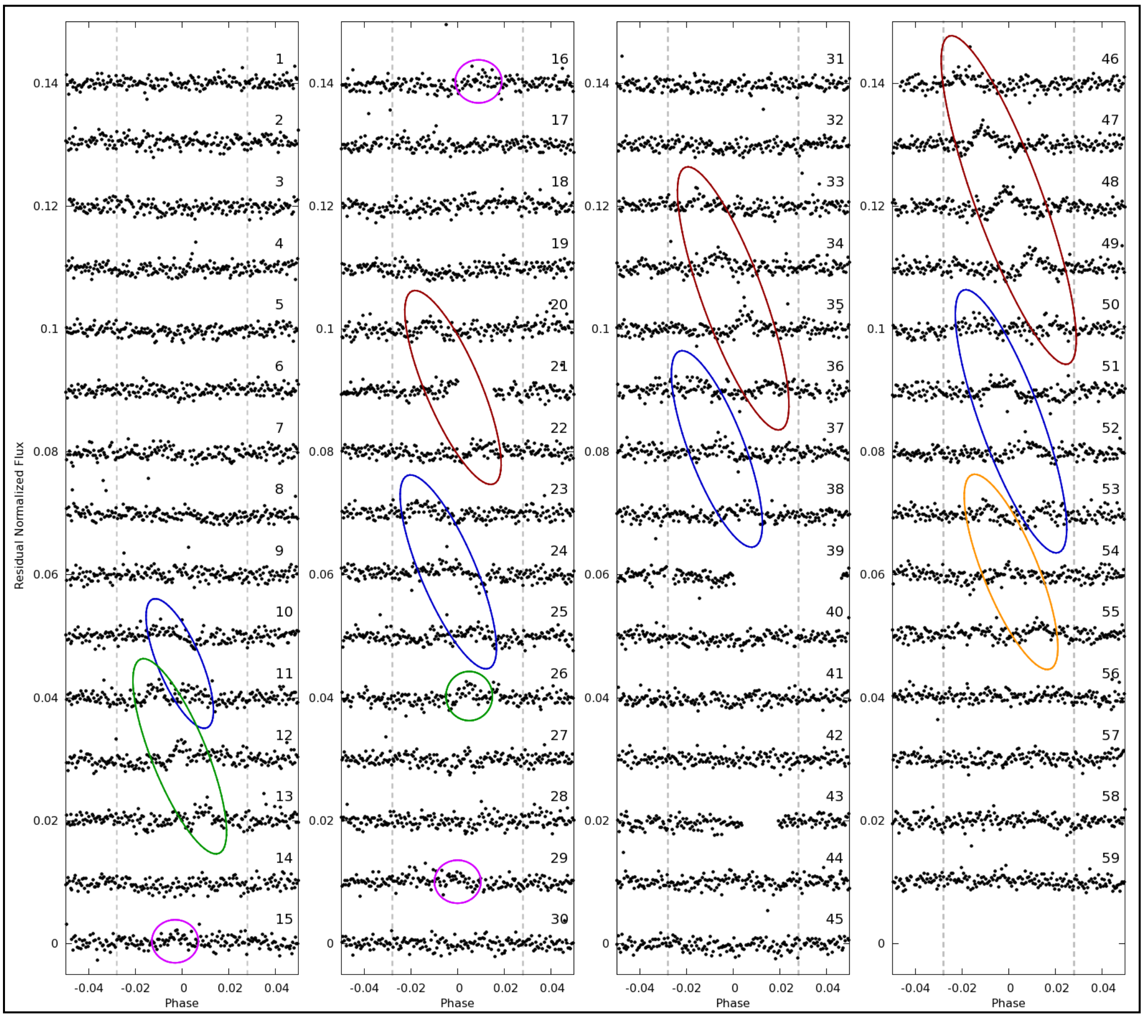

Figure 8.5: Starspot occultations in the model-subtracted light curve of Qatar-2b. Vertical dashed lines specify the extent of the transit. Sets of recurring occultations are marked with ellipses. Ellipses of the same colour correspond to the same starspot.

Although the rotational modulation shown in Fig. 8.1 is produced by a contribution from several detected starspots and likely also by some unocculted and therefore undetected starspots, we found a tentative correlation between the main

Table 8.3: Phase and stellar topocentric longitude positions of every detected starspot occultation event. The change of BIC provides an estimate of each occultation's detectability.

Transit number	Phase	Stellar longitude[a] (°)	ΔBIC
10	-0.0087 ± 0.0012	-21.1 ± 3.0	13.8
11	-0.0112 ± 0.0007	-27.5 ± 1.9	15.2
11	0.0027 ± 0.0010	6.4 ± 2.4	12.7
12	-0.0006 ± 0.0004	-1.4 ± 1.0	28.8
13	0.0098 ± 0.0005	23.9 ± 1.3	23.6
15	-0.0025 ± 0.0008	-5.9 ± 1.9	17.7
16	0.0102 ± 0.0014	24.9 ± 3.7	7.5
20	-0.0128 ± 0.0007	-31.9 ± 1.9	9.8
21	-0.0012 ± 0.0027	-2.8 ± 6.4	9.8
22	0.0104 ± 0.0012	25.4 ± 3.2	9.3
23	-0.0155 ± 0.0008	-39.8 ± 2.4	17.6
24	-0.0049 ± 0.0012	-11.7 ± 2.9	27.9
25	0.0070 ± 0.0009	16.8 ± 2.2	14.5
26	0.0045 ± 0.0005	10.7 ± 1.2	20.8
29	-0.0010 ± 0.0012	-2.4 ± 2.8	9.2
33	-0.0151 ± 0.0005	-38.6 ± 1.5	16.4
34	-0.0062 ± 0.0006	-14.8 ± 1.5	32.4
35	0.0051 ± 0.0003	12.2 ± 0.7	42.1
36	-0.0141 ± 0.0011	-35.6 ± 3.1	8.5
36	0.0152 ± 0.0008	38.9 ± 2.5	11.3
37	-0.0060 ± 0.0008	-14.3 ± 2.0	12.1
38	0.0060 ± 0.0007	14.3 ± 1.7	9.0
46	-0.0185 ± 0.0011	-49.8 ± 3.9	13.8
47	-0.0106 ± 0.0005	-26.0 ± 1.3	46.1
48	-0.0008 ± 0.0004	-1.9 ± 1.0	42.1
49	0.0104 ± 0.0010	25.4 ± 2.7	36.2
50	-0.0147 ± 0.0020	-37.4 ± 5.7	10.4
50	0.0198 ± 0.0011	54.8 ± 4.8	7.3
51	-0.0028 ± 0.0010	-6.6 ± 2.4	16.3
52	0.0084 ± 0.0007	20.3 ± 1.8	17.6
53	-0.0096 ± 0.0005	-23.4 ± 1.3	9.9
53	0.0150 ± 0.0012	38.3 ± 3.7	6.0
54	0.0001 ± 0.0010	0.2 ± 2.4	8.4
55	0.0130 ± 0.0010	32.5 ± 2.9	23.5

Note: [a] Stellar topocentric longitude runs from -90° (first planetary contact), through 0° (central meridian) to 90° (last contact).

modulation components and individual detected starspots. The starspot marked blue in Fig. 8.5 is seen near mid-transit close to the main rotational modulation's minima, suggesting that this was then the largest among Qatar-2's starspots. The occultation events marked red in Fig. 8.5 cluster near the plateaus or secondary minima (seen clearest near BJD 2457244 and 2457282 in Fig. 8.1). On the other hand, the rotational modulation's maxima occur when no or only small starspot occultation events are detected.

8.8.2 Rotational Period

The stellar rotational period can be calculated from the changes in starspot positions on the rotating stellar surface and the timing of the occultation events. The position of the starspot is defined by stellar longitude and latitude and in general both parameters are needed for accurate determination of the starspot's position changes. However, in aligned systems such as Qatar-2 (see Section 8.8.3) and in the presence of recurring sets of recurring occultations, the most relevant starspot parameter is longitude.

Fig. 8.6 shows the measured phase and longitude positions of all the occultation events from Table 8.3. Using the best-fitting longitude vs. phase dependence for every recurring set, and the known orbital period of the planet, we were able to calculate the rotational period for every starspot. Their uncertainties were calculated from the slope uncertainties quoted by the `SciPy` fitting routine. The resulting rotational periods and their uncertainties are given in Table 8.4 and are based on the assumptions that starspots have circular shapes and that the starspots' positions change only due to stellar rotation, i.e. that starspot longitudinal migration is negligible. The latter assumption is justified by the solar observations which reveal that the longitudinal migration of sunspots is 4 orders of magnitude smaller than the solar rotation rate (Gyenge, Baranyi & Ludmány 2014). The weighted mean rotational period of 18.0 ± 0.2 d is in agreement with the rotational modulation period (see Section 8.7). We also performed a simultaneous fit of all recurring sets with a common rotational period and obtained the same result as a weighted mean. Because rotational modulations depend strongly on starspots coming and going, which causes modulational phase shifts, the period derived from starspot occultation events is more accurate and reliable than the period determined from the rotational modulation.

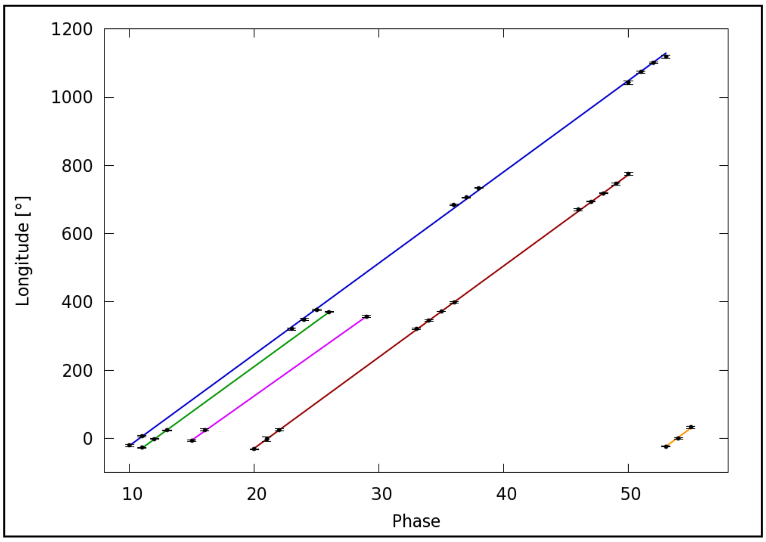

Figure 8.6: Longitude and phase positions of all recurring occultations. We added 360° to stellar longitudes from Table 8.3 for every stellar rotation. Each best-fitting straight line corresponds to a different starspot, which are marked with the same colours as in Fig. 8.5. The good fits to straight lines of very similar slopes suggests that occultation events of each recurring set were very likely caused by the same starspot. A few outliers and weak skewing trends, such as in the recurring set 50–53, may be attributed to non-circular and evolving starspot shapes, supported by the variable and non-Gaussian appearance of occultation events in Fig. 8.5.

Table 8.4: Stellar rotational period of every starspot.

Transit numbers	Rotational period (d)
10–11+23–25+36–38+50–53	18.00 ± 0.03
11–13+26	18.11 ± 0.07
15–16+29	18.58 ± 0.17
20–22+33–36+46–50	18.01 ± 0.04
53–55	18.00 ± 0.97
weighted mean	**18.03 ± 0.24**

The recurring set of starspot occultations during transits 15–16 and 29 indicated a 0.5 d (2.3σ) longer rotational period than the weighted mean (see Table 8.4), possibly caused by a differential rotation. However, we were unable to investigate the effect of differential rotation due to the relatively small differences in rotational periods among different spots and because of poorly constrained starspot latitudes (see Section 8.8.3).

Our rotational period disagrees with the previously reported value of 14.8 ± 0.3 d by Mancini et al. (2014, 2016). Their rotational period was based on two starspot occultation events separated by 12 d, which were consistent with the projected rotational velocity of 2.8 ± 0.5 km s^{-1} by Bryan et al. (2012). With our robust rotational period of 18.0 ± 0.2 d it now seems reasonable to conclude that the two starspot occultation events analysed by Mancini et al. (2014, 2016) (spots #1 and #2) were in fact caused by two different spots and that the projected rotational velocity by Bryan et al. (2012) was overestimated by at least 1.5σ. A slower rotation than previously thought is further supported by the latest measurements of projected rotational velocity which place it at 2.0 ± 1.0 km s^{-1} (Esposito et al. 2017).

8.8.3 Obliquity

The angle between the stellar rotational axis and the planetary orbital axis results in a gradual latitudinal positional drift of the recurring starspot occultation events. In misaligned systems the starspot occultations may occur only at preferential transit phases where the active latitudinal regions cross the planetary transit chord, such as in the HAT-P-11 system (Sanchis-Ojeda & Winn 2011). In the Qatar-2 system the starspot occultation events occur uniformly along the transit chord and in consecutive transits (see Fig. 8.5) which indicates that the system is aligned, as in the case of the Kepler-17 system (Désert et al. 2011).

We fitted the starspot occultation events with the Planetary Retrospective Integrated Starspot Model (`PRISM`; Tregloan-Reed, Southworth & Tappert 2013; Tregloan-Reed et al. 2015) and searched for any gradual starspot latitudinal drifts. We used the fixed input system parameters from Section 8.5 and searched for best-fitting starspot topocentric longitude, latitude, radius and contrast. We explored the entire starspot parameter space for each occultation event in each set of recurring occultations. Since `PRISM` was designed to model starspots with circular shapes, some of the occultation events in the Qatar-2 light curve were fitted poorly owing to their non-Gaussian shapes (e.g. set 50–53 indicated that the spot was elongated along the transit chord, possibly a strip of spots). We also found a high degree of degeneracy and non-physically rapid and non-monotonic starspot parameter variations among consecutive occultation events within several sets. Therefore, we decided to find the starspot radius and contrast that gave the best and most consistent fit within each set of consecutively recurring occultations and kept them fixed while refitting for starspot longitude and latitude positions. By using this approach we ignore starspot evolution, which may be correct only for time-scales significantly shorter than starspot lifetimes, and we assume that starspot contrast does not change as a function of the spot's distance from the stellar disc centre. The latter assumption is justified by the findings of Lanza et al. (2003) who calculated that sunspot contrast changes only by a few per cent from the solar disc centre to the limb. Having the starspot radius and contrast fixed, the best-fitting latitudes could be determined from the widths and heights of each of the occultation events within the same set. This approach lifted the degeneracy and provided a physically more plausible solution.

In this paper we only present the obliquity results that were derived from the longest individual set of consecutively recurring occultations (transits 46–50), which yielded the most robust obliquity measurement with the smallest uncertainty. Firstly, this set exhibited pronounced Gaussian-like occultation events which enabled a reliable starspot parameter fitting. And secondly, by exhibiting five occultation events in consecutive transits it provided the largest longitudinal starspot coverage in the shortest possible time-span of 5 d, which is essential when assuming no starspot evolution.

The light curves and visualisations of the best-fitting starspot models for transits 46–50 are shown in Fig. 8.7. Starspot position parameters are listed in Table 8.5. The stellar longitude and latitude uncertainties in Table 8.5 are 1σ uncertainties as given by `PRISM`, which estimates uncertainties from the distribution of starspot parameters in the MCMC chain. We show the starspot longitudinal and latitudinal positions in Fig. 8.8 and find that they change linearly. If the stellar inclination was significant, the starspots' path would act as a quadratic function. We find no evidence for non-linear starspot paths which indicates that the stellar rotation must be close to edge-on. Using the system parameters from Section 8.5 and the fitted relation between the starspot longitudinal and latitudinal positions from Fig. 8.8, we derive the sky-projected obliquity of -0.2 ± 0.7°. For a degenerate but less-likely scenario in which a starspot appears below the transit chord, we obtain a similar sky-projected obliquity of 0.1 ± 0.8°. Both calculations are based on the assumption that the starspot's size and contrast do not change throughout the set and that the starspot's latitudinal position only changes due to obliquity, i.e. neglects the contribution of latitudinal starspot migration. Therefore, the uncertainty is likely to be underestimated. In a very conservative approach of Désert et al. (2011), we set the upper uncertainty limit to 8°, which is the largest possible sky-projected obliquity to still be able to see occultation events in five consecutive transits of Qatar-2b. The realistic uncertainty is expected to lie somewhere in between the two given values. However, because we were unable to quantify all the systematic errors and realistic ranges of starspot contrast and radius variability, we adopt 8° as the final conservative uncertainty. A similar obliquity constraint was provided by Dai et al. (2017) who claim that Qatar-2's sky-projected obliquity is smaller than 10°.

The small obliquity angle agrees with the empirical indication that systems with host stars cooler than 6250 K are generally aligned (Winn et al. 2010a; Albrecht et al. 2012).

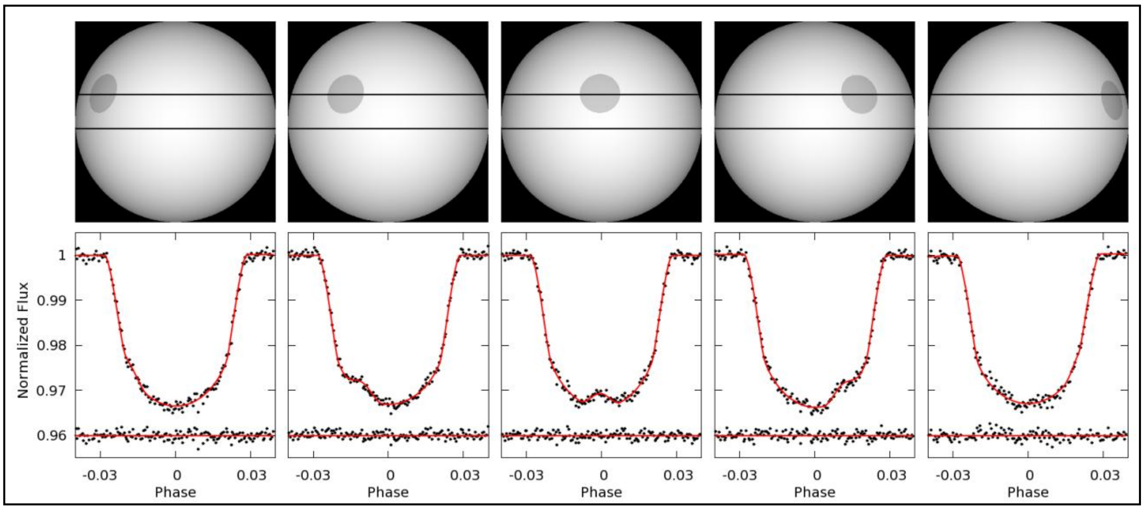

Figure 8.7: Best-fitting starspot models for transits 46–50. Upper panels: starspot visualisations. Horizontal lines indicate the position of the transit chord. Lower panels: corresponding best-fitting light curve models. Shown below are the residual light curves after subtracting the starspot models. A notable residual in transit 50 at phase -0.015 is caused by another starspot (see Table 8.3 and Fig. 8.5).

Table 8.5: Best-fitting starspot positions with `PRISM` for the longest individual set of recurring occultations, using the fixed starspot angular radius of 11.6 ± 2.5°[a] and contrast of 0.810 ± 0.058[b].

Transit number	Stellar longitude[c] (°)	Stellar latitude[d] (°)
46	-50.1 ± 2.4	16.51 ± 0.99
47	-26.8 ± 1.1	16.15 ± 0.66
48	-0.99 ± 0.80	16.55 ± 0.73
49	27.86 ± 0.94	16.08 ± 0.64
50	60.2 ± 2.1	12.5 ± 6.6

Notes: [a] Angular radius runs from 0 to 90°, where 90° covers half of the stellar surface. An angular radius of 11.6 ± 2.5° corresponds to an actual radius of (9.9 ± 2.1)×10^4 km.

[b] Contrast runs from 0 to 1, where a value of 1 corresponds to the brightness of the surrounding photosphere.

[c] Longitude runs from -90° (first planetary contact), through 0° (central meridian) to 90° (last contact).

[d] Latitude runs from -90° (stellar south pole), through 0° (equator) to 90° (north pole).

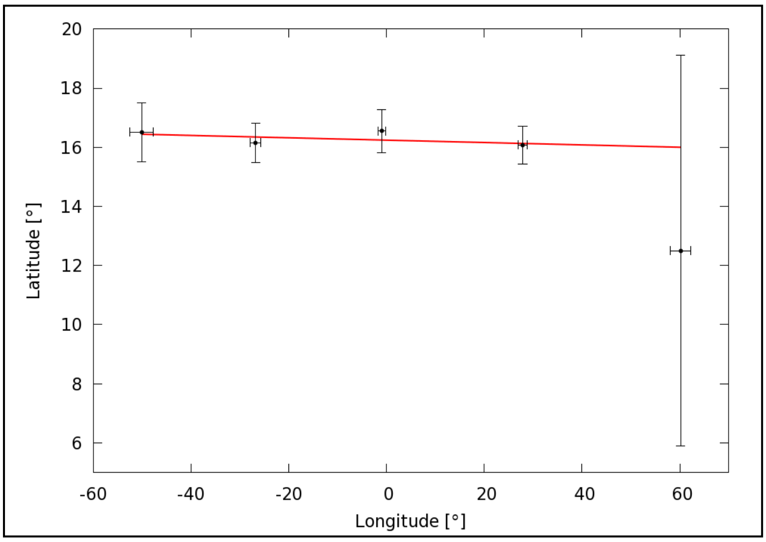

Figure 8.8: Latitude and longitude positions for starspots in transits 46–50. The fit corresponds to the sky-projected obliquity angle of -0.2 ± 0.7°. The large uncertainty of the right-most data point (transit 50) is because of the starspot's proximity to the stellar limb and a low signal to noise of the occultation event.

8.8.4 Starspot Lifetimes

In the longest recurring set of recurring occultations (transits 10–11, 23–25, 36–38 and 50–53), the starspot is seen during three full stellar rotations, spanning over 43 transits. This sets the minimum starspot lifetime to 58 d. Fig. 8.5 also reveals that the shapes of recurring occultation events are changeable, indicative of starspot evolution.

The typical fitted starspot radius was of the order of 10^5 km, which is of similar size as in the case of Kepler-17. Extrapolating the Gnevyshev–Waldmeier empirical relation between sunspot radii and their lifetimes (Gnevyshev 1938; Waldmeier 1955) to a radius of 10^5 km suggests a starspot lifetime of about 1000 d. However, Bradshaw & Hartigan (2014) have claimed that according to turbulent magnetic diffusivity starspot lifetimes depend strongly on supergranule sizes and that Gnevyshev–Waldmeier relation may not be applicable to stars other than the Sun. Using the relation of Bradshaw & Hartigan (2014), the fitted starspot radius, and the minimum starspot lifetime for Qatar-2, we can constrain the supergranule sizes only weakly as being smaller than $0.2\,R_{\odot}$, compared to solar supergranule sizes of $0.016\,R_{\odot}$.

8.9 Phase-curve Modulation

The three main phase-curve modulation components of planetary systems in the optical wavelengths covered by the *K2* bandpass (420–900 nm) are: (1) reflection of starlight from an orbiting planet, (2) rotation of the star that is gravitationally distorted into an ellipsoidal shape, and (3) Doppler beaming of starlight by the orbital motion of the host star (Esteves, De Mooij & Jayawardhana 2013). To search for these phase-curve modulation components we first removed the rotational modulation and normalized the *K2* light curve by dividing it with the median of second-order polynomial fits with window and step size of 3 and 0.3 d, respectively. Using this approach, we effectively removed the low-frequency rotational modulation while retaining any potential high-frequency phase-curve modulation, as confirmed by successful phase-curve signal injection and recovery tests. Next, we phase-folded the normalized light curve on the orbital period of Qatar-2b and applied binning to reduce the white noise (Fig. 8.9).

Using the system parameters from Table 8.2, the theoretically expected semi-amplitudes of the reflection, ellipsoidal and Doppler beaming phase-curve components are $595 \cdot A_g$ ppm, 12 ppm, and 8 ppm, respectively, where A_g is the planet's geometrical albedo (Mazeh & Faigler 2010). We tentatively detect a sinusoidal signal peaking at orbital phases 0.25 and 0.75 with a minimum at phase 0.5, characteristic of ellipsoidal modulations. Its best-fitting semi-amplitude of 18 ± 4 ppm is close to the theoretically expected value. We were able to detect this modulation with a similar amplitude in the whole, first half and second half of the light curve, and also using three additional artefact removal procedures (`K2SFF`, `K2SC` and `EVEREST`). This strengthens the assumption that the detection of ellipsoidal modulation is real. However, the fit improves the reduced χ^2 only slightly from 1.62 to 1.50. The light curve exhibits significant red noise such as SFF artefacts or residuals of the imperfect removal of the pronounced rotational modulation, and therefore this detection of ellipsoidal modulation should be regarded only as probable.

A reflectional modulation would peak at phase 0.5. A simultaneous MCMC fit of all three possible phase-curve modulation components gives the best-fitting reflectional modulation semi-amplitude of 2 ppm, though given the presence of red noise a conservative upper limit would be much higher, at 30 ppm. This reflection modulation upper limit of 30 ppm implies that the planet's optical geometric albedo has to be lower than 0.05. Low albedos at optical wavelengths are common for hot Jupiters (Esteves, De Mooij & Jayawardhana 2013), and are consistent with theoretical models which predict cloudless planetary atmospheres (Burrows, Ibgui & Hubeny 2008). The lowest optical geometric albedo has been measured for the TrES-2 system of less than 0.01 (Kipping & Bakos 2011).

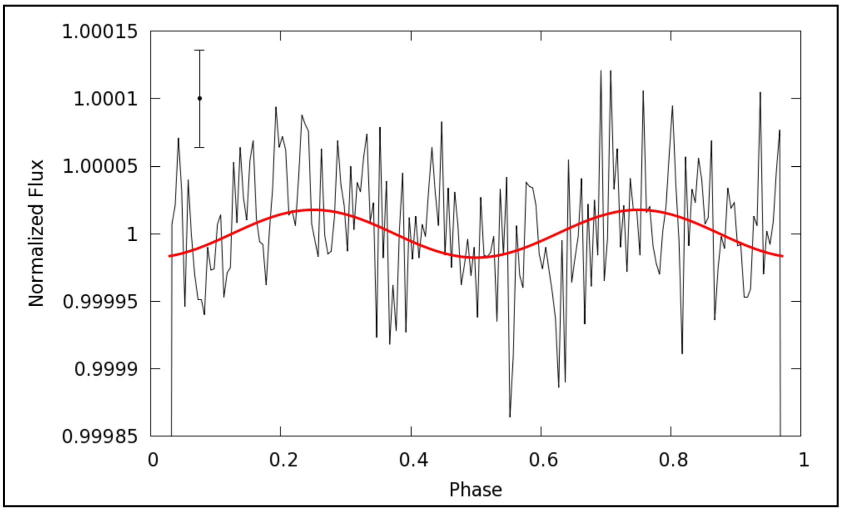

Figure 8.9: Phase-curve of Qatar-2, binned to 200 bins. The red line denotes a possible detection of the ellipsoidal modulation with the best-fitting semi-amplitude of 18 ± 4 ppm. Rotational and Doppler beaming modulation components are not significantly detected. One representative error bar is shown in the top left corner.

As of the time of writing, the phase-curve modulations have been detected for 26 planetary systems, 19 of which are from *Kepler* observations according to NASA Exoplanet Archive[13]. If our possible detection of ellipsoidal modulation is real, it would be the first phase-curve modulation detection of any of the planetary systems observed by *K2*.

8.10 No Additional Transiting Planets

We searched for any additional transiting planets in the normalized *K2* light curve with low-frequency modulations removed. First, we removed Qatar-2b's transits from the light curve by replacing the measured normalized flux values around transits with unity. We then produced the periodogram to search for any remaining periodic transit-like features with `PyKE` tool `kepbls` which is based on the box-least-square fitting algorithm by Kovács, Zucker & Mazeh (2002). The periodogram did not reveal any significant peaks between 0.5 and 30 d period with a transit depth upper limit of 280 ppm.

8.11 Age of the Host Star

We estimate the stellar age first from the rotational period. Young stars rotate rapidly and gradually slow down as they lose angular momentum through magnetised stellar winds (Barnes 2003). We used the gyrochronological relation by Barnes (2007) to estimate that Qatar-2 is 0.59 ± 0.10 Gyr old.

Comparing stellar parameters to theoretical stellar models provides another age estimate. As in Močnik et al. (2016b), we compared stellar density and effective

---

[13] http://exoplanetarchive.ipac.caltech.edu/

temperature of 4645 K to isochrones and evaluated the age of the star using the Bayesian mass and age estimator `BAGEMASS` (Maxted, Serenelli & Southworth 2015a). The stellar evolution models used in `BAGEMASS` were calculated using the `GARSTEC` code (Weiss & Schlattl 2008). The best-fitting stellar evolution track gives an age estimate of 9.4 ± 3.2 Gyr.

The huge discrepancy between gyrochronological and isochronal age estimates has also been seen in other exoplanet host stars, in particular K-type stars hosting a hot Jupiter (Maxted, Serenelli & Southworth 2015b; Mancini et al. 2017). It has been suggested that these discrepancies could be caused by the tidal interactions which could transfer angular momentum from an orbital motion of a planet to the rotation of a host star (Maxted, Serenelli & Southworth 2015b). Thus, Qatar-2 may have been spun-up by the hot Jupiter and it is actually older than the gyrochronological age estimate. Another explanation for the age discrepancy is the radius anomaly of late type stars, where the observed stellar radii are larger than stellar model predictions (Popper 1997), which could result in isochronal ages being overestimated.

Obtaining a reliable age estimate for Qatar-2 would require additional age estimators such as the photospheric Li abundance, or an in-depth modelling to account for the two above-mentioned mechanisms that are probably contributing to the age discrepancy.

8.12 Conclusions

We used the *K2* short-cadence observations of Qatar-2 from observing Campaign 6 to refine the system parameters, search for transit-timing variations, additional transiting planets, phase-curve modulations, and mainly to analyse the starspot activity.

The light curve of Qatar-2 exhibits pronounced rotational modulation with a period of 18.2 ± 1.6 d and an amplitude of about 2 per cent. The stellar activity is further manifested through 34 detected starspot occultation events among 59 transits. The majority of the occultations are seen repeatedly in up to five consecutive transits, owing to the low obliquity angle and a large ratio between stellar rotational and planet's orbital period. Moreover, sets of recurring occultations also reappear after several stellar rotations. The longest recurring set of recurring starspot occultations spans over three stellar rotations, which sets the longest starspot lifetime to at least 58 d. By fitting the recurring occultation events we derived the stellar rotational period of 18.0 ± 0.2 d, in agreement with the rotational modulation period, and zero sky-projected obliquity with a conservative error bar of ±8°.

We detect a probable ellipsoidal phase-curve modulation with a semi-amplitude of 18 ± 4 ppm, close to the theoretically expected value.

9 WASP-118 and WASP-107

This chapter is based on Močnik et al. (2017), MNRAS, 469, 1622. Contributions from the co-authors are as follows: CH supervised the research and provided general advice; DRA submitted the *K2* downlink proposal for C8 and C10, and helped examining whether the starspot occultations found in WASP-107 are recurring; BJMC removed stellar pulsations from the light curve of WASP-118; JS performed light curve simulations that were used in the downlink proposal. Compared to the published version of the paper, I added in this chapter Fig. 9.9 to visualize the position of WASP-118 on the Hertzsprung–Russel map of pulsation types. I also added a brief mention in Section 9.12 on the suitability of WASP-107 for transmission spectroscopy studies.

9.1 Abstract

By analysing the *K2* short-cadence photometry we detect starspot occultation events in the light curve of WASP-107, the host star of a warm-Saturn exoplanet. WASP-107 also shows a rotational modulation with a period of 17.5 ± 1.4 d. Given that the rotational period is nearly three times the planet's orbital period, one would expect in an aligned system to see starspot occultation events to recur every three transits. The absence of such occultation recurrences suggests a misaligned orbit unless the starspots' lifetimes are shorter than the star's rotational period. We also find stellar variability resembling γ Doradus pulsations in the light curve of WASP-118, which hosts an inflated hot Jupiter. The variability is multi-periodic with a variable semi-amplitude of $\sim$200 ppm. In addition to these findings we use the *K2* data to refine the parameters of both

systems, and report non-detections of transit-timing variations, secondary eclipses and any additional transiting planets. We used the upper limits on the secondary-eclipse depths to estimate upper limits on the planetary geometric albedos of 0.7 for WASP-107b and 0.2 for WASP-118b.

9.2 Introduction

The *Kepler* (Borucki et al. 2010) and *K2* (Howell et al. 2014) missions have provided the community with high-precision photometric observations of 2449 confirmed transiting exoplanets to date among a total of 2716 confirmed transiting exoplanets, according to NASA Exoplanet Archive[14]. In addition, *K2* is also observing exoplanets previously found by the ground-based transit surveys such as WASP (Pollacco et al. 2006). WASP-107 and WASP-118 are among the brightest systems observed by *K2*, which allows for detailed characterization owing to high-precision light curves combined with existing spectroscopic observations performed by Anderson et al. (2017) and Hay et al. (2016).

WASP-107b is a warm Saturn in a 5.7-d orbit around a V = 11.6, K6 main-sequence star (Anderson et al. 2017). The planet lies in the transition region between ice giants and gas giants, with a mass of 2.2 $M_{\rm Nep}$ or 0.12 $M_{\rm Jup}$, but an inflated radius of 0.94 $R_{\rm Jup}$. The WASP discovery photometry revealed a possible stellar rotational modulation with a period of ∼17 d and an amplitude of 0.4 per cent. This led Anderson et al. (2017) to propose that the host star is magnetically active.

WASP-118b is an inflated hot Jupiter with a mass of 0.51 $M_{\rm Jup}$ and a radius of 1.4 $R_{\rm Jup}$. It orbits a V = 11.0 F6IV/V star every 4.0 d (Hay et al. 2016).

---

[14] http://exoplanetarchive.ipac.caltech.edu/

If a transiting planet crosses a starspot it will produce a temporary brightening in the transit (Silva 2003). Starspot occultation events can provide an accurate measurement of the stellar rotational period and the obliquity, i.e. the angle between the stellar rotational axis and the planet's orbital axis. Obliquities can tell us about a planet's dynamical history and about planet migration mechanisms. If the obliquity is small, the same starspot can be occulted recurrently at different stellar longitudes, such as in the case of an aligned Qatar-2 system (Močnik, Southworth & Hellier 2017; Dai et al. 2017). Alternatively, if a system is misaligned, the transit chord will cross stellar active latitudes only at certain preferential phases, such as in the case of HAT-P-11b (Sanchis-Ojeda & Winn 2011).

The presence of a massive close-in planet may induce tides that can lead to multi-periodic non-radial pulsations, and in special cases radial pulsations of the host star (Schuh 2010; Herrero et al 2011). However, only a handful of pulsating exoplanet hosts have been found so far. V391b, for example, has been found orbiting an sdB star through pulsation-timing variations (Silvotti et al. 2007). The first main-sequence star where asteroseismology was applied to exoplanetary research is μ Arae (Bazot et al. 2005). High precision and long-term *Kepler* observations have led to the discovery of several transiting exoplanet host stars which exhibited solar-like oscillations (Davies et al. 2016), whose typical semi-amplitudes are of the order of a few ppm for main-sequence stars (Baudin et al. 2011).

WASP-33 was the first transiting-exoplanet host star exhibiting δ Scuti pulsations, with a semi-amplitude of about 900 ppm (Collier Cameron et al. 2010b; Herrero et al. 2011). One of the harmonics has a frequency 26 times the orbital frequency, suggesting that WASP-33's pulsations might be induced by the planet. A more confident claim for the planet-induced stellar pulsations was made recently for HAT-P-2 system, a possible low-amplitude δ Scuti pulsator with an 87 minutes pulsation period and an amplitude of

40 ppm (de Wit et al. 2017). Its pulsation modes correspond to exact harmonics of the planet's orbital frequency and are thought to be induced by the transient tidal interactions with its massive (8 M_{Jup}), short-period (5.6 d) and highly eccentric ($e = 0.5$) planet (de Wit et al. 2017). Systems such as WASP-33 and HAT-P-2 provide a laboratory to study star–planet interactions. The observations provided by the *K2* mission have led to the discovery of another pulsating transiting exoplanet host star, namely HAT-P-56 which is likely a γ Doradus pulsator (Huang et al. 2015). While the exact asteroseismic analysis approach can vary depending on the class of variability, one can investigate any potential star–planet interactions and derive precise stellar mass, radius and the depth-dependant chemical composition, given the appropriate modelling capabilities (Schuh 2010).

In this paper, we present a detection of starspots in the *K2* light curve of WASP-107, and pulsations in the light curve of WASP-118. We also refine system parameters for both systems, search for transit-timing variations, phase-curve modulations and any additional transiting planets, and provide a measurement of the rotational period for WASP-107.

Simultaneously with our paper, Dai & Winn (2017) have announced an analysis of the same *K2* short-cadence observations of WASP-107. Their results are in a good agreement with ours.

9.3 The *K2* Observations

WASP-107 was observed by *K2* in the 1-min short-cadence observing mode during Campaign 10 between 2016 July 6 and 2016 September 20. The dominant systematics present in the *K2* light curves are the sawtooth-shaped artefacts caused by the drift of the spacecraft. We attempted to correct for the drift artefacts using the same self-flat-fielding (SFF) procedure as described in Močnik et al. (2016a). However, since the drifts of the spacecraft were variable during this observing campaign, we obtained better results using the K2 Systematic Correction pipeline (`K2SC`; Aigrain, Parviainen & Pope 2016), which uses Gaussian processes and break-points to isolate different drift behaviours to overcome the issue of inconsistent drifts. The `K2SC` procedure was designed for the *K2* long-cadence observing mode and had to be modified slightly to accept the short-cadence data. The main modification was to split the input short-cadence light curve into smaller overlapping sections, which were processed individually by `K2SC` and then merged back together using the overlapping sections. However, since the WASP-107 light curve exhibits pronounced modulations, the `K2SC` failed to correct the drift artefacts properly at three different 2-d-long sections centred at BJD 2457624.7, 2457631.8 and 2457638.3. We replaced these sections with the light curve we obtained using the above-mentioned SFF procedure. Using this approach we achieved a median 1-min photometric precision of 260 ppm, compared to 870 ppm before the artefact correction, and 300 ppm using only the SFF procedure. The final drift-corrected light curve of WASP-107 is shown in Fig. 9.1. We used this light curve to study the rotational modulation of the host star in Section 9.7. For all other analyses we used the normalized version of the light curve, which we produced with `PyKE` tool `kepflatten` (Still & Barclay 2012), which divides the measured flux with a low-order polynomial fit with window and step sizes of 3 and 0.3 d, respectively, which effectively removed any low-frequency modulations.

WASP-118 was observed during the *K2* Campaign 8 between 2016 January 4 and 2016 March 23, also in the short-cadence mode. Because the spacecraft's drifts were more consistent during Campaign 8, we produced a slightly better light curve with our SFF procedure than with `K2SC`. The drift-corrected light curve of WASP-118 is shown

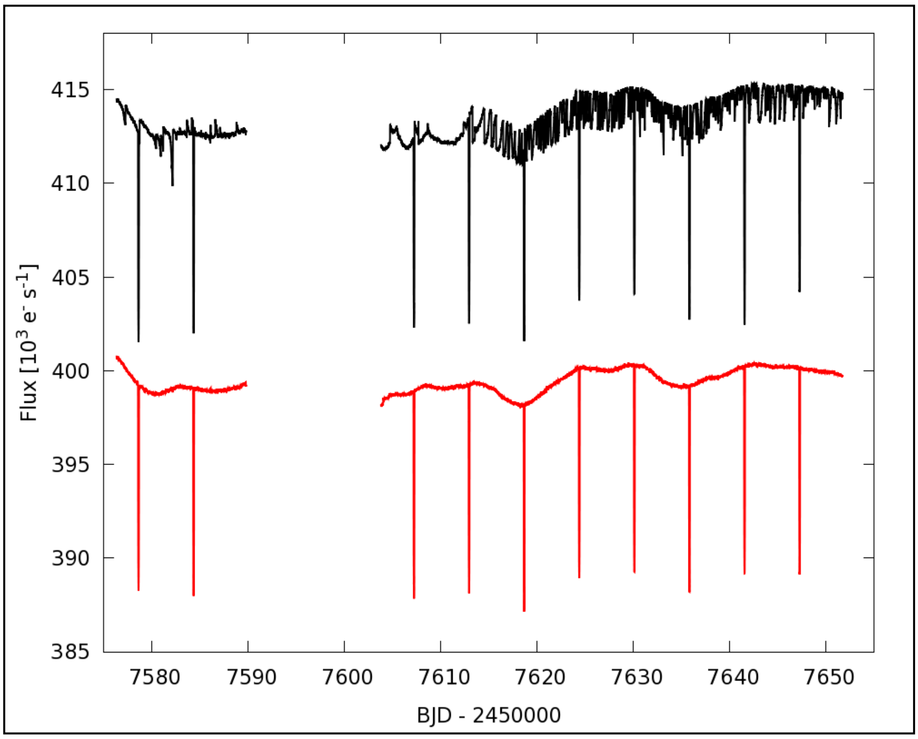

Figure 9.1: The binned light curve of WASP-107 shown before (in black) and after the drift correction (red). A 10-min binning was used to reduce the white noise and to display the drift artefacts more clearly. Note the presence of 10 transits and a rotational modulation. The 14-d data gap in the first half of the observing campaign was caused by a failure of CCD module 4, which temporarily powered off the entire photometer. The corrected light curve is shown with an offset of -14,000 e$^-$ s^{-1} for clarity.

in red in Fig. 9.2. In addition to the transits, the light curve exhibits variability with a ~5-d time-scale. The variability is inconsistent and incoherent, and cannot be interpreted as a rotational modulation with confidence. We produced the normalized version of the light curve in the same way as for WASP-107. The normalized light curve revealed multi-periodic higher-frequency variability with a semi-amplitude of ~200 ppm (see Fig. 9.3). We suggest that this variability is produced by the weakly pulsating host star (see Section 9.8).

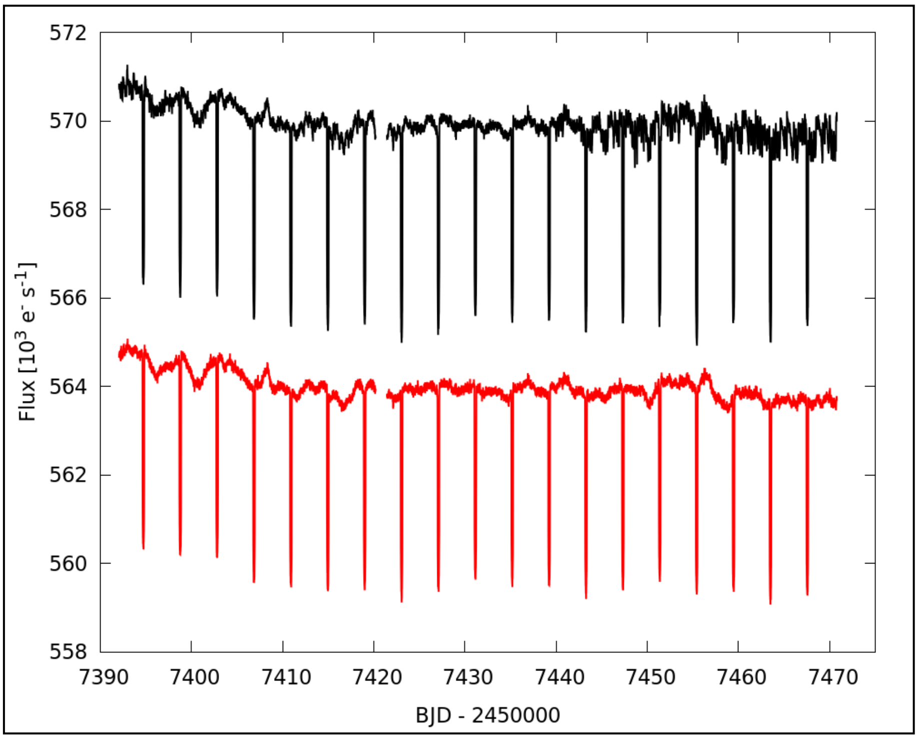

Figure 9.2: The binned light curve of WASP-118 shown before (in black) and after the drift correction (red). As in Fig. 9.1, we applied a 10-min binning to reduce the white noise. 19 transits are visible along with other variability. The corrected light curve is shown with an offset of -6,000 e$^-$ s^{-1}.

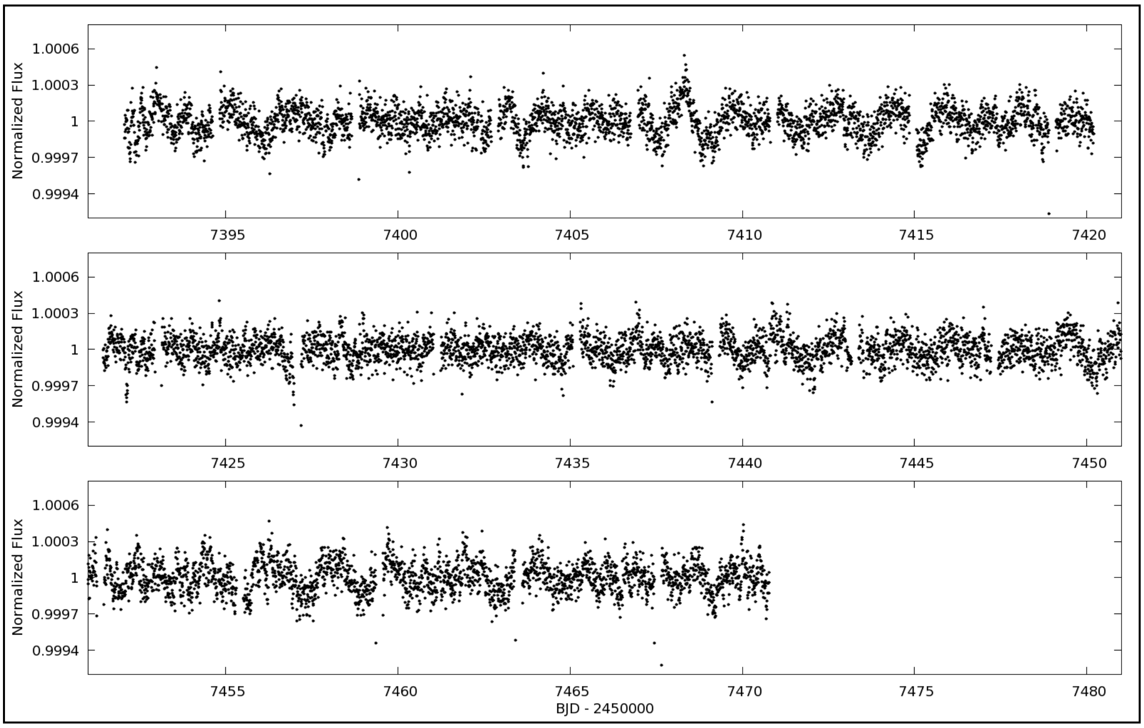

Figure 9.3: Stellar variability of WASP-118 resembling weak γ Doradus pulsations. We show the normalized light curve with 10-min binning.

Because the presence of pulsations in the light curve of WASP-118 could affect the analysis, we used the light curve with embedded pulsations only for the pulsations analysis in Section 9.8. For every other aspect of analysis we produced another light curve in which we removed these higher-frequency, low-amplitude pulsations. This was done by modifying our SFF procedure. Instead of the usual 5-d time-steps, we split the light curve into sections of individual spacecraft drifts before applying the SFF correction. Since the typical 6-h time-scale at which the drifts occur is considerably shorter than the observed pulsation time-scales, our modified SFF procedure effectively removed the pulsations from the light curve, along with any other variabilities at longer time-scales. This produced the light curve with a final median 1-min photometric precision of 210 ppm. We used this version of light curve for every aspect of the analysis, except for the analysis of pulsations in Section 9.8.

9.4 System Parameters

To determine the system parameters we simultaneously analysed the *K2* transit photometry and radial-velocity measurements for both planets using a Markov Chain Monte Carlo (MCMC) code (Collier Cameron et al. 2007; Pollacco et al. 2008; Anderson et al. 2015). We used all the radial-velocity datasets that have been reported in the corresponding discovery papers (Anderson et al. 2017 and Hay et al. 2016), except the HARPS-N in-transit dataset for WASP-118. This dataset was excluded in order to prevent biasing the system parameters owing to a large scatter and underestimated error bars, as pointed out by the authors of the discovery paper. It may be that some of this scatter results from the pulsations that we now report. Limb darkening was accounted for using a four-parameter law, with coefficients calculated for the *Kepler* bandpass and interpolated from the tabulations of Sing (2010).

For the MCMC analysis of WASP-107 we used the normalized light curve, from which we excluded any starspot occultation events (see Section 9.6), because failing to do so may lead to inaccurate system parameter determination, as discussed by Oshagh et al. (2013). Similarly, the presence of pulsations in the light curve of WASP-118 may have affected the precise transit analysis and so we instead used the light curve with pulsations removed.

We first imposed a circular orbit in the main MCMC analysis for both planets. We then estimated the upper limits on eccentricities in a separate MCMC run by allowing the eccentricities to be fitted as a free parameter. To improve the precision of the orbital ephemerides we also ran another MCMC analysis for both systems that included all the available ground-based photometric datasets used in the discovery papers which expanded the observational time-span and reduced the uncertainty on the orbital period by factors of 6.5 for WASP-107 and 2.3 for WASP-118. For these additional photometric datasets, we used limb-darkening coefficients from Claret (2000, 2004), as appropriate for different bandpasses.

The resulting system parameters are given in Table 9.1 and the corresponding transit models are shown in Figs. 9.4 and 9.5.

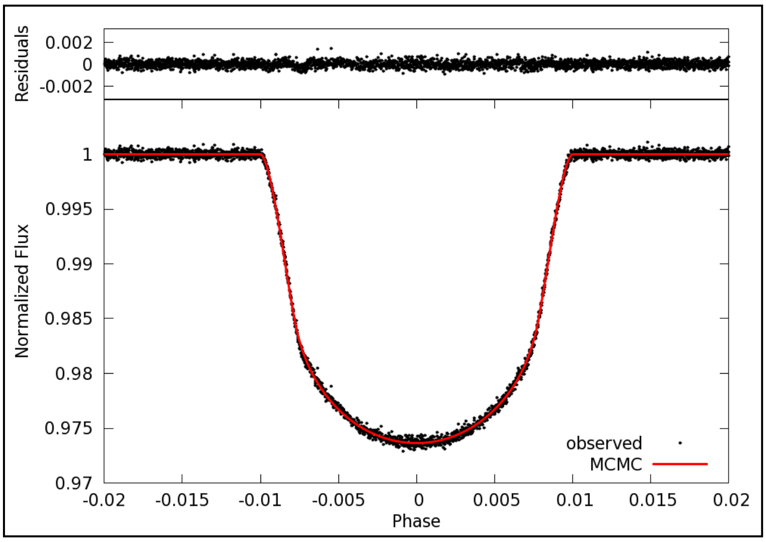

Figure 9.4: Best-fitting MCMC transit model and its residuals for WASP-107.

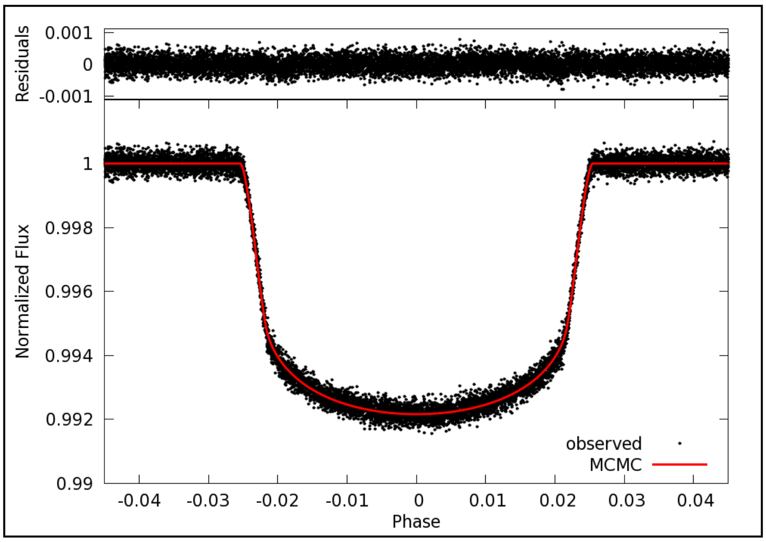

Figure 9.5: Best-fitting MCMC transit model and its residuals for WASP-118.

Table 9.1: MCMC system parameters for WASP-107 and WASP-118.

Parameter	Symbol	WASP-107 value	WASP-118 value	Unit
Transit epoch	t_0	2457584.329746 ± 0.000011	2457423.044825 ± 0.000020	BJD
Orbital period	P	5.72149242 ± 0.00000046	4.0460407 ± 0.0000026	d
Area ratio	$(R_\mathrm{p}/R_*)^2$	0.020910 ± 0.000058	0.006679 ± 0.000010	…
Transit width	t_{14}	0.11411 ± 0.000081	0.20464 ± 0.00010	d
Ingress and egress duration	t_{12}, t_{34}	0.01467 ± 0.00012	0.01610 ± 0.00012	d
Impact parameter	b	0.139 ± 0.024	0.206 ± 0.015	…
Orbital inclination	i	89.560 ± 0.078	88.24 ± 0.14	°
Orbital eccentricity	e	0 (adopted; <0.025 at 2σ)	0 (adopted; <0.028 at 2σ)	…
Orbital separation	a	0.0553 ± 0.0013	0.05450 ± 0.00049	au
Stellar mass	M_*	0.691 ± 0.050	1.319 ± 0.035	$\mathrm{M}_\odot$
Stellar radius	R_*	0.657 ± 0.016	1.754 ± 0.016	$\mathrm{R}_\odot$
Stellar density	ρ_*	2.441 ± 0.023	0.2445 ± 0.0024	$\rho_\odot$
Planet mass	M_p	0.119 ± 0.014	0.52 ± 0.18	M_Jup
Planet radius	R_p	0.924 ± 0.022	1.394 ± 0.013	R_Jup
Planet density	ρ_p	0.152 ± 0.017	0.193 ± 0.066	ρ_Jup
Planet equilibrium temperature[a]	T_p	736 ± 17	1753 ± 34	K
Limb-darkening coefficients	a_1, a_2, a_3, a_4	0.710, –0.773, 1.520, –0.641	0.522, 0.313, –0.071, –0.045	…

Note: [a] Planet equilibrium temperature is based on assumptions of zero Bond albedo and complete heat redistribution.

9.5 No TTV or TDV

Inter-planet gravitational interactions can cause transit-timing variations (TTVs) and transit-duration variations (TDVs) (Algol et al. 2005). The detection of these variations can therefore reveal additional planets in the system. Typical reported TTV amplitudes range from a few seconds and up to several hours with periods of the order of a few days (Mazeh et al. 2013). TDVs are expected to be in phase with the TTVs but at a significantly lower amplitude (Nesvorný et al. 2013).

To search for TTVs and TDVs we ran another MCMC analysis on individual transits for both systems. We again removed the starspot occultation events from the WASP-107 light curve and used the pulsation-free light curve of WASP-118 since the light curve variability could affect the timing accuracy (Oshagh et al. 2013).

Against the hypothesis of equal transit timing spacings and constant transit durations the measured TTVs and TDVs for WASP-107 correspond to χ^2 values of 11.1 and 6.6, respectively, for 10 degrees of freedom. Similarly, for WASP-118 the TTV and TDV χ^2 values are 26.8 and 15.7, respectively, for 19 degrees of freedom. Thus there are no significant TTVs or TDVs. The upper limits for WASP-107 are 20 and 60 s for TTVs and TDVs respectively, for periods shorter than 80 d. For WASP-118 the upper limits are 40 and 100 s. Given the absence of any statistically significant TTV or TDV variations, we can conclude that any additional close-in, massive planets are unlikely in either of the two systems.

9.6 Starspots on WASP-107

In Fig. 9.6, we show the light curve of WASP-107 centred at individual transits after subtracting the best-fitting MCMC transit model from Section 9.4. The residual light curve reveals several starspot occultation events. Each of us has individually examined the residual light curve by eye and marked the events as definite or possible occultations. Here we report occultation events that were marked by at least two colleagues. This gives 5 definite starspot occultation events (marked with dark-red

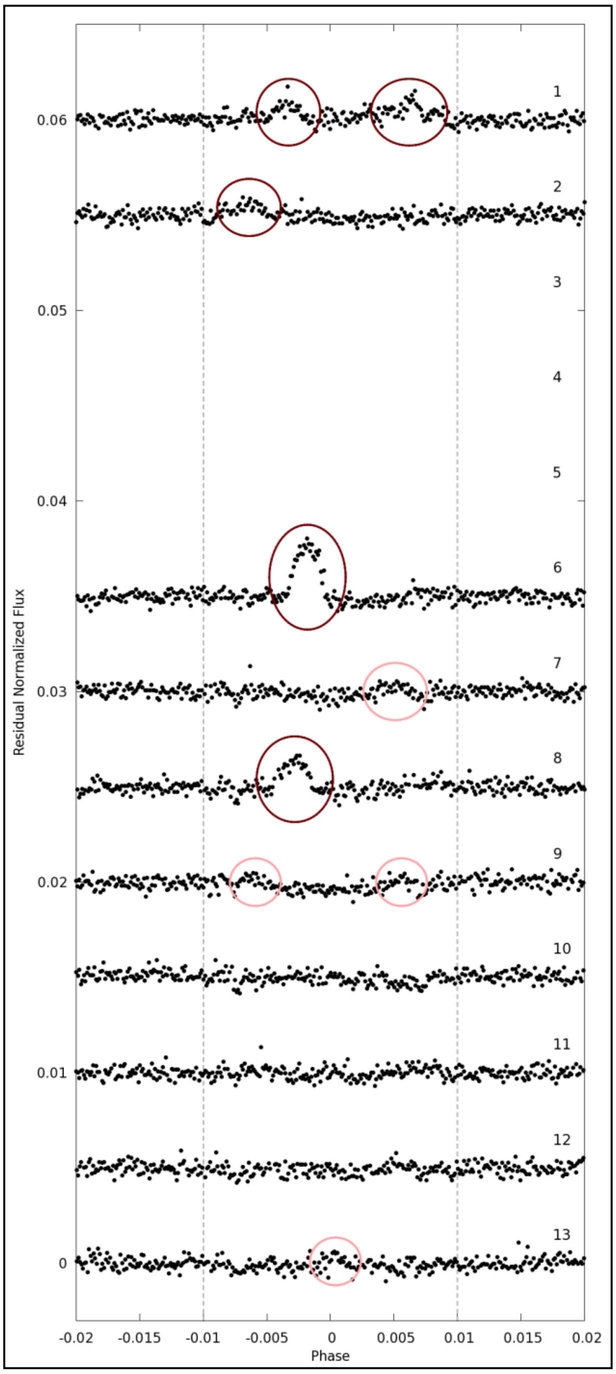

Figure 9.6: Starspot occultations in the model-subtracted light curve of WASP-107. Vertical dashed lines show the extent of the transit. Dark-red ellipses mark definite starspot occultation events and light-red ellipses mark possible starspots. Transits 3–5 were not observed owing to the 14-d data gap.

ellipses in Fig. 9.6) and 4 possible events (marked with light-red ellipses) within the 10 observed transits. Table 9.2 lists all the marked definite and possible occultation events, measured orbital phases at which they occur and the corresponding stellar longitudes which we calculated using the system parameters from Table 9.1. There may well be additional, smaller-amplitude spots present in some of the transits, in addition to those listed.

Table 9.2: Phase and longitude positions of every detected starspot occultation event.

Transit number	Phase	Stellar longitude[a] (°)
1	-0.0033 ± 0.0002	-22.4 ± 1.6
1	0.0062 ± 0.0002	45.0 ± 2.2
2	-0.0064 ± 0.0002	-47.6 ± 2.4
6	-0.0018 ± 0.0002	-12.1 ± 1.4
7	0.0051 ± 0.0002	36.2 ± 1.9
8	-0.0028 ± 0.0002	-18.5 ± 1.5
9	-0.0059 ± 0.0002	-42.9 ± 2.1
9	0.0056 ± 0.0002	40.3 ± 2.0
13	0.0004 ± 0.0002	2.4 ± 1.3

Note: [a] Longitude runs from -90° (first planetary contact), through 0° (central meridian) to 90° (last contact).

Given the stellar rotational period of $17.5 \pm 1.4\,\mathrm{d}$ (see Section 9.7) and the planet's orbital period of $5.72\,\mathrm{d}$ (see Table 9.1), one would expect in an aligned system to see the same starspot being occulted again three transits later, with a longitude shift of $-7^{\circ}{}^{+31}_{-26}$. Occultations one, two or four transits later would be hard to detect, since the phase shifts would be in multiples of 120°, and therefore the spots would either be close to the limb, where they are hard to detect owing to limb darkening, or not on the visible face at all.

There is only one pair of starspot occultations that might be a recurrence. If the occultation event in transit 6 and the first occultation in transit 9 (see Fig. 9.6) were caused by the same starspot, they would imply an orbital period of 18.8 ± 0.2 d.

Although this is compatible with the 17.5 ± 1.4-d rotational period derived from the rotational modulation (see Section 9.6) there are reasons to doubt that the pair was actually caused by the same starspot. Firstly, a starspot from transit 8 does not produce an occultation pair at a similar phase shift in transit 11. Secondly, the starspot lifetimes for main-sequence stars are of the order of days (Bradshaw & Hartigan 2014 and citations therein), which means that in 17 d, the time it takes for the planet to orbit its host star three times, a starspot could disappear.

Overall, we do not find compelling evidence for recurring starspots, which would suggest that the system might be misaligned. However, because of the 17-d time span between recurrences that could be readily observed, we cannot exclude the possibility that it is an aligned system with relatively short starspot lifetimes.

9.7 Rotational Modulation of WASP-107

The light curve of WASP-107 in Fig. 9.1 reveals a low-frequency modulation with a semi-amplitude of about 0.2 per cent. To measure the periodicity of this modulation we removed the planetary transits and calculated a Lomb–Scargle periodogram (see Fig. 9.7). The highest peak in the periodogram and its full width at half maximum correspond to a periodicity of 17.5 ± 1.4 d.

Knowing that the stellar surface harbours starspots (see Section 9.6), we believe that this modulation is caused by the stellar rotation. Using the stellar radius from Table 9.1 and assuming that the rotational axis is orthogonal to the line of sight, the measured rotational modulation period implies a stellar rotational velocity of $1.9 \pm 0.2\,\mathrm{km\,s^{-1}}$. This value agrees with the spectroscopic projected rotational velocity of 2.5 ± 0.8 km $\mathrm{s^{-1}}$ (Anderson et al. 2017). Our rotational modulation period and amplitude also agree well

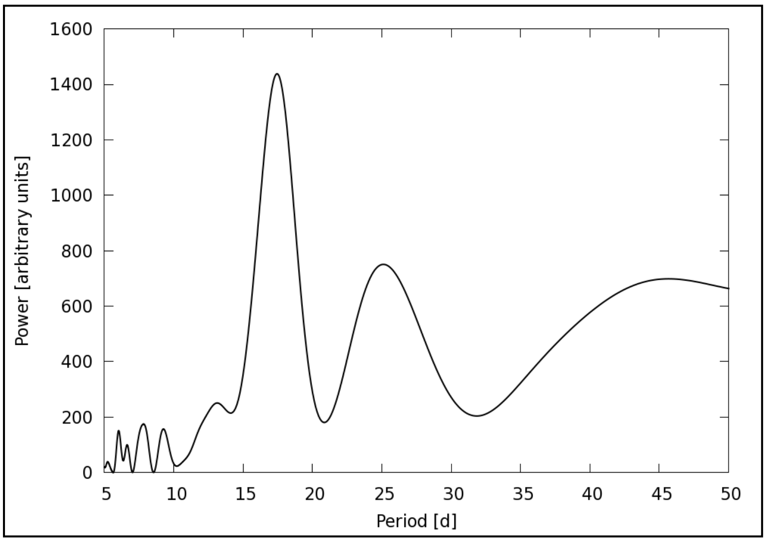

Figure 9.7: Lomb–Scargle periodogram of WASP-107’s rotational modulation. The highest peak implies a rotational period of 17.5 ± 1.4 d.

with the period of 17 ± 1 d and amplitude of 0.4 per cent that were derived from the ground-based photometry and reported in the discovery paper by Anderson et al. (2017).

9.8 Stellar Pulsations of WASP-118

Fig. 9.3 provides a close-up view of the higher-frequency photometric variability in the light curve of WASP-118, after removing incoherent low-frequency modulations. This variability is not correlated with the spacecraft’s drifts, is preserved using four different data-reduction procedures, is not present in the *K2* light curves of other nearby stars, and is not correlated with the orbital phase.

The variability cannot be realistically considered as a rotational modulation because its short 2-d period would require the star to rotate three times faster than the spectroscopically measured projected rotational velocity. This would only be possible if the system were hugely misaligned, in contradiction with the Rossiter–McLaughlin measurements by Hay et al. (2016) who suggested that the system is aligned. The variability is therefore most likely to be weak pulsations of the host star.

The semi-amplitude of the pulsations is ∼200 ppm. The Lomb–Scargle periodogram reveals that the variability is multi-periodic (see Fig. 9.8) with the highest peak at 1.9 d. To check whether the normalization procedure affected the detected pulsations we ran signal injection tests and found that the applied normalization procedure preserves 80 per cent of the variability at the peak pulsation period near 1.9 d.

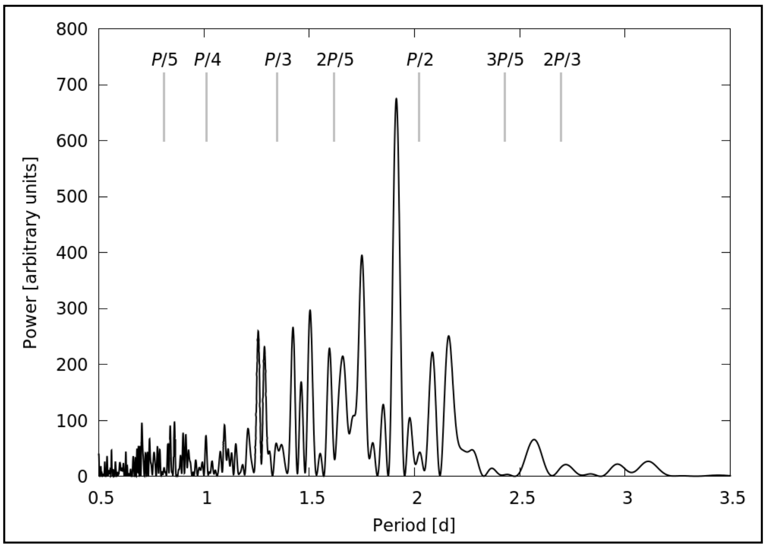

Figure 9.8: The Lomb–Scargle periodogram of WASP-118's higher-frequency variability in the normalized version of the light curve. Several peaks between 1 and 2.5 d indicate that the higher-frequency variability is multi-periodic. Also shown are some of the main harmonics of the planet's orbital period, which demonstrate a mismatch with the pulsation periodicities. Note that we show here only a few of the main harmonics for clarity. The power spectral density for periods longer than 3.5 d is virtually zero because of the applied flattening normalization procedure.

Kaye et al. (1999) introduced a γ Doradus pulsating type for main-sequence and subgiant stars of spectral types A7–F5. γ Doradus stars exhibit non-radial, high-order and low-degree multiperiodic pulsations with periods of 0.4–3 d and amplitudes below 0.1 mag. The pulsation amplitude of such stars may vary during an observing season by as much as a factor of 4.

The spectral type and variability characteristics of WASP-118 suggest that the star is probably a weak, late-type γ Doradus pulsator (see Fig. 9.9).

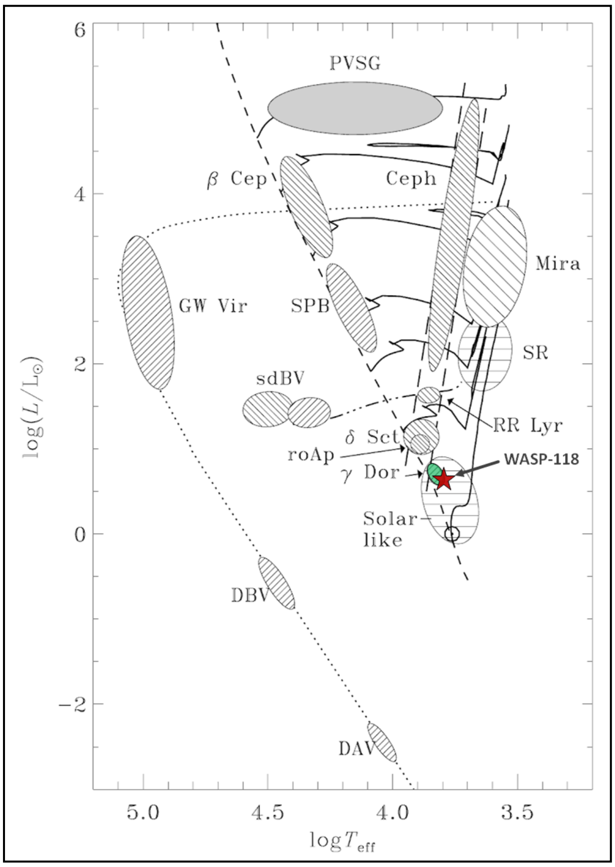

Figure 9.9: Position of WASP-118 (marked with a red star symbol) in the Hertzsprung–Russell diagram showing various pulsation types. The region with *γ* Doradus pulsators is marked green. Adopted from Aerts, Christensen-Dalsgaard & Kurtz (2010).

If the stellar pulsations were induced by the star–planet interactions, we would expect them to appear at exact harmonics of the planet's orbital period, such as in the cases of WASP-33 (Herrero et al. 2011) and HAT-P-2 (de Wit et al. 2017). We found no match when comparing the main harmonics of the WASP-118b's orbital period with the measured pulsations' periodicities (see Fig. 9.8). Despite the lack of any commensurabilities with the main harmonics, we cannot yet reject any complex commensurabilities nor the possibility that the pulsations were induced by the orbiting planet. A detailed follow-up asteroseismic analysis is required to further investigate the star–planet interactions as a possible cause for the observed pulsations in the light curve of WASP-118.

9.9 No Phase-curve Modulations

Phase curves in exoplanet systems consist of three main components at optical wavelengths: (1) ellipsoidal modulation, (2) Doppler beaming, and 3) planetary reflection (e.g. Esteves, De Mooij & Jayawardhana 2013). Additionally, a transiting planet may produce a secondary eclipse, an occultation of the planet by its host star, which blocks the reflected light during the occultation. Therefore, the depth of the secondary eclipse is twice the semi-amplitude of the reflectional modulation.

To produce a phase curve of WASP-107 we had to remove the significant rotational modulation prior to phase-folding the light curve. However, because the ratio between the 5.7-d orbital period and the 17-d rotational modulation is not small enough, this would also remove any phase-curve modulations. For WASP-118 we again removed stellar variability which would again remove any phase-curve modulations. However, in both systems the procedures would not have removed any secondary eclipses present. A non-detection of secondary eclipses in both systems therefore allowed us to estimate conservative upper limits on the secondary-eclipse depths of 100 ppm for WASP-107 and 50 ppm for WASP-118.

Using the system parameters from Table 9.1, the theoretically expected semi-amplitudes of ellipsoidal, Doppler beaming and reflectional modulation for WASP-107 are 0.03, 0.2 and $75 \cdot A_g$ ppm, respectively, where A_g is the planet's geometrical albedo. For WASP-118, the expected semi-amplitudes are 1, 0.7 and $150 \cdot A_g$ ppm. These amplitudes have been calculated using the relations from Mazeh & Faigler (2010). While the expected amplitudes for the ellipsoidal and Doppler beaming modulations are below the *K2* photometric precision, the inflated planetary radii could produce a significant reflectional modulation in both systems. Using the upper limits for secondary eclipse depths and theoretically expected amplitudes for reflectional modulations allows us to constrain the planetary geometric albedos to less than 0.7 for WASP-107b and less than 0.2 for WASP-118b.

9.10 No Additional Transiting Planets

To search for signatures of any additional transiting planets in the normalized light curves of both systems, we first removed the transits of the known transiting planets and then calculated the box-least-square periodograms of any other periodic signals with the `PyKE` tool `kepbls`. The absence of any significant residual signals in the period range 0.5–30 d results in transit-depth upper limits of 130 ppm for any additional transits in the WASP-107 system and 140 ppm in WASP-118.

9.11 Ages of the Host Stars

We estimated the ages of both host stars by comparing the measured stellar densities from Table 9.1 and the published spectroscopic effective temperatures to isochrones computed from the stellar evolution models. This was done with the Bayesian mass and age estimator `BAGEMASS` (Maxted, Serenelli & Southworth 2015a), which uses the `GARSTEC` code (Weiss & Schlattl 2008) to compute the evolution models. The best-fitting stellar evolution tracks provided the age estimates of 8.3 ± 4.3 Gyr for WASP-107 and 2.3 ± 0.5 Gyr for WASP-118.

The rate at which a star rotates acts as another age estimator. Over time, stars lose angular momentum through magnetised stellar winds and gradually slow down (Barnes 2003). Knowing the rotational period of WASP-107 from the detected rotational modulation (see Section 9.7), we estimated the stellar age with the gyrochronological relation by Barnes (2007) to obtain $0.6 \pm 0.2\,\mathrm{Gyr}$.

Our isochronal age estimate for WASP-118 agrees well with the age provided by Hay et al. (2016) who used the same approach but using the system parameters derived only from the ground-based observations.

The age discrepancy between the isochronal and gyrochronological age estimate for WASP-107 is significant. Similar discrepancies have been observed for many other K-type stars hosting transiting exoplanets (e.g. Maxted, Serenelli & Southworth 2015b). It has been suggested that stars hosting massive short-period planets may have been spun-up by the tidal interaction with the planet and thus exhibit a lower gyrochronological age (Maxted, Serenelli & Southworth 2015b). However, the warm-Saturn WASP-107b is not massive enough and does not orbit close enough to its host star to cause a significant tidal spin-up. A more probable reason for the observed age discrepancy in the case of WASP-107 is the radius anomaly, in which late-type stars exhibit larger radii than is predicted by the stellar models (Popper 1997). The radius anomaly is an active research topic driven by the advances in simulating convections in low-mass stars (Ludwig, Caffau & Kučinskas 2008) and incorporating magnetic fields into stellar models (Feiden & Chaboyer 2013). Morales et al. (2010) have demonstrated that the presence of starspots near the poles of low-mass stars could affect the stellar radii and cause the observed radius anomaly. The age discrepancy of magnetically active K-type WASP-107 may therefore be tentatively attributed to starspots.

9.12 Conclusions

The two main results presented in this paper are the direct detection of magnetic activity in the short-cadence *K2* light curve of WASP-107 and the detection of stellar variability of WASP-118.

The magnetic activity of WASP-107 is manifest firstly as a rotational modulation which gives a stellar rotational period of $17.5 \pm 1.4\,\mathrm{d}$. We also detect a total of 5 definite and 4 possible starspot occultation events. With the planet's orbital period being nearly one-third of the rotational period of the star, we might expect to see the same starspot recurring every three transits. Since we found no evidence of recurring starspots, we suggest that the system is misaligned, unless the starspots' lifetimes are shorter than the rotational period of the star.

The multi-periodic variability in the light curve of WASP-118 indicates that the star is likely a low-amplitude γ Doradus pulsator. WASP-118 is a good target for a follow-up asteroseismic analysis in order to obtain more precise stellar parameters and to investigate star–planet interactions as a possible cause for the observed stellar pulsations.

Our refinement of WASP-107 system parameters may also prove beneficial, since the planet's large scale height and the small, bright host star make it is one of the best targets for atmospheric characterization studies (Kreidberg et al. 2018). Furthermore, the planet lies in the transition region between ice and gas giants. Knowing precise system parameters of such planets is crucial for understanding why some ice giants do not become gas giants.

10 WASP-28 and WASP-151

This chapter is based on the paper Močnik, Hellier & Anderson (2017), arXiv:1710.08892, submitted to AJ. CH supervised the research and provided general advice; DRA submitted the *K2* downlink proposal for both targets. Compared to the submitted version of the paper, I implemented some of the referee's comments. I added Figs. 10.3 and 10.4 to demonstrate the brightening events that were likely caused by the passage of Mars through the *K2*'s FOV during Campaign 12. I also added Fig. 10.5 to visualize the passage of an asteroid near WASP-151.

10.1 Abstract

By analysing the short-cadence *K2* photometry from the observing Campaign 12, we refine the system parameters of hot Jupiter WASP-28b and hot Saturn WASP-151b. We report the non-detection and corresponding upper limits for transit-timing and transit-duration variations, starspots, rotational and phase-curve modulations and additional transiting planets. We discuss the cause of several background brightening events detected simultaneously in both planetary systems and conclude that they are likely associated with the passage of Mars across the field of view.

10.2 Introduction

Since the failure of a second reaction wheel, the *Kepler* mission was redesigned to observe fields along the ecliptic and renamed into *K2* (Howell et al. 2014). Its observing strategy minimize the pointing drift by balancing the spacecraft against the solar radiation pressure, which not only allows to restore photometric performances but also enables photometric follow-up observations of exoplanetary systems discovered by the ground-based surveys such as WASP (Pollacco et al. 2006). The *K2* mission has so far observed 10 previously-discovered WASP planetary systems during the first 14 observing campaigns, each with a time-span of around 80 d.

In this paper we present the results from analysing the short-cadence *K2* observations of WASP-28 (Anderson et al. 2015) and WASP-151 (Demangeon et al. 2018), both observed during the Campaign 12. Many close-in planets have been found to possess radii well in excess of the standard planet cooling and contraction model (Leconte et al. 2009). Knowing precise system parameters is crucial for inferring their bulk composition and their dynamical history, and for understanding what causes the observed radius inflation.

The dearth of short-period Neptune-sized planets, also referred to as Neptunian desert, has indicated that hot Jupiters and hot super-Earths might have formed by different mechanisms (e.g. Mazeh, Holczer & Faigler 2016). WASP-151 was found to lie on the upper boundary of Neptunian desert (Demangeon et al. 2018). In this context, it is particularly beneficial to refine parameters for planetary systems that lie close to the Neptunian desert to refine the desert boundaries.

Beside refining the system parameters, we used the *K2* short-cadence data to search for any transit-timing (TTV) and transit-duration variations (TDV), starspot occultations, phase-curve modulations and additional transiting planets. We also provide isochronal age estimates for both systems.

10.3 Targets

WASP-28 is an inflated hot Jupiter, transiting an F8 $V = 12.0$ star with an orbital period of 3.41 d. The planet was discovered by Anderson et al. (2015) using the WASP photometry, two follow-up transit light curves and two sets of radial-velocity measurements obtained by CORALIE (Queloz et al. 2000a) and in-transit HARPS (Mayor et al. 2003) observations. The system was further photometrically followed-up with ground-based telescopes first by Petrucci et al. (2015) who obtained four additional transit light curves and later by Maciejewski et al. (2016) with three additional transits. Both follow-up surveys refined the system parameters and reported the absence of any detectable long-term transit-timing variations.

WASP-151 is an inflated hot Saturn, transiting a G1 $V = 12.9$ star with an orbital period of 4.53 d. The discovery of the planet was recently announced by (Demangeon et al. 2018). Beside WASP photometry, they used five follow-up transit light curves from ground-based telescopes and the raw long-cadence *K2* data from the observing Campaign 12. The two accompanying RV datasets were obtained with SOPHIE (Bouchy et al. 2009) and CORALIE.

10.4 *K2* Observations and Data Reduction

WASP-28 and WASP-151 were both observed by *K2* in the 1-min short-cadence mode during the observing Campaign 12, which ran between 2016 December 15 and 2017 March 4.

The *K2* light curve for WASP-151 has already been presented in the discovery paper (Demangeon et al. 2018), but was generated only from the raw 30-min long-cadence data, which were made publicly available almost immediately after the downlink. The light curves presented in this paper were generated using the short-cadence target pixel files, provided following the official data release. Not only does the increased cadence of observations enable transit modelling with higher precision, but officially released data also undergo Science Operations Center's calibration pipeline (Quintana et al. 2010). This level-1 pipeline corrects the data in several ways, such as removing the readout smearing effect, subtracting modelled background, assigning quality flags, etc. Compared to the raw data, the level-1 pipelined target pixel files are used to generate more reliable light curves with lower white noise and to exclude data points which might be affected by cosmic rays or instrumental effects.

We downloaded the short-cadence target pixel files for both systems from the Mikulski Archive for Space Telescopes. We performed the photometric extraction with the `PyKE kepextract` command (Still & Barclay 2012) using a fixed aperture mask of 32 and 30 pixels, centred at WASP-28 and WASP-151, respectively. The pixel mask sizes were chosen by trial and error to extract as much stellar flux as possible while covering fewest background pixels.

The dominant systematic error present in the *K2* data is the sawtooth-shaped flux variations, caused by the pointing drift of the spacecraft and consequent pointing corrections by the thruster firings on roughly 6-h time-scales. To correct for these drift artefacts, we used the modified *K2* Systematic Correction pipeline `K2SC`; Aigrain, Parviainnen & Pope 2016), optimised for the *K2* short-cadence data (Močnik et al. 2017). With the removal of drift artefacts, we improved the 1-min photometric precision from 1505 to 370 ppm for WASP-28 and from 1317 to 641 ppm for WASP-151.

We did not find any evidence of rotational modulations or any other low-frequency periodic light-curve modulations in the drift-corrected version of the light curves. Any other non-periodic low-frequency light-curve modulations were removed with the `PyKE kepflatten` command, which divides the light curve with the mean of the best-fit second-order polynomials with step and window sizes of 0.3 and 3 days, respectively, 2σ clipping and 5 iterations.

We present in Figs. 10.1 and 10.2 the normalized and flattened light curves before and after the drift correction, with all the brightening events from Table 10.1 removed (see Section 10.4.1). The 5.3-d loss of data collection around BJD 2457790 occurred during the safe mode, which was likely triggered by the spacecraft's software reset.

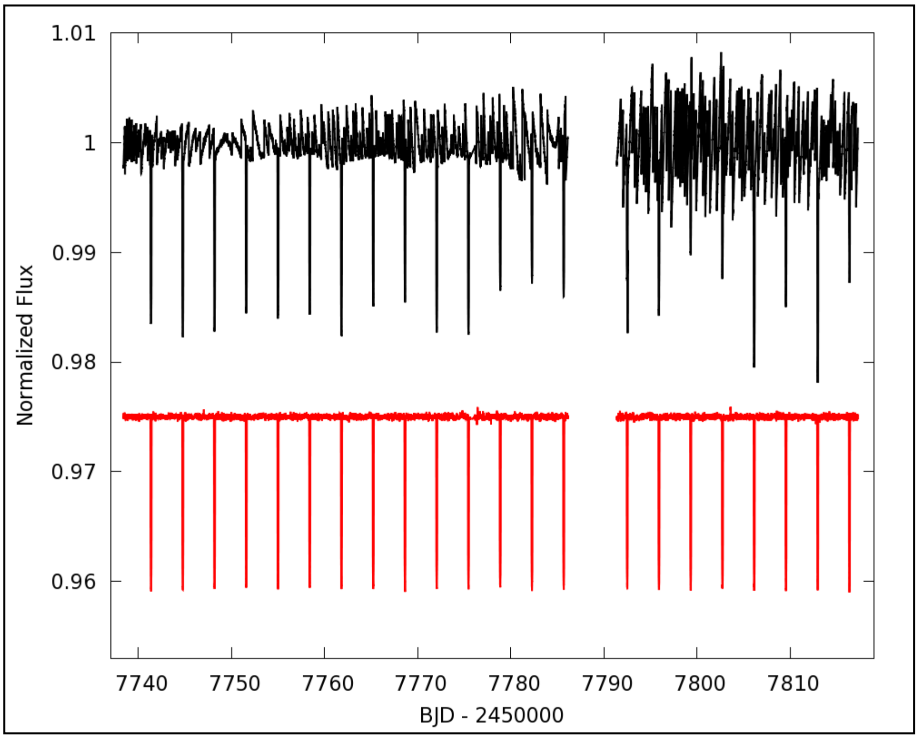

Figure 10.1: Normalized light curve of WASP-28 before (shown in black) and after the drift correction (red), with brightening events and any low-frequency non-periodic modulations removed. The drift-corrected light curve is offset by -0.025 for clarity. The observing Campaign 12 covers a total of 22 transits of WASP-28b.

WASP-28 was also observed during the Engineering Campaign between 2014 February 4 and 13. We reduced these data in a similar way as for Campaign 12. Because the time stamps in the target pixel files from the Engineering Campaign are not corrected to the solar system barycenter, we applied the barycentric time correction ourselves with an IDL tool `UTC2BJD` (Eastman, Siverd & Gaudi 2010). We used the

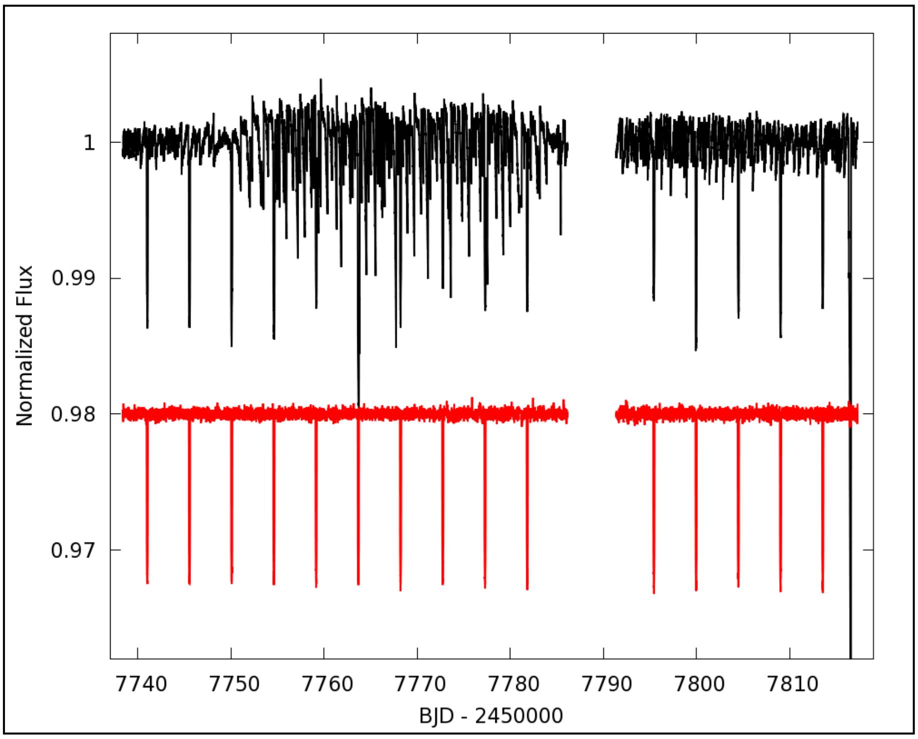

Figure 10.2: Normalized light curve of WASP-151 before (shown in black) and after the drift correction (red), with brightening events and any low-frequency non-periodic modulations removed. The drift-corrected light curve is offset by -0.02 for clarity. The observing Campaign 12 covers a total of 15 transits of WASP-151b.

reduced light curve for visual inspection of any potentially interesting events, refinement of the ephemeris, and for the analysis of long-term TTVs. However, we avoided using the light curve for any other aspect of the analysis because the target pixel files from the Engineering Campaign were not fully calibrated by the level-1 pipeline and thus exhibit higher noise and uncertainty which might skew the results.

10.4.1 Background Brightening Events

Upon visual inspection of the corrected light curves we found five episodes where the intensity of the background increased (these are listed in Table 10.1 and shown in Fig. 10.3).

Two uniform background brightening events occurred at BJD 2457770 and 2457774 in both light curves, each lasting for ∼1 h. A similar event affected the WASP-

28 background at BJD 2457775 while a 4.8-h-long event affected WASP-151 at BJD 2457781. The longest brightening event lasted nearly 0.5 d, and was non-uniform and seen only in WASP-28 light curve around BJD 2457776.

We believe that these background brightening events may have been caused by the passage of Mars through the field of view. This is surprising because both targets are located far from the areas on the *K2* detector affected by the direct, spilled or ghost images of Mars (WASP-28 was located on CCD module 9-1 and WASP-151 on module 15-4; see Fig. 10.4). All the uniform brightenings coincide within one hour with the centre of Mars entering or leaving certain CCD modules (see Table 10.1 and Fig. 10.3). Although this might be a coincidence, it suggests that the uniform brightening events may have been caused by some sort of instrumental effect such as a video crosstalk. We did not find any correlation between Martian CCD module crossings and the longest and non-uniform background brightening event in WASP-28, which may instead have been caused by a (reflected) ghost image of Mars.

Table 10.1: Light-curve brightening events (listed are the first and last BJD of when the event is taking place, relative peak brightening and a suspected cause for the event).

BJD – 2457700	$F_{\max}$	Cause
WASP-28		
70.022	0.0053	Mars enters module 24-3
74.312	0.0045	Mars leaves module 24-2
75.181	0.0053	Mars enters module 19-3
75.650	0.0097	ghost image of Mars (?)
WASP-151		
70.006	0.0081	Mars enters module 24-3
74.303	0.0070	Mars leaves module 24-2
80.940	0.0063	Mars enters module 13-1
99.483	0.0075	asteroid flyby

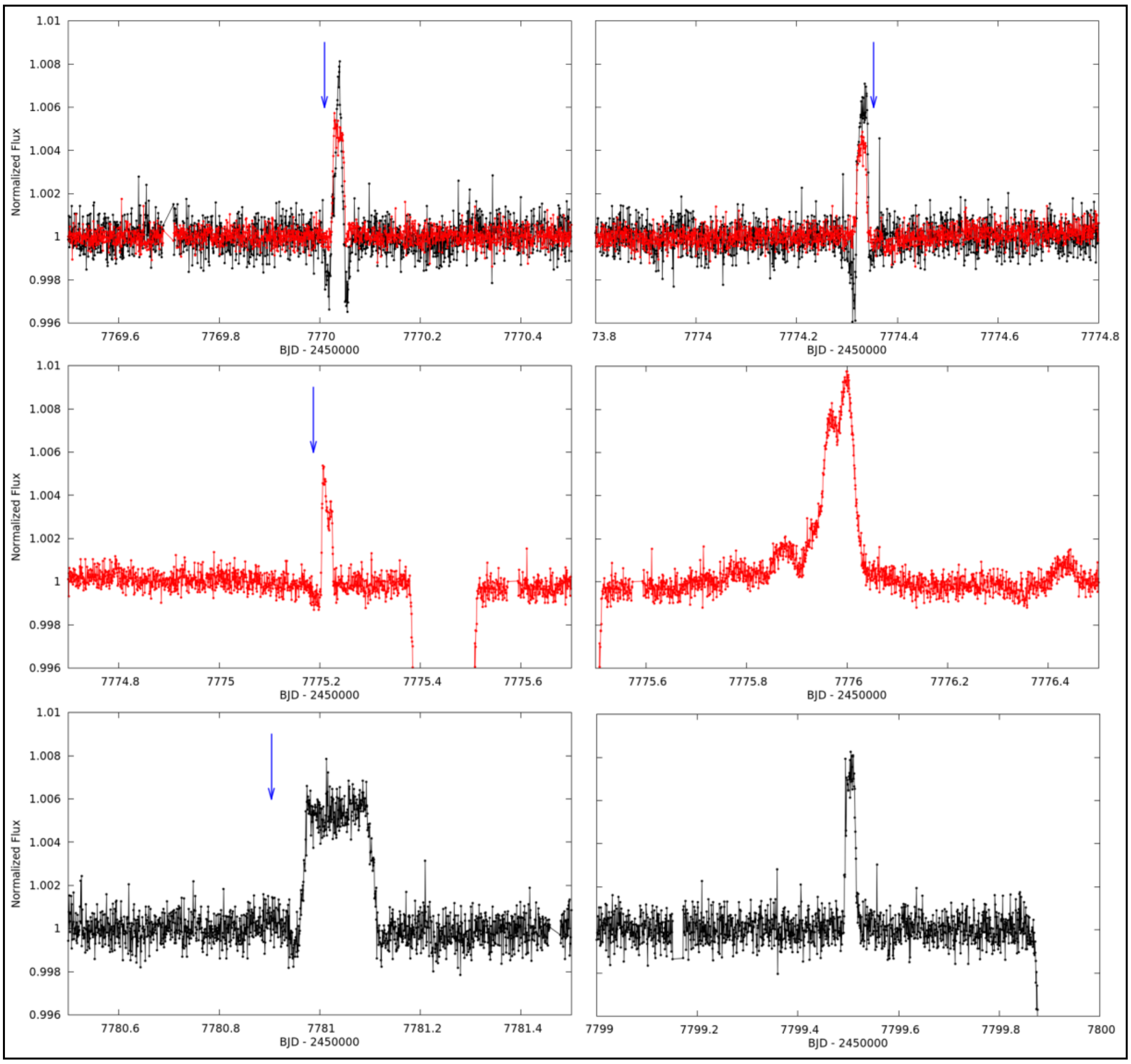

Figure 10.3: Brightening events in the normalized light curves of WASP-28 (red) and WASP-151 (black). Axis range is kept fixed in all images. Blue arrows represent timings of when the centre of Mars enters or leaves certain CCD modules (see Table 10.1 and Fig. 10.4).

In addition to the above background brightening events, the light curve of WASP-151 exhibited another brightening event centred at BJD 2457799. Inspection of individual images revealed that this was caused by an asteroid flyby, whose path crossed the centre of WASP-151 (see Fig. 10.5).

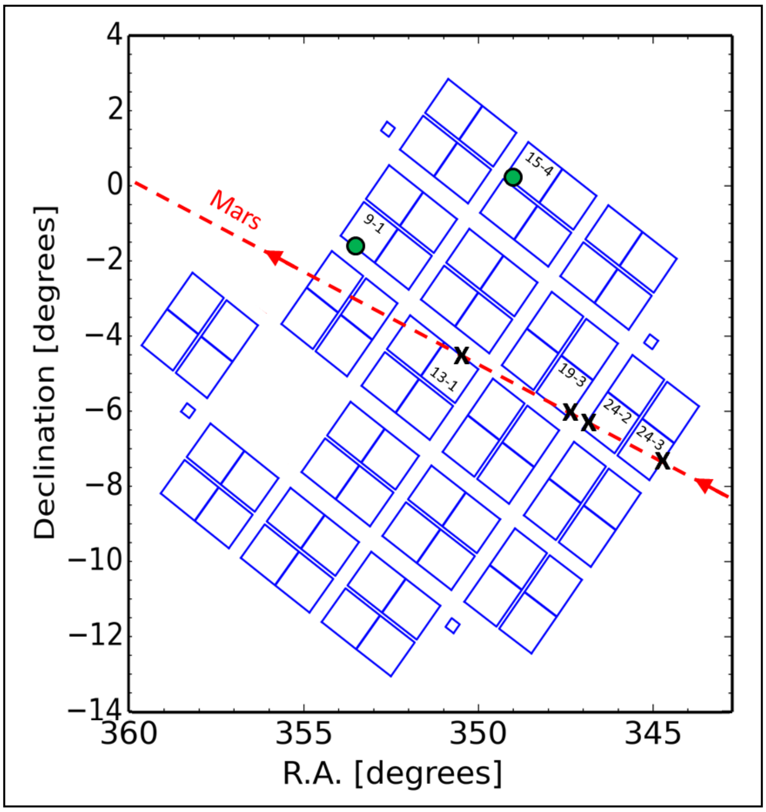

Figure 10.4: The passage of Mars through the *K2*'s FOV during Campaign 12. Marked with green circles are the positions of WASP-28 and WASP-151 in the output channels 9-1 and 15-4, respectively. Black crosses are the entries and departures of Mars to certain CCD modules, which appear to be the cause of the background brightening events (marked with arrows in Fig. 10.3). The base of the plot was produced with `K2onSilicon` tool[15].

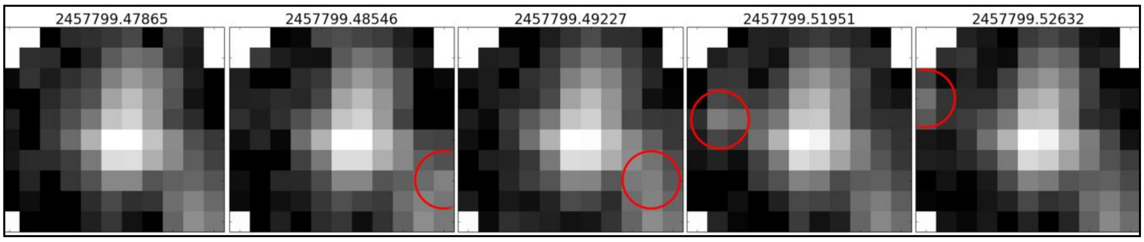

Figure 10.5: WASP-151 asteroid flyby, causing the brightening event at BJD 2457799.

All the light-curve brightening events combined affected a total of 0.66 d (0.9%) and 0.37 d (0.5%) of WASP-28 and WASP-151 observations, respectively. We removed the brightening events from the light curves to avoid any potential impact on the following analysis.

---

[15] https://keplerscience.arc.nasa.gov/software.html#k2fov

10.5 System Parameters

We obtained the system parameters with the simultaneous Markov chain Monte Carlo (MCMC) analysis of the transit light curves and radial velocity (RV) measurements. The MCMC procedure is presented in Collier Cameron et al. (2007) and Pollacco et al. (2008). The photometric input for each system was the normalized and flattened *K2* Campaign 12 light curve from Section 10.4. The spectroscopic inputs were the publicly available RV measurements published in the corresponding discovery papers, Anderson et al. (2015) for WASP-28 and Demangeon et al. (2018) for WASP-151. Because the HARPS RV dataset for WASP-28 covered the planetary transit, we were able to fit also the Rossiter–McLaughlin effect. The four-parameter limb-darkening coefficients were interpolated through the tables of Sing (2010).

The stellar masses were determined with the Bayesian mass and age estimator `BAGEMASS` (Maxted, Serenelli & Southworth 2015a). `BAGEMASS` compares the stellar density and stellar spectroscopic effective temperature to stellar evolution models, and applies the MCMC procedure to find best-fitting isochrone. The stellar densities were derived from the transit observables with the initial MCMC system parameter analyses and the stellar effective temperatures were taken from the corresponding discovery papers. The stellar masses obtained with the `BAGEMASS` procedure were fed back into the main MCMC system parameter analysis as a two-step iteration process. The derived isochronal age estimates are given along with the system parameters in Tables 10.2 and 10.3.

Because the close-in planets are expected to circularise on very short time-scales, we imposed circular orbits in the main MCMC run as suggested by Anderson et al. (2012). In a consequent MCMC run, we then set the eccentricity to be fitted as a free parameter. This allowed us to estimate the eccentricity upper limit from the resulting MCMC chain.

To improve the ephemeris, we performed another MCMC analysis, which employed all the publicly available photometric datasets from the discovery and photometric follow-up papers. We also included the WASP-28 light curve from the *K2* Engineering Campaign from Section 10.4. As there were several different telescopes with different filters used to obtain these datasets, we sourced the additional limb-darkening coefficients from the appropriate tables of Claret et al. (2000) and Claret (2004). This approach increased the observations baseline from 79 days to 8.3 years for WASP-28 and 8.6 years for WASP-151, which improved the orbital period precision by factors of 10.8 and 3.4, respectively.

The final MCMC transit models are shown in Figs. 10.6 and 10.7, plotted over the measured *K2* Campaign 12 light curves of WASP-28 and WASP-151, respectively. The resulting system parameters are given in Tables 10.2 and 10.3, which also serve as a comparison to the previous studies. We find system parameters largely in agreement with the previous results, generally with significantly improved precision.

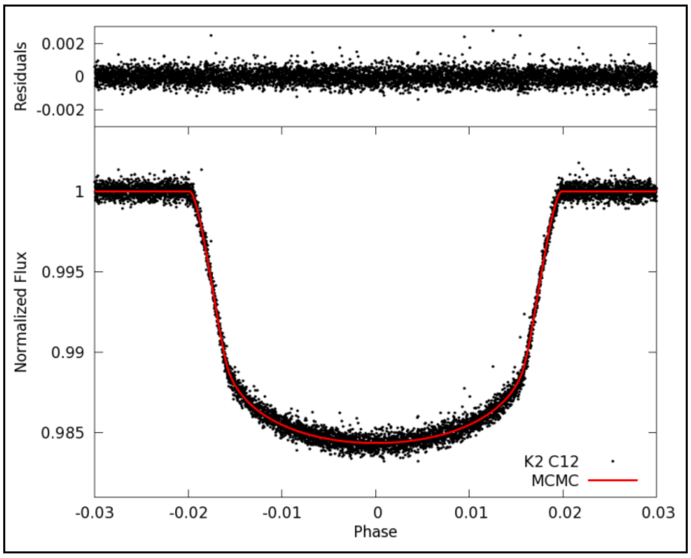

Figure 10.6: Phase-folded light curve of WASP-28 from Campaign 12. The best-fitting MCMC transit model is shown in red. The residuals are shown in the upper panel.

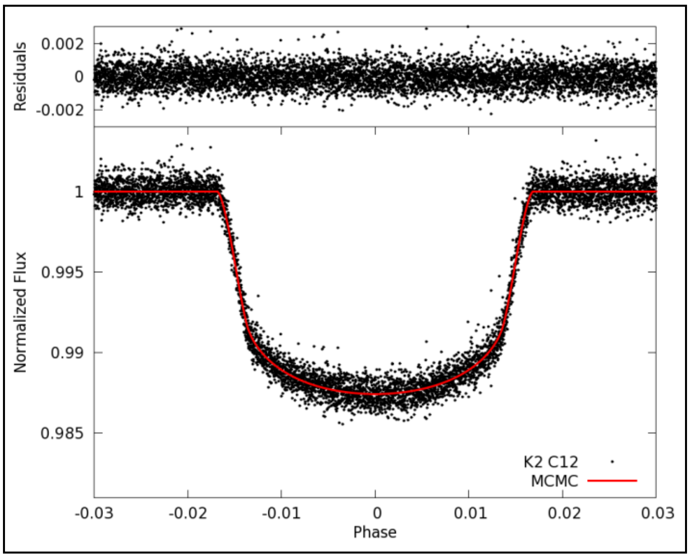

Figure 10.7: Phase-folded light curve of WASP-151 from Campaign 12. The figure layout and axes scales are the same as in Fig. 10.6.

Table 10.2: MCMC system parameters for WASP-28.

Parameter (unit)[a]	this work value	Anderson et al. (2015) value	Petrucci et al. (2015) value	Maciejewski et al. (2016) value
t_0 (BJD)	2457642.502126 ± 0.000014	2455290.40519 ± 0.00031	2455290.40551 ± 0.00102	2455290.40595 ± 0.00046
P (d)	3.40883495 ± 0.00000015	3.4088300 ± 0.000006	3.408840 ± 0.000003	3.4088387 ± 0.0000016
$(R_p/R_*)^2$	0.013396 ± 0.000026	0.01300 ± 0.00027	...	...
t_{14} (d)	0.13495 ± 0.000083	0.1349 ± 0.0010	...	...
t_{12}, t_{34} (d)	0.01469 ± 0.00010	0.01441 ± 0.00070	...	...
b	0.228 ± 0.013	0.21 ± 0.10	...	$0.25^{+0.14}_{-0.25}$
i (°)	88.514 ± 0.090	88.61 ± 0.67	...	$88.35^{+1.65}_{-0.92}$
e	0 (adopted) (<0.075 at 2σ)	0 (adopted) (<0.14 at 2σ)	...	...
a (au)	0.0442 ± 0.0010	0.04469 ± 0.00076	0.0445 ± 0.0004	0.04464 ± 0.00073
M_* ($M_\odot$)	0.993 ± 0.067	1.021 ± 0.050	1.011 ± 0.028	...
R_* ($R_\odot$)	1.083 ± 0.025	1.094 ± 0.031	1.123 ± 0.052	$1.083^{+0.020}_{-0.044}$
ρ_* ($\rho_\odot$)	0.7815 ± 0.0068	0.784 ± 0.058	...	$0.804^{+0.018}_{-0.089}$
M_p (M_{Jup})	0.889 ± 0.058	0.907 ± 0.043	0.899 ± 0.035	0.927 ± 0.049
R_p (R_{Jup})	1.219 ± 0.028	1.213 ± 0.042	1.354 ± 0.166	$1.250^{+0.029}_{-0.053}$
ρ_p (ρ_{Jup})	0.491 ± 0.027	0.508 ± 0.047	...	$0.474^{+0.041}_{-0.065}$
T_p (K)[b]	1456 ± 40	1468 ± 37	1473 ± 30	...
λ (°)[c]	6 ± 17	8 ± 18	...	...
τ_{iso} (Gyr)	5.5 ± 2.6	5^{+3}_{-2}	4.2 ± 1.0	...
a_1, a_2	0.386, 0.602	...	...	...
a_3, a_4	-0.356, 0.057	...	...	...

Notes: [a] Meanings of system parameter symbols are given in Table 10.3.

[b] Planet equilibrium temperature is based on assumptions of zero Bond albedo and complete heat redistribution.

[c] Projected spin-orbit misalignment angle was fitted with Hirano model (Hirano et al. 2011) for the Rossiter–McLaughlin effect.

Table 10.3: MCMC system parameters for WASP-151.

Parameter	Symbol	this work value	Demangeon et al. (2018) value	Unit
Transit epoch	t_0	2457763.676241 ± 0.000040	$2457741.0081^{+0.0001}_{-0.0002}$	BJD
Orbital period	P	4.5334775 ± 0.0000023	4.533471 ± 0.000004	d
Area ratio	$(R_\mathrm{p}/R_*)^2$	0.010664 ± 0.000048	$0.01021^{+0.00010}_{-0.00007}$	...
Transit width	t_{14}	0.15268 ± 0.00023	$0.15250^{+0.00083}_{-0.00042}$	d
Ingress and egress duration	t_{12}, t_{34}	0.01564 ± 0.00027	...	d
Impact parameter	b	0.304 ± 0.023	...	...
Orbital inclination	i	88.25 ± 0.14	89.2 ± 0.6	°
Orbital eccentricity	e	0 (adopted; <0.15 at 2σ)	<0.003	...
Orbital separation	a	0.0550 ± 0.00084	0.055 ± 0.001	au
Stellar mass	M_*	1.081 ± 0.049	1.077 ± 0.081	$M_\odot$
Stellar radius	R_*	1.181 ± 0.020	1.14 ± 0.03	$R_\odot$
Stellar density	ρ_*	0.656 ± 0.014	$0.72^{+0.02}_{-0.04}$	$\rho_\odot$
Planet mass	M_p	0.316 ± 0.031	$0.31^{+0.04}_{-0.03}$	M_Jup
Planet radius	R_p	1.187 ± 0.021	1.13 ± 0.03	R_Jup
Planet density	ρ_p	0.189 ± 0.018	$0.22^{+0.03}_{-0.02}$	ρ_Jup
Planet equilibrium temperature[a]	T_p	1312 ± 16	1290^{+20}_{-10}	K
Isochronal age	τ_iso	5.5 ± 1.3	5.1 ± 1.3	Gyr
Limb-darkening coefficients	a_1, a_2, a_3, a_4	0.599, -0.116	...	...

Note: [a] Planet equilibrium temperature is based on assumptions of zero Bond albedo and complete heat redistribution.

10.6 No TTV or TDV

The long-term deviations of transit timings from the expected ephemeris can be caused by an orbital decay due to the tidal interactions between a transiting planet and its host star (e.g. Murgas et al. 2014), whereas periodic TTVs are indicative of the gravitational influence of additional planetary or stellar companions in the system (e.g. Holman & Murray 2005). Similarly, the gravitational interactions can also produce TDVs, albeit at lower amplitudes (e.g. Nesvorný et al. 2013).

To measure the TTVs and TDVs from the *K2* datasets, we ran an MCMC analysis of system parameters as described in Section 10.5 on each transit individually by keeping all MCMC jump parameters fixed at values listed in Tables 10.2 and 10.3, except the transit epoch and period. Then, we subtracted the individual transit timings and durations from the ephemeris given in Tables 10.2 and 10.3.

Petrucci et al. (2015) and Maciejewski et al. (2016) have both provided a long-term TTV upper limit for WASP-28 of about 3 min. Adding our TTV measurements from the *K2* data confirms the absence of long-term TTVs, with a weighted standard deviation of 23 s and a χ^2_{red} of 1.32. We show in Fig. 10.8 our TTVs from Campaign 12 and Engineering Campaign (listed in Table 10.4), along with the measurements from the previous surveys. One TTV measurement around BJD 2456510 from Petrucci et al. (2015) and one *K2* measurement at BJD 2457810 have been excluded as >3σ outliers.

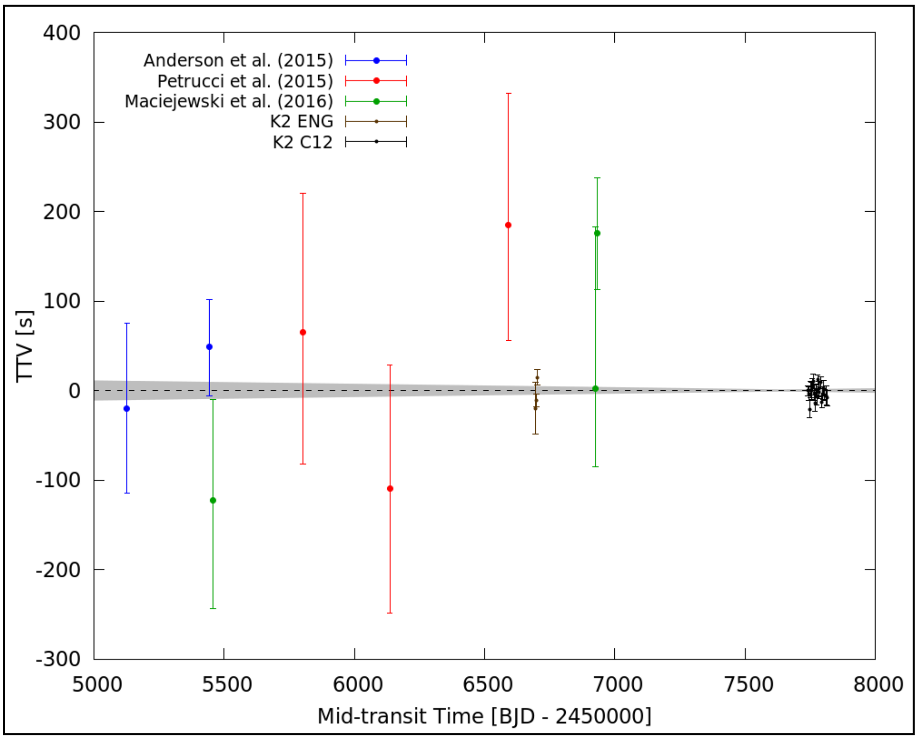

Figure 10.8: The long-term transit-timing stability of WASP-28. The data points clustered around BJD 2456700 and 2457800 correspond to the data taken during the *K2* Engineering Campaign and Campaign 12, respectively. Lighter-coloured data points are TTVs from the various ground-based follow up surveys, sourced from a collective table published in Maciejewski et al. (2016). The gray area is the 1-σ ephemeris uncertainty as given in Table 10.2.

Table 10.4: Transit timings of WASP-28b and WASP-151b from the *K2* Engineering Campaign and Campaign 12.

BJD – 2450000	
WASP-28b	WASP-151b
6694.845773 ± 0.000335	7741.00902 ± 0.00019
6698.254710 ± 0.000080	7745.54231 ± 0.00025
6701.663845 ± 0.000102	7750.07617 ± 0.00016
7741.358331 ± 0.000065	7754.60937 ± 0.00021
7744.767126 ± 0.000085	7759.14284 ± 0.00017
7748.175763 ± 0.000108	7763.67619 ± 0.00020
7751.584844 ± 0.000105	7768.20995 ± 0.00016
7754.993674 ± 0.000111	7772.74295 ± 0.00023
7758.402583 ± 0.000081	7777.27675 ± 0.00018
7761.811468 ± 0.000092	7781.81004 ± 0.00021
7765.220151 ± 0.000098	7795.41069 ± 0.00023
7768.628849 ± 0.000103	7799.94422 ± 0.00020
7772.037865 ± 0.000072	7804.47761 ± 0.00021
7775.446607 ± 0.000103	7809.01089 ± 0.00023
7778.855658 ± 0.000065	7813.54409 ± 0.00015
7782.264378 ± 0.000100	
7785.673165 ± 0.000073	
7792.490961 ± 0.000077	
7795.899545 ± 0.000078	
7799.308482 ± 0.000075	
7802.717405 ± 0.000085	
7806.126141 ± 0.000067	
7809.535271 ± 0.000076	
7812.943799 ± 0.000118	
7816.352606 ± 0.000103	

We also do not find any statistically significant short-term periodicities or drifts in the TTV or TDV measurements during the Campaign 12 data alone in either of the two planetary systems. With the hypothesis of linear transit timings, the χ^2_{red} for TTVs were 1.14 for WASP-28 and 1.52 for WASP-151, with 2-σ semi-amplitude upper limits of 16 s and 33 s for periods shorter than 80 d. For TDV, the assumption of constant transit durations yields the χ^2_{red} values of 0.54 for WASP-28 and 1.07 for WASP-151, with corresponding semi-amplitude upper limits of 31 s and 90 s. The non-detections of periodic TTVs or TDVs render the existence of any non-transiting close-in massive planets highly unlikely.

WASP-28 will be observed again during the Campaign 19 if the spacecraft's propellant lasts long enough. Adding to the two existing *K2* observations, this will result in one of the best constraints on the multi-year period change of any hot Jupiter.

10.7 No Starspots

If a planet occults a starspot it produces a short in-transit brightening event (e.g. Silva et al. 2003). Recurring starspot occultation events can be used to derive a stellar rotational period and a constraint on the spin-orbit misalignment angle. Even the non-recurring occultations can in some configurations constrain the misalignment angle if the transit chord passes the active stellar latitudes at only certain transit phases, such as in the case of a misaligned HAT-P-11 system (Sanchis-Ojeda & Winn 2011).

Močnik et al. (2016a) have demonstrated that the detection of starspot occultation events is possible with two-wheeled *K2* observations, as revealed by the detection of several recurring starspot occultations in the *K2* light curve of an aligned WASP-85 system.

To search for occultation events in the *K2* light curves of WASP-28 and WASP-151 we subtracted the best fitting MCMC transit models and carefully visually examined the residual transit light curves for in-transit occultation "bumps". We found no occultation events with amplitudes above conservative upper limits of 750 and 1000 ppm, for WASP-28 and WASP-151, respectively.

The non-detection of occultation events is consistent with the spectral types of F8 for WASP-28 and G1 for WASP-151, and is in agreement with the absence of any detectable rotational modulation in both systems.

10.8 No Phase-curve Modulations

In addition to the transit, the orbit of a planet around its host star can produce a reflectional and thermal modulation, Doppler beaming, ellipsoidal modulation, and secondary eclipse (e.g. Esteves, De Mooij & Jayawardhana 2013). Because a secondary eclipse is a result of a temporarily-blocked reflectional and thermal modulation, its depth is greater or equal to the reflectional modulation's amplitude. However, the planet's thermal emission is expected to be weak in the optical wavelengths of the *K2* telescope (Shporer et al. 2017).

To look for such effects we first removed any low-frequency non-periodic variabilities using the `kepflatten` tool with window and step sizes of 3 and 0.3 days, for WASP-28, and 5 and 1 day, for WASP-151, respectively. The window and step sizes were chosen as the best compromise between the efficiency of removing the unwanted non-periodic variability and retaining as much phase-curve modulations signal as possible. Next, we phase-folded the flattened and normalized light curves and binned the phase curves to 200 bins.

We found no phase-curve modulations, and conservatively estimate the semi-amplitude upper limits to be 80 and 90 ppm, for WASP-28 and WASP-151, respectively. These upper limits take into account the possible partial removal of the phase-curve signal by the light-curve flattening procedure, which we estimated by signal-injection and recovery tests. However, we are able to provide tighter semi-amplitude upper limits for the reflectional modulations from the absence of secondary eclipses, because the light-curve flattening procedure did not affect phase-curve signals at such short $\sim$3-hour-long time-scales. These are 40 ppm for WASP-28 and 80 ppm for WASP-151.

Using the system parameters from Section 10.5, the theoretically expected semi-amplitudes for reflectional modulation, Doppler beaming and ellipsoidal modulations are $166 \cdot A_g$ ppm, 1.6 ppm and 1.2 ppm, respectively for WASP-28, where A_g is the planet's geometric albedo (see the equations of Mazeh & Faigler 2010). For WASP-151 the predicted semi-amplitudes are $88 \cdot A_g$ ppm, 0.5 ppm and 0.3 ppm. We can see that the non-detections of Doppler beamings and ellipsoidal modulations are not surprising, given their small predicted semi-amplitudes. On the other hand, the non-detection of secondary eclipses in WASP-28 system suggests that the planet's albedo is smaller than 0.24. For WASP-151 the planet's albedo remains almost unconstrained with an upper limit of around 0.9.

10.9 No Additional Transiting Planets

To search for additional transiting planets, we first removed the transits of the known planet in each of the two light curves by replacing the transits' normalized and flattened flux with unity. We then used `PyKE`'s `kepbls` tool, which calculates a box-least-square periodogram as formulated by Kovács, Zucker & Mazeh (2002). The periodograms did not reveal any significant periodicity peaks in the period range between 0.5 and 30 d with transit depths upper limits of 160 ppm for WASP-28 and 220 ppm for WASP-151.

10.10 Conclusions

We analysed the short-cadence light curves of WASP-28 and WASP-151 which have been observed by the *K2* during Campaign 12. This work significantly refines the system parameters compared to the previous studies, owing to the short cadence and high photometric precision of the drift-corrected *K2* photometry. We did not detect any

TTVs, TDVs, starspots, rotational modulations, phase-curve modulations or any additional transiting planets. Instead, we provide tight upper limits.

We observed several episodes where the *K2* background level is brighter than expected. We associated these with the passage of Mars through the *K2*'s field of view during the Campaign 12, although both targets were positioned on the detector far from any of the areas where the contamination by Martian light was expected. Instead, we think that the brightenings might be caused by some instrumental effect such as a video cross talk induced by the presence of Mars in the field. This might also be affecting other Campaign 12 datasets.

11 K2-140

This short chapter is based on the research note Močnik, Hellier & Anderson (2018), RNAAS, 2, 22. CH contributed to this research by pointing out the availability of WASP data and providing the general advice; DRA retrieved the periodogram file from the WASP data archive.

11.1 Ephemeris Refinement

K2-140b (EPIC 228735255b) is a weakly inflated hot Jupiter discovered by Giles et al. (2018). The discovery photometry was comprised of the *K2* (Howell et al. 2014) long-cadence observations from Campaign 10b, which ran between 2016 July 13 and 2016 September 20, and of one partial-transit dataset from 2017 March 18 obtained by the 1-m telescope of the Las Cumbres Observatory telescope network in South Africa (LCO; Brown et al. 2013). Their photometric datasets cover a baseline of 8.2 months, which led to the determination of the orbital period of $6.569300^{+0.000017}_{-0.000020}$ days with an epoch of BJD 2457588.28380 ± 0.00014 (Giles et al. 2018).

The field containing K2-140 had previously been observed by the WASP-South station of the WASP survey (Wide Angle Search for Planets) between 2008 June and 2010 June. For a detailed description of the WASP telescopes, observing strategy, data reduction, candidate identification, and selection procedures, see Pollacco et al. (2006, 2008) and Collier Cameron et al. (2007).

K2-140 was flagged in 2012 by search routines looking for transit candidates in the WASP data, but it was not considered a reliable enough detection for follow-up observations. With a magnitude of $V = 12.5$ K2-140 is at the faint end of the WASP survey, and with a transit period of 6.57 days (fairly long for hot Jupiters) fewer transits get covered. Further, there is another star of comparable brightness on the edge of the WASP photometric extraction aperture, which degrades the photometry of K2-140. Nevertheless, the periodogram of WASP data recovers the correct transit period (see Fig. 11.1). The WASP transit features cover the time period from BJD 2454914 to 2455348 and produce a transit mid-point of 2455151.1052 ± 0.0084.

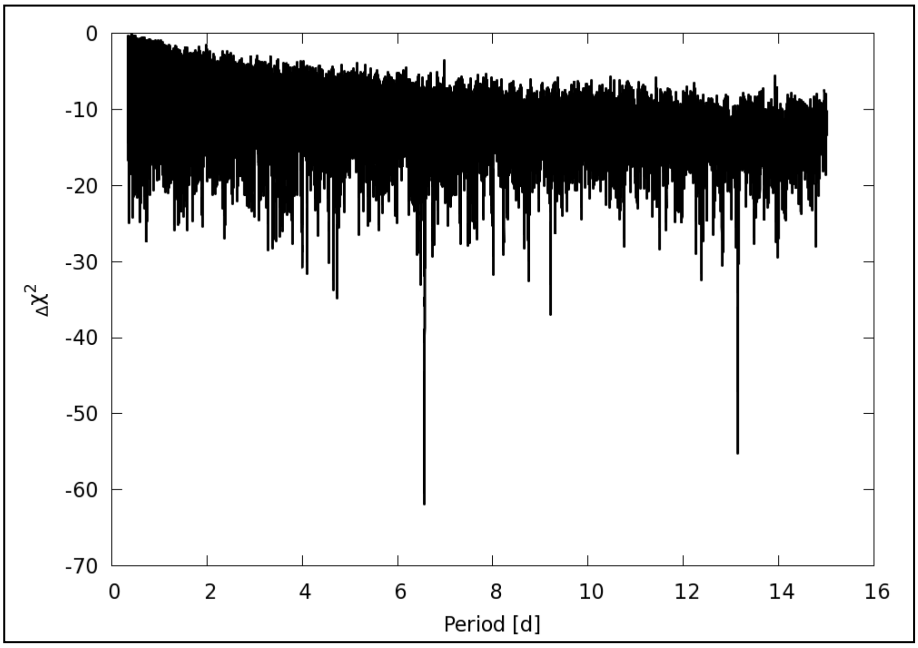

Figure 11.1: Box-least-square periodogram of the WASP light curve. The two peaks at 6.6 and 13.1 days correspond to the orbital period and its second multiple, respectively. The periodogram was calculated using the method of Collier Cameron et al. (2006).

In this research note we present a refined period and epoch of K2-140b, by extending the photometric baseline from 8 months to 8 years following the inclusion of the WASP light curve. To refine the ephemeris, we ran a simultaneous Markov chain Monte Carlo (MCMC) analysis of our WASP transit photometry and all the photometric and radial-velocity datasets provided by the discovery paper. The MCMC code is presented in Collier Cameron et al. (2007) and further described in Pollacco et al.

(2008) and Anderson et al. (2015). We sourced the limb-darkening parameters from Sing (2010), Claret (2000), and Claret (2004) as appropriate for different filters.

The resulting period and epoch from the best-fitting MCMC transit model were 6.569228 ± 0.000010 days and BJD $2457621.13089 \pm 0.00010$, respectively. The refined period is 3.6σ shorter and has a 45% smaller uncertainty than the period reported in Giles et al. (2018). The improved accuracy, resulting from the longer photometric baseline, will be useful for planning future transit observations of this system.

This research note demonstrates the potential for refining transit ephemerides with archived WASP light curves even for planets that were not selected for follow-up directly from the WASP data. The upcoming *Transiting Exoplanet Survey Satellite* (*TESS*; Ricker et al. 2015) in particular is expected to find many planets whose transits might have been detected also by WASP, which will allow better orbital-period determinations.

12 WASP-104

This chapter is based on the accepted paper Močnik, Hellier & Southworth (2018), arXiv:1804.05334, which will be published in AJ. Contributions from the co-authors were: CH supervised the research and provided general advice; JS helped interpreting low-frequency photometric modulations by calculating the false alarm probabilities. Compared to the accepted version of the paper, I expanded Fig. 12.5 with additional panels showing phase-curve models with fewer components.

12.1 Abstract

By analysing the *K2* short-cadence data from Campaign 14 we detect phase-curve modulation in the light curve of the hot-Jupiter host star WASP-104. The ellipsoidal modulation is detected with high significance and in agreement with theoretical expectations, while Doppler beaming and reflection modulations are detected tentatively. We show that the visual geometric albedo is lower than 0.03 at 95% confidence, making it one of the least-reflective planets found to date. The light curve also exhibits a rotational modulation, implying a stellar rotational period likely to be near 23 or 46 days. In addition, we refine the system parameters and place tight upper limits for transit timing and duration variations, starspot occultation events, and additional transiting planets.

12.2 Introduction

Planetary phase curves consist of four components: (1) reflection of starlight from the surface of the orbiting planet (Jenkins & Doyle 2003); (2) the planet's thermal emission (Charbonneau et al. 2005); (3) Doppler beaming caused by the orbital motion of the host star (Loeb & Gaudi 2003); and (4) ellipsoidal modulation caused by the rotation of the host star which is gravitationally distorted into an ellipsoid by the planet (Pfahl, Arras & Paxton 2008). Additionally, transiting planets also produce secondary eclipses whenever their reflected and emitted light is blocked by the occulting star (e.g. Angerhausen, DeLarme & Morse 2015). Typical amplitudes of the individual phase-curve modulation components in planetary systems reported so far are of the order of a few tens of parts per million (ppm) at optical wavelengths (e.g. Esteves, De Mooij & Jayawardhana 2013). Detection of phase-curve modulations can reveal any non-transiting planets (e.g. Millholland & Laughlin 2017), can provide an independent determination of planet-to-star mass ratio, and enable a basic insight into the planetary atmospheric or surface characteristics such as the planetary albedo, day-night temperature contrast and the location offset of the hottest region from the sub-stellar point (e.g. Shporer (2017) and citations therein).

Theoretical atmospheric models suggest that cloud-free hot Jupiters have low geometric albedos at visual wavelengths due to strong and broad absorption lines of atomic Na and K (e.g. Rowe et al. 2008). Heng & Demory (2013) have shown that there is no clear trend between the geometric albedo and the incident stellar flux and suggested that the correlation is hindered by the opacity effects in the planetary atmospheres, such as condensates or clouds, and atmospheric circulation. Expanding the sample of planets with known albedos to a wider variety of planetary systems and at different wavelengths is important for better understanding the underlying reflection mechanisms.

The *K2* spacecraft (Howell et al. 2014) provides the community with high-precision long- (30 min) and short-cadence (1 min) photometry with nearly-continuous ~80-day observing campaigns. This makes *K2* well suited for the search of phase-curve modulations in visual wavelengths.

We present the analysis of the *K2* short-cadence observations of WASP-104 (Smith et al. 2014). Beside the detection of individual phase-curve modulation components, we also detect the rotational modulation, refine planetary system parameters, search for starspot occultation events, additional transiting planets, and transit-timing (TTVs) and transit-duration variations (TDVs).

WASP-104b is a transiting hot Jupiter in a 1.76-day circular orbit around a $V = 11.1$ G8 main-sequence star (Smith et al. 2014). The planet has a mass of $1.3\,M_{\mathrm{Jup}}$ and a radius of $1.1\,R_{\mathrm{Jup}}$. Unlike many other hot Jupiters, WASP-104b is not inflated. Smith et al. (2014) also reported a non-detection of rotational modulation with an upper limit of 4 mmag at 95% confidence.

12.3 *K2* Observations and Data Reduction

WASP-104 was observed by *K2* during the observing Campaign 14, which covered a time-span of 80 days between 2017 June 1 and 2017 August 19. We downloaded the short-cadence target pixel file from the Mikulski Archive for Space Telescopes (MAST) and performed a data reduction procedure as described in Močnik et al. (2016a) with `PyRAF` tools for *Kepler* (`PyKE`; Still & Barclay 2012), optimized for short-cadence data.

We first defined a fixed and circular photometric extraction mask of 37 pixels, centered near the mean position of the target. The optimal mask size was chosen by trial and error as the best compromise between capturing as much starlight as possible and fewest possible background pixels. Choosing the mask too small resulted in larger residual systematics in the final reduced light curve and choosing the mask too large yielded higher white noise. Once the mask was defined, we extracted the light curve by summing the recorded flux values for each pixel within the extraction mask for every image in the target pixel file. The background was already subtracted as part of the Science Operations Center's calibration pipeline (Quintana et al. 2010).

The main systematic errors present in the *K2* light curves are the sawtooth-like artefacts caused by the pointing drift of the spacecraft. To correct for these artefacts we first removed any low-frequency variability by dividing the observed flux with the mean of the overlapping second-order polynomials with a 3-day window size, 0.3-day step size and a 3-σ rejection threshold. After the flattening, we performed a self-flat-fielding (SFF) procedure presented in Močnik et al. (2016a). In short, we used the Gaussian convolution to find a correlation between the measured flattened flux and the arclength of the spacecraft's drift. The SFF correction was split in 5-day time windows, outliers masked as 4-σ outliers, and the width of the Gaussian kernel was chosen as 50 data points. All parameters were chosen based on trial and error to minimize the artefact residuals. We also masked planetary transits with a phase width of 0.045 to improve the rejection of data points for obtaining the SFF correlation near the beginning of ingress and end of egress. To remove the drift artefacts, we divided the flattened and normalized flux values with the measured correlation for each data point. This procedure removed virtually every trace of drift artefacts (see Fig. 12.1) and improved the median 1-min photometric precision from 362 ppm before the SFF correction to 326 ppm after the correction. For comparison, the theoretical uncertainty propagation for similarly bright stars through the data processing pipeline of the *Kepler* mission was ~290 ppm (Koch et al. 2010). The applied SFF procedure was highly effective firstly because the direction of spacecraft drifts was more consistent than on average in other observing campaigns, and secondly, because WASP-104 was placed in the central CCD module where the contribution of the spacecraft rotation to drift artefacts is smallest. Finally, we reintroduced the low-frequency modulations by multiplying the SFF-corrected flattened and normalized light curve with the same function as we used to flatten the light curve prior to SFF procedure. After rejecting the quality-flagged data points, such as thruster firing or cosmic ray events, we retained 113,127 of the original 117,030 data points present in the target pixel file. Fig. 12.1 shows the binned, fluxed light curve before and after the SFF correction.

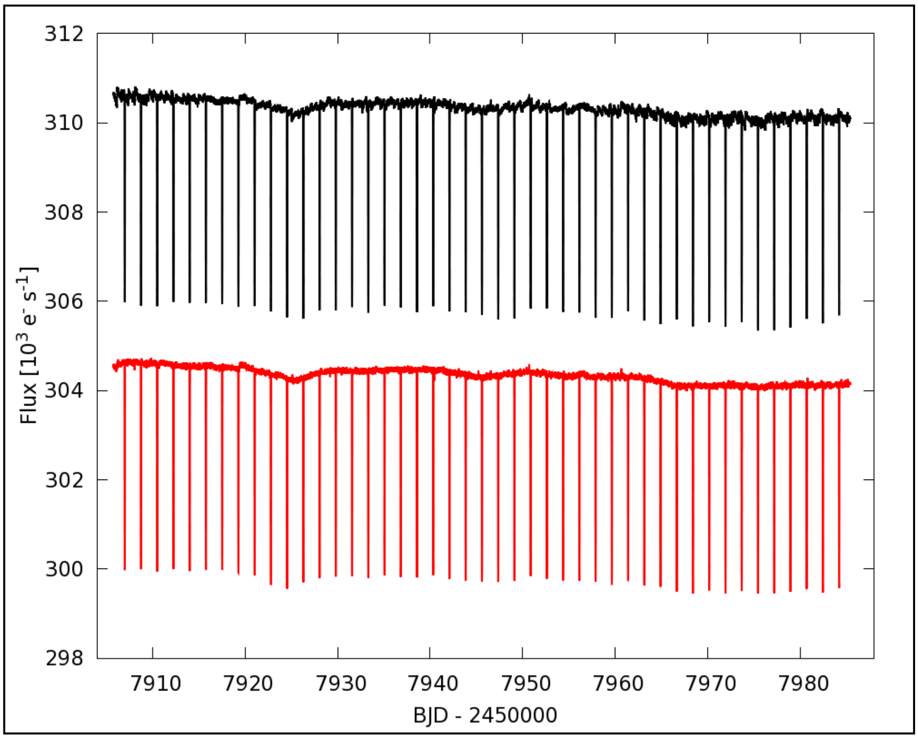

Figure 12.1: Light curve of WASP-104 before (shown in black) and after the drift correction (red). Both light curves are shown with 10-min binning and contain 45 transits. The drift-corrected light curve is offset by -6000 e$^-$ s^{-1} for clarity.

The corrected light curve in Fig. 12.1 reveals not only the hot Jupiter's transits but also indicates the presence of a stellar rotational modulation (see Section 12.6) and a dropping trend in brightness. The latter is seen in the *K2* light curves of each of the 8 stars within 5 arcmin distance from WASP-104. This suggests that the gradual dimming is not astrophysical, and is possibly caused by the imperfect modelling of the background brightness by the Science Operations Center's calibration pipeline.

We used the flattened and normalized light curve for all aspects of the analysis presented in this paper, except for the rotational modulation analysis in Section 12.6 where we used the fluxed version of the light curve.

12.4 Refinement of System Parameters

We used the Markov chain Monte Carlo (MCMC) procedure presented in Collier Cameron et al. (2007), Pollacco et al. (2008) and Anderson et al. (2015) to obtain the planetary and stellar parameters. With this MCMC procedure we simultaneously analysed the flattened, normalized *K2* transit light curve and the radial velocity (RV) measurements provided by the discovery paper (Smith et al. 2014), namely 10 and 11 out-of-transit RV measurements from CORALIE (Queloz et al. 2000a) and SOPHIE (Bouchy et al. 2009), respectively. The stellar limb darkening was accounted for by interpolating through the tables of four-parameter limb-darkening coefficients that were calculated by Sing (2010) for the *K2* bandpass.

After the initial MCMC run, we used the best-fitting transit parameters along with the spectroscopic stellar effective temperature 5450 ± 130 K and metallicity $+0.32 \pm 0.09$ given in the discovery paper as inputs to estimate the stellar mass and age with the `BAGEMASS` tool (Maxted, Serenelli & Southworth 2015a). We used this refined stellar mass estimate in consecutive MCMC runs and noted that the derived system parameters converged already after one such iteration.

Using equation (1) of Jackson, Greenberg & Barnes (2008) and adopting their best-fitting stellar and planetary tidal dissipation parameters of $10^{5.5}$ and $10^{6.5}$, respectively, we estimated the circularization time-scale of WASP-104b as 68 Myr. Due to this very short circularization time-scale, we imposed a fixed circular orbit in the main MCMC analysis and estimated the eccentricity upper limit in a separate MCMC run where the eccentricity was fitted as a free orbital parameter.

To refine the transit ephemeris, we performed another MCMC run with all the available additional transit photometry from the discovery paper (Smith et al. 2014). Beside the *K2* light curve presented in this paper, we included the discovery WASP photometry (Pollacco et al. 2006), four transit light curves obtained by TRAPPIST (Jehin et al. 2011) and two light curves by the Euler Telescope (Lendl et al. 2012). To avoid any potential bias in this analysis, we corrected the WASP photometry for the diluted signal of the approximately equally bright star located 29 arcsec to the north. Other light curves, including the *K2*, were not affected as the photometric extraction masks were significantly smaller. Due to the different filters used to obtain the additional light curves, we sourced the four-parameter limb-darkening coefficients for appropriate filters from Claret (2000, 2004). Adding the much-higher photometric precision *K2* light curve to the datasets used by Smith et al. (2014) extended the photometric baseline of transits from 4.1 to 8.4 years and reduced the uncertainty of the orbital period by a factor of 19.

We show in Fig. 12.2 the *K2* transit light curve and the best-fitting transit model. The planetary system parameters given in Table 12.1 agree within 2σ and generally have smaller uncertainties than the values presented in Smith et al. (2014).

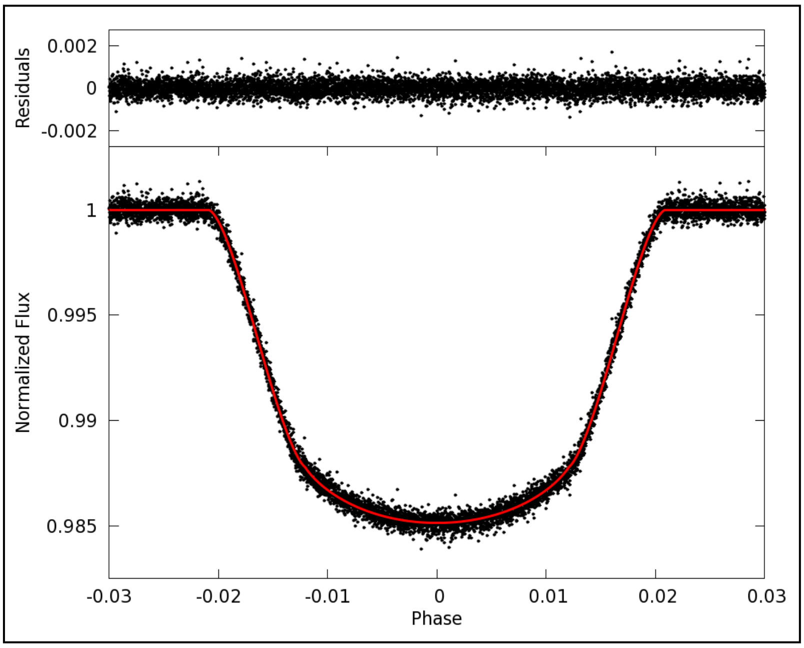

Figure 12.2: Phase-folded *K2* light curve of WASP-104. The red line is the best-fitting MCMC transit model. Shown in the upper panel are the residuals from the transit model.

Table 12.1: MCMC system parameters for WASP-104 and WASP-104b.

Parameter	Symbol	Value	Unit
Transit epoch	t_0	2457935.0702321 ± 0.0000086	$\mathrm{BJD_{TDB}}$
Orbital period	P	1.75540636 ± 0.00000014	d
Area ratio	$(R_\mathrm{p}/R_*)^2$	0.014641 ± 0.000020	...
Transit width	t_{14}	0.072827 ± 0.000046	d
Ingress and egress duration	t_{12}, t_{34}	0.015364 ± 0.000079	d
Impact parameter	b	0.7278 ± 0.0016	...
Orbital inclination	i	83.612 ± 0.026	°
Orbital eccentricity	e	0 (adopted; <0.030 at 2σ)	...
Orbital separation	a	0.0286 ± 0.00047	au
Stellar mass	M_*	1.011 ± 0.050	$\mathrm{M_\odot}$
Stellar radius	R_*	0.940 ± 0.016	$\mathrm{R_\odot}$
Stellar density	ρ_*	1.2178 ± 0.0070	$\rho_\odot$
Stellar surface gravity	$\log g_*$	4.4963 ± 0.0074	cgs
Planet mass	M_p	1.311 ± 0.053	M_J
Planet radius	R_p	1.106 ± 0.019	R_J
Planet density	ρ_p	0.969 ± 0.028	ρ_J
Planet surface gravity	$\log g_\mathrm{p}$	3.390 ± 0.010	cgs
Planet equilibrium temperature[a]	T_p	1507 ± 39	K
Isochronal age estimate	τ_iso	3.5 ± 2.4	Gyr
Limb-darkening coefficients	a_1, a_2, a_3, a_4	0.693, -0.426, 0.991, -0.486	...

Note: [a] Planet equilibrium temperature is based on assumptions of zero Bond albedo and complete heat redistribution.

12.5 No TTV or TDV

The time intervals between successive transits and their durations are always the same for an unperturbed planet. However, the transiting planet can exchange energy and angular momentum with a third body. This gravitational interaction causes short-term oscillations of semi-major axes and eccentricities, which may result in measurable TTVs (e.g. Holman et al. 2010) or TDVs (e.g. Nesvorný et al. 2013). Largest variation amplitudes are expected for planets near low-order resonance orbits with perturbing objects (Lithwick, Xie & Wu 2012). The detection of such variations allows the determination of orbital periods and masses of additional objects in planetary systems (Holman & Murray 2005).

We measured the TTVs and TDVs of WASP-104b by modelling each transit in the short-cadence *K2* light curve individually and subtracting the measured individual transit timings and durations from the best-fitting ephemeris given in Table 12.1. The MCMC procedure of transit modelling was similar to that in Section 12.4, except that we fitted only the transit timings and durations while keeping other observables fixed at their best-fitting values from Table 12.1. Under an assumption of white noise distribution around zero, we calculated the χ^2 values as

$$\chi^2 = \sum_{i=1}^{45} \frac{(O_i - \langle O \rangle)^2}{(\Delta O_i)^2} \quad , \tag{12.1}$$

where i is the transit number, O_i is observed TTV or TDV of the i^{th} transit, $\langle O \rangle$ is the mean of the observed TTVs or TDVs and ΔO_i is the TTV or TDV uncertainty of the i^{th} transit. We obtain χ^2_{TTV} = 57.4 and χ^2_{TDV} = 30.3, for 44 degrees of freedom. Thus, we do not detect any statistically significant periodic signals in either TTVs nor TDVs. We place the semi-amplitude upper limits at 20 s and 47 s for TTVs and TDVs, respectively, for periods shorter than 80 days. The upper limits were determined as three times the weighted standard deviations. As an illustration, by using the equations from Lithwick, Xie & Wu (2012), the obtained TTV upper limit implies the absence of any non-transiting planets within 10% of the 2:1 resonance circular orbits and masses above $23\,M_{\mathrm{Earth}}$.

12.6 Rotational Modulation

Starspots can induce brightness modulations as they are coming and going from the field of view while the star rotates. The periodicity of rotational modulation is therefore indicative of the stellar rotational period (e.g. McQuillan, Aigrain & Mazeh 2013).

A brightness modulation with a time-scale of tens of days is visible even in Fig. 12.1. The modulation can be seen much more clearly in Fig. 12.3 where we show the light curve at a larger scale with transits and a linear dropping brightness trend removed, and binned by a factor of 50 to reduce white noise. The modulation is not correlated with the position of the target on the detector and is not present in the *K2* light curves of other nearby stars, which indicates the modulation to be of astrophysical origin. The most likely cause of the observed modulation is the presence of starspots on the surface of the rotating host star.

To determine the period of the modulation, we calculated the Lomb–Scargle periodogram (see Fig. 12.4) of the light curve shown in Fig. 12.3. The two highest peaks are at 46^{+15}_{-7} and 23.4 ± 2.7 days. The rotational period is likely to be one of these, though the *K2* data do not cover enough cycles to be sure. The periodicity near 46 days would correspond to a rotational period longer than half of the 80-day baseline and is therefore not reliable. If the true period were 23 days then peaks at 46 and 10.5 days would be aliases at twice and half of the rotational period.

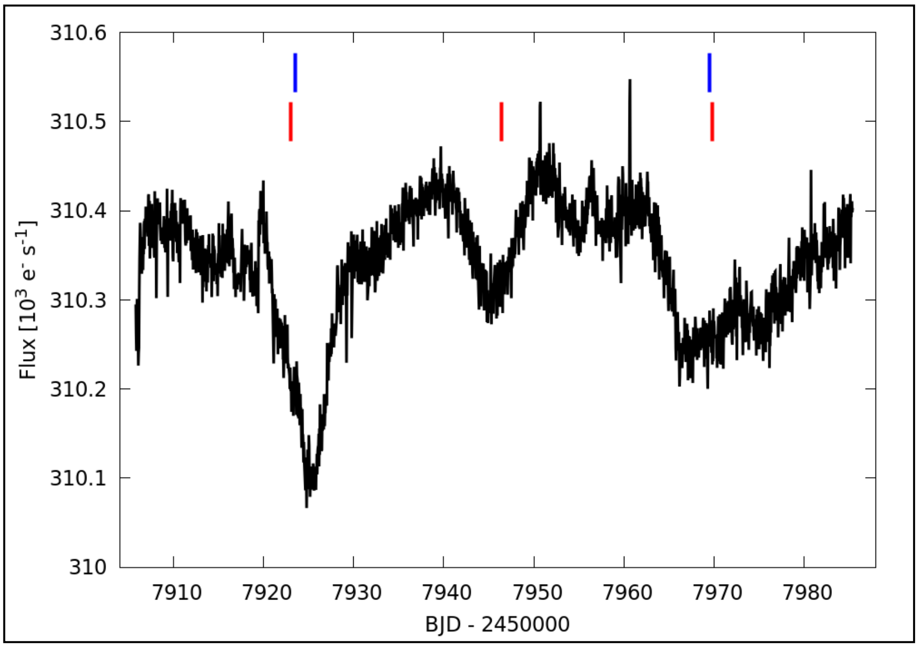

Figure 12.3: Binned *K2* light curve with transits and a linear dropping brightness trend removed. The rotational modulation is clearly visible, with ticks indicating the potential minima of either the 23- (red) or the 46-day (blue) periodicity.

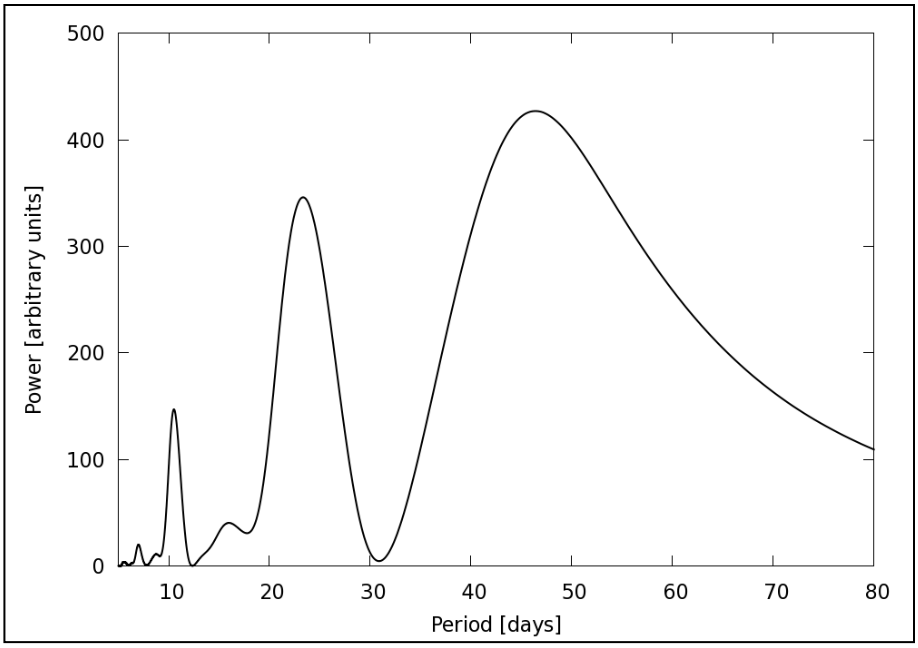

Figure 12.4: Lomb–Scargle periodogram showing a probable rotational period of 23.4 ± 2.7 or 46^{+15}_{-7} days.

The non-detection of such rotational modulation by Smith et al. (2014) is unsurprising, given that their semi-amplitude upper-limit was 4 mmag. Their detection threshold was an order of magnitude above our detection from the *K2* data which reveal a modulation with a semi-amplitude of about 400 ppm.

Smith et al. (2014) provided a stellar projected rotational velocity of $0.4 \pm 0.7\,\mathrm{km\,s^{-1}}$, which for the stellar radius given in Table 12.1 yields a 1-σ lower limit of rotational period of 43 days assuming that the star rotates edge on. This slow stellar rotation is compatible with the potential 46-day rotational period. Alternatively, the 23-day period would be in agreement with the projected rotational period only if the inclination of the stellar rotational axis were smaller than ∼33°.

12.7 No Starspot Occultations

Starspot occultations are the in-transit brightening events that occur whenever a starspot is occulted by a transiting planet (Silva 2003). The same starspot may be occulted repeatedly in several transits (e.g. Tregloan-Reed, Southworth & Tappert 2013), or different starspots may be occulted at similar preferential transit phases (e.g. Sanchis-Ojeda & Winn 2011). Starspot occultation events may be used for an independent and precise measurement of the stellar rotational period (Silva-Valio 2008) and a measurement of the misalignment angle between stellar rotational and planet’s orbital axis (Nutzman, Fabrycky & Fortney 2011).

Močnik et al. (2016a) have shown that detecting starspot occultation events in the *K2* datasets is possible despite the reduced pointing stability of the spacecraft.

We subtracted the best-fitting transit model from the short-cadence *K2* light curve of WASP-104 and searched by eye for any in-transit starspot occultation events. As we found no occultations, we set an occultation amplitude upper limit to 840 ppm, equal to twice the highest in-transit standard deviation.

The presence of a rotational modulation (see Section 12.6) suggests that starspots should be present. However, the amplitude of the modulation is much lower than in other systems that show starspot occultation events. For example, Qatar-2 has a rotational modulation with an amplitude of about 2% (Močnik, Southworth & Hellier 2017), which is 25 times higher than that in WASP-104. If the starspot occultations were also 25 times smaller than those seen in Qatar-2 then they would not be observable.

However, if the rotational modulation in WASP-104 were caused by a single spot, that was completely occulted in transit, then we might expect a starspot occultation with an amplitude comparable to the amplitude of the rotational modulation (800 ppm), which would be marginally detectable. On the other hand, the likelihood of the transit chord passing over a single spot is low.

If the planet’s orbit is aligned, then the transit chord could be at a different latitude than stellar active regions. Indeed, this would be expected given that the impact parameter of the planet is large at 0.73, and knowing that most sunspots occur within 40° of the solar equator (Mandal, Karak & Banerjee 2017). If, instead, the planet’s orbit is misaligned, then over 45 consecutive transits, the transit chord samples many more latitudes and so the likelihood that it crosses a spot is much higher.

Thus, without knowing the alignment of the orbit, we cannot draw firm conclusions from the absence of detectable starspot occultations. It may therefore be worth obtaining Rossiter–McLaughlin observations of this system to measure the alignment.

12.8 Phase-curve Modulation

For the phase-curve analysis we used the *K2* light curve which was flattened and normalized as described in Section 12.3. Flattening was needed to remove any low-frequency brightness variability such as the rotational modulation (see Section 12.6). As a test to ensure that the flattening procedure did not affect also the phase-curve modulation, we injected a suite of phase-curve signals prior to flattening and successfully recovered them after the flattening.

All panels in Fig. 12.5 show the final phase curve with a binning of 50 bins. The binning factor was chosen by trial and error to find a good compromise between lowering the white noise and retaining the phase-resolution. As can be seen even by eye in Fig. 12.5, the phase curve exhibits a signal resembling an ellipsoidal modulation. We ran an MCMC procedure to model the phase curve with three phase-curve modulation components (Mazeh & Faigler 2010):

$$F_{\mathrm{ell}} = -A_{\mathrm{ell}} \cos\left(\frac{2\pi}{P_{\mathrm{orb}}/2} t\right) \tag{12.2}$$

$$F_{\mathrm{Dop}} = A_{\mathrm{Dop}} \sin\left(\frac{2\pi}{P_{\mathrm{orb}}} t\right) \tag{12.3}$$

$$F_{\mathrm{ref}} = -A_{\mathrm{ref}} \cos\left(\frac{2\pi}{P_{\mathrm{orb}}} t\right) + F_{\mathrm{sec}}\ , \tag{12.4}$$

where F_{ell}, F_{Dop}, and F_{ref} are ellipsoidal, Doppler beaming, and reflection modulation components in the normalized phase curve, respectively. A_{ell}, A_{Dop}, and A_{ref} are the corresponding semi-amplitudes, P_{orb} is the orbital period, and t is time from mid-transit. F_{sec} is a simplified secondary eclipse signal, whose depth equals to the reflection amplitude and the duration is the same as for the transit given in Table 12.1. Because the thermal emission is expected to be small compared to the reflected light in the *K2* optical bandpass, in this paper we refer to the combined signal from the planetary reflection and its thermal emission simply as reflection modulation.

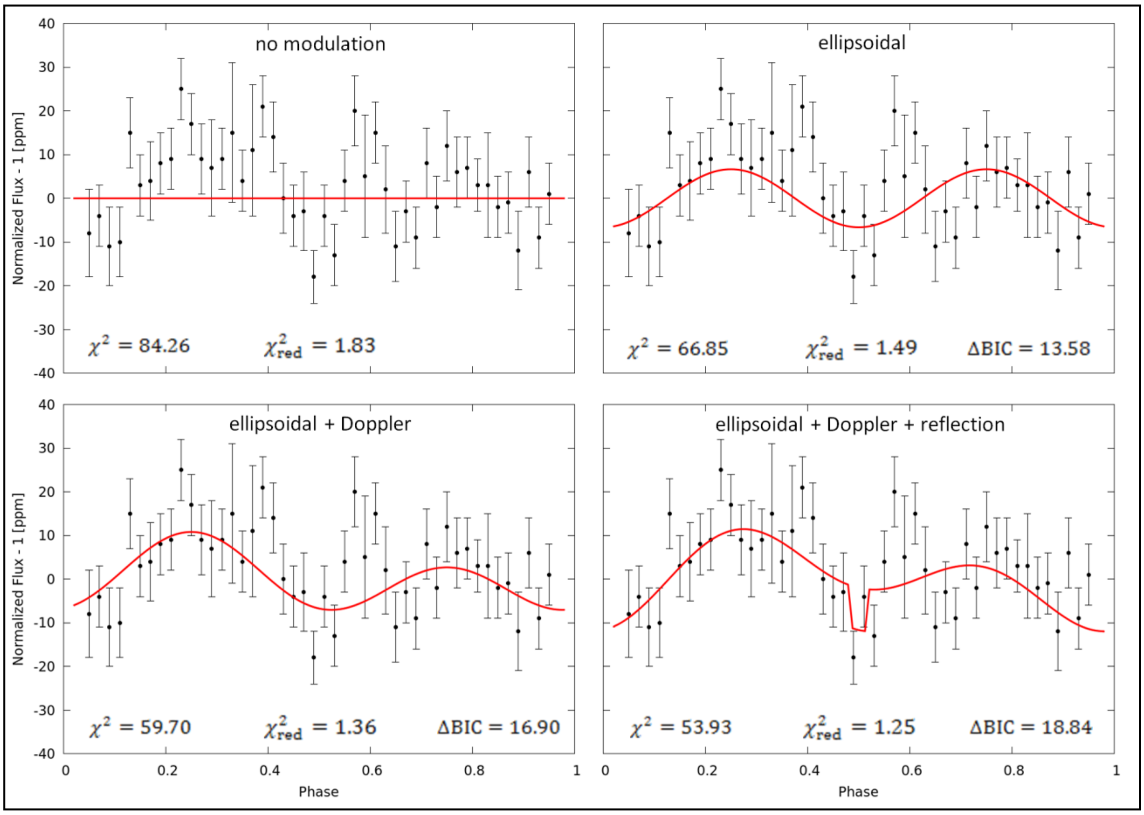

Figure 12.5: Binned phase curve of WASP-104. Panels show the best-fitting MCMC phase-curve models with increasing number of fitted phase-curve components. The ellipsoidal modulation component is detected with high significance, whereas the detections of Doppler and reflection components are tentative.

The best-fitting MCMC phase-curve model is shown with a red line in the bottom-right panel in Fig. 12.5 and corresponds to the ellipsoidal, Doppler and reflection signals with semi-amplitudes of 6.9 ± 2.2, 4.2 ± 1.9, and 4.8 ± 2.1 ppm, respectively. Modelling only the ellipsoidal modulation yields a change in the Bayesian information criterion (BIC) of 13.6, while adding first Doppler and then also the reflection modulations further increases the ΔBIC to 16.9 and 18.8, respectively. This implies that the detection of ellipsoidal modulation is strong, while the Doppler and reflection modulation detections are tentative.

As a test, we repeated the analysis using only the first and then only the second half of the light curve, and found that the modelled phase-curve modulations are in agreement with the results obtained from analysing the full light curve. We also performed the same analysis on the much-noisier publicly available long-cadence light curve reduced with the `K2SFF` procedure (Vanderburg & Johnson 2014) and somewhat noisier short-cadence light curve detrended with `K2SC` (Aigrain, Parviainen & Pope 2016), optimized for short-cadence data (Močnik et al. 2017). In both cases we detect ellipsoidal modulation in agreement with our detection, however, we cannot confirm the Doppler and reflection modulations with these two light curves.

Using the system parameters from Table 12.1 and equations (7–10) of Mazeh & Faigler (2010), we estimate the theoretical semi-amplitudes of ellipsoidal, Doppler, and reflection modulations to be 5.7, 2.7, and $330 \cdot A_g$ ppm, respectively, where A_g is the geometric albedo of the planet. The semi-amplitudes of our ellipsoidal and Doppler detections agree with the theoretically predicted values. For the same to be true also for reflection, the A_g would have to be of the order of one percent. Because the detection of the reflection modulation is tentative, we provide here only the 2-σ upper limit for the visual geometric albedo of 0.03.

At such small reflectivity the thermal emission may contribute significantly to the detected combined phase-curve signal. Thermal emission is strongest for planets with large day-night temperature contrasts, resulting in an emission phase-curve component resembling reflection. Weakest thermal emission is produced by planets with low day-night temperature contrasts, with a flat emission phase-curve signal (Heng & Demory 2013). By using the refined system parameters, we calculated that the planet's thermal emission in the *K2* bandpass contributes a minimum of 1 ppm deeper occultation depth and no sinusoidal reflection-like phase-curve signal in the case of complete heat redistribution in the planet's atmosphere. In the case of no heat redistribution and tidal locking, the emission phase-curve signal would superimpose with reflection by adding 3.3 ppm to its semi-amplitude. Therefore, the true geometric albedo is likely to be significantly lower than the upper limit given above. To break the degeneracy between reflection and emission, we would require a set of phase-curve observations in another wavelength region, preferably in the infrared where the planetary emission component is much stronger.

12.9 No Additional Transiting Planets

Kovács, Zucker & Mazeh (2002) introduced a box-fitting least squares (BLS) algorithm to detect periodic transit-like signals in photometric datasets. We searched for any additional transiting planets with the BLS algorithm in our flattened and normalized *K2* light curve, from which we removed the data points within 0.025 phase from transit mid-points of WASP-104b. This was done by using the online BLS periodogram service provided by the NASA Exoplanet Archive[16]. We then converted the obtained BLS signal residuals into estimated transit depths of potential transiting planets (Kovács, Zucker & Mazeh 2002):

$$\delta = \frac{SR}{\sqrt{r(1-r)}} \quad , \tag{12.5}$$

where δ is the transit depth, *SR* is BLS signal residual, and *r* is the relative time spent in transit, which we approximated with the transit phase-width a potential planet would have at a particular orbital period.

---

[16] https://exoplanetarchive.ipac.caltech.edu/cgi-bin/Pgram/nph-pgram

We found no statistically significant periodogram peaks in the period region 0.5–30 days, and set a transit depth upper limit to 110 ppm, which equals the highest peak in the residual transit-depth periodogram.

12.10 Conclusions

WASP-104 was observed by the *K2* in the short-cadence mode during the observing Campaign 14. By analysing these data we refined the system parameters and searched for TTVs, TDVs, rotational modulations, starspot occultations, phase-curve modulations, and additional transiting planets.

We detect the rotational modulation with a probable rotational period of 23 or 46 days. Despite the apparent presence of starspots, we did not detect any starspot occultation events, possibly due to the large impact parameter of the transiting planet or because the occultations did not exceed our detection threshold.

WASP-104 is, to the best of our knowledge, only the third transiting planetary system with detected phase-curve modulation from the *K2* mission (after Qatar-2 (Močnik, Southworth & Hellier 2017; Dai et al. 2017) and K2-141 (Malavolta et al. 2018)). We unequivocally detect ellipsoidal modulation with a semi-amplitude of 7 ppm, in agreement with the theoretically expected value. We also tentatively detect Doppler beaming and reflectional modulations. The latter yields a conservative upper limit for the planet's visual geometric albedo of 0.03, lower than the reflectance of some types of charcoal (Ascough, Bird & Scott 2010). The very low albedo rules out any highly reflective clouds in the WASP-104b's atmosphere.

TrES-2b is one of very few hot Jupiters at least as dark as WASP-104b. Kipping & Spiegel 2011) have measured its visual geometric albedo to be 0.025 ± 0.007 if the detected reflectional modulation in the *Kepler* data was caused entirely by reflection, and even lower than 1% after taking into account their thermal emission model. Another example is HAT-P-7b, with a visual geometric albedo $\lesssim 0.03$, based on the detection of the secondary eclipse in the *Kepler* light curve (Morris, Mandell & Deming 2013).

In general, hot Jupiters exhibit a large range of visual geometric albedos (e.g. Sheets & Deming 2017), depending on their temperature which controls the cloud properties (Sudarsky, Burrows & Pinto 2000). Typical visual geometric albedos of hot Jupiters are of the order of 0.1 (Schwartz & Cowan 2015) and are statistically lower than for hot super-Earths (Demory 2014) and Neptunes (Sheets & Deming 2017). According to the atmospheric models, the lower albedos may be attributed to the presence of alkali metals as well as TiO and VO in hot-Jupiter atmospheres, which causes significant absorption in the visual wavelengths (Demory et al. 2011).

13 Results Overview

In this thesis I present the analysis of 12 planetary systems, 10 of which were observed in the *K2* short-cadence observing mode and two in the long-cadence mode. Together with colleagues we announced the results for 11 systems in eight publications, whereas the findings for WASP-47, which we also analysed, were announced by Becker et al. (2015).

Beside the systems presented here, there were only four other transiting planetary systems observed by the *K2* in the short-cadence mode within the first 14 observing campaigns. These were analysed and reported by others, namely HATS-9, HATS-11 (both by Bayliss et al. 2017), TRAPPIST-1 (Luger et al. 2017) and K2-234 (Van Eylen et al. 2018). Therefore, the thesis presents the majority of the transiting planetary systems observed by *K2* in the short-cadence observing mode.

Table 13.1 summarizes the analysis of the planetary systems presented in this thesis and outlines the detectability of various astrophysical signals. The results for WASP-47 are given for reference and are as reported by Becker et al. (2015).

I detected starspot occultation events in the short-cadence light curves of three host stars (WASP-85, Qatar-2 and WASP-107). Because starspots also produce rotational modulations it is unsurprising that the same three stars also exhibit rotational modulations. The rotational periods derived from the recurring starspot occultation events for WASP-85 and Qatar-2 agree with the periods implied by the rotational modulations. In addition, I detected the low-amplitude rotational modulation in WASP-104 and a tentative periodicity was seen also in WASP-75 and WASP-118. Because the

Table 13.1: Overview of performed analysis and detections. Cells are colour-coded to represent reliable detections (green), tentative detections (yellow), non-detections (red), or segments that were not analysed (gray).

Target	System param.	TTV	Rotat. mod.	Starspots	Phase curve	Pulsa-tions	Add. tran. planets	Publi-cation
W85	🟩	8s	13.6d	15.1d, <14°	<50ppm	🟥	<160ppm	1
W47	🟩	7min	🟥	🟥	🟥	🟥	2	2
W75	🟩	<35s	11.2d	🟥	<30ppm	🟥	<190ppm	3
W55	🟩	<25s	🟥	🟥	<50ppm	🟥	<280ppm	3
W157	🟩	<60s	🟥	▨	<20ppm	🟥	<250ppm	4
Q2	🟩	<10s	18.2d	18.0d, <8°	18ppm	🟥	<280ppm	5
W118	🟩	<40s	~5d	🟥	<25ppm	γ Dor	<140ppm	6
W107	🟩	<20s	17.4d	>40°	<50ppm	🟥	<130ppm	6
W28	🟩	<20s	🟥	🟥	<40ppm	🟥	<160ppm	7
W151	🟩	<30s	🟥	🟥	<80ppm	🟥	<220ppm	7
K2-140	t_0, P_{orb}	▨	▨	▨	▨	▨	▨	8
W104	🟩	<20s	23d or 46d	🟥	7ppm	🟥	<110ppm	9

Key for publications:
1: Močnik et al. (2016a)
2: Becker et al. (2015)
3: Clark et al. (2018)
4: Močnik et al. (2016b)
5: Močnik, Southworth & Hellier (2017)
6: Močnik et al. (2017)
7: Močnik, Hellier & Anderson (2017)
8: Močnik, Hellier & Anderson (2018)
9: Močnik, Hellier & Southworth (2018)

occultations of starspots by hot Jupiters typically last on the order of a few tens of minutes, it is practically impossible to detect them in the 30-min long-cadence light curves.

Compared to the long cadence, the short-cadence mode also provides significantly higher precision in determining system parameters and TTVs. The latter were tentatively detected only in WASP-85 (more likely produced by the photometric activity rather than gravitational interactions) and in the WASP-47 system, which remains the only planetary system found to date to host a hot Jupiter in a compact configuration with two smaller close-in planets. No additional transiting planets were found in any other planetary system from Table 13.1.

I also detected phase-curve modulations produced by Qatar-2b and WASP-104b, which are the two hot Jupiters with the shortest orbital periods among the analysed systems. For other planetary systems I provide modulations' upper limits which I use to constrain the planets' geometric albedos.

WASP-118 is the only analysed target with detectable pulsations. At the time of writing the corresponding paper, WASP-118 was only the second ever discovered γ Doradus pulsator that is hosting a transiting exoplanet.

WASP-157 and K2-140 were both observed in the long-cadence mode. However, for K2-140 I only used the *K2* light curve together with WASP photometry to refine the ephemeris.

Figs. 13.1 and 13.2 display the positions of analysed planets among the known population of transiting planets. The fact that the analysed targets have larger than average radii is unsurprising because they were selected for the *K2* observations following the initial ground-based detection, which are biased towards larger planets. In contrast, most known transiting planets have been discovered by the *Kepler* mission whose precision was high enough to detect a larger population of smaller planets.

Fig. 13.2 highlights the deviations of planetary radii from the empirically determined radius–mass relation for exoplanets (Bashi et al. 2017):

$$R_\mathrm{p} \propto M_\mathrm{p}^{0.55\pm0.02} \qquad \text{if } M_\mathrm{p} < 0.39\, M_\mathrm{Jup} \tag{13.1}$$

$$R_\mathrm{p} \propto M_\mathrm{p}^{0.01\pm0.02} \qquad \text{if } M_\mathrm{p} > 0.39\, M_\mathrm{Jup} \;\; . \tag{13.2}$$

The transition in the radius–mass relation is thought to be due to the characteristic boundary between mostly H/He gaseous planets and planets with various compositions. Several planets presented in this thesis are inflated (see Section 14.3). WASP-107b in particular has a radius 60% larger than the empirically-determined relation (see Fig. 13.2), making it one of the best targets for transmission spectroscopy given its bright ($V = 11.6$) and small host star (0.66 $R_\odot$).

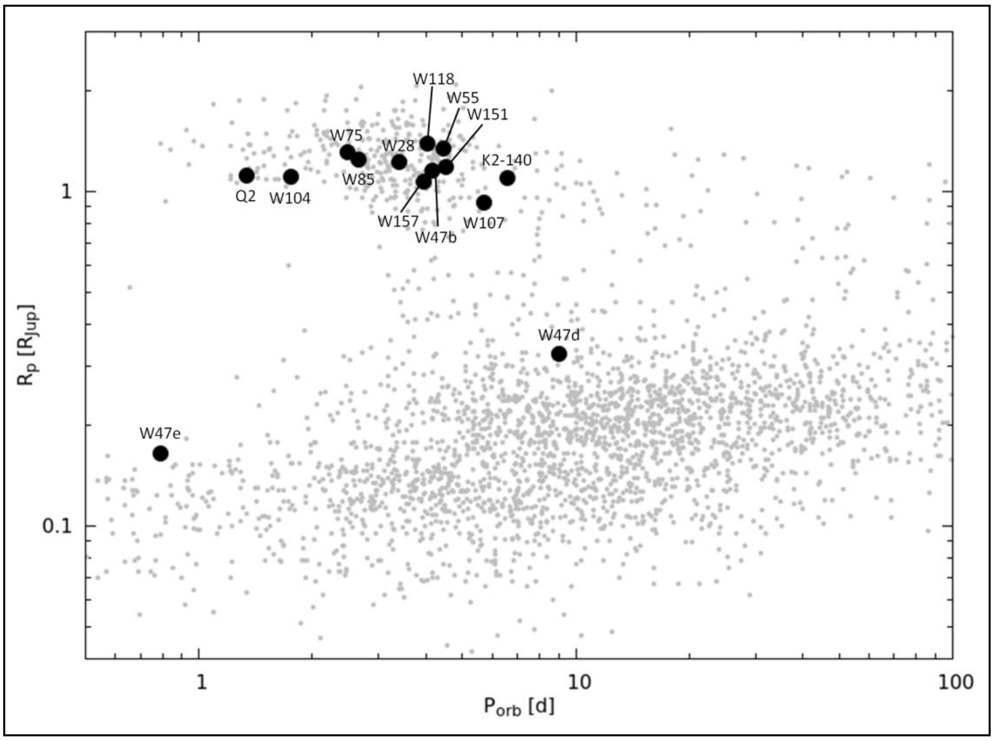

Figure 13.1: Positions of analysed planets in the radius versus orbital period distribution. Large labelled black data points are planets analysed by this research project, and small grey points are other confirmed transiting planets sourced from NASA Exoplanets Archive.

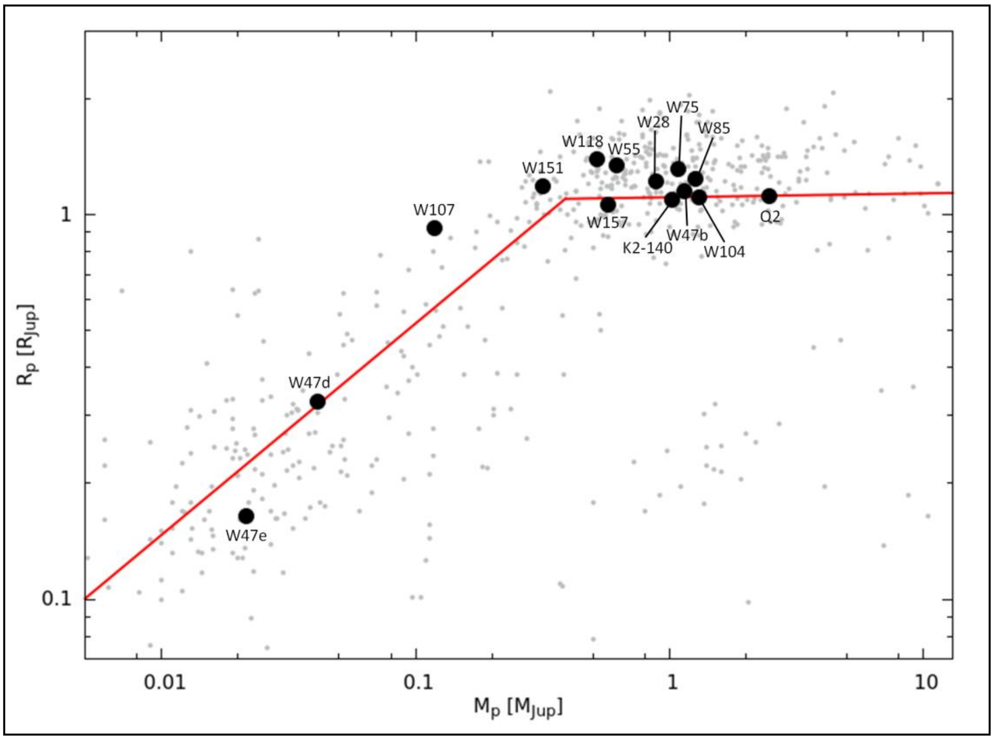

Figure 13.2: Similar as Fig. 13.1, but showing radius versus mass. The solid line is the radius–mass relation from equations (13.1 and 13.2) of Bashi et al. (2017). Note that many fewer planets are shown in this plot compared to Fig. 13.1 because masses of many smaller transiting planets have not been measured yet.

14 Discussion

14.1 Stellar Activity

Rotational modulations and starspot occultation events are photometric signatures of stellar magnetic activity. I detected rotational modulations with confidence in four out of 12 analysed planetary systems, 11 of which were analysed for the rotational modulations. Despite this very small sample, the fraction of stars with detectable rotational modulations and their amplitudes compare well with the findings of McQuillan, Mazeh & Aigrain (2014), who detected rotational modulations in 25.6% of the 133,030 stars observed in the long-cadence mode during the *Kepler* mission with amplitudes ranging between 950 and 22,700 ppm (5th and 95th percentile, respectively). For WASP-85, Qatar-2 and WASP-107 the rotational periods derived from the rotational modulations are all significantly shorter than that of the Sun, implying that these stars are either young or spun up by their planets (Pont 2009). For WASP-104 the rotational period is inconclusive and is either 23 or ∼46 days, which would correspond to stellar ages of 3 or ∼8 Gyr, respectively, using the gyrochronology relations of Barnes (2007) for the G8 spectral type of the host star.

Starspot occultation events can only be detectable in data sets with high enough photometric precision (up to a few hundred ppm per cadence) and short enough cadence (shorter than ∼10 min to sample a Jupiter-sized starspot fully occulted by a hot Jupiter with at least 3 data points). *Kepler* telescope delivered such observations, which led to the detection of occultation events in nine planetary systems observed as part of the *Kepler* mission (Dai et al. 2018). However, doubts have been raised initially that the *K2* mission would not be able to reveal starspot occultation events due to adverse impact of drift artefacts on its photometric performance. By detecting recurring starspot occultation events in the short-cadence *K2* light curve of WASP-85, I demonstrated that detecting occultations is possible with the *K2* observations. I later detected starspot occultations also in the Qatar-2 and WASP-107 systems, which remain together with WASP-85 the only three planetary systems in the *K2* mission with detected starspot occultation events within the first 14 observing campaigns.

The recurring starspot occultation events in the light curves of WASP-85 (spectral type G5) and Qatar-2 (K4) prove that the two systems are aligned, namely with projected misalignment angles smaller than 14° and 8°, respectively. This is in agreement with the general observational trend highlighted by Winn et al. (2010a) that stars with effective temperatures lower than 6250 K are more likely to host hot Jupiters in aligned orbits than hotter stars. The transition, also called the Kraft break (Kraft 1967), is thought to be related to the presence of convective envelopes which provide an efficient tidal dissipation mechanism for cooler stars (Winn et al. 2010a). Although WASP-107 (K6) is also well below the Kraft break, it appears to be misaligned. Misaligned planetary systems with cool host stars all have scaled semi-major axes ($a_{\min}/R_*$) $\gtrsim$8 (Dai & Winn 2017), including WASP-107 with $a/R_* = 18.13 \pm 0.07$, where the gravitational interactions and thus tidal dissipation are weaker.

The time span between the first and last recurring occultation event of the presumably-same starspot reveals its minimum lifetime. In the case of WASP-85, the recurring occultations were seen in pairs of consecutive transits, giving only the weakly-constrained minimum starspot lifetime equal to one orbital period of 2.7 days. On the other hand, in Qatar-2 system, I detected recurring occultations in up to 5 consecutive transits and even after three full stellar rotations, revealing its minimum lifetime of 58 days.

Beside stellar rotational period, obliquity and starspot lifetimes, occultations may also reveal spots' physical parameters. However, starspots' latitudes, radii and contrasts are largely degenerate and simultaneous observations in different bandpasses would be needed to break this degeneracy (e.g. Mancini et al. 2014).

14.2 Photometric Signatures of Orbital Motion

Phase-curve modulations were and are routinely discovered from ground for compact objects in short-period binaries (e.g. Maxted, Marsh & North 2000; Geier et al. 2007; Shporer 2010). However, exoplanet companions which have lower mass, longer orbital periods and larger orbital separations produce phase-curve modulations with significantly lower amplitudes (see equations 1.20–1.24). Phase-curve modulations produced by hot Jupiters have amplitudes lower than a few tens of ppm in the optical wavelengths (e.g. Esteves, De Mooij & Jayawardhana 2013). High photometric precision and long-term observations covering several orbital periods are needed to be able to detect them. Most phase-curve modulations in planetary systems were detected in the data collected with the space-based *Spitzer* (IR wavelengths) and *Kepler* (optical) missions.

Among the targets analysed in this research project, I detected phase-curve modulations in two planetary systems (see Table 13.1). In the Qatar-2 system, I detected probable ellipsoidal modulations, and in WASP-104 definite ellipsoidal modulations in addition to tentative detections of Doppler and reflection modulations. This proves that phase-curve modulations of planetary systems are detectable using the *K2* data. To the best of my knowledge, the detection of reflectional modulation in K2-141 (Malavolta et al. 2018) is currently the only other reported phase-curve detection among planetary systems observed by *K2*.

Companions' masses estimated from ellipsoidal and Doppler modulations do not always match (e.g. Barclay et al. 2012), which can be attributed to the degeneracy between the amplitude of Doppler modulations and phase shifts of the thermal emission component (e.g. Shporer 2017). The detected phase-curve modulations in Qatar-2 and WASP-104 do not reveal any significant phase shifts and agree with theoretical predictions which are based on the system parameters obtained from transit photometry and RV measurements.

The phase-curve analysis of Qatar-2 and WASP-104 also yielded the tightest upper limits for visual geometric albedos among the planets presented in this thesis, namely <5% and <3%, respectively. Low albedos have been measured for several other hot Jupiters (e.g. Kipping & Spiegel 2011; Bell et al. 2017), which can be explained by the presence of optical absorbers in the atmospheres of such hot planets (e.g. Rowe et al. 2008). The non-detections of reflectional modulations for other planets in the sample constrained the geometric albedos much more loosely, between <20% for WASP-118b and <90% for WASP-151b.

14.3 Planetary Radii Inflation

Many transiting close-in gas giant planets exhibit radii significantly larger than expected from the standard theory of planet cooling and contraction (e.g. Burrows et al. 2000; Fortney & Nettelmann 2010). It has become apparent that planets' radii are strongly correlated with the proximity to their host stars (e.g. Hartman et al. (2016) and citations therein). Several mechanisms have been proposed to explain the anomalously large radii through excess internal heat that prevents planet contraction. First, planets' radii could be inflated by insulation, by which a fraction of the absorbed incident stellar flux is transported deeper into the planet's atmosphere (e.g. Weiss et al. 2013). Second, tidal interactions and in particular eccentricity damping could provide internal heat for transient planet inflation (Leconte et al. 2010). Third, strong atmospheric opacity (Burrows et al. 2007) or internal convection barriers (Chabrier & Baraffe 2007) could slow the cooling of the planets and give rise to delayed contraction. However, none of the proposed mechanisms received a general consensus, and a combination of mechanisms may be required to explain the observed large radii. Planetary radii depend on many parameters, some of which are non-observable or only poorly constrained, such as the planet's core mass, internal composition, age, atmospheric opacity, etc. (Sestovic, Demory & Queloz 2018). However, while the understanding of any particular planet is hindered by the relatively small number of accessible observables, we can improve our knowledge of radius inflation mechanisms by building a large sample of inflated planets and look for correlations that are emerging (Fortney & Nettelmann 2010).

Shown in Fig. 14.1 is the distribution of planetary radii against mass and insulation for all 12 gas giant planets in the analysed sample (plotted with large symbols), and 263 other gas giants (small symbols) sourced from NASA Exoplanets Archive for which the required parameters were available. I calculated the time-averaged incident flux (F) for each planet with (Weiss et al. 2013)

$$F = \sigma T_{\text{eff}}^4 \frac{R_*^2}{a^2} \sqrt{\frac{1}{1-e^2}} \ , \tag{14.1}$$

where σ is the Stefan–Boltzman constant, T_{eff} effective temperature of the host star, R_* stellar radius, a semi-major axis of the planet's orbit and e is the eccentricity (assumed to be 0 where unavailable).

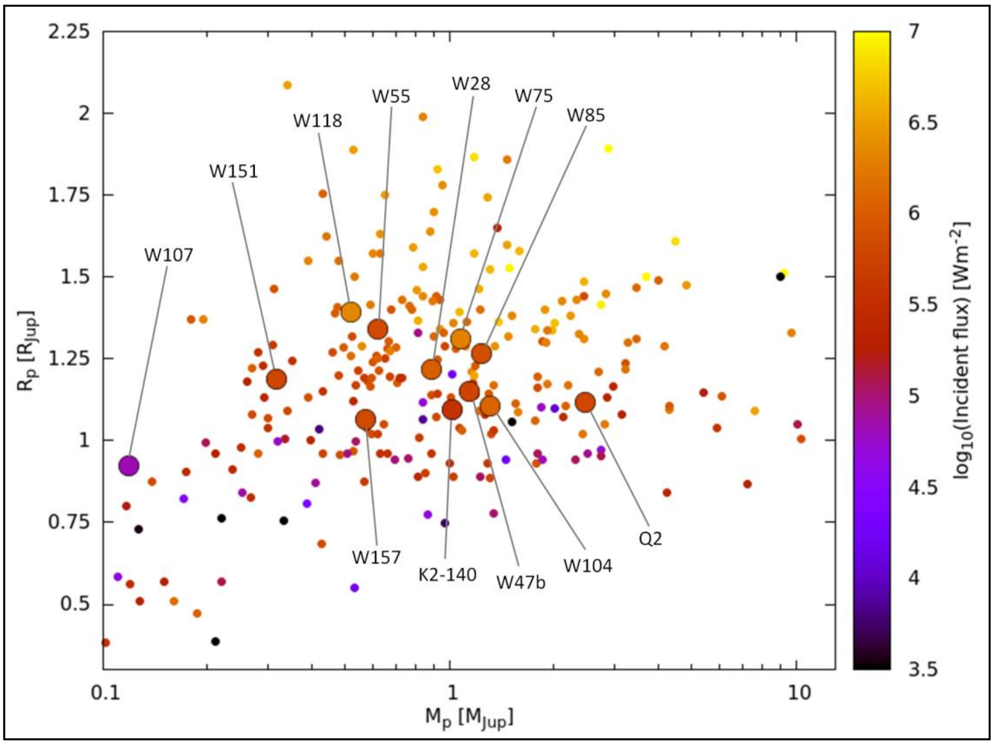

Figure 14.1: The dependence of planet radius inflation on mass and insulation. Large labelled symbols represent planets analysed in this work, and smaller symbols correspond to planets sourced from NASA Exoplanet Archive. Adapted from Sestovic, Demory & Queloz (2018).

As can be seen from Fig. 14.1, planets that are exposed to higher levels of insulation generally exhibit larger radii, with most pronounced effect of radius inflation in the mass range between 0.4 and 1 M_{Jup}. The bulk of my sample is exposed to insulations between $10^{5.5}$ and $10^{6.3}$ W m^{-2}, which give rise to more pronounced inflation for lower mass planets (e.g. WASP-118b or WASP-151b both having planet densities of 0.19 ρ_{Jup}) and weaker or no inflation for higher mass planets (e.g. Qatar-2b or WASP-104b with densities of 1.8 and 1.0 ρ_{Jup}, respectively), in agreement with other planets sourced from the Archive. Surprisingly, however, the most inflated planet in the analysed sample is WASP-107b (with a density of only 0.15 ρ_{Jup}) despite the smallest insulation ($10^{4.8}$ W m^{-2}). This might be explained with latent heat from the planet formation if the planet is young (τ_{gyro} = 0.6 ± 0.2 Gyr, τ_{iso} = 8.3 ± 4.3 Gyr; see Section 9.11), or with tidal heating.

This thesis helps in improving our knowledge of planet inflation by adding a moderately inflated hot Jupiter WASP-157b to the sample and significantly improving the precision of system parameters for most other analysed planets.

15 Conclusions and Future Work

15.1 *K2* and My Research Contribution

Since the approval of the *K2* mission on 2014 May 16 (Sobeck & Johnson 2014), the *K2* telescope provided the community with photometric observations from 18 scientific observing campaigns along the ecliptic, each lasting for ∼80-days. A total of 508,931 different targets were observed altogether during Campaigns C0–C17, with most of them downlinked only in the 30-min long-cadence mode and about 0.4% also in the 1-min short cadence mode. The data from the *K2* mission have led to the discovery of 312 exoplanets as of the time of writing (2018 June 3) and resulted in 346 refereed papers, half of which are related to exoplanet science.

With only two functional reaction wheels left, the pointing of the *K2* spacecraft is less stable than during the *Kepler* mission, which causes pronounced drift artefacts in obtained light curves. In collaboration with Ben Clark, I optimized the publically available `kepsff` tool for correcting drift artefacts in *K2* short-cadence light curves. The implementation of Gaussian convolution in the decorrelation procedure and other minor modifications nearly doubled the photometric precision of the corrected light curves compared to the original `kepsff` performance. With this procedure, I was able to restore the near-original *Kepler*-like photometric precision for short-cadence light curves whenever the pointing drifts were consistent. However, in certain observing campaigns the pointing drifts were less consistent, which prompted the use of a different method to correct them. Aigrain, Parviainen & Pope (2016) presented the `K2SC` procedure which uses Gaussian processes to correct such artefacts efficiently from the long-cadence *K2* light curves. To be able to use it also for the short-cadence data, I split the light curves into smaller overlapping sections, corrected drift artefacts from each of them with `K2SC` and merged them back together using the overlapping regions. Using the modified `kepsff` and `K2SC` procedures, I corrected drift artefacts from all short-cadence light curves analysed in this research project.

In this thesis I present the analysis of the majority (10 out of 14) of transiting exoplanet systems observed in the short-cadence mode within the first 16 observing campaigns (CEng, C0–C14). I detected recurring starspot occultation events in WASP-85 and Qatar-2 systems and non-recurring occultations in WASP-107, which are currently the only three planetary systems with detected starspot occultations within the *K2* mission. This proved that the restored photometric precision of *K2* is sufficient to detect starspot occultations, and I used them to measure stellar rotational periods and to constrain the misalignment angle between stellar rotation and planetary orbit. I detected rotational modulations with high significance in four systems (WASP-85, Qatar-2, WASP-107 and WASP-104), which provided another measurement of stellar rotational period. I detected phase-curve modulations in the light curves of Qatar-2 and WASP-104, which are together with K2-141 currently the only three planetary systems observed by the *K2* with detected phase-curve modulations. I discovered to the best of my knowledge only the second γ Doradus pulsator to host a transiting exoplanet, WASP-118. The high photometric precision and cadence also allowed me to refine system parameters with typically significantly improved precision compared to the previous studies, and to provide tight upper limits on transit timing variations and transit depths of any additional transiting planets.

In addition to 10 analysed targets observed in the short-cadence mode, I used the long-cadence data for two other planetary systems. First, as part of the follow-up photometry of the newly discovered hot Jupiter WASP-157b, and second, to refine the ephemeris together with WASP data for K2-140b.

The results presented in this thesis have been announced in six lead-authored papers, one research note and one co-authored paper.

Future work related to *K2* short-cadence observations of transiting exoplanets include analysing the already-released data for K2-38 and K2-34 from observing Campaigns 15 and 16, respectively. The observations from Campaign 17 (WASP-157, K2-99 and K2-110) have already been downlinked and are currently available as raw data with the official data release expected later this year. *K2* is currently executing Campaign 18, which overlaps with Campaigns 5 and 16, and therefore contains many already-discovered *K2* planets that will be observed in the short-cadence mode. If Campaign 19 executes successfully, it will deliver another short-cadence dataset for WASP-28 and two multi-planet systems TRAPPIST-1 and GJ-9827.

The *K2* spacecraft is expected to run out of fuel in the second half of 2018, probably sometime during observing Campaigns 18 or 19 (Geert Barentsen, private communication). However, the exact quantity of the remaining fuel is unknown and it might be possible to execute also Campaign 20 (as announced by the Call for *K2* Cycle 7 Proposals[17]).

15.2 *TESS*

The *Transiting Exoplanet Survey Satellite* (*TESS*; Ricker et al. 2015) is the first space-based telescope dedicated to exoplanet science after *Kepler*. It was launched on 2018 April 18 with science observations expected to begin following two-month-long orbital

---

[17] https://keplerscience.arc.nasa.gov/call-for-k2-go-cycle-7-proposals-for-campaign-20.html

adjustments and testing. It is designed to conduct a nearly all-sky photometric search for transiting planets orbiting bright nearby stars.

The minimum duration of the *TESS* mission is two years. *TESS* will observe targets in the southern hemisphere during the first year and in the northern hemisphere during the second year. The spacecraft could remain operable for up to 10 years and it is likely that the mission will be significantly extended (e.g. Bouma et al. 2017; also see Fig. 15.2).

The nominal two-year mission is expected to yield around 1250 ± 70 transiting exoplanets (Barclay, Pepper & Quintana 2018) among the pre-selected 200,000 main-sequence stars that will be observed in the short 2-min cadence. Most of these will be sub-Neptunes, and around 20% will be super-Earths or smaller (Barclay, Pepper & Quintana 2018). Additional planets are expected to be found from around 20,000 additional short-cadence targets proposed through the Guest Investigator Programme and from the full-frame images that will be obtained at 30-min cadence.

The ground-based follow-up observations will provide the necessary measurements to derive the planetary system parameters, including planets' radii and masses. Knowing the bulk compositions of hundreds of *TESS* transiting planets will serve as a valuable testbed for planet formation and migration theories. Many planets discovered by *TESS* will also be excellent targets for atmospheric characterization studies since their host stars will be bright enough. The *James Webb Space Telescope* (*JWST*) in particular will source targets for transmission and emission spectroscopy from among the *TESS* planets (Beichman et al. 2014).

Although *TESS*' photometric precision will be lower than that of *Kepler* (200 ppm per long-cadence for $I_c = 10$, see Fig. 15.1) it will still be able to detect starspot occultation events similar to those seen in Qatar-2 system at 3σ. This may provide stellar rotational periods and misalignment angles for planetary systems with orbital periods short enough to be able to detect several starspot occultation recurrences within the 27-day long light curves which will be provided for the majority of targets observed during the first two years of the mission.

The relative contribution of thermal emission and reflected light to the atmospheric phase-curve component is wavelength-dependent. With the wavelength coverage of 600–1000 nm (Ricker et al. 2015), *TESS* will be more sensitive to redder light compared to *Kepler* (435–845 nm; Thompson et al. 2017). Comparing phase curves from the *Kepler* and *K2* missions with *TESS* phase curves may therefore provide some wavelength phase-curve information and offer limited ability to separate reflected from emitted light (Shporer 2017). Although the overlap between the fields observed along the ecliptic by the *K2* mission and the nominal 2-year *TESS* mission is minimal (Collins et al. 2018), some observing scenarios for the extended *TESS* mission are specifically designed to cover the ecliptic and provide an opportunity to follow-up the *K2* discoveries (Bouma et al. 2017).

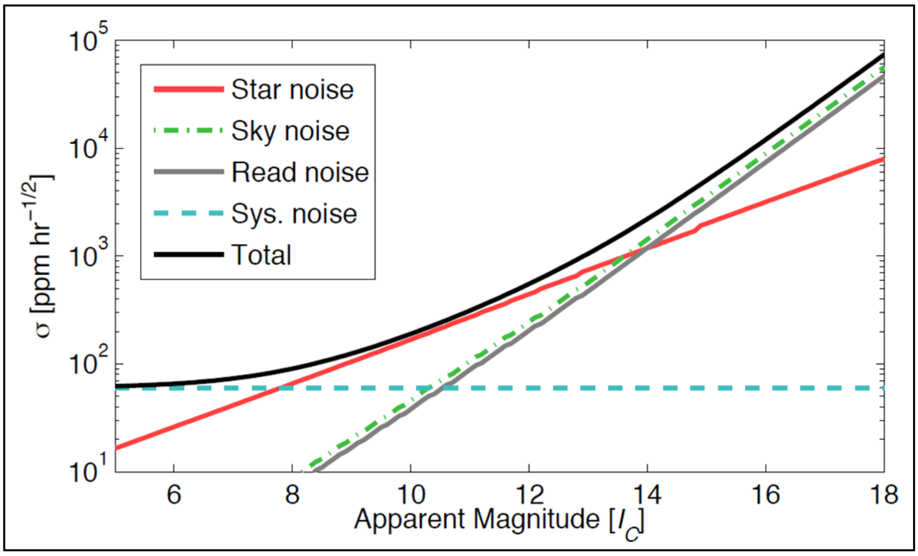

Figure 15.1: Expected photometric performance of *TESS* telescope. Credit: Ricker et al. (2015).

15.3 Overview of Upcoming Space-based Missions

The main data source for this thesis was the *K2* space-based telescope, which will soon be succeeded by the *TESS* mission (see Section 15.2). In this section I provide a brief overview of other upcoming space-based missions with significant contributions to exoplanet science.

The *CHaracterising ExOPlanet Satellite* (*CHEOPS*; Broeg et al. 2013) is currently scheduled for launch towards the end of 2018 (see Fig. 15.2). Its main scientific goal will be to measure accurate radii of transiting planets that already have masses estimated from the RV ground-based surveys. The 33-cm aperture will provide photon-noise-limited photometric precision of 150 ppm min^{-1} for a $V = 9$ star. The planned mission duration will be 3.5 years, with a goal of extending it to 5 years[18].

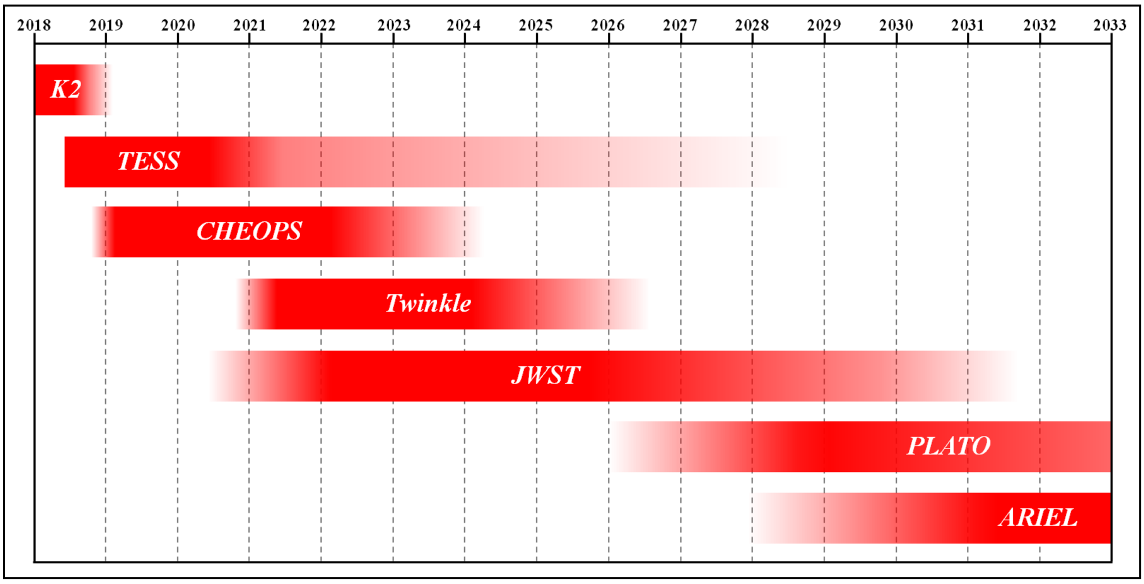

Figure 15.2: Expected mission durations of the current and future space-based missions related to exoplanets. The intensity of the colour corresponds to the probability that the mission will be operational at a given time. The plot is correct as of the time of writing (2018 June 5) using various references given in Sections 15.1–15.3.

---

[18] http://sci.esa.int/cheops/54030-summary/

Twinkle (Savini et al. 2016) is an upcoming space-based mission to deliver visible and near-IR spectroscopic and photometric observations with its 45-cm telescope. *Twinkle*'s main goals are to measure atmospheric compositions of at least 100 known transiting planets, and to provide follow-up transit and eclipse photometry of more than 1000 exoplanets. The satellite is planned to be launched into a low Earth orbit in late 2020, with a minimum mission duration of 3 years and a possible extension to 5 years[19].

The *James Webb Space Telescope* (*JWST*; Gardner et al. 2006) is a 6.5-m IR-optimized space telescope with current expected launch date near the Earth's second Lagrangian point (L2) in mid-2020 (Wang, Cole & Norton 2018). The telescope will be used in several areas in astronomy, with around 25% of available observing time allocated to exoplanets. Its main scientific goal in the field of exoplanets will be the atmospheric characterization through transmission and occultation spectroscopy, and thermal-emission phase curves (Beichman et al. 2014). The nominal 5-year mission duration with the 25% time allocation and a duty cycle of 70% will provide 320 days of observing time for exoplanets (Cowan et al. 2015). If transits and occultations will both be observed with four different *JWST* instruments, each hot gas giant will require two days of observing time. Alternatively, a complete atmospheric characterization of a temperate terrestrial planet would require 100 days of observing time to reach sufficient S/N (Cowan et al. 2015). The final number of atmospherically characterised planets depends on the selected combination of observed planet types and can be doubled following the anticipated mission extension to 10 years[20]. *JWST* will source its targets mainly from among the nearby transiting planets discovered by the *TESS* mission.

The *PLAnetary Transits and Oscillations of stars* (*PLATO*; Rieke et al. 2014) spacecraft will consist of 26 12-cm optical cameras, together providing a combined FOV of $2230\,\mathrm{deg}^2$ and a photometric precision better than $34\,\mathrm{ppm\ hour}^{-1}$ for $V < 11$ stars.

---

[19] http://www.twinkle-spacemission.co.uk/mission-overview/#status

[20] https://jwst.nasa.gov/faq.html#howlong

The data from 24 cameras will be read-out and downlinked at a 25-s cadence, and at a 2.5-s cadence for two cameras to allow observations of bright stars and used as fine guidance sensor (Aerts et al. 2017). Its mission concept will be similar to that of *Kepler* and *K2* with long-term continuous photometric monitoring of hundreds of thousands of stars in at least two different pointings. The main goal of the mission is to detect and photometrically characterize terrestrial planets orbiting bright nearby stars. The estimated planet yield for the observing strategy that involves two two-year pointings is ~4700 planets of any size, any orbital period and host stars brighter than $V = 13$. Of these, ~770 should be smaller than 2 R_{Earth} with host stars brighter than $V = 11$, and 6–260 in the habitable zone, depending on the assumed planet occurrence rates (Aerts et al. 2017). The high photometric precision will enable the determination of accurate planetary radii from transit photometry (better than 3% for most planets), and radii, masses and ages of host stars from asteroiseizmology. ESA has selected the *PLATO* mission in 2014 and adopted it in its Science Programme in 2016. The current target launch date for *PLATO* spacecraft is 2026. The duration of the nominal science operations is four years, with a possible mission extension for another four years (Aerts et al. 2017).

The *Atmospheric Remote-sensing Infrared Exoplanet Large-survey* (*ARIEL*; Tinetti et al. 2016) has been selected as ESA's medium-class space mission in March 2018 with a target launch date of 2028. The spacecraft will orbit the L2 point. The telescope will consist of an oval 1.1×0.7-m primary mirror, low- and medium-resolution IR spectrographs, and visible and near-IR photometers. In its nominal 4-year mission duration, *ARIEL* will conduct the first large-scale atmospheric characterization of exoplanets by measuring transmission and eclipse spectra of a large diverse sample of 1000 planets. The mission may be extended for two further years[21].

---

[21] http://sci.esa.int/ariel/59798-summary/

The recently-launched *TESS* and the upcoming space-based missions listed in this section will reduce the uncertainty of the current planet occurrence rates of terrestrial planets, characterise a large number of transiting planets and their host stars with high precision, and provide unprecedented insight into exoplanetary atmospheres which may improve our understanding of how planets form and migrate.

This research project has demonstrated the detectability of elusive and scientifically valuable astrophysical photometric signals in short-cadence *K2* light curves. Upcoming space-based photometric missions will be able to detect such signals for a much larger number of host stars. Detections of starspot occultation events for a larger variety of planetary systems will provide obliquity constraints needed for refining planet migration models. The common disagreement between the gyrochronological and isochronal age estimates, also reported in this research work, is currently poorly understood and our understanding of this discrepancy will benefit from precise characterisation of a large number of host stars that are expected to be discovered by the upcoming photometric space-based missions. WASP-47 is currently the only known compact multi-planet system with a close-in hot Jupiter, which has important implications on our understanding of planet formation and migration. The high photometric precision and near-all-sky coverage of the *TESS* mission will provide an excellent platform to search for planetary configurations similar to WASP-47 and provide clues on how rare they are. This research project refined the system parameters of highly-inflated warm super-Neptune WASP-107b and revealed that its orbit is misaligned with stellar rotation. Its large atmospheric scale height and a bright but small host star make WASP-107 a prime target for atmospheric characterisation by *JWST*, which may provide additional clues on which mechanism(s) triggered the pronounced inflation of the planet.

Our knowledge of exoplanets has improved immensely through the *Kepler* and *K2* missions, which pioneered the space-based observations dedicated to exoplanets. Now with *TESS* already launched, and other upcoming space-based exoplanet surveys, we are destined to learn more than ever before about planets orbiting stars other than the Sun.

Acronyms

BJD	barycentric Julian date
BLS	box-fitting least squares
FOV	field of view
FWHM	full width at half maximum
LS	Lomb–Scargle (periodogram)
MAST	Mikulski Archive for Space Telescopes
MCMC	Markov chain Monte Carlo
ppm	parts per million
PRF	pixel response function
PSF	point spread function
RM	Rossiter–McLaughlin (effect)
RV	radial velocity
SFF	self-flat-fielding
TDV	transit-duration variation
TPF	target pixel file
TTV	transit-timing variation
WASP	Wide Angle Search for Planets

Publications

In this chapter I list all publications that were submitted during my PhD, between 2015 January 5 and 2018 June 7. Publications are ordered from earliest to most recent.

Lead-authored

The Central Star Candidate of the Planetary Nebula Sh2-71: Photometric and Spectroscopic Variability
Močnik T., Lloyd M., Pollacco D., Street R. A.
MNRAS, 2015, 451, 870
(based on the MSc research project)

Starspots on WASP-85
Močnik T., Clark B. J. M., Anderson D. R., Hellier C., Brown D. J. A.
AJ, 2016, 151, 150

WASP-157b, a Transiting Hot Jupiter Observed with *K2*
Močnik T., Anderson D. R., Brown D. J. A., Collier Cameron A., Delrez L., Gillon M., Hellier C., Jehin E., Lendl M., Maxted P. F. L., Neveu-VanMalle M., Pepe F., Pollacco D., Queloz D., Ségransan D., Smalley B., Southworth J., Triaud A. H. M. J., Udry S., West R. G.
PASP, 2016, 128, 124403

Starspots on WASP-107 and Pulsations of WASP-118
Močnik T., Hellier C., Anderson D. R., Clark B. J. M., Southworth J.
MNRAS, 2017, 469, 1622

Recurring Sets of Recurring Starspot Occultations on Exoplanet Host Qatar-2
Močnik T., Southworth J., Hellier C.
MNRAS, 2017, 471, 394

***K2* Looks towards WASP-28 and WASP-151**

Močnik T., Hellier C., Anderson D. R.

AJ, submitted, 2017, arXiv:1710.08892

Ephemeris Refinement of a Hot Jupiter K2-140b

Močnik T., Hellier C., Anderson D. R.

RNAAS, 2018, 2, 22

WASP-104b is Darker than Charcoal

Močnik T., Hellier C., Southworth J.

AJ, accepted, 2018, arXiv:1804.05334

Co-authored

First EURONEAR NEA Discoveries from La Palma Using the INT

Vaduvescu O., Hudin L., Tudor V., Char F., Močnik T., and 49 others

MNRAS, 2015, 449, 1614

(observing, searching and measuring positions of asteroids in INT images)

The EURONEAR Lightcurve Survey of Near Earth Asteroids

Vaduvescu O., and 26 others

EM&P, 2017, 120, 41

(observing at INT)

280 One-opposition Near-Earth Asteroids Recovered by the EURONEAR with the Isaac Newton Telescope

Vaduvescu O., Hudin L., Močnik T., and 80 others

A&A, 2018, 609, A105

(observing, searching and measuring positions of asteroids in INT images)

An Analysis of Transiting Hot Jupiters Observed with *K2*: WASP-55b and WASP-75b

Clark B. J. M., Anderson D. R., Hellier C., Turner O. D., Močnik T.

PASP, 2018, 130, 034401

(initial data reduction, quick search for interesting astrophysical signals)

References

Aerts C., Christensen-Dalsgaard J., Kurtz D. W., 2010, Asteroseismology, A&A Library, Springer, London
Aerts C. et al., 2017, PLATO Red Book, ESA-SCI(2017)1
Agol E., Steffen J., Sari R., Clarkson W., 2005, MNRAS, 359, 567
Aigrain S., Hodkin S. T., Irwin M. J., Lewis J. R., Roberts S. J., 2015, MNRAS, 447, 2880
Aigrain S., Parviainen H., Pope B. J. S., 2016, MNRAS, 459, 2408
Akeson R. L. et al., 2013, PASP, 125, 989
Albrecht S. et al., 2012, ApJ, 757, 18
Anderson D. R. et al., 2012, MNRAS, 422, 1988
Anderson D. R. et al., 2015, A&A, 575, A61
Anderson D. R. et al., 2017, A&A, 604, A110
Angerhausen D., DeLarme E., Morse J. A. 2015, PASP, 127, 1113
Armstrong D. J. et al., 2016, MNRAS, 456, 2260
Ascough P. L. et al., 2010, Journal of Archaeological Science, 37, 1590
Asplund M., Grevesse N., Sauval A. J., Scott P., 2009, ARA&A, 47, 481
Baglin A. et al., 2006, in ESA Special Publication, 1306
Bakos G. et al., 2004, PASP, 116, 266
Ballard S. et al., 2010, PASP, 122, 1341
Barclay T. et al., 2012, ApJ, 761, 53
Barclay T., Pepper J., Quintana E. V., 2018, arXiv:1804.05050
Barentsen G., 2016, Kadenza: v1.0.0, doi:10.5281/zenodo.45051
Barentsen G., 2017, KeplerGO/kadenza: v2.0.2, doi:10.5281/zenodo.344973
Barentsen G., 2018, K2 Campaign Fields, [electronic source], available at: https://keplerscience.arc.nasa.gov/k2-fields.html (accessed 2018 May 24)
Barnes S. A., 2003, ApJ, 586, 464
Barnes S. A., 2007, ApJ, 669, 1167
Barros S. C. C., Demangeon O., Deleuil M., 2016, A&A, 594, 100
Bashi D., Helled R., Zucker S., Mordasini C., 2017, A&A, 604, A83
Basri G. et al., 2010, ApJL, 713, L155
Baudin F. et al., 2011, A&A, 529, A84
Baumann P., Ramírez I., Meléndez J., Asplund M., Lind K., 2010, A&A, 519, A87
Bayliss D. et al., 2017, arXiv:1706.03858
Bazot M., Vauclair S., Bouchy F., Santos N. C., 2005, A&A, 440, 615
Becker J. C., Vanderburg A., Adams F. C., Rappaport S. A., Schwengeler H. M., 2015, ApJL, 812, L18
Beichman C. et al., 2014, PASP, 126, 1134
Bell T. J. et al., 2018, ApJL, 847, L2
Borucki W. J. et al., 2010, Science, 327, 977
Borucki W. J. et al., 2011, ApJ, 736, 19
Bouchy F. et al., 2009, A&A, 505, 853
Bouma L. G., Winn J. N., Kosiarek J., McCullough P. R., 2017, arXiv:1705.08891
Bradshaw S. J., Hartigan P., 2014, ApJ, 795, 79
Broeg C. et al., 2013, in European Physical Journal Web of Conferences, Vol. 47, European Physical Journal Web of Conferences, 03005
Brown D. J. A. et al., 2014, arXiv:1412.7761
Brown T. M. et al., 2013, PASP, 125, 1031
Bryan M. L. et al., 2012, ApJ, 750, 84
Bryan M. L. et al., 2014, ApJ, 782, 121

Bryson S. T. et al., 2010a, in Proc. SPIE Vol. 7740, Software and Cyberinfrastructure for Astronomy, 77401D
Bryson S. T. et al., 2010b, ApJL, 713, L97
Burrows A. et al., 1996, NuPhS, 51, 76
Burrows A. et al., 2000, ApJL, 534, L97
Burrows A., Hubeny I., Budaj J., Hubbard W. B., 2007, ApJ, 661, 502
Burrows A., Ibgui L., Hubeny I., 2008, ApJ, 682, 1277
Campante T. L. et al., 2016, ApJ, 819, 85
Carrington R. C., 1863, Observations of the Spots on the Sun from November 9, 1853, to March 24, 1861, made at Redhill, London/Edinburgh
Chabrier G., Baraffe I., 2007, ApJL, 661, L81
Charbonneau D. et al., 2005, ApJ, 626, 523
Christian D. J. et al., 2006, MNRAS, 372, 1117
Christiansen J. L. et al., 2012, PASP, 124, 1279
Claret A., 2000, A&A, 363, 1081
Claret A., 2004, A&A, 428, 1001
Clark B. J. M., Anderson D. R., Hellier C., Turner O. D., Močnik T., 2018, PASP, 130, 034401
Cochran W. D. et al., 2011, ApJS, 197, 7
Collier Cameron A. et al., 2006, MNRAS, 373, 799
Collier Cameron A. et al., 2007, MNRAS, 380, 1230
Collier Cameron A., Bruce V. A., Miller G. R. M., Triaud A. H. M. J., Queloz D., 2010a, MNRAS, 403, 151
Collier Cameron A. et al., 2010b, MNRAS, 407, 507
Collins K. A. et al., 2018, arXiv:1803.01869
Cowan N. B., Agol E., Charbonneau D., 2007, MNRAS, 379, 641
Cowan N. B. et al., 2015, PASP, 127, 311
Cox A. N., 2000, in Allen's Astrophysical Quantities, Springer, New York
Cumming A., Marcy G. W., Butler R. P., 1999, ApJ, 526, 890
Daemgen S. et al., 2009, A&A, 498, 567
Dai F., Winn J. N., Yu L., Albrecht S., 2017, AJ, 153, 40
Dai F., Winn J. N., 2017, AJ, 153, 205
Dai F. et al., 2018, AJ, 155, 177
Davies G. R. et al., 2016, MNRAS, 456, 2183
de Wit J. et al., 2017, ApJ, 836, L17
Demangeon O. D. S. et al., 2018, A&A, 610, A63
Demory B.-O. et al. 2011, ApJL, 735, L12
Demory B.-O., 2014, ApJL, 789, L20
Désert J.-M. et al., 2011, ApJS, 197, 14
Dobbs-Dixon I., Lin D. N. C., Mardling R. A., 2004, ApJ, 610, 464
Doyle A. P. et al., 2013, MNRAS, 428, 3164
Doyle A. P., Davies G. R., Smalley B., Chaplin W. J., Elsworth Y., 2014, MNRAS, 444, 3592
Dumusque X., Boisse I, Santos N. C., 2014, ApJ, 796, 132
Eastman J., Siverd R., Gaudi B. S., 2010, PASP, 122, 935
Espinosa Lara F., Rieutord M., 2011, A&A, 533, A43
Esposito M. et al., 2017, A&A, 601, A53
Esteves L. J., De Mooij E. J. W., Jayawardhana R., 2013, ApJ, 772, 51
Evans D. F. et al., 2016, A&A, 589, A58
Feiden G. A., Chaboyer B., 2013, ApJ, 779, 183
Foreman-Mackey D., 2016, The Journal of Open Source Software, 24, doi:10.5281/zenodo.45906
Fortney J. J., Nettelmann N., 2010, SSRv, 152, 423
Fressin F. et al., 2013, ApJ, 766, 81
Gardner J. P. et al., 2006, SSRv, 123, 485
Gaudi B. S., Winn J. N., 2007, ApJ, 655, 550
Geier S. et al., 2007, A&A, 464, 299
Giles H. A. C. et al., 2018, MNRAS, 475, 1809
Gillon M. et al., 2009, A&A, 501, 785

Gillon M. et al., 2011, in European Physical Journal Web of Conferences, Vol. 11, European Physical Journal Web of Conferences, 06002
Goldreich P., Tremaine S., 1980, ApJ, 241, 425
Gómez Maqueo Chew Y. et al., 2013, A&A, 559, A36
Groot P. J., 2012, ApJ, 745, 55
Gyenge N., Baranyi T., Ludmány A., 2014, Sol. Phys., 289, 579
Haas M. R. et al., 2010, ApJL, 713, L115
Hartman J. D. et al., 2011, AJ, 141, 166
Hartman J. D. et al., 2016, AJ, 152, 182
Hay K. L. et al., 2016, MNRAS, 463, 3276
Hellier C. et al., 2009, Nature, 460, 1098
Hellier C. et al., 2011, A&A, 535, L7
Hellier C. et al., 2011, ApJL, 730, L31
Hellier C. et al., 2012, MNRAS, 426, 739
Heng K., Demory B.-O., 2013, ApJ, 777, 100
Herrero E., Morales J. C., Ribas I., Naves R., 2011, A&A, 526, L10
Hirano T. et al, 2011, ApJ, 742, 69
Hirano T. et al., 2012, A&A, 545, 109
Høg E. et al., 2000, A&A, 355, L27
Holman M. J., Murray N. W., 2005, Science, 307, 1288
Holman M. J. et al., 2010, Science, 330, 51
Howard A. W. et al., 2012, ApJS, 201, 15
Howell S. B. et al., 2014, PASP, 126, 398
Huang C. X. et al., 2015, AJ, 150, 85
Huber D. et al., 2016, ApJS, 224, 2
IAU, 2006, 26th General Assembly of the IAU, Resolution 5A, [electronic source], available at: http://www.iau.org/news/pressreleases/detail/iau0603/ (accessed 7 May 2018)
Jackson B., Greenberg R., Barnes R., 2008, ApJ, 678, 1396
Jackson B. K. et al., 2012, ApJ, 751, 112
Jehin E. et al., 2011, The Messenger, 145, 2
Jenkins J. M., Doyle L. R., 2003, ApJ, 595, 429
Jones E., Oliphant T., Peterson P., 2001, SciPy: Open Source Scientific Tools for Python, available at: http://www.scipy.org/
Kaye A. B., Handler G., Krisciunas K., Poretti E., Zerbi F. M., 1999, PASP, 111, 840
Kipping D. M., 2009, MNRAS, 392, 181
Kipping D., Bakos G., 2011, ApJ, 733, 36
Kipping D. M., Spiegel D. S., 2011, MNRAS, 417, L88
Kipping D. M., 2012, MNRAS, 427, 2487
Konacki M., Wolszczan A., 2003, ApJL, 591, L147
Kovács G., Zucker S., Mazeh T., 2002, A&A, 391, 369
Kraft R. P., 1967, ApJ, 150, 551
Kreidberg L. et al., 2018, ApJL, 858, L6
Kron G. E., 1947, PASP, 59, 261
Lanza A. F., Rodonò M., Pagano I., Barge P., Llebaria A., 2003, A&A, 403, 1135
Leconte J., Baraffe I., Chabrier G., Barman T., Levrard B., 2009, A&A, 506, 385
Leconte J., Chabrier G., Baraffe I., Levrard B., 2010, A&A, 516, A64
Lendl M. et al., 2012, A&A, 544, A72
Lin D. N. C., Bodenheimer P., Richardson D. C., 1996, Nature, 380, 606
Lithwick Y., Xie J., Wu Y., 2012, ApJ, 761, 122
Loeb A., Gaudi. B. S., 2003, ApJL, 588, L117
Ludwig H.-G., Caffau E., Kučinskas A., 2008, in Deng L., Chan K. L., eds, IAU Symp. Vol. 252, The Art of Modelling Stars in the 21st Century. Cambridge Univ. Press, Cambridge, p. 75
Luger R. et al., 2016, AJ, 152, 100
Luger R., Kruse E., Foreman Mackey D., Agol E., Saunders N., 2017, arXiv:1702.05488
Luger R. et al., 2017, NatAs, 1, 0129
Maciejewski G. et al., 2016, Acta Astron., 66, 55

Madhusudhan N., Burrows A., 2012, ApJ, 747, 25
Mallama A., Krobusek B., Pavlov H., 2016, Icarus, 282, 19
Malavolta L. et al., 2018, AJ, 155, 107
Mamajek E. E., Hillenbrand L. A., 2008, ApJ, 687, 1264
Mancini L. et al., 2014, MNRAS, 443, 2391
Mancini L. et al., 2016, MNRAS, 462, 4266
Mancini L. et al., 2017, MNRAS, 465, 843
Mandal S., Karak B. B., Banerjee D., 2017, ApJ, 851, 70
Mandel K., Agol E., 2002, ApJ, 580, L171
Maxted P. F. L., Marsh T. R., North R. C., 2000, MNRAS, 317, L41
Maxted P. F. L. et al., 2011, PASP, 123, 547
Maxted P. F. L., Serenelli A. M., Southworth J., 2015a, A&A, 575, A36
Maxted P. F. L., Serenelli A. M., Southworth J., 2015b, A&A, 577, A90
Maxted P. F. L. et al., 2016, A&A, 591, A55
Mayor M., Queloz D., 1995, Nature, 378, 355
Mayor M. et al., 2003, The Messenger, 114, 20
Mazeh T., 2008, EAS Publications Series, 29, 1
Mazeh T., Faigler S., 2010, A&A, 521, L59
Mazeh T. et al., 2013, ApJS, 208, 16
Mazeh T., Holczer T., Faigler S., 2016, A&A, 589, A75
McIntosh P. S., 1981, in Cram L. E., Thomas J. H., eds, The Physics of Sunspots. Sacramento Peak National Observatory, Sunspot, NewMexico, p. 7
McLaughlin D. B., 1924, ApJ, 60, 22
McQuillan A., Aigrain S., Roberts S., 2012, A&A, 539, A137
McQuillan A., Aigrain S., Mazeh T., 2013, MNRAS, 432, 1203
McQuillan A., Mazeh T., Aigrain S., 2014, ApJS, 211, 24
Millholland S., Laughlin G., 2017, AJ, 154, 83
Močnik T., Clark B. J. M., Anderson D. R., Hellier C., Brown D. J. A., 2016a, AJ, 151, 150
Močnik T. et al., 2016b, PASP, 128, 124403
Močnik T., Hellier C., Anderson D. R., Clark B. J. M., Southworth J., 2017, MNRAS, 469, 1622
Močnik T., Southworth J., Hellier C., 2017, MNRAS, 471, 394
Močnik T., Hellier C., Anderson D. R., 2017, arXiv:1710.08892
Močnik T., Hellier C., Anderson D. R., 2018, RNAAS, 2, 22
Močnik T., Hellier C., Southworth J., 2018, arXiv:1804.05334
Morales J. C., Gallardo J., Ribas I., Jordi C., Baraffe I., Chabrier G., 2010, ApJ, 718, 502
Mordasini C., Alibert Y., Klahr H., Henning T., 2012, A&A, 547, A111
Morris B. M., Mandell A. M., Deming D., 2013, ApJL, 764, L22
Morris B. M., Agol E., Hebb L., Hawley S. L., 2018, AJ, 156, 91
Morris S. L., 1985, ApJ, 295, 143
Mortier A. et al., 2013, A&A, 558, A106
Morton T. D. et al., 2016, ApJ, 822, 86
Murgas F. et al., 2014, A&A, 563, A41
Nesvorný D. et al., 2013, ApJ, 777, 3
Neilson H. R. et al., 2017, ApJ, 845, 65
Nielsen M. B., Gizon L., Schunker H., Karoff C., 2013, A&A, 557, L10
Noyes R. W., Hartmann L. W., Baliunas S. L., Duncan D. K., Vaughan A. H., 1984, ApJ, 279, 763
Nutzman P. A., Fabrycky D. C., Fortney J. J., 2011, ApJL, 740, L10
Oshagh M. et al., 2013, A&A, 556, A19
Pepe F. et al., 2002, A&A, 388, 632
Petrucci R., Jofré E., Melita M., Gómez M., Mauas P., 2015, MNRAS, 446, 1389
Pfahl E., Arras P., Paxton B., 2008, ApJ, 679, 783
Pizzolato N., Maggio A., Micela G., Sciortino S., Ventura P., 2003, A&A, 397, 147
Pollacco D. L. et al., 2006, PASP, 118, 1407
Pollacco D. L. et al., 2008, MNRAS, 385, 1576
Pont F., 2009, MNRAS, 396, 1789

Popper D. M., Etzel P. B., 1981, AJ, 86, 102
Popper D. M., 1997, AJ, 114, 1195
Prša A. et al., 2016, ApJS, 227, 29
Queloz D. et al., 2000a, A&A, 354, 99
Queloz D. et al., 2000b, A&A, 359, L13
Queloz D. et al., 2001, A&A, 379, 279
Quintana E. V. et al., 2010, in Proc. SPIE, Vol. 7740, Software and Cyberinfrastructure for Astronomy, 77401X
Rauer H. et al., 2014, Experimental Astronomy, 38, 249
Rebull L. M. et al., 2016, AJ, 152, 113
Ricker G. R. et al., 2015, JATIS, 1, 014003
Rodríguez A., Ferraz-Mello S., Michtchenko T. A., Beaugé C., Miloni O., 2011, MNRAS, 415, 2349
Rossiter R. A., 1924, ApJ, 60, 15
Rowe J. F. et al., 2008, ApJ, 689, 1345
Rowe J. F. et al., 2014, ApJ, 784, 45
Rybicki G. B., Lightman A. P., 1979, Radiative Processes in Astrophysics, Wiley Interscience, New York
Sanchis-Ojeda R. et al., 2011, ApJ, 733, 127
Sanchis-Ojeda R., Winn J. N., 2011, ApJ, 743, 61
Sanchis-Ojeda R. et al., 2012, Nature, 487, 449
Sanchis-Ojeda R. et al., 2013, ApJ, 775, 54
Savini G. et al., 2016, in Proc. SPIE Vol. 9904, Space Telescopes and Instrumentation 2016, 99044M
Schuh S., 2010, Astron. Nachr., 331, 489
Schwartz J. C., Cowan N. B., 2015, MNRAS, 449, 4192
Seager S., Mallén-Ornelas G., 2003, ApJ, 585, 1038
Seager S., 2010. Exoplanets, University of Arizona Press, Tuscon
Sestito P., Randich S., 2005, A&A, 442, 615
Sestovic M., Demory B.-O., Queloz D., 2018, arXiv:1804.03075
Shapiro A. I., Solanki S. K., Krivova N. A., Yeo K. L., Schmutz W. K., 2016, A&A, 589, A46
Shaya E. J., Olling R., Mushotzky R., 2015, AJ, 150, 188
Sheets H. A., Deming D., 2017, AJ, 154, 160
Shen Y., Turner E. L., 2008, ApJ, 685, 553
Shporer A. et al., 2010, ApJL, 725, L200
Shporer A., 2017, PASP, 129, 072001
Silva A. V. R., 2003, ApJL, 585, L147
Silva-Valio A., 2008, ApJL, 683, L179
Silvotti R. et al., 2007, Nature, 449, 189
Silvotti R. et al., 2014, A&A, 570, A130
Sing D. K., 2010, A&A, 510, A21
Smith A. M. S. et al., 2014, A&A, 570, A64
Sobeck C., Johnson M., 2014, *K2* has been Approved, [electronic source], available at: https://www.nasa.gov/content/ames/kepler-mission-manager-update-k2-has-been-approved (accessed 2018 May 15)
Solanki S. K., 2003, A&ARv, 11, 153
Souami D., Souchay J., 2012, A&A, 543, A133
Southworth J., Maxted P. F. L., Smalley B., 2004, MNRAS, 351, 1277
Southworth J., 2011, MNRAS, 417, 2166
Southworth J., 2013, A&A, 557, A119
Southworth J. et al., 2016, MNRAS, 457, 4205
Stark D., Wöhl H., 1981, A&A, 93, 241
Still M., Barclay T., 2012, PyKE: Reduction and Analysis of Kepler Simple Aperture Photometry Data, Astrophysics Source Code Library, ascl:1208.004
Still M., 2013, Signal-to-Noise Characteristics, [electronic source], available at: http://keplergo.arc.nasa.gov/CalibrationSN.shtml (accessed 2018 May 21)
Stumpe M. C. et al., 2012, PASP, 124, 985

Sudarsky D., Burrows A., Pinto P., 2000, ApJ, 538, 885

Teachey A., Kipping D. M., Schmitt A. R., 2018, AJ, 155, 36

Thompson S. E., Fraquelli D., Van Cleve J. E., Caldwell D. A., 2016, Kepler Archive Manual, KDMC-10008-006

Tinetti G. et al., 2016, in Proc. SPIE Vol. 9904, Space Telescopes and Instrumentation 2016, 99041X

Tregloan-Reed J., Southworth J., Tappert C., 2013, MNRAS, 428, 3671

Tregloan-Reed J. et al., 2015, MNRAS, 450, 1760

Triaud A. H. M. J. et al., 2010, A&A, 524, A25

Triaud A. H. M. J., 2017, The Rossiter–McLaughlin Effect in Exoplanet Research. In: Deeg H., Belmonte J. (eds) Handbook of Exoplanets. Springer, Cham

Van Cleve J., Caldwell D. A, Haas M. R., Howell S. T., 2016a, Kepler Instrument Handbook, KSCI-19033-002

Van Cleve J. E. et al., 2016b, PASP, 128, 075002

Van Cleve J., Bryson S., 2017, K2 Handbook, KSCI-19116-001

Van Eylen V. et al., 2018, arXiv:1805.01860

Vanderburg A., Johnson J. A., 2014, PASP, 126, 948

Vogt S. S., 1975, ApJ, 199, 418

Wang J., Fischer D. A., Horch E. P., Huang X., 2015, ApJ, 799, 229

Wang J. R., Cole S., Northon K., 2018, JWST Press Release 18-019, [electronic source], available at: https://www.nasa.gov/press-release/nasa-s-webb-observatory-requires-more-time-for-testing-and-evaluation-new-launch (accessed 2018 June 6)

Wang X.-B. et al., 2014, AJ, 147, 92

Weiss A., Schlattl H., 2008, Ap&SS, 316, 99

Weiss L. M. et al., 2013, ApJ, 768, 14

Welsh W. F. et al., 2010, ApJL, 713, L145

WGESP, 2003, Definition of a Planet, [electronic source], available at: http://w.astro.berkeley.edu/~basri/defineplanet/IAU-WGExSP.htm (accessed 2018 May 7)

Winn J. N. et al., 2005, ApJ, 631, 1215

Winn J. N., Fabrycky D., Albrecht S., Johnson J. A., 2010a, ApJL, 718, L145

Winn J. N. et al., 2010b, ApJL, 723, L223

Winn J. N., 2010, Exoplanet Transits and Occultations. In: Seager S. (ed.) Exoplanets, University of Arizona Press, pp 55–77, arXiv:1001.2010

Winn J. N., Fabricky D. C., 2015, ARA&A, 53, 409

Wong I. et al., 2016, ApJ, 823, 122

Wright J. T. et al., 2012, ApJ, 753, 160